

AD-A258 001


2

FINAL REPORT

Air Force Office of Scientific Research

Award #F49620-89-C-0056 P00004

Wafer Scale Union

from 4/01/89 to 5/31/92

Principal Investigator:

Harold Fetterman

Professor

Department of Electrical Engineering

UCLA

Los Angeles, CA 90024

Scientific Program Officer:

Dr. H.R. Schlossberg

Directorate of Electronic and Material Sciences

AFOSR/NE Bldg 410

Bolling AFB

Washington, DC 20332-6448

and is
-12

DTIC
ELECTE
NOV 25 1992
S A D

This document has been approved
for public release and sale; its
distribution is unlimited.

REPORT DOCUMENTATION PAGE

Form Approved
OMB No. 0704-0188

Public reporting burden for this collection of information is estimated to average 1 hour per response, including the time for reviewing instructions, searching existing data sources, gathering and maintaining the data needed, and completing and reviewing the collection of information. Send comments regarding this burden estimate or any other aspect of this collection of information, including suggestions for reducing this burden, to Washington Headquarters Services, Directorate for Information Operations and Reports, 1215 Jefferson Davis Highway, Suite 1204, Arlington, VA 22202-4302, and to the Office of Management and Budget, Paperwork Reduction Project (0704-0188), Washington, DC 20503.

1. AGENCY USE ONLY (Leave blank)		2. REPORT DATE		3. REPORT TYPE AND DATES COVERED FINAL 01 Apr 89 TO 31 May 92	
4. TITLE AND SUBTITLE Wafer Scale Union				5. FUNDING NUMBERS F49620-89-C-0056	
6. AUTHOR(S) Professor Harold Fetterman					
7. PERFORMING ORGANIZATION NAME(S) AND ADDRESS(ES) Univ of California Department of Electrical Engineering Los Angeles, CA 90024				8. PERFORMING ORGANIZATION REPORT NUMBER AFOSR-TR 92 69 24	
9. SPONSORING / MONITORING AGENCY NAME(S) AND ADDRESS(ES) AFOSR/NE Bldg 410 Bolling AFB Washington DC 20332-6448 Dr. Howard Schlossberg				10. SPONSORING / MONITORING AGENCY REPORT NUMBER 2301/AS	
11. SUPPLEMENTARY NOTES					
12a. DISTRIBUTION / AVAILABILITY STATEMENT APPROVED FOR PUBLIC RELEASE: DISTRIBUTION IS UNLIMITED				12b. DISTRIBUTION CODE	
13. ABSTRACT (Maximum 200 words) The program we have completed will be discussed in three basic sections. The first will deal with the important developments in optically controlled generation of millimeter waves. This work started from earlier results of mixing high frequencies internally using FETs and HEMTs. In this study, these initial experiments were successfully extended to radiating systems in free space to using new HBTs and semiconductor laser. Section (B) will deal with our advanced picosecond measurements and HEMTs, HBTs and Hot Electron Transistors. It will also present our measurement of bandwidths of channel guides on wafer using our mixing and picosecond techniques. Finally, in section (C), we discuss the new Quantum Well Impatt, polymer modulators, optical guide developments and InSb devices. Many of these new concepts are just becoming experiment. The overall view of integration is discussed in this third section.					
14. SUBJECT TERMS				15. NUMBER OF PAGES	
				16. PRICE CODE	
17. SECURITY CLASSIFICATION OF REPORT		18. SECURITY CLASSIFICATION OF THIS PAGE		19. SECURITY CLASSIFICATION OF ABSTRACT	
UNCLASSIFIED		UNCLASSIFIED		UNCLASSIFIED	
20. LIMITATION OF ABSTRACT				21. LIMITATION OF ABSTRACT	
UNLIMITED				UNLIMITED	

NSN 7540-01-280 5300

Standard Form 298 (Rev. 2-89)
Prescribed by ANSI Std. Z39.18
298-102

Table of Contents

Introduction	1
Program Description	2
Section A: Optical Generation of Millimeter Waves	3
Section B: High Frequency Testing	10
Optical Interconnection	16
Section C: New Device and Material Technology	18
Modulator and Phase Shifter	24
Conclusion	28

Accession For	
NTIS CRA&I	<input checked="" type="checkbox"/>
DTIC TAB	<input type="checkbox"/>
Unannounced	<input type="checkbox"/>
Justification	
By	
Distribution /	
Availability Codes	
Dist	Availability / Special
A-1	

DTIC QUALITY INSPECTED 4

92-30164



13680

Wafer Scale Union

Final Report

Introduction

This report covers the period 4/01/89 to 5/31/92 of contract #F49620-89-C-0056 P00004. The investigation supported by this contract was a study of the optical control and interconnection of high frequency devices. In particular, the control aspect studied the use of light to generate millimeter waves from three-terminal semiconductor devices. The interconnection portion involved on-wafer light guides, high frequency polymer modulators, and the use of picosecond, mode locked semiconductor lasers.

New devices and systems were extensively explored as part of this effort. These range from the direct-write polyimide waveguide and polymer modulators to new types of hot electron transistors and optically driven Quantum Well Impatts. In an effort to integrate our systems with silicon, we also fabricated InSb devices on silicon using a radical new approach.

Our picosecond testing program was also significantly extended to measurements of optical responses of HEMTs and HBTs to well over 100 GHz. Other response experiments were made on hot electron and MMIC circuits for the first time. These picosecond measurements were also used to measure our optical guide bandwidth in a series of novel experiments.

Virtually all of the pieces discussed in our Wafer Scale Union

proposal have been successfully investigated. The actual components are currently being brought together to examine the concept of actually using them in a wafer scale integrated system.

Program Description

The program we have completed will be discussed in three basic sections. The first will deal with the important developments in optically controlled generation of millimeter waves. This work started from earlier results of mixing high frequencies internally using FETs and HEMTs. In this study, these initial experiments were successfully extended to radiating systems in free space to using new HBTs and semiconductor lasers.

Section (B) will deal with our advanced picosecond measurements and HEMTs, HBTs and Hot Electron Transistors. It will also present our measurements of bandwidths of channel guides on wafers using our mixing and picosecond techniques.

Finally, in section (C), we discuss the new Quantum Well Impatt, polymer modulators, optical guide developments and InSb devices. Many of these new concepts are just becoming sufficiently developed to be useful in our Wafer Scale Union experiment. The overall view of integration is discussed in this third section.

Section A: Optical Generation of Millimeter Waves

Numerous researchers have demonstrated that FETs, HEMTs and HBTs can be used as optical detectors. Using mixing techniques we have shown that these systems can work well over 100 GHz. They have performance considerably above f_T since they have reduced input parasitics in this application. Our effort here is unique in that we actually generate radiating millimeter waves from optically coupled devices.

Picosecond excitation was first used in these experiments because of its power levels and simplicity of operation. In Figure 1, we showed the basic system using an antenna structure developed

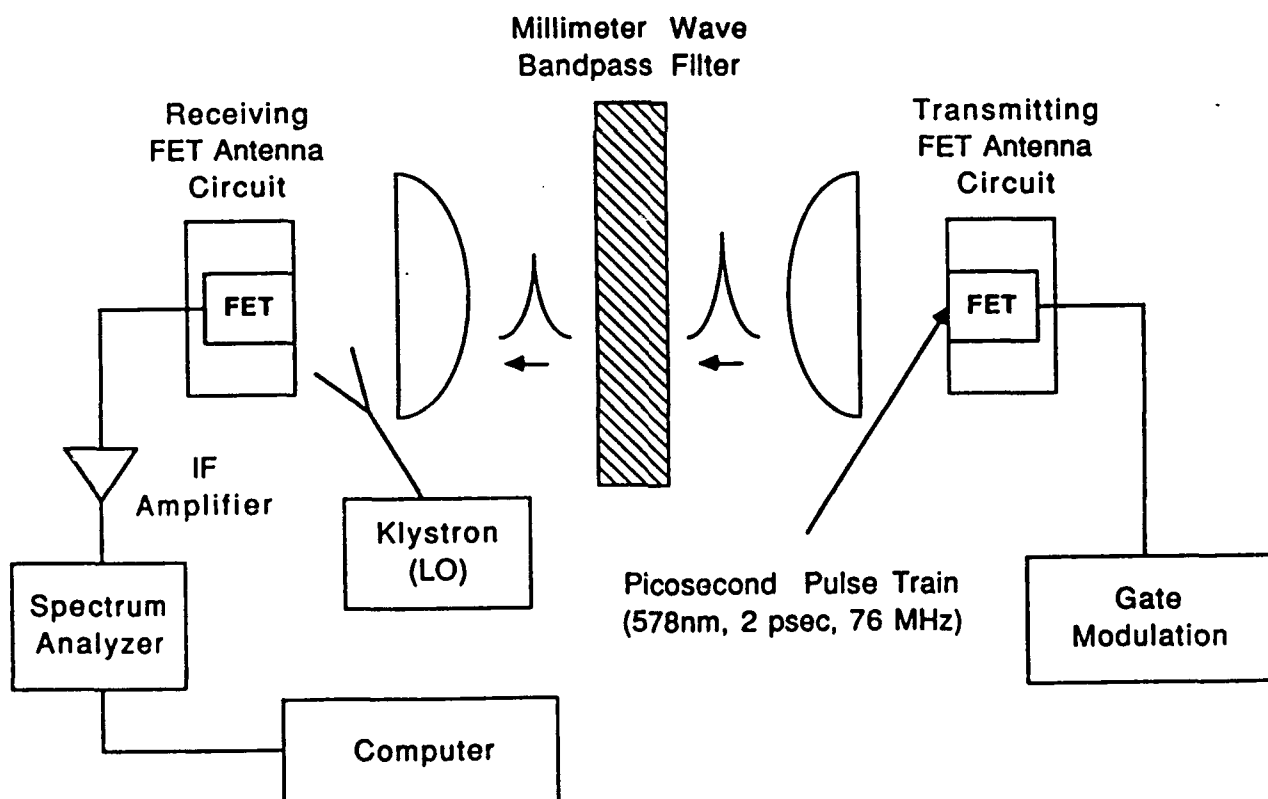


Figure 1: System using FETs switched with optical picosecond pulses and having integrated antenna structures.

earlier. The signal (Figure 2) was radiated and heterodyne

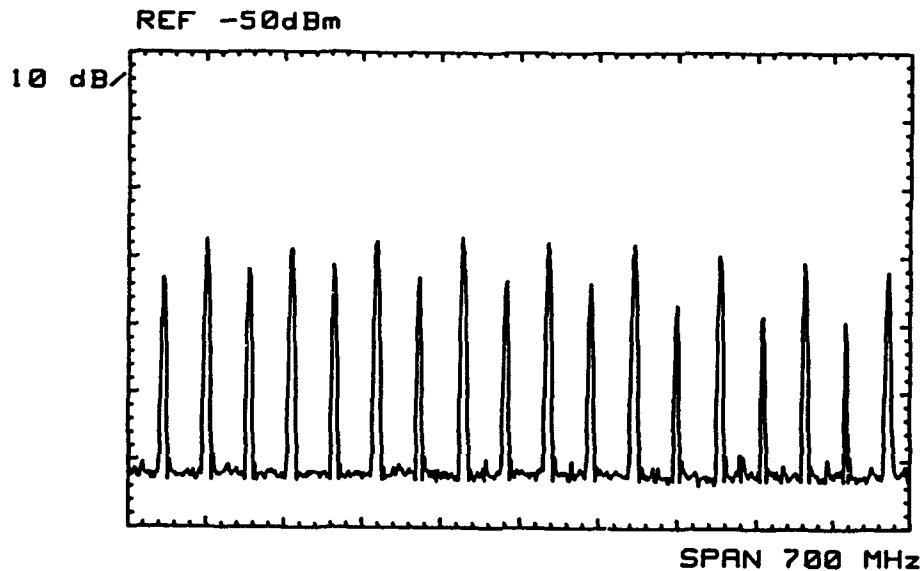


Figure 2: Millimeter wave signal mixed and displayed on spectrum analyzer.

detected by a similar FET-planar antenna system. The system had immediate application for real time spectroscopy and the results are shown in Figure 3.

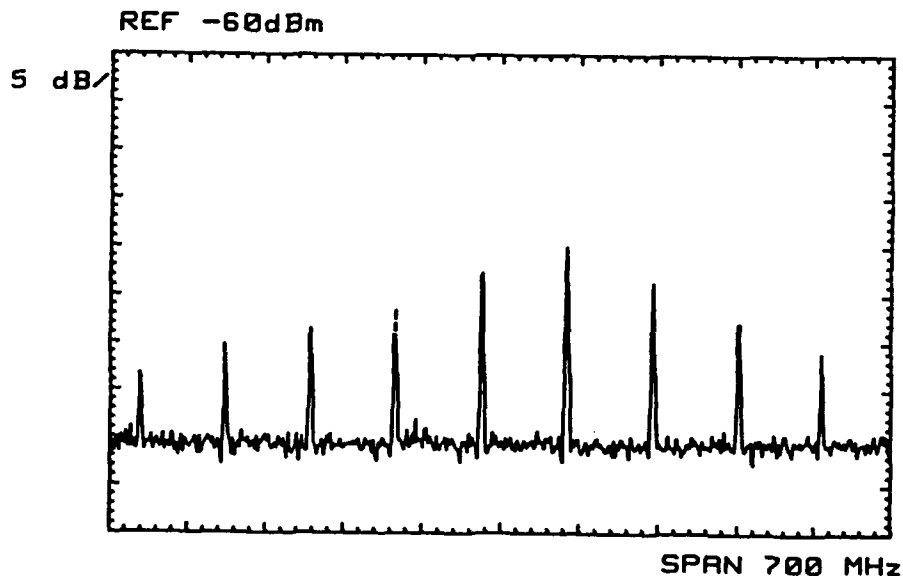


Figure 3: Transmitted signal through filter. Note that the lower sideband is completely attenuated.

The next step was to do this generation experiment via mixing cw lasers. Configured in a transmitter/receiver system (Figure 4),

CW Millimeter Wave Radiation

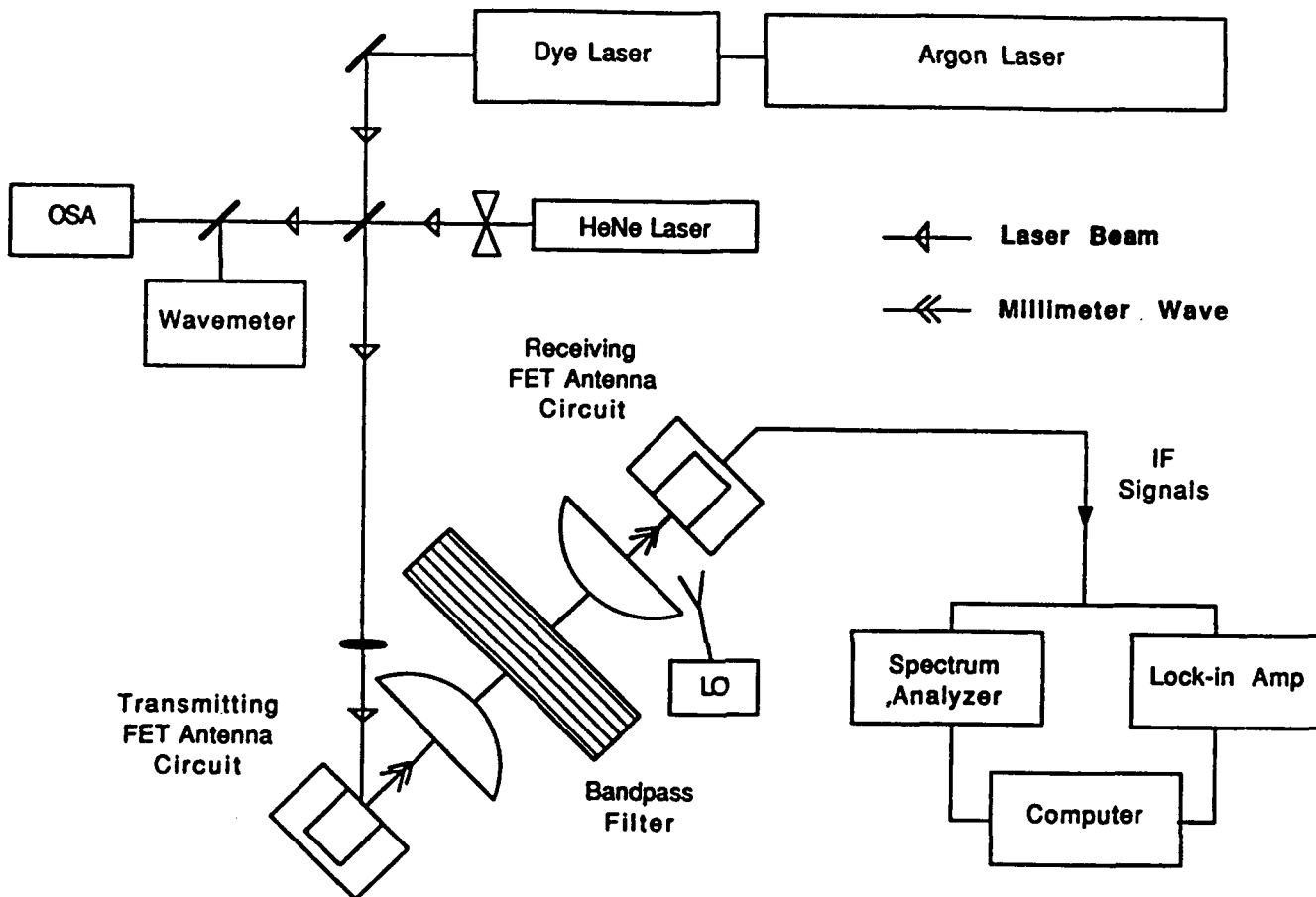


Figure 4: Setup for CW generation of millimeter waves using a tunable dye laser.

we obtained the mixing signal shown in Figure 5. It was possible to hold the HeNe laser frequency constant and tune the dye laser over 30 GHz to get tunable output². Furthermore, by putting a microwave signal on the gate, it was possible to continuously tune the system for high resolution studies (Figure 6). Expanding further, the next step was to increase the power and flexibility of this approach by adding fiber optical inputs and MMIC amplifiers³

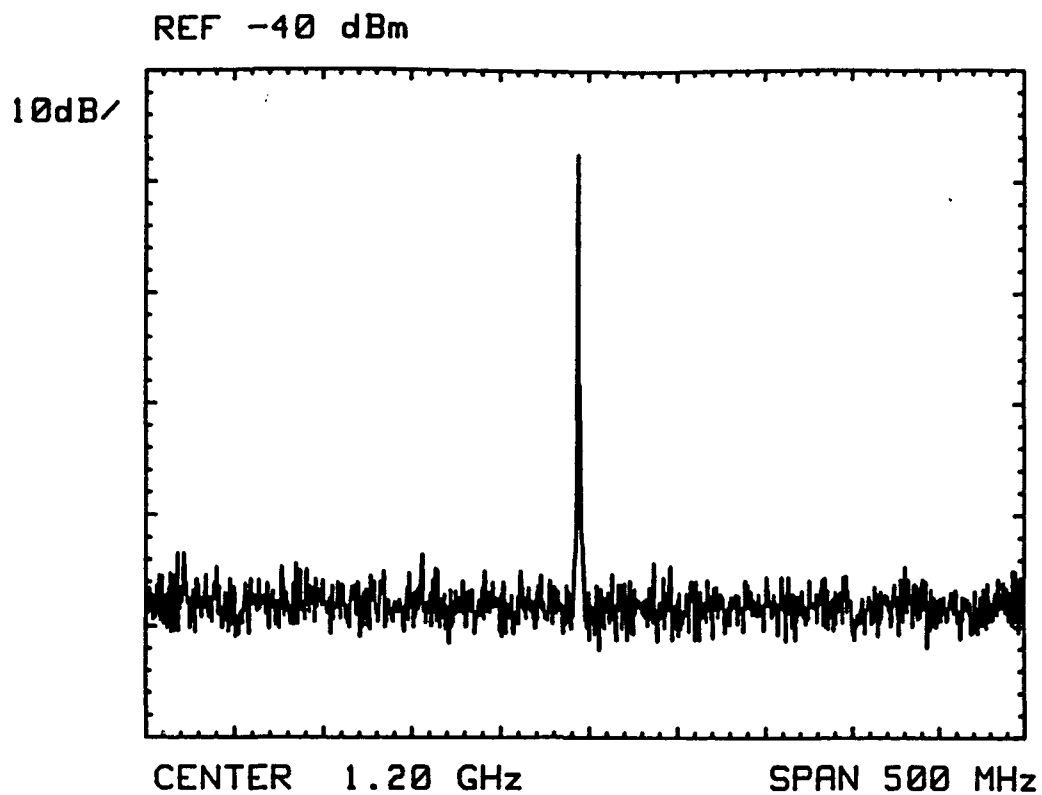


Figure 5: *Spectrum analyzer output of signal levels. Stability is on the order of one megahertz.*

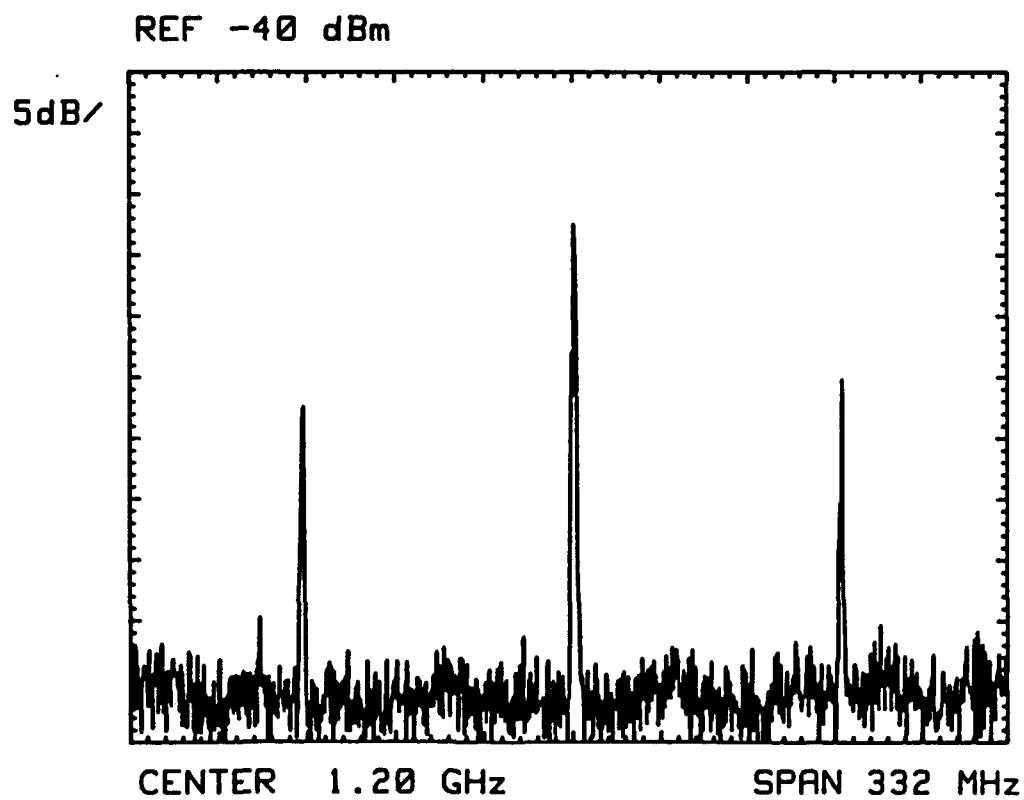


Figure 6: *Sideband generation obtained from FET.*

after the initial detection element (Figure 7). Use of high frequency HEMT devices further extended our response and efficiency.

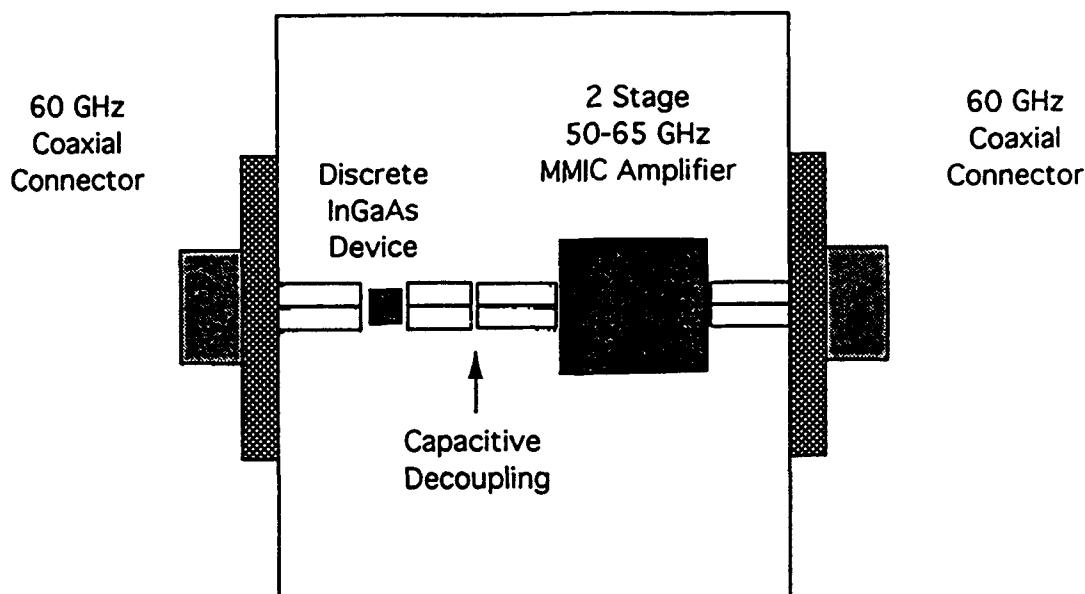


Figure 7: FET optodetector linked up with a MMIC Amplifier to increase conversion efficiency.

Next, we explored heterojunction bipolar transistors in this optical millimeter wave generation effort. The devices we used were designed for optical coupling and had a window in the emitter. We found excellent response at 60 GHz, even though these devices were relatively slow, $f_T < 30$ GHz. One of the most interesting experiments was when we substituted a mode locked semiconductor laser for the two gas lasers used in mixing (Figure 8). Using this configuration, we immediately generated substantial radiation at 65 GHz (Figure 9). Clearly, the system could be reduced to very compact sizes in our wafer scale program. The mode locked lasers, combined with the optical detector, in some sense represents a new

optoelectronic oscillator capable of going well into submillimeter wave ranges.

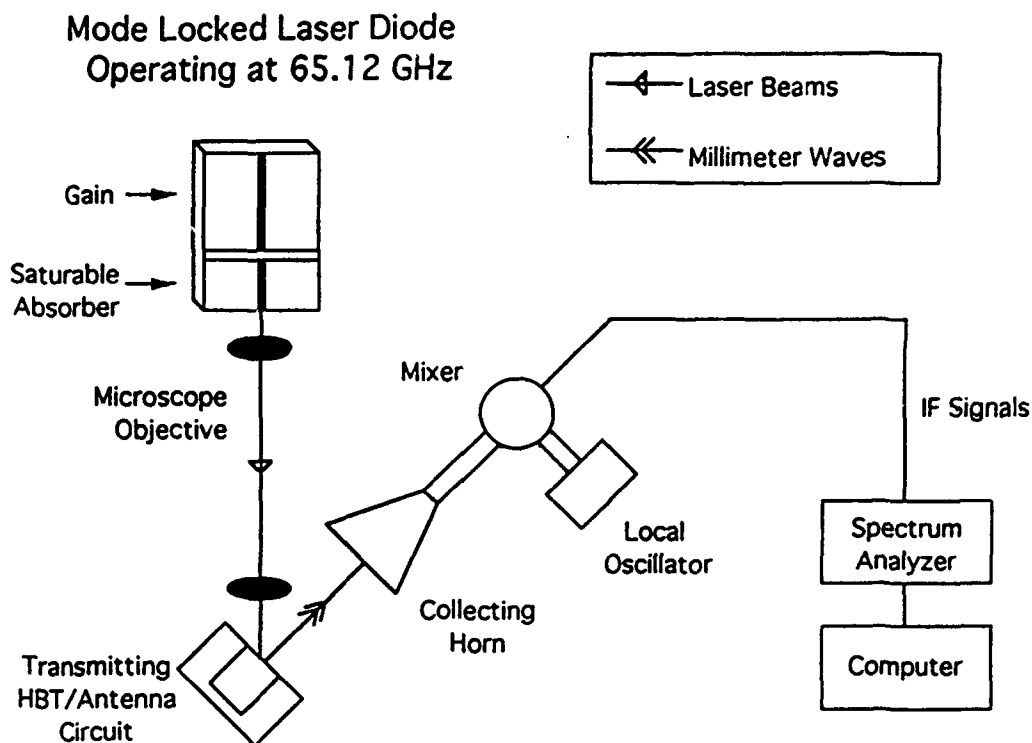


Figure 8: Optoelectronic millimeter wave oscillator using mode locked diode laser and Heterojunction Bipolar photo transistor.

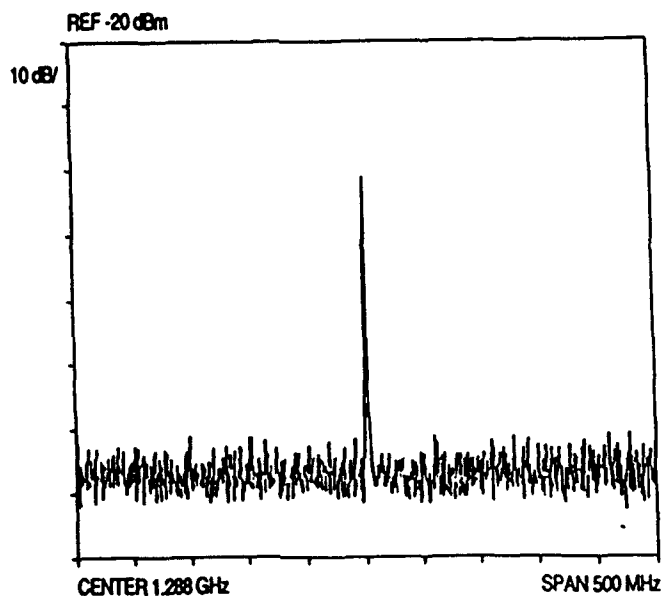


Figure 9: Mixed output signal at 65 GHz from system shown in Figure 8.

In addition to the semiconductor mode locked lasers, we also looked at mixing using two tunable DFB lasers as shown in Figure 10. This yielded the results exhibited in Figure 11 and demonstrated that active frequency locking is essential for this technology to be used in viable sources.

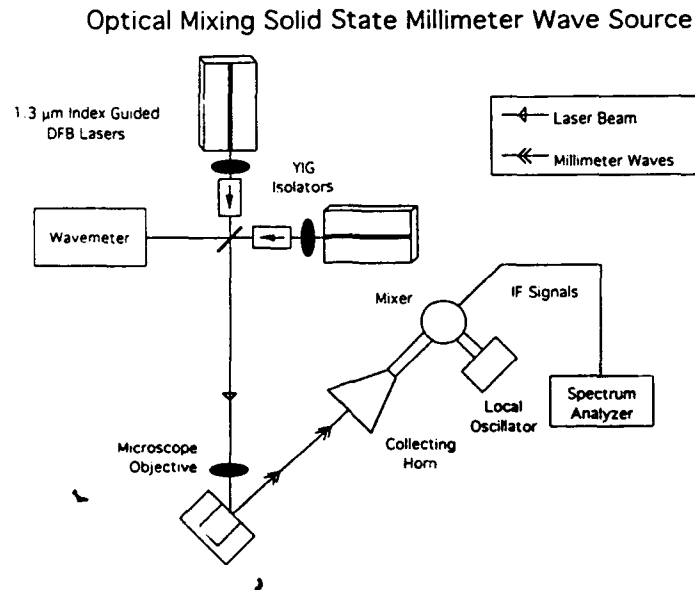


Figure 10: Solid state mixing to generate millimeter wave signals.

64.1 GHz Output

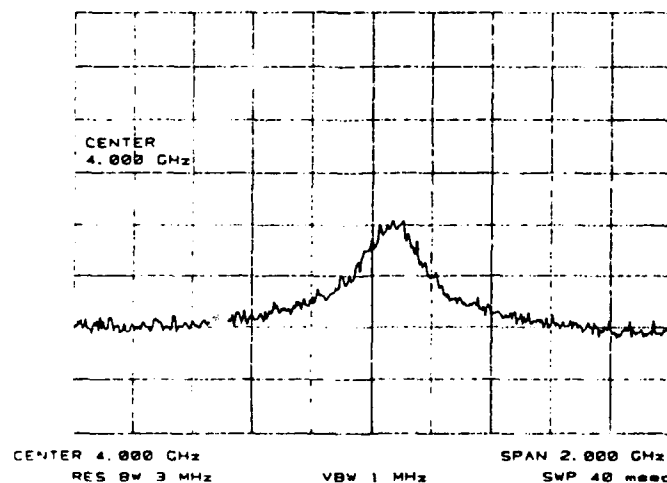


Figure 11: Radiated mixing signals showing need to frequency lock diode sources to achieve good frequency control.

Section B: High Frequency Testing

In order to extend our measurements to millimeter wave frequencies, we have refined and extended our picosecond capabilities (Figure 12).

OPTOELECTRONIC MEASUREMENT SYSTEM

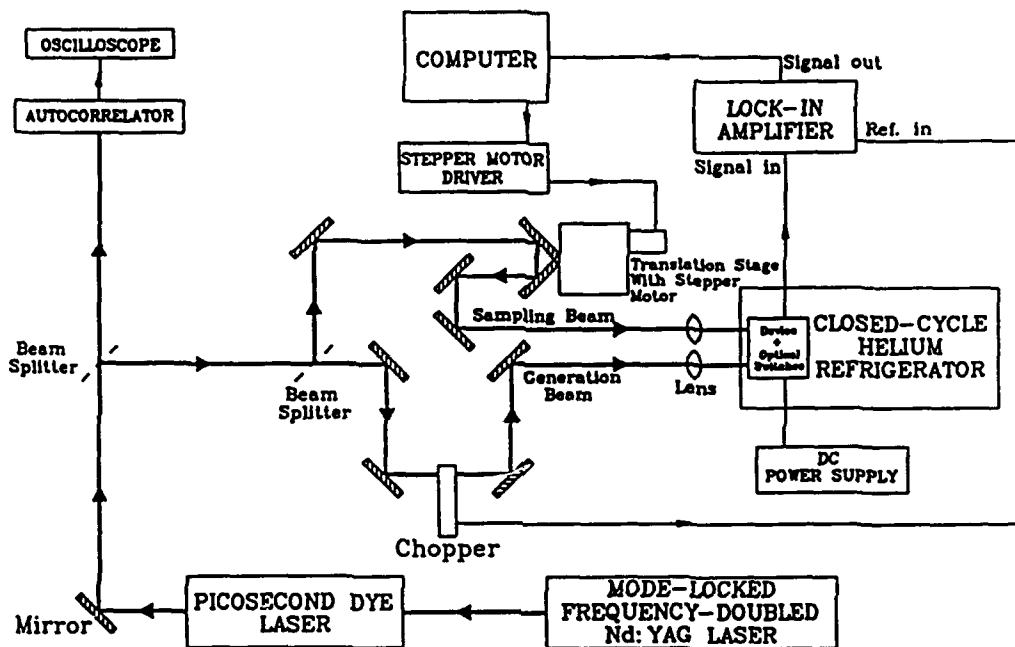


Figure 12: Picosecond system using mode locked laser to pump dye. Note that the sample is incorporated into cooled dewar.

Our results have been intensively calibrated so that we can extend our measurements to Wafer Scale configurations with confidence. Tests have been made at millimeter wave frequencies of new types of MMIC circuits. These measurements were taken at both room and low temperatures and are shown in Figures 13 and 14. Measurements were also made on the highest frequency HEMT and HBT devices obtained

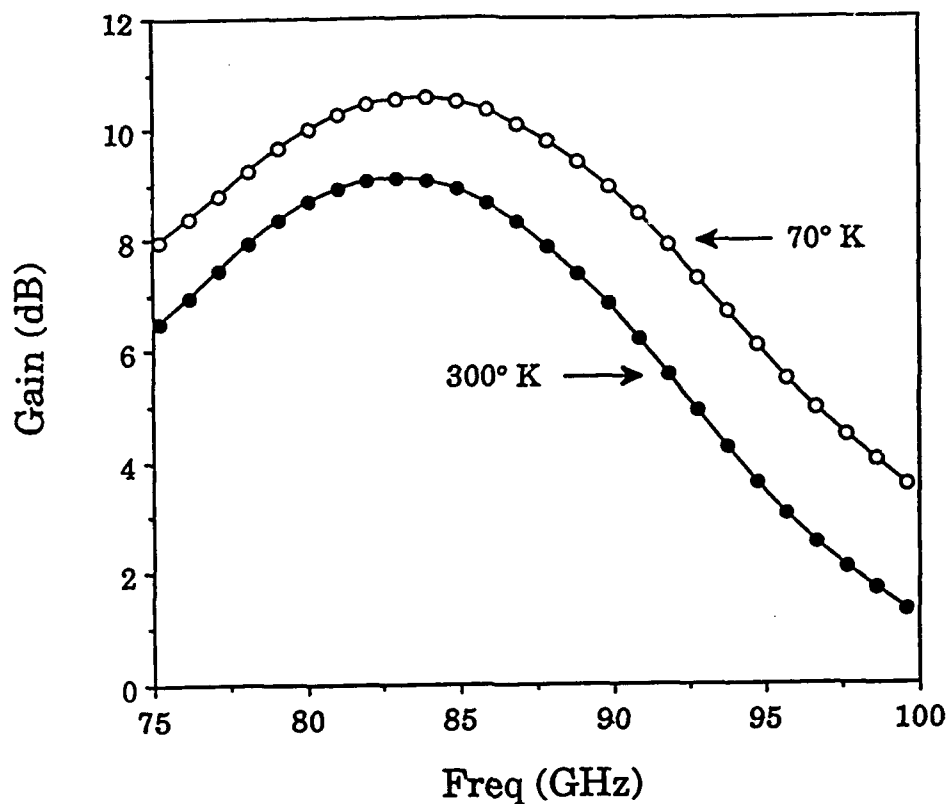


Figure 13: Measurement of gain of a W Band Amplifier at both room and low temperatures.

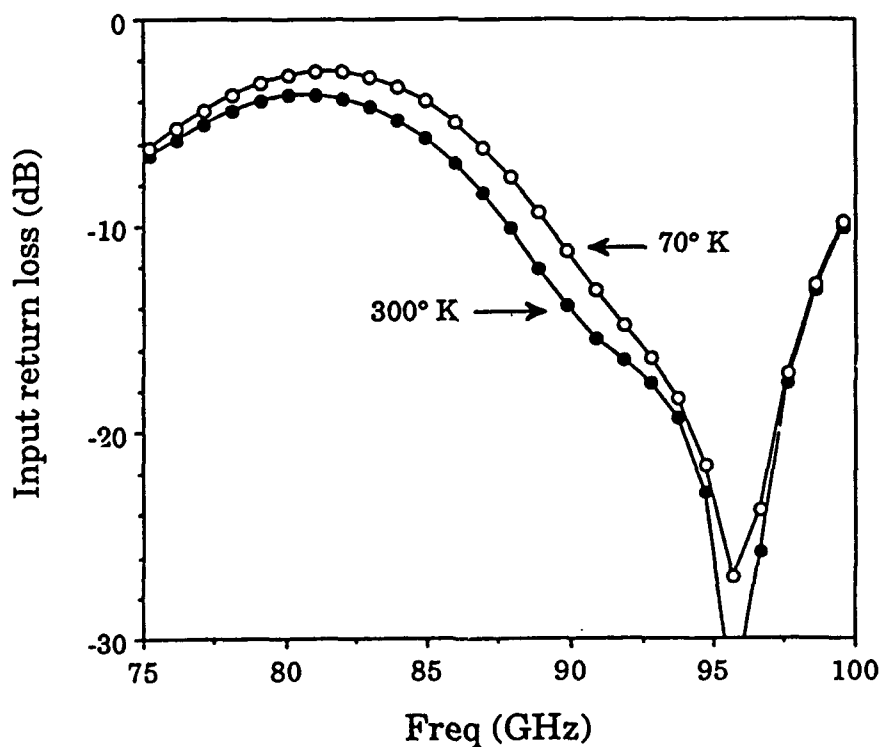


Figure 14: Return losses at both temperatures of the same device as Figure 13. All of the S parameters can be measured in this manner.

from Rockwell (Figure 15), TRW, Hughes and recently from Aerojet.

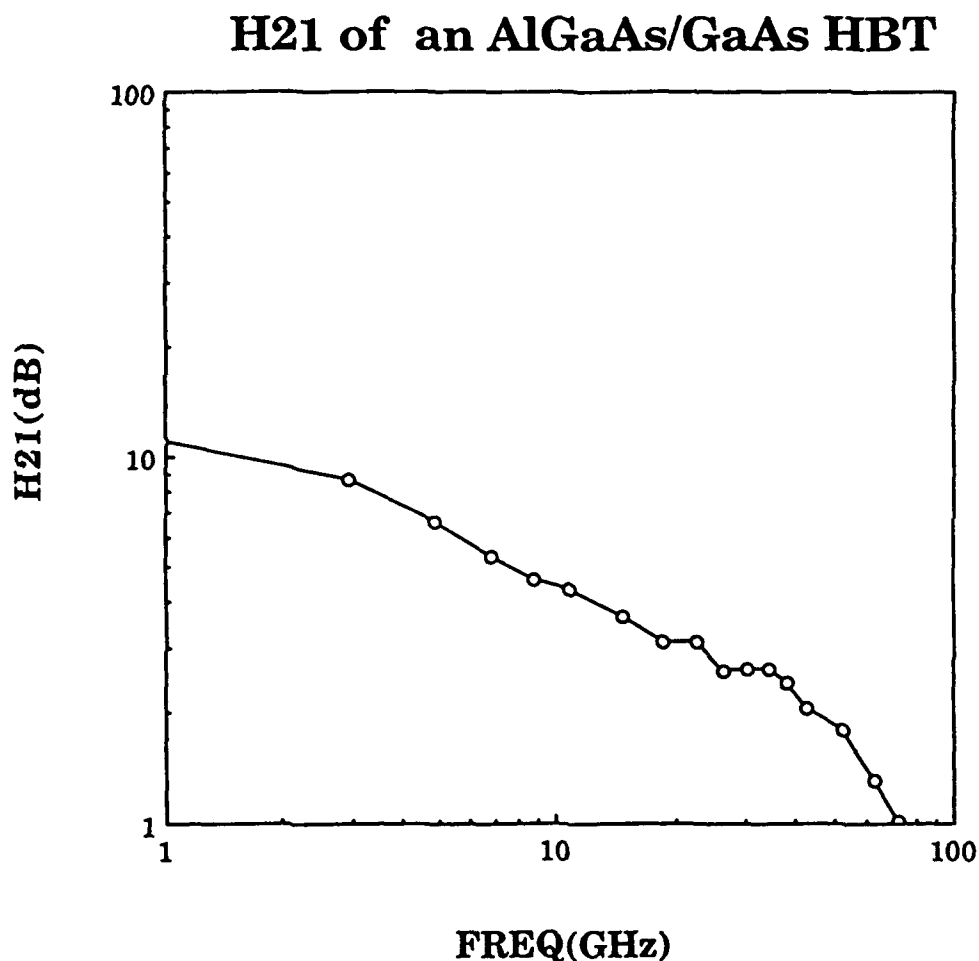


Figure 15: Optical measurement of current gain of high frequency HBT.

The measurements in each case were validated against other techniques and the bond wire losses and substrate discontinuities actually determined. In addition to measuring the electrical properties, the results from direct optical injection into the active region are also examined in Figures 16 and 17. Some of the fastest optical responses we have seen were found in these experiments at low temperature. Low temperature measurements are

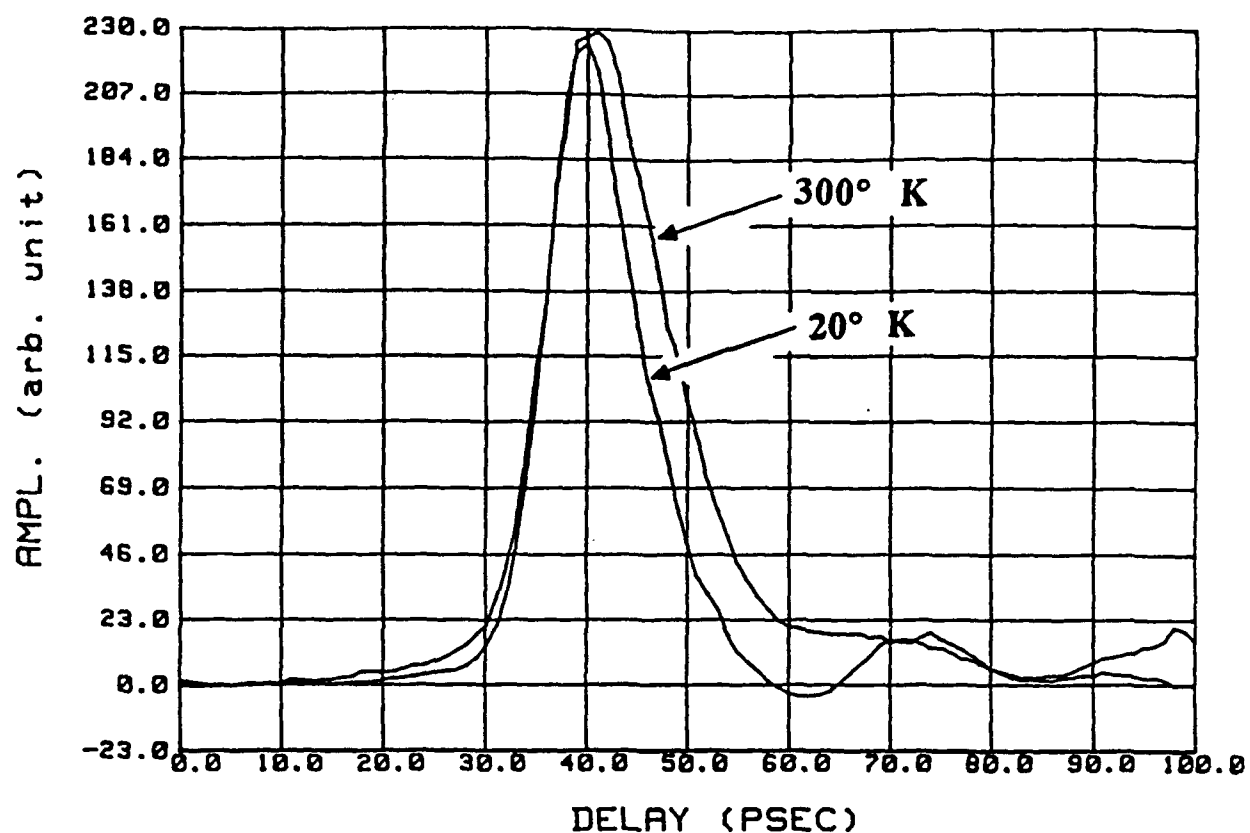


Figure 16: Response of Rockwell HBT illuminating the base with optical radiation.

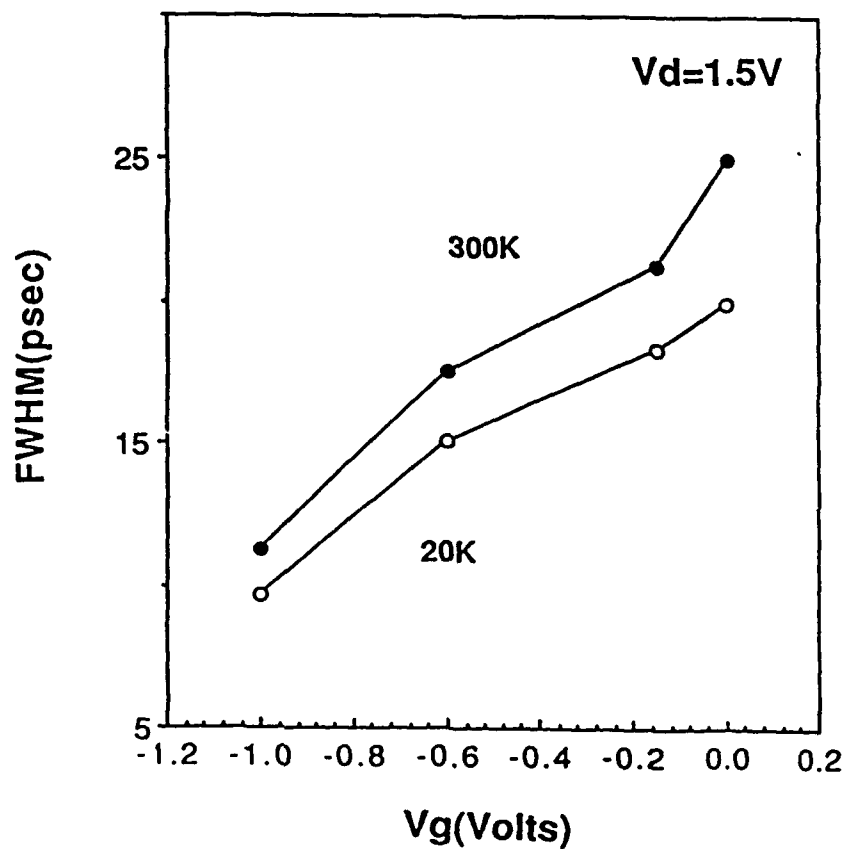


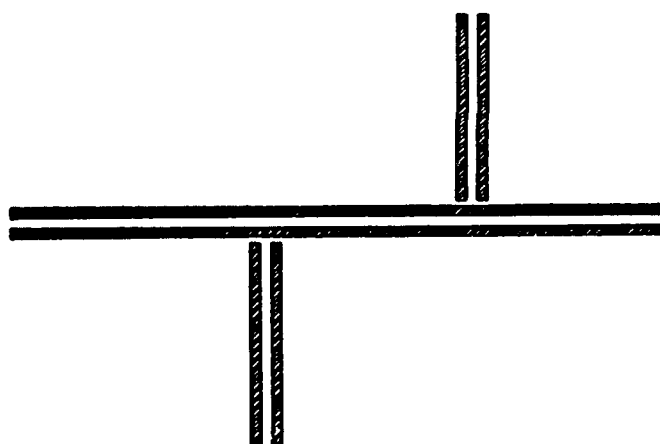
Figure 17: Time response of HEMT device to optimal radiation as a function of gate voltage.

particularly well suited to our optical technique since we never have to run high frequency lines into the vacuum chambers.

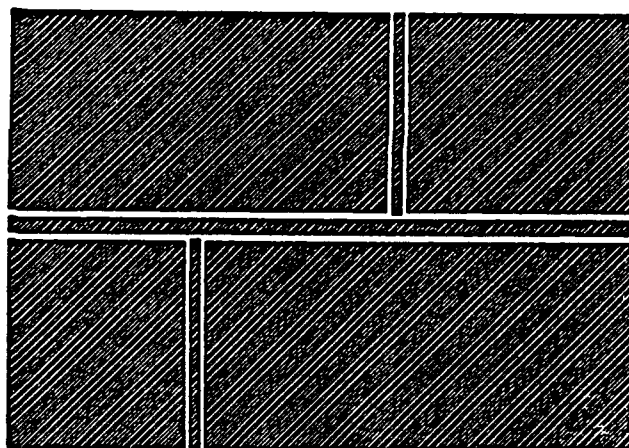
A new series of coplanar low temperature switches have recently been developed to extend our measurements to higher frequencies (Figure 18).

Coplanar Photoconductive Switches

Photoconductor Materials : SOS, GaAs, LT GaAs, α -Si



Coplanar Strip



Coplanar Waveguide

Materials from USC, TRW and Aerojet

Figure 18: New switches using a coplanar geometry and low temperature grown GaAs and α -Si.

These measurements using direct injection have now been extended into the infrared where we will benefit from the "windowing effect" of the wider bandgap materials. In addition to the extraordinary range of state-of-the-art three terminal devices obtained from local industry, we have also tested the highest frequency PIN diodes available, obtained from Hughes Research.

Optical Interconnection

In terms of optically interconnecting our optoelectronic devices, we have, in conjunction with Physical Optics Corporation, demonstrated 60 GHz board to board optical interconnection using polymer bases and microprism couplers. The actual diagram of the experiment is shown in Figure 19 . The signal after traveling into,

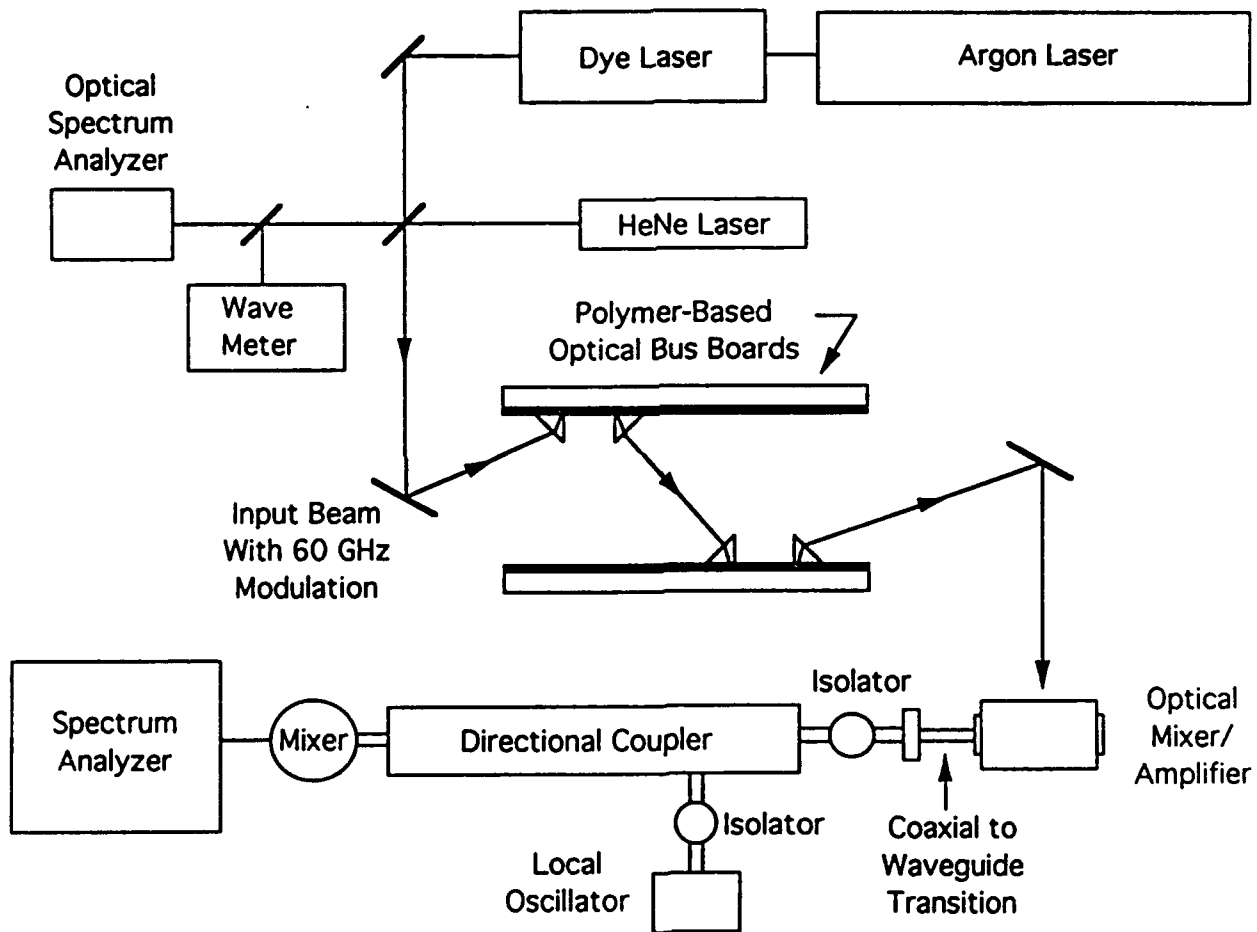


Figure 19: High frequency interconnection using optical techniques.

through and between two optical bus boards with graded index (GRIN) polymer waveguides total 55 cm. The 22 dB signal to noise ratio corresponds to a bit error rate (BER) of 10^{-10} at 60 GHz.

We also used picosecond pulses to characterize the bandwidth of polymer gelatin thin film waveguides. Both step index profiles and graded-index have been examined. The results are shown in Figure 20 and indicate that the graded device has significantly higher bandwidth because of its lower dispersion.

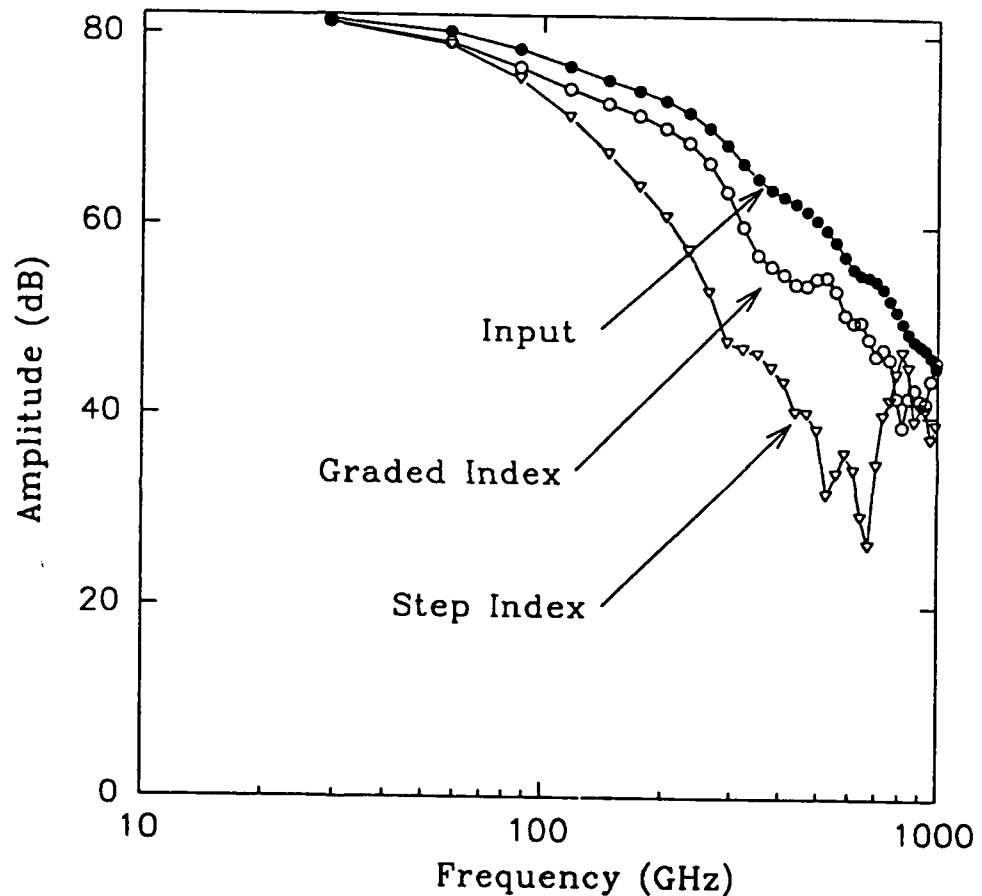


Figure 20: Measurement of polymer gelatin thin film waveguides using picosecond techniques.

Section C: New Device and Material Technology

In our measurements of new ultrafast devices, we have also fabricated and tested, with aid from TRW, a ballistic transport transistor as shown in Figure 21. By raising and lowering the

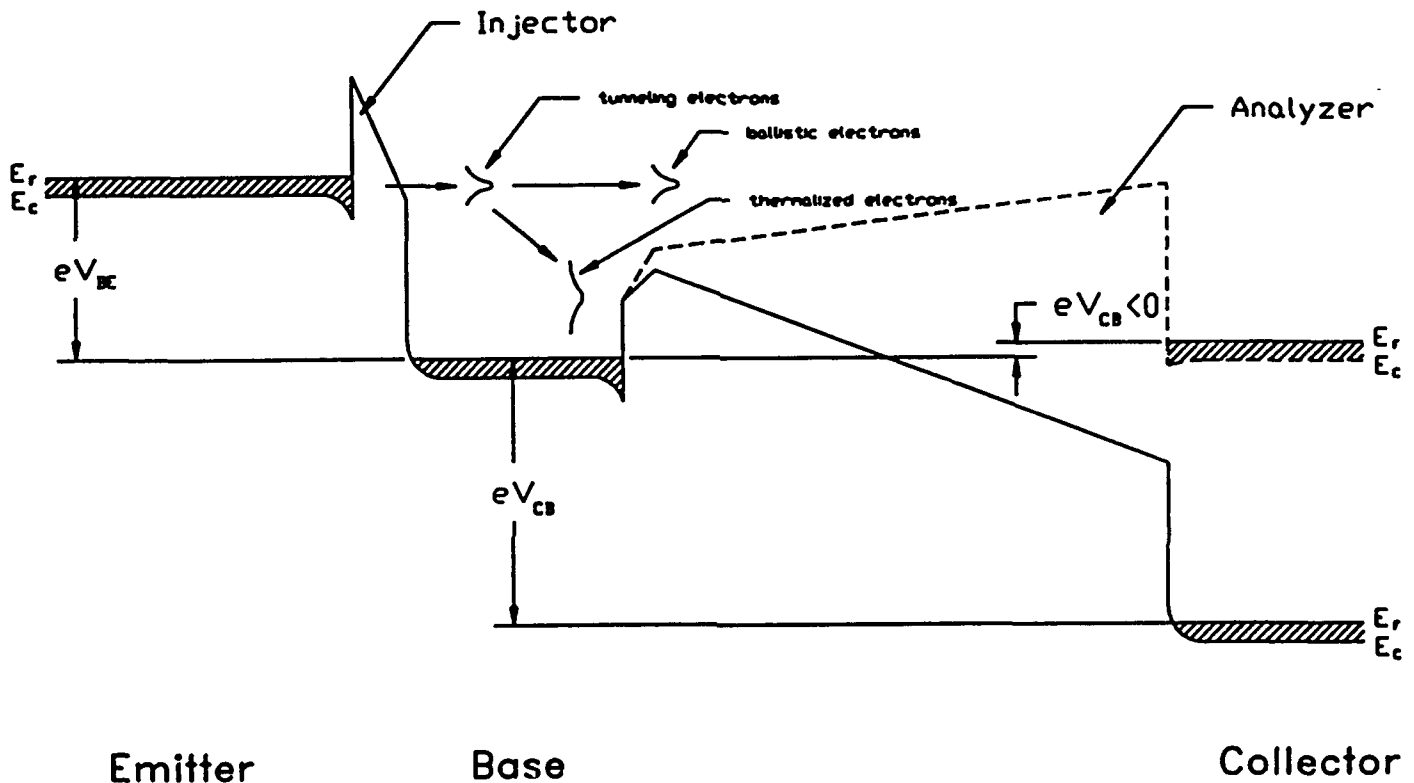


Figure 21: Hot electron transfer made at UCLA to examine optical response of ballistic systems.

analyzer barrier potential, we have demonstrated ballistic transport using dc measurements in these devices (Figure 22). The optical measurements made with the picosecond laser are shown in Figure 23. The frequency limitations of our first generation of devices are dominated by parasitics and the use of such structures is being examined to new device applications.

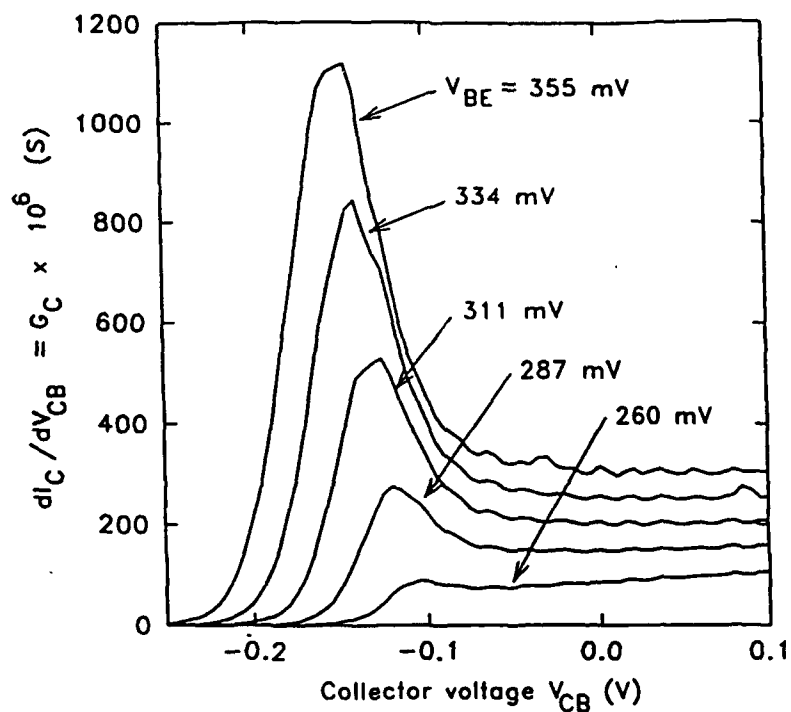


Figure 22: Electrical test of hot electron device using collector barrier to determine ballistic contribution.

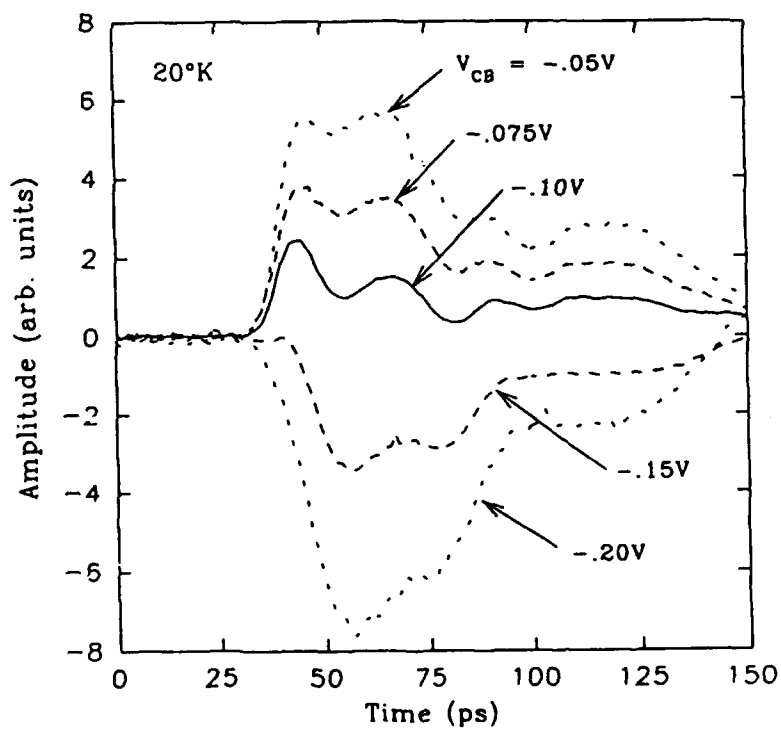


Figure 23: Visible optical response of a common-base GaAs/AlGaAs THETA at different collector-base voltages.

Because of the limitations of just using new structures, part of our effort was to investigate the possibility of introducing new materials, suitable for infrared frequencies, grown in conjunction with Si. We chose InSb for a number of reasons including its small, direct bandgap and high mobility. A technique we developed using BaF_2 layers to accommodate the lattice mismatch (Figure 24). The results are shown in the X-ray diffraction pattern of Figure 25. This material has shown excellent mobility (Figure 26) and we have fabricated simple MOSFETs (Figure 27) suitable for use in infrared phototransistors.

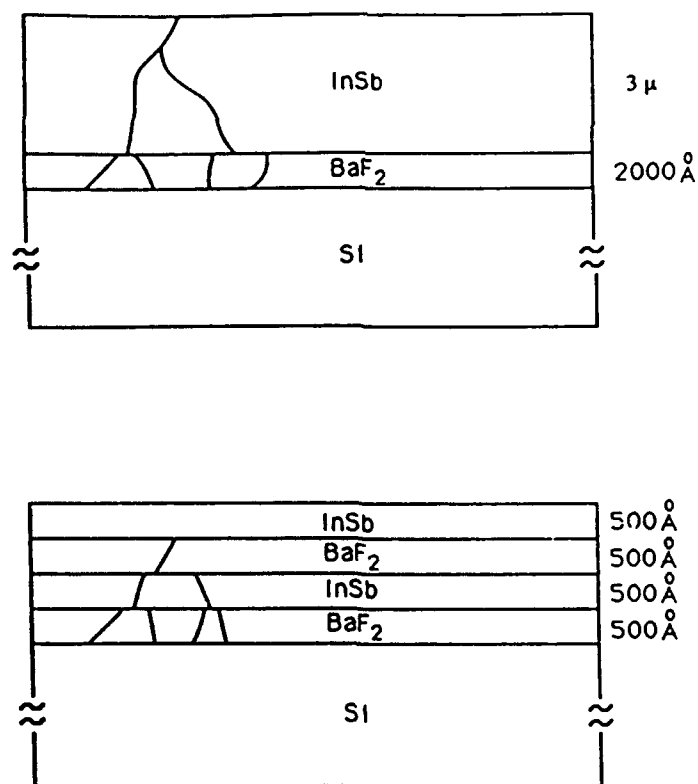


Figure 24: *InSb, for infrared phototransistors grown on Si using layers of BaF_2 .*

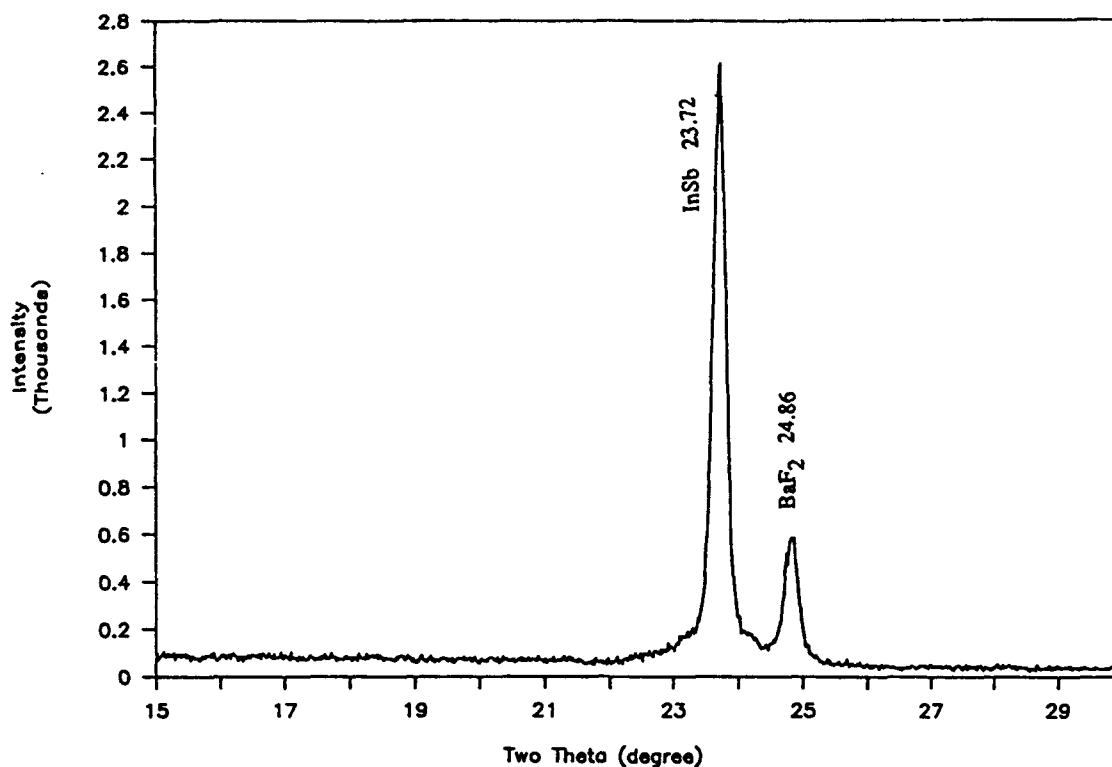


Figure 25: Pattern showing successful single crystal growth.

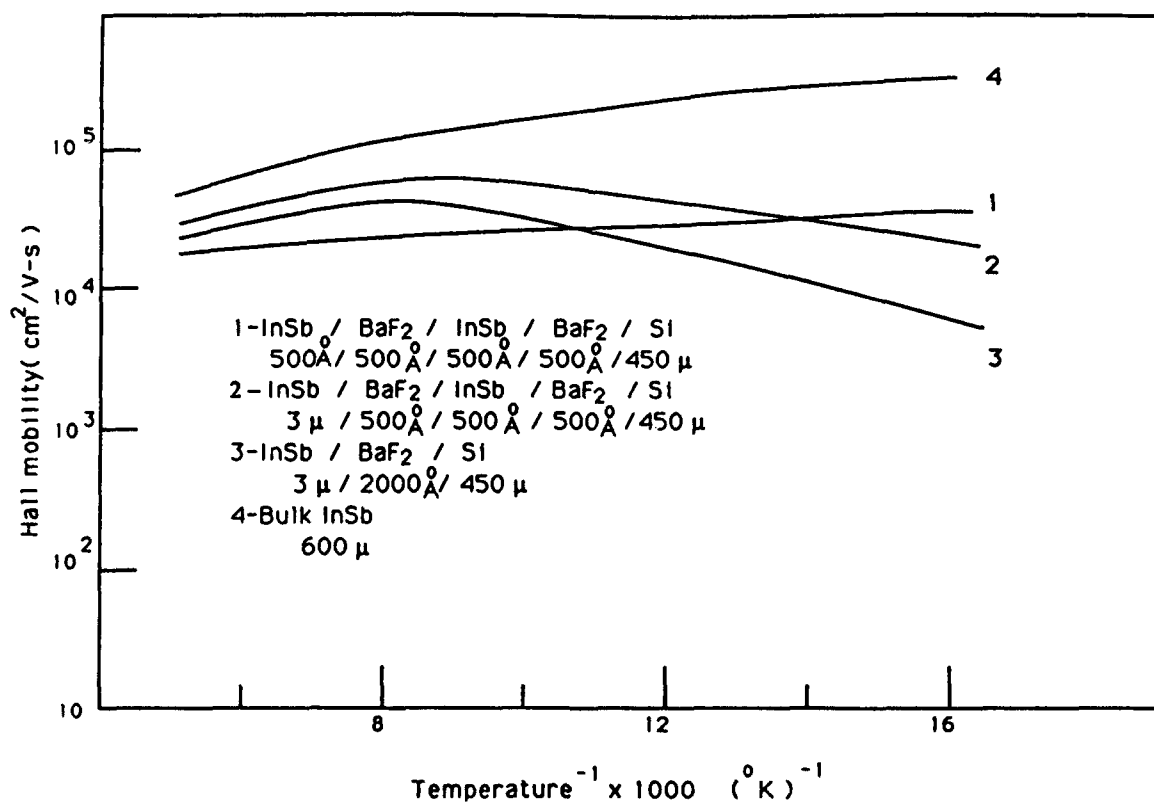


Figure 26: Mobility of thin film system compares favorable with bulk and thick layers.

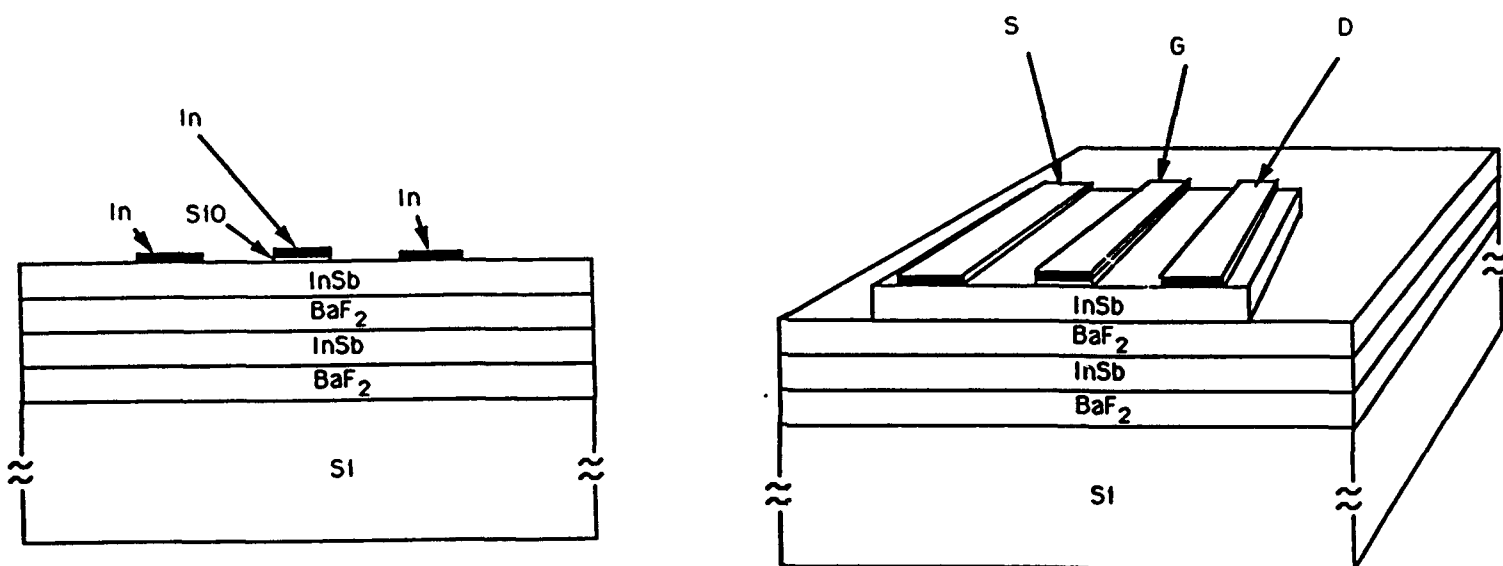


Figure 27 MOSFET transistor fabricated with InSb material.

Another device that we have recently fabricated is a Quantum Well Impatt for use in optically controlled systems. This Avalanche device is the first of it's kind and operates far above conventional devices. The actual system is shown in Figure 28a and 28b and the output, as a free running oscillator at 100 GHz, is shown in Figure 28c and 28d. This novel device represents a major step in the development of two terminal devices using modern MBE techniques. Efforts are now in progress to examine high power optical control at 100 GHz using these oscillators.

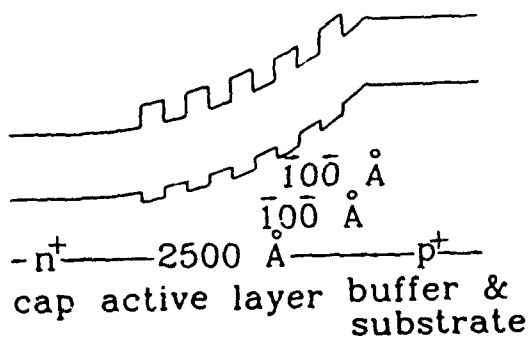


Fig. 28a: Band diagram of a W-band MQW IMPATT structure.

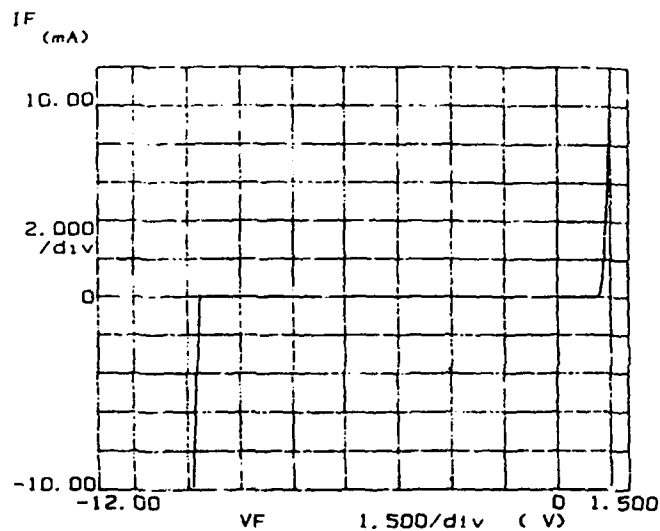


Fig. 28b: Room temperature I-V curve for the MQW IMPATT structure in Fig. 28a.

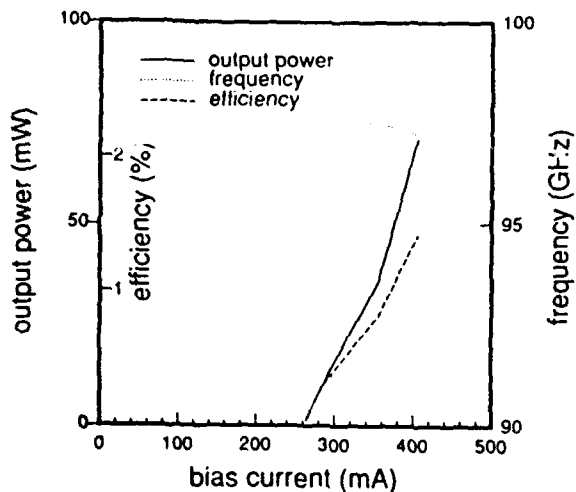


Fig. 28c: Output power, frequency and efficiency as a function of bias current for an MQW IMPATT oscillator under pulsed operation.

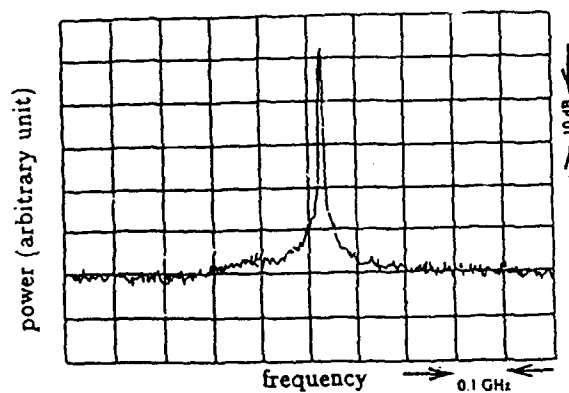
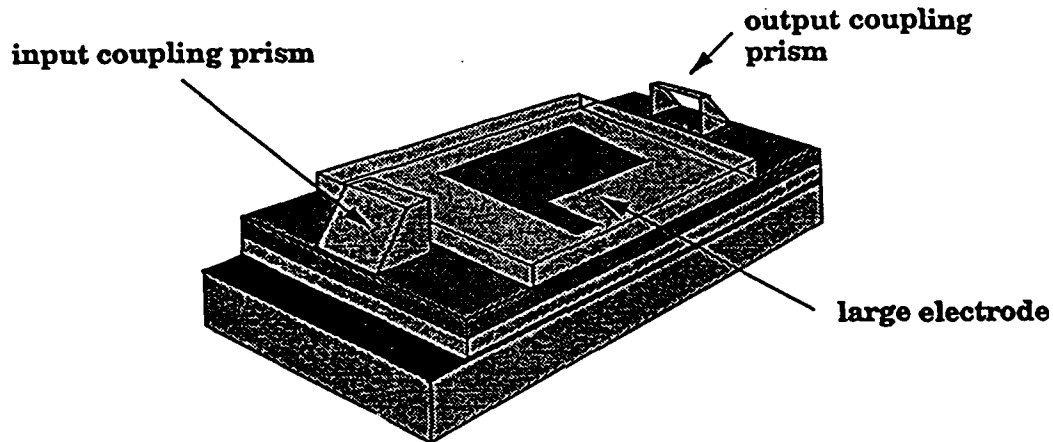


Fig. 28d: Spectrum of the C.W. MQW IMPATT diode at 101.3 GHz, the resolution bandwidth is 3 MHz. Both Fig. 28c and Fig. 28d correspond to the same device.

Modulator and Phase Shifter

Another device that was essential to our millimeter wave optical wafer scale effort was the optical modulator and phase shifter. Because of the limitations on frequency and with integration, we decided to look at polymer systems. The system we developed is shown in Figure 29 and uses a thermally set



- top cladding, polystyrene (5 um)
- electro-optically active polymer (2 um)
- bottom cladding, polyurethane (3 um)
- quartz substrate (0.15 x 1.5 x 3.5 cm)
- chromium (200 Å) and gold (5000 Å)

Figure 29: Polymer modulator using prism coupling and dc electrode.

polyurethane polymer with disperse red dye 19 groups.

The traveling wave structure uses the poled polymer with two cladding layers and the microstrip line aligned above the channel.

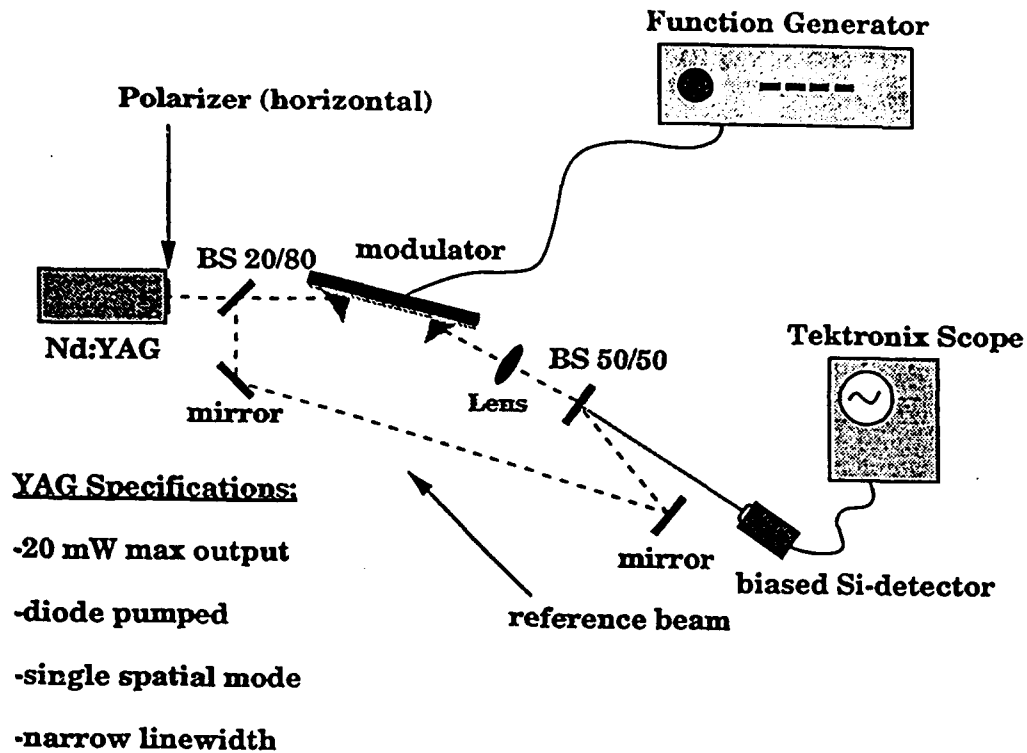


Figure 30: System for demonstrating phase modulation using polymer modulator.

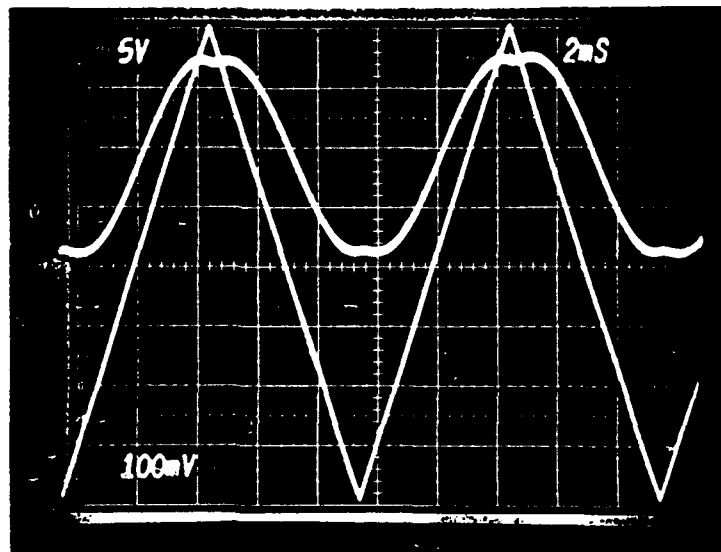


Figure 31: Photo of low frequency phase modulation in a channel guide configuration.

We have tested it electronically to 26 GHz and found that the microwave loss is under 10 dB over the entire range. Our initial phase modulation experiment at 100 KHz used the configuration shown in Figure 30 with the resulting signal shown in Figure 31. Experiments are now in progress with the system shown in Figure 32 up to 26 GHz. The geometry has also been adjusted to support both polarizations and permit direct amplitude modulation as shown in Figure 31.

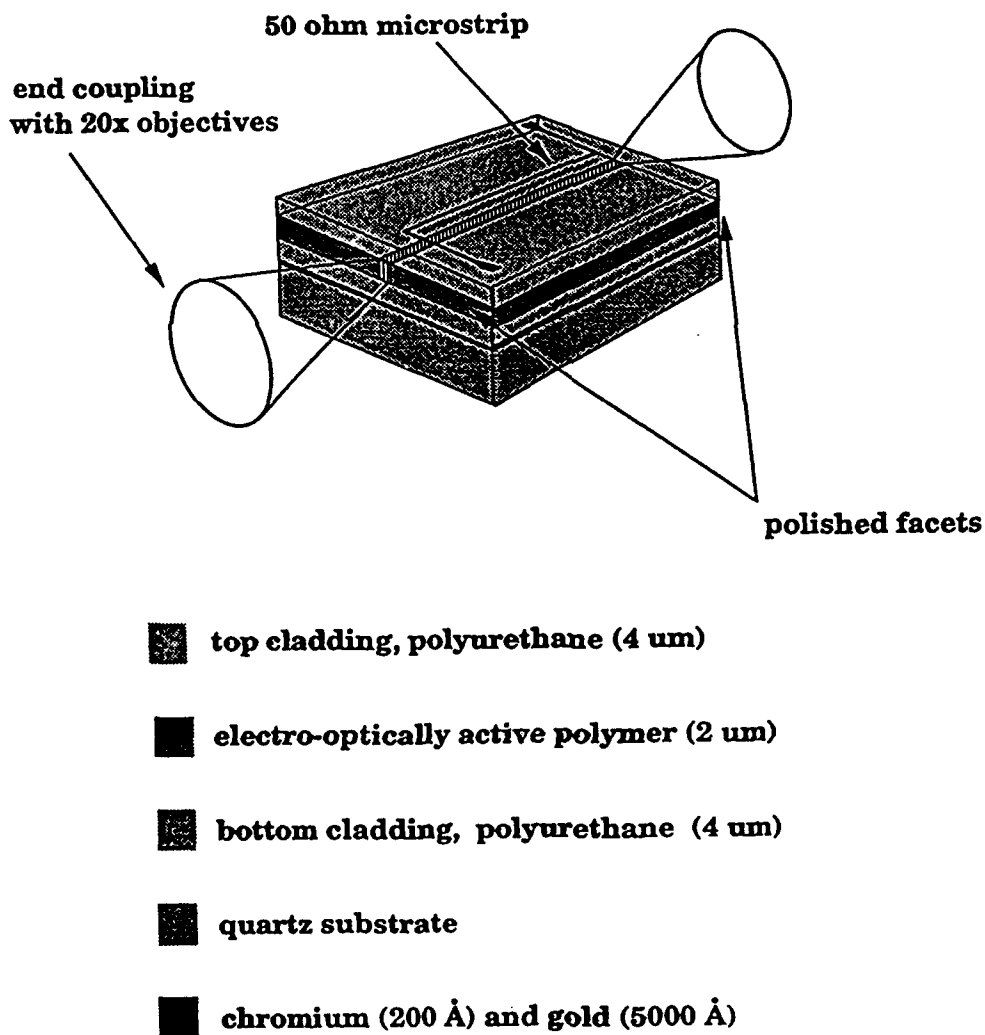
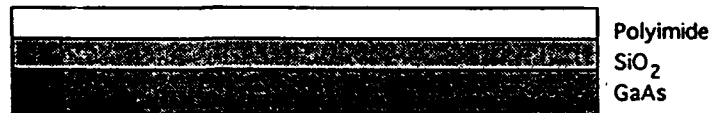


Figure 32: High frequency traveling wave modulator currently under test to 26 GHz.

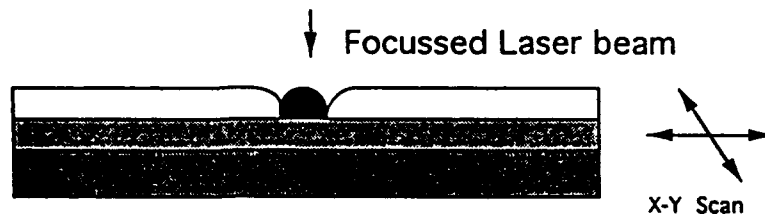
Using transitions to microstrip from waveguides developed as part of an earlier AFOSR proposal, we can now extend these measurements up to the 75 to 110 GHz band.

In another experiment as part of our program, we developed a polyimide channel waveguide interconnect system which is suitable for use on both GaAs and Si substrates. The commercially available polyimide is spin coated upon the substrates using a buffer layer of SiO_2 . We then use a direct write laser system, as shown in Figure 33, to form our channel waveguides. Heterodyne systems

Step 1. Deposition of polyimide film



Step 2. Localized laser thermal curing



Step 3. Removal of uncured Polyimide



Figure 33: Direct write system for optical connections on wafer surface.

where we couple into our HEMT optical detectors show that this has acceptable losses (~ 2 dB/cm) and is extremely versatile. Branching structures and power dividers are now being examined for system applications using lower loss filtered polyimide.

Conclusion

Virtually every phase of the Wafer Scale Union program has been successfully investigated. Papers that have been generated are included in Appendix A. The next step is to bring these parts together as shown in Figure 34 to form useful circuits. The program has had major results in establishing the ability to generate high frequency cw signals from three terminal devices, using optical control, for the first time.

All semiconductor systems have been configured and used as sources. Polymer modulators and optical on-wafer guides have been tested. Finally, a number of new devices and materials have been developed. The basic concepts of Wafer Scale Union for millimeter systems using optical control and interconnections has been demonstrated.

Millimeter Wave Wafer Scale Union

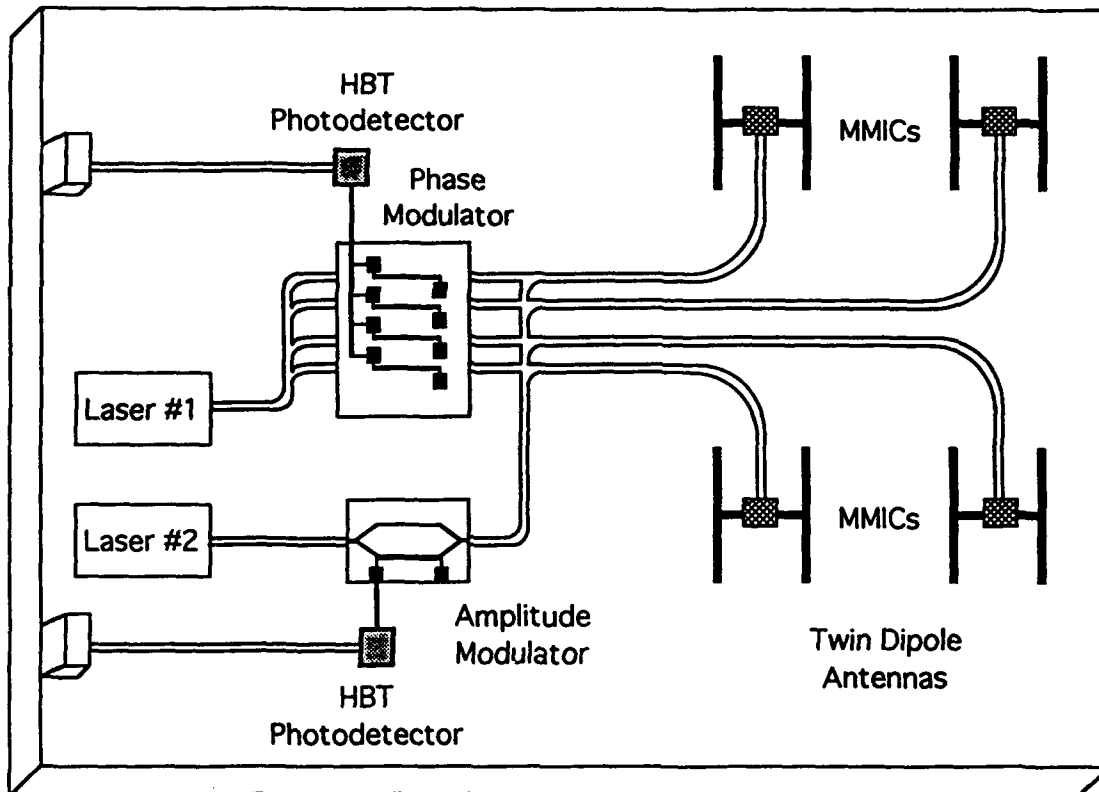


Figure 34: Combined system using modulators, phase shifters, optical transistors, on wafer optical guides and integrated antenna structures. This is the direction of our millimeter wave.

APPENDIX A

PAPERS ON WAFER SCALE UNION EFFORT

Wide-Band Millimeter Wave Characterization of Sub-0.2 Micrometer Gate-Length AlInAs/GaInAs HEMT's

Mehran Matloubian, *Member, IEEE*, Steven E. Rosenbaum, *Member, IEEE*, Harold R. Fetterman, *Fellow, IEEE*, and Paul T. Greiling, *Fellow, IEEE*

Abstract—The S parameters of an AlInAs/GaInAs high electron mobility transistor (HEMT) were measured using a picosecond optoelectronic system over a bandwidth of 100 GHz. These picosecond optoelectronic measurements were validated by comparing low frequency measurements to those obtained using on wafer RF probes/vector network analyzer, and W -band results to measurements done using a waveguide-to-microstrip transition/vector network analyzer frequency extender. This is the widest bandwidth of measured S parameters reported on a single transistor.

I. INTRODUCTION

HIGH electron mobility transistors (HEMT's) are increasingly replacing GaAs MESFET's in microwave and millimeter wave circuits [1, 2]. Their higher cutoff frequencies combined with lower noise make them more attractive in applications such as millimeter wave low-noise amplifiers [3] and mixers [4]. In particular $\text{Al}_{0.48}\text{In}_{0.52}\text{As}/\text{Ga}_{0.47}\text{In}_{0.53}\text{As}$ HEMT's have demonstrated superior performance over HEMTs made from other material systems [5, 6]. However, these transistors have cutoff frequencies well beyond the bandwidth that can be measured conveniently using conventional network analyzers. As a result only a small amount of data exists describing the performance of HEMT's in the W band. By using external mixers the present bandwidth of network analyzers has been extended to about 100 GHz. But several difficulties arise in characterization of devices in the millimeter wave region. At high frequencies the transistors have to be mounted in test fixtures with waveguide-to-microstrip transitions. It is difficult to design wide bandwidth waveguide-to-microstrip transitions that have low insertion and return loss. The actual S parameters of the transistor have to be de-embedded from the test fixture and using transitions having a high insertion/return loss can cause erroneous results.

In order to improve and optimize performance of millimeter wave transistors it is important to have a simple technique for direct characterization of devices at very high frequencies. Using picosecond optoelectronic techniques ultrafast electrical pulses can be generated and sampled [7]–[9]. These electrical pulses can be used to test the response of high speed semicon-

ductor devices [10] and integrated circuits [11] over a wide bandwidth. Using photoconductive switches, picosecond electrical pulses can be generated and sampled at a very short distance from a device. Therefore, the high frequency signals do not have to travel through long sections of transmission lines and waveguide transitions, making this technique superior to conventional network analyzers. In this study S parameters of $\text{Al}_{0.48}\text{In}_{0.52}\text{As}/\text{Ga}_{0.47}\text{In}_{0.53}\text{As}$ HEMTs were measured using picosecond optoelectronic techniques over a 100-GHz bandwidth. To validate the optoelectronic measurements the S parameters were also measured using on wafer RF probes/network analyzer (over the frequency range of 1–26 GHz) and a network analyzer frequency extender (over the frequency range of 75–100 GHz).

II. MEASUREMENTS

The cross section of the $\text{Al}_{0.48}\text{In}_{0.52}\text{As}/\text{Ga}_{0.47}\text{In}_{0.53}\text{As}$ HEMT is shown in Fig. 1. The gate-length of the transistor is less than 0.2 μm with a gate-width of 50 μm . The maximum transconductance of the device is greater than 1000 ms/mm . For the optoelectronic measurements the AlInAs/GaInAs HEMT was mounted in a test fixture as shown in Fig. 2. The microstrip lines were fabricated using Cr/Au on silicon-on-sapphire (SOS) substrates. The sapphire substrates were about 125 μm thick and the microstrip lines were designed to have a 50 Ω impedance. The silicon epi-layer was about 0.5 μm thick and was heavily implanted with silicon ions to shorten the carrier lifetime.

On each side of the HEMT there are two photoconductive switches that consist of 25 μm gaps in the side microstrip lines. By applying a DC bias to a photoconductive switch and focusing a picosecond laser beam on the gap, fast electrical pulses are generated that propagate on the center transmission line. A second photoconductive switch is used for sampling of the electrical pulses. The details of the measurements are described elsewhere [12].

Depending on which one of the four optical switches is used as the generator and which one as the sampler the HEMT can be characterized completely in the time-domain. By taking the Fourier transform of the reflected and transmitted signals and normalizing it to the Fourier transform of the appropriate input signal the S parameters of the device can be determined [10].

III. RESULTS

Using the picosecond optoelectronic system the time-domain response of the HEMT was measured and the S parameters of the HEMT were determined over a bandwidth of 100 GHz. This is the widest bandwidth of S parameters measured on a single transistor. To validate these measurements the S parameters of similar HEMTs were measured using a wafer RF probe and a conventional network analyzer (HP8510) over the frequency of

Manuscript received October 17, 1990. This work was supported in part by the Hughes Research Laboratories under the California MICRO program and in part by the Air Force Office of Scientific Research.

M. Matloubian and S. E. Rosenbaum were with the Department of Electrical Engineering, University of California, Los Angeles, CA 90024. They are now with Hughes Aircraft Company, Research Laboratories, Malibu, CA 90265.

H. R. Fetterman is with the Department of Electrical Engineering, University of California, Los Angeles, CA 90024.

P. T. Greiling is with Hughes Aircraft Company, Research Laboratories, Malibu, CA 90265.

IEEE Log Number 9041650.

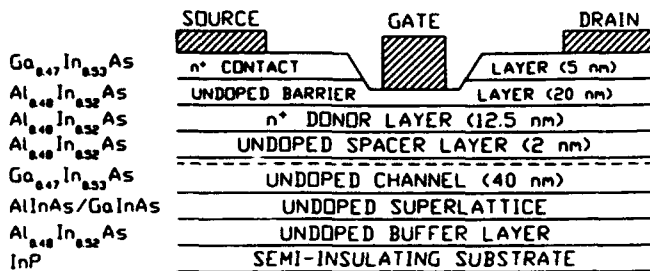
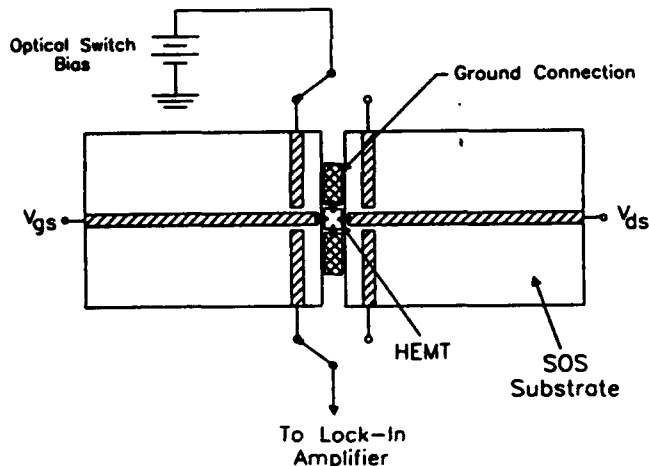
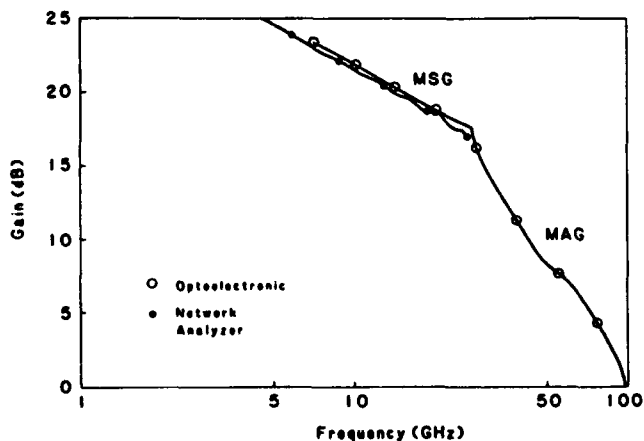
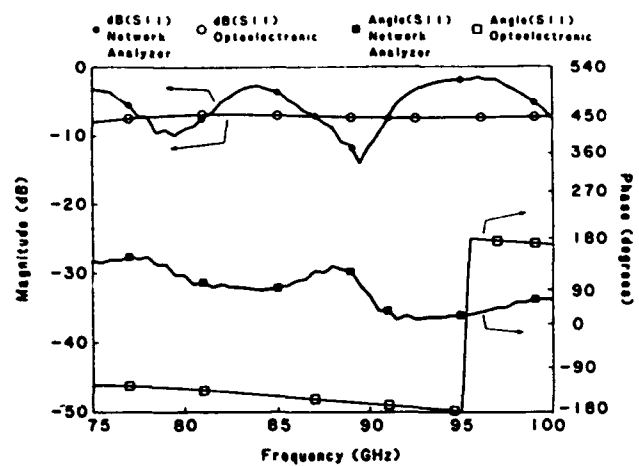
Fig. 1. Cross section of $\text{Al}_{0.48}\text{In}_{0.52}\text{As}/\text{Ga}_{0.47}\text{In}_{0.53}\text{As}$ HEMT.

Fig. 2. Picosecond optoelectronic test fixture with HEMT wire-bonded to center microstrip lines.

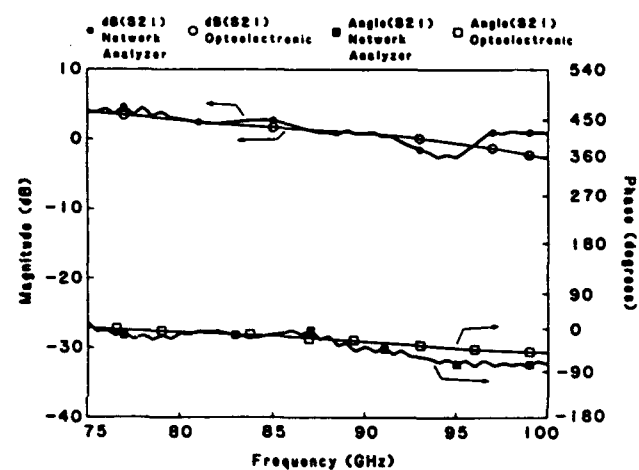
Fig. 3. Maximum available gain (MAG)/maximum stable gain (MSG) versus frequency of $\text{AlInAs}/\text{GaInAs}$ HEMT calculated from measured S parameters by optoelectronic system (O), and from network analyzer measurements using on wafer RF probes (●).

1–26 GHz. From the measured S parameters the maximum available gain (MAG) of the device was calculated. The plot of MAG versus frequency (maximum stable gain (MSG) for conditionally stable case) for both the optoelectronic measurements and network analyzer measurements are shown in Fig. 3. Very good agreement can be seen between both techniques over the range of frequency overlap.

It is also important to find the accuracy of the optoelectronic measurements at millimeter wave frequencies. For this purpose an $\text{AlInAs}/\text{GaInAs}$ HEMT was tested using a W -band (75–100 GHz) network analyzer frequency extender. The device was



(a)



(b)

Fig. 4. Magnitude and phase versus frequency over frequency range of 75–100 GHz for optically measured S parameters and measurements by network analyzer frequency extender (a) S_{11} , (b) S_{21} .

mounted in a W -band ridged waveguide-to-microstrip transition which consists of a Chebyshev stepped impedance transformer between the WR-10 waveguide and the 50 Ω microstrip transmission line [13]. This type of transition was chosen for its broadband characteristics with a center frequency of 90 GHz and a passband from 70–110 GHz. The microstrip transmission lines were fabricated on 0.005 in. fused silica. The return loss of the fixture was measured to be more than 5 dB and the insertion was less than 5 dB across the band. The measured data was de-embedded from the fixture response using a two tiered technique [13].

Figs. 4(a) and 4(b) show comparison between S_{11} and S_{21} measured by the optoelectronic system and network analyzer frequency extender over the range of 75–100 GHz. Measurement of the W band test fixture revealed a distinct resonant waveguide mode propagating from input to output in addition to the microstrip transmission line. This resonance has a tendency to mask the performance of the device under test to some degree. Measurements of S_{11} and S_{22} are affected most by the resonance; S_{21} and S_{12} are impacted to a lesser degree. The effect of this resonance on the transistor data may be seen as a distinct ripple in the magnitudes of S parameters. From Fig. 4(b) the agreement between S_{21} measurements using the two

techniques is quite good. Due to the ripples in network analyzer measurements S_{11} results have discrepancies. Both the network analyzer and the picosecond optoelectronic measurements show the effects of source inductance due to the bond wires. This will be discussed in connection with the equivalent circuit model and high frequency performance elsewhere [14].

IV. CONCLUSION

S parameters of an AlInAs/GaInAs HEMT was measured using picosecond optoelectronic techniques over a bandwidth of 100 GHz. The results show good qualitative agreement with measurements of a similar HEMT using on-wafer RF probes and a conventional vector network analyzer over the bandwidth of the network analyzer (26 GHz). Comparison with measurements by a W -band network analyzer showed excellent agreement for S_{21} and S_{12} but there were limited by de-embedding in the case of S_{11} and S_{22} . This study demonstrates the advantages of wide bandwidth characterization of high frequency transistors using picosecond optoelectronic techniques.

ACKNOWLEDGMENT

The authors would like to thank Drs. U. Mishra, A. Brown, and M. Delaney for providing the HEMTs used in this study and Dr. J. East and B. Denheyer for help with the W band measurements.

REFERENCES

- [1] P. M. Smith, P. C. Chao, K. H. G. Duh, L. F. Lester, B. R. Lee, and J. M. Ballingall, "Advances in HEMT technology and applications," in *IEEE MTT-S Int. Microwave Symp. Digest*, 1987, pp. 749-752.
- [2] U. K. Mishra, J. F. Jensen, A. S. Brown, M. A. Thompson, L. M. Jelloian, and R. S. Beaubien, "Ultra-high-speed digital circuit performance in 0.2- μ m gate-length AlInAs/GaInAs HEMT technology," *IEEE Electron Device Lett.*, vol. EDL-9, no. 9, pp. 482-484, 1988.
- [3] S. Vaughn, K. White, U. K. Mishra, M. J. Delaney, P. Greiling, and S. Rosenbaum, "High performance V -band low noise amplifiers," in *IEEE MTT-S Int. Microwave Symp. Dig.*, 1989, pp. 801-804.
- [4] S. A. Maas, "Design and performance of a 45-GHz HEMT mixer," *IEEE Trans. Microwave Theory Tech.*, vol. MTT-34, no. 7, pp. 799-803, 1986.
- [5] U. K. Mishra, A. S. Brown, S. E. Rosenbaum, C. E. Hooper, M. W. Pierce, M. J. Delaney, S. Vaughn, and K. White, "Microwave performance of AlInAs-GaInAs HEMT's with 0.2- and 0.1- μ m gate length," *IEEE Electron Device Lett.*, vol. EDL-9, no. 12, pp. 647-649, 1988.
- [6] U. K. Mishra, A. S. Brown, M. J. Delaney, P. T. Greiling, and C. F. Krumm, "The AlInAs-GaInAs HEMT for microwave and millimeter-wave applications," *IEEE Trans. Microwave Theory Tech.*, vol. MTT-37, no. 9, pp. 1279-1285, 1989.
- [7] D. H. Auston, "Impulse response of photoconductors in transmission lines," *IEEE J. Quantum Electron.*, vol. QE-19, no. 4, pp. 639-648, 1983.
- [8] K. J. Weingarten, M. J. W. Rodwell, and D. M. Bloom, "Picosecond optical sampling of GaAs integrated circuits," *IEEE J. Quantum Electron.*, vol. QE-24, no. 2, pp. 198-220, 1988.
- [9] J. A. Valdmanis and G. Mourou, "Subpicosecond electrooptic sampling: Principles and applications," *IEEE J. Quantum Electron.*, vol. QE-22, no. 1, pp. 69-78, 1986.
- [10] D. E. Cooper and S. C. Moss, "Picosecond optoelectronic measurement of the high-frequency scattering parameters of a GaAs FET," *IEEE J. Quantum Electron.*, vol. QE-22, no. 1, pp. 94-100, 1986.
- [11] P. Polak-Dingles, H.-L. Hung, T. Smith, H. Huang, K. Webb, and C. H. Lee, "On wafer characterization of monolithic millimeter-wave integrated circuits by picosecond optical electronic technique," *IEEE MTT-S Int. Microwave Symp. Digest*, 1988, pp. 237-240.
- [12] M. Matloubian, H. Fetterman, M. Kim, A. Oki, J. Camou, S. Moss, and D. Smith, "Picosecond optoelectronic measurement of S parameters and optical response of an AlGaAs/GaAs HBT," *IEEE Trans. Microwave Theory Tech.*, vol. MTT-38, no. 5, pp. 683-686, 1990.
- [13] K. J. Moeller, J. H. Schaffner, and H. R. Fetterman, " W -band six-port network analyzer for two-port characterization of millimeter wave transistors," *Rev. Sci. Instrum.*, vol. 60, no. 3, pp. 433-438, 1989.
- [14] M. Matloubian, S. E. Rosenbaum, H. R. Fetterman, and P. T. Greiling, "Modeling of AlInAs/GaInAs HEMTs at microwave and millimeter wave frequencies," to be published.

Use of Picosecond Optical Pulses and FET's Integrated with Printed Circuit Antennas to Generate Millimeter Wave Radiation

D. C. Ni, D. V. Plant, M. Matloubian, and H. R. Fetterman

Abstract—Millimeter wave radiation has been generated from FET's and HEMT's, integrated with printed circuit antennas, and illuminated with picosecond optical pulses. Modulation of the millimeter waves was achieved by applying a swept RF signal to the transistor gate. Using this technique, tunable electrical sidebands were added to the optically generated carrier providing a method of transmitting information and doing high resolution spectroscopy. Heterodyne detection demonstrated that the system continuously generated tunable radiation, constrained by the high gain antenna, from 45 to 75 GHz.

RECENT experiments have shown that optoelectronic switches monolithically integrated with planar antenna structures can be used to generate electromagnetic radiation in the microwave and millimeter wave regions [1]–[3]. In these experiments, an optical pump and probe arrangement is used to coherently generate and sample the microwave and millimeter wave radiation. The bandwidth of these systems, when driven by picosecond optical pulses, is from below 10 GHz to greater than 200 GHz [4], [5]. Femtosecond optical pulses have now been used to extend this frequency coverage to greater than 2.0 THz [6]. Measurements of the transient far-field radiation properties of integrated optoelectronic antennas have provided both the temporal and spatial characteristics of these devices [7]. Spectroscopic applications of these systems include measurements of the frequency dependent loss and dispersion properties of materials in the 10–130 GHz range, with a frequency resolution of 4.94 GHz [5]. In addition, the optical generation and control of millimeter waves has attracted considerable attention because its importance in distributed communications and radar systems [8], [9].

In this letter, we report an alternative approach to the two terminal switch concept for generating millimeter waves which utilizes three terminal devices integrated with printed circuit antennas. This technique employs GaAs FET's and AlGaAs–GaAs HEMT's mounted with printed circuit antennas and illuminated with picosecond optical pulses. Unlike two terminal devices, using three terminal devices provides a way of both optimizing output and incorporating information signals on the carrier signal. Also, using three terminal devices improves the signal power since the devices are driven an order of magnitude lower in impedance by the light than the switches.

Manuscript received October 3, 1990. This work was supported by the Air Force Office of Scientific Research.

D. C. Ni was with the Department of Electrical Engineering, University of California, Los Angeles, CA 90024. He is now with AT&T Bell Laboratories, Middletown, NJ 07748.

D. V. Plant and H. R. Fetterman are with the Department of Electrical Engineering, University of California, Los Angeles, CA 90024.

M. Matloubian was with the Department of Electrical Engineering, University of California, Los Angeles, CA 90024. He is now with Hughes Research Laboratory, Malibu, CA 90265.

IEEE Log Number 9143131.

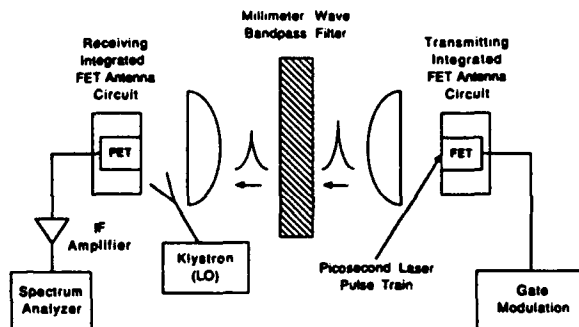


Fig. 1. Schematic of the experimental setup. The optical beam was injected onto the device at an angle of 30° with respect to the plane of the transmitting antenna, and the teflon lenses were separated by 10 cm.

Heterodyne detection rather than photoconductive sampling is used to measure the radiation with the measured signals displayed in real time on a spectrum analyzer. Electrical modulation is applied to the transmitter gate and thus produces a tunable sideband on the optically generated carrier. The technique also provides increased resolution for use in spectroscopic applications. The high resolution capabilities of this technique, on the order of 1 MHz, are demonstrated by measuring the transmission response of a narrow bandpass filter.

A schematic representation of the experimental arrangement is illustrated in Fig. 1. FET's (NEC/NE7100) and HEMT's (Rockwell International Science Center) were integrated on printed circuit RT/Duroid microstrip antennas. Identical twin dipole antennas with integrated devices were used both to transmit and to receive the radiation. In the case of the transmitter, the drain and source of the device were connected to the antenna, and in the case of the receiver, the gate and source were connected to the antenna. The full characterization of an integrated FET antenna circuit as a microwave gate mixer has been described previously, and results show the circuit has a conversion loss of approximately 6 dB when used as a heterodyne detector [10].

In these experiments, the active region of the transmitting device was illuminated by 1.5 ps, 578 nm optical pulses obtained from a synchronously pumped mode-locked Rhodamine 6 G dye laser (Coherent 701-2). The dye laser pump source was an actively mode-locked frequency doubled Nd:YAG laser operating at 76 MHz (Coherent Antaries). The active region of the device was excited by 50 to 150 mW of average power focused to 10 μ m in diameter with a 5 \times lens. Using a sweep oscillator, a RF electrical modulation was applied to the transmitter gate. A klystron, tunable from 55.5 to 62.0 GHz, was used as a local oscillator for heterodyne detection of the radiation. Two teflon lenses with 25.4 mm focal lengths were placed between the

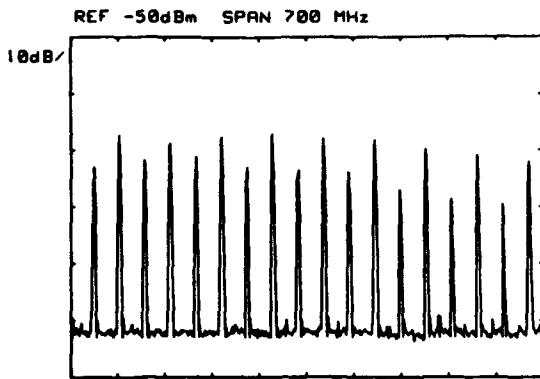


Fig. 2. Millimeter wave radiation comb produced by optical excitation for a local oscillator frequency of 61.4 GHz. Signals located in the upper sideband (61.52 to 63.02 GHz) are the larger amplitude signals, and signals located in the lower sideband (59.78 to 61.28 GHz) are the lower amplitude signals.

transmitter and the receiver to create a collimated beam into which millimeter wave filters were inserted. The detected output from the receiver was sent through various IF amplifiers (0.75–2 GHz with a gain of 37 dB, and 6–18 GHz with a gain of 25 dB) and displayed in real time on a spectrum analyzer. A Hewlett Packard 9836 computer was used for data acquisition and processing.

The repetitive picosecond excitation produces a millimeter wave radiation comb whose signals are spaced at the laser mode-locking frequency (76 MHz). Because heterodyne detection is used, mixed signals which fall within the bandwidth of the IF amplifier from both the high- and the low-frequency side of the local oscillator will be detected. This is seen in Fig. 2 where a spectrum analyzer trace of the detected radiation for a local oscillator frequency of 61.4 GHz is shown. These data were taken using the 0.75–2 GHz IF amplifier and the devices biased as follows: the transmitting FET with $V_{ds} = 2.0$ V and $V_{gs} = -3.0$ V, and the receiving FET with $V_{ds} = 2.0$ V and $V_{gs} = -0.6$ V. By tuning the local oscillator ± 5.0 MHz the signals located in the upper sideband could be distinguished from those located in the lower sideband. In Fig. 2, the larger amplitude signals are in the upper sideband (61.52–63.02 GHz) and the lower amplitude signals are in the lower sideband (59.78–61.28 GHz). Using various IF amplifiers, we measured the bandwidth of the radiation comb and found it extended from 45 to 75 GHz. The average power in the millimeter wave beam was also measured using a slow response time liquid helium cooled silicon bolometer, and this measurement yielded an estimated power of > 100 nW.

Next, an electrical modulation was applied to the transmitter gate in addition to the dc bias, and this RF modulation produced tunable sidebands on the millimeter wave radiation. These sidebands could be used to completely fill in the transmission spectrum of a millimeter wave bandpass filter. In order to demonstrate this capability, we placed a Fabry-Perot interferometer with a narrow passband into the millimeter wave beam. The filter consisted of two 50 lines/inch metal meshes mounted on optically flat retaining rings. Fig. 3(a) is a spectrum analyzer trace of the transmission response of this filter without gate modulation. The filter both rejects the signals in the lower sideband (the lower amplitude signals in Fig. 2) and filters the signals in the upper sideband that are out of the passband of the filter. Fig. 3(b) is spectrum analyzer trace of the filter after applying a swept electrical modulation to the transmitting FET

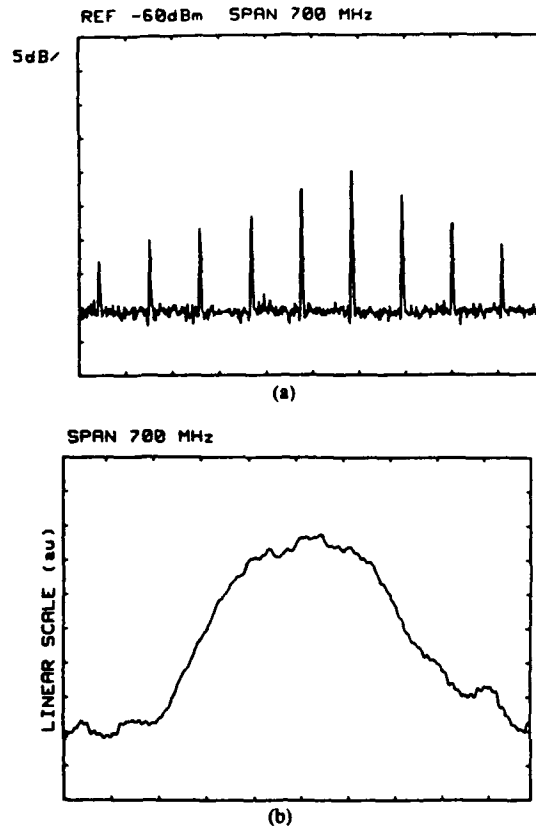


Fig. 3. (a) Transmission response of a metal mesh Fabry-Perot interferometer without transmitter gate modulation. The filter is tuned to 62.27 GHz, and the local oscillator is tuned to 61.4 GHz. The filter rejects signals in the lower sideband and filters signals in the upper sideband that fall outside the passband. (b) Transmission response of the same filter with a swept 0 dBm electrical modulation applied to the transmitting FET antenna circuit. This result demonstrates the high spectral resolution obtainable with this technique.

gate. The filter is tuned to approximately 62.27 GHz and has a FWHM of approximately 250 MHz, which is in good agreement with the calculated finesse. This result demonstrates the high spectral resolution obtainable with this technique.

Measuring the radiating millimeter wave signal strength under various conditions of bias and illumination also provides a method of optimizing the transmitting device's frequency response. Studies of the pulsed response of FET's and HEMT's have shown that the intrinsic device speed can be improved by increasing the negative gate bias [11], [12]. The components of the signal power at 60 GHz were measured as a function of both pulse width and gate bias. Fig. 4(a) is plot of signal power versus optical pulse width for an enhancement type HEMT. If a hypersecant shaped optical pulse is assumed, the 3 dB point of the device performance is 7 ps. This value corresponds to a 70 GHz bandwidth, which is in good agreement with the device specifications. The frequency response of the device can be enhanced by appropriate biasing of the gate terminal, as shown in Fig. 4(b) where a plot of signal power and drain current versus gate bias is shown. For a gate bias of -2.5 V, the power of the received signal is increased by 4 dB over a zero bias condition.

In conclusion, we have demonstrated a technique for generating high power millimeter wave radiation utilizing active three terminal devices rather than two terminal switches. In addition, application of an electrical sideband to the optically generated

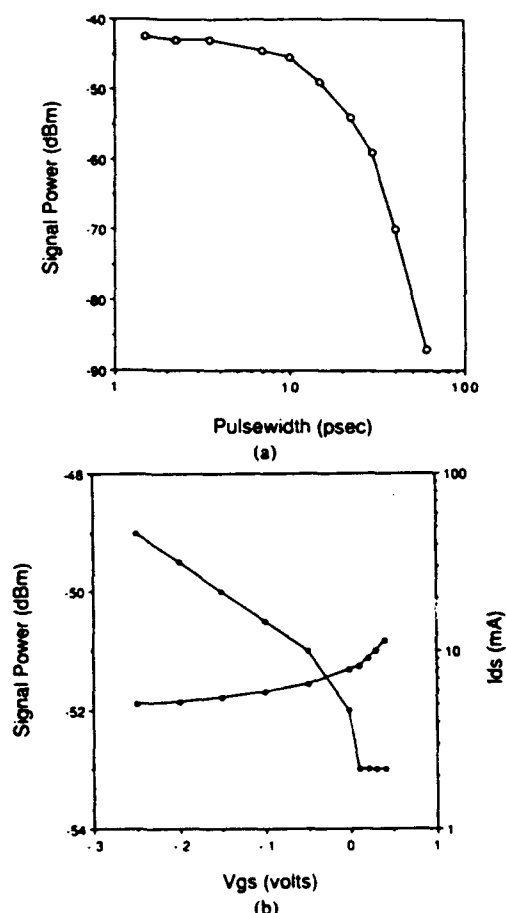


Fig. 4. (a) Signal power at 60 GHz versus optical pulsewidth, and (b) signal power at 60 GHz (dark circles), and transmitter drain current I_{ds} (light circles), versus gate bias (V_{gs}) for an enhancement type HEMT.

carrier provided a method of transmitting information and increasing spectral coverage. Signals were detected in real time thus eliminating the need for photoconductive sampling and Fourier transforming the detected transient radiation. Although fundamental mixing with the local oscillator frequency was used, detecting the millimeter wave radiation could also be accomplished using harmonics of a lower frequency local oscillator. Signals could be applied via a coaxial cable to the receiver gate at subharmonics of the desired local oscillator frequency, thus eliminating the need for a high frequency source.

The bandwidth of the radiation was limited primarily by the high-gain antenna and future improvements to this technique include broad-band, high-frequency antennas integrated with high-speed three terminal devices. Recently, work has been done to characterize some of the optical and electrical properties of FET's, HEMT's, and HBT's, and the results of these investigations indicate such devices have gain at frequencies in excess of 100 GHz [13]. Integrating high-speed three terminal devices with broad-band antennas could potentially lead to complete frequency coverage up to 300 GHz. Tailoring the transmitting device to increase optical absorption will also increase signal strength. In addition, more efficient coupling of the light into the devices's active region can be accomplished using fiber optics. An array of device/antenna circuits, driven by light, and modu-

lated electrically could potentially provide a way of constructing a pulsed, optically controlled millimeter wave transmission system.

ACKNOWLEDGMENT

The authors would like to thank Dr. W. Chew for helpful discussions.

REFERENCES

- [1] R. Heidemann, TH. Pfeiffer, and D. Jager, "Optoelectronically pulsed slot-line antennas," *Electron. Lett.*, vol. 19, pp. 316-317, 1983.
- [2] D. H. Auston, K. P. Cheung, and P. R. Smith, "Picosecond photoconducting hertzian dipoles," *Appl. Phys. Lett.*, vol. 45, pp. 284-286, 1984; P. R. Smith, D. H. Auston, and M. C. Nuss, *IEEE J. Quantum. Electron.*, vol. QE-24, p. 255, 1988.
- [3] J. R. Karin, P. M. Downey, and R. J. Martin, "Radiation from picosecond photoconductors in microstrip transmission lines," *IEEE J. Quantum. Electron.*, vol. QE-22, pp. 677-681, 1986.
- [4] A. P. DeFonzo, M. Jarwala, and C. Lutz, "Transient response of planar integrated optoelectronic antennas," *Appl. Phys. Lett.*, vol. 50, pp. 1155-1157, 1987; A. P. DeFonzo and C. Lutz, "Optoelectronic transmission and reception of ultrashort electrical pulses," *Appl. Phys. Lett.*, vol. 51, pp. 212-214, 1987.
- [5] Y. Pastol, G. Arjavalingam, J.-M. Halbout, and G. V. Kopcsay, "Coherent broad-band microwave spectroscopy using picosecond optoelectronic antennas," *Appl. Phys. Lett.*, vol. 54, pp. 307-309, 1989; G. Arjavalingam, Y. Pastol, J.-M. Halbout, and G. V. Kopcsay, "Broad-band microwave measurements with transient radiation from optoelectronically pulsed antennas," *IEEE Trans. Microwave Theory Tech.*, vol. MTT-38, pp. 615-621, 1990.
- [6] Ch. Fattinger and D. Grischkowsky, "Point source terahertz optics," *Appl. Phys. Lett.*, vol. 53, pp. 1480-1482, 1988; Ch. Fattinger and D. Grischkowsky, "Terahertz beams," *Appl. Phys. Lett.*, vol. 54, pp. 490-492, 1989; M. van Exter, Ch. Fattinger, and D. Grischkowsky, "High-brightness terahertz beams characterized with an ultrafast detector," *Appl. Phys. Lett.*, vol. 55, pp. 337-339, 1989.
- [7] C. R. Lutz and A. P. DeFonzo, "Far-field characteristics of optically pulsed millimeter wave antennas," *Appl. Phys. Lett.*, vol. 54, pp. 2186-2188, 1989.
- [8] R. Simons, *Optical Control of Microwave Devices*. Boston, MA: Artech House, 1990, and references therein.
- [9] H. R. Fetterman, W. Y. Wu, and D. Ni, "Optical control of millimeter wave devices," *Proc. SPIE*, vol. 789, pp. 50-53, 1987; H. R. Fetterman and D. Ni, "Control of millimeter wave devices by optical mixing," *Microwave Opt. Technol. Lett.*, vol. 1, pp. 34-39, 1988; D. C. Ni, H. R. Fetterman, and W. Chew, "Millimeter-wave generation and characterization of a GaAs FET by optical mixing," *IEEE Trans. Microwave Theory Tech.*, vol. MTT-38, pp. 608-614, 1990.
- [10] W. Chew and H. R. Fetterman, "Printed circuit antennas with integrated FET detectors for millimeter-wave quasi optics," *IEEE Trans. Microwave Theory Tech.*, vol. MTT-37, pp. 593-597, 1989.
- [11] J. C. Gammel and J. M. Ballantyne, "The OPFET: A new high speed optical detector," in *Digest Int. Electron Devices Meet*, vol. 150, 1978, pp. 120-123.
- [12] C. Y. Chen, Y. M. Pang, A. Y. Cho, and P. A. Garbinski, "New minority hole sinked photoconductive detector," *Appl. Phys. Lett.*, vol. 43, pp. 1115-1117, 1983.
- [13] M. Matloubian, H. R. Fetterman, M. Kim, A. Oki, J. Camou, S. Moss, and D. Smith, "Picosecond optoelectronic measurement of S parameters and optical response of an AlGaAs/GaAs HBT," *IEEE Trans. Microwave Theory Tech.*, vol. MTT-38, pp. 683-686, 1990; M. Matloubian, S. E. Rosenblum, H. R. Fetterman, and P. T. Greiling, "Wide band millimeter wave characterizations of Sub-0.2 micrometer gate-length AlInAs/GaInAs HEMT's," *IEEE Microwave Guided Wave Lett.*, vol. 1, pp. 32-34, 1991.

Generation of Millimeter-Wave Radiation by Optical Mixing in FET's Integrated with Printed Circuit Antennas

D. V. Plant, D. C. Scott, D. C. Ni, and H. R. Fetterman

Abstract—Using optical mixing, we have demonstrated the generation of continuous wave 60-GHz millimeter wave radiation from FET's integrated with planar antennas. The radiation was propagated through narrow band quasi-optical Fabry-Perot filters and heterodyne detected in a second FET antenna structure. In addition to spectroscopic applications, this transmitter/receiver system demonstrates the feasibility of having optically fed arrays of millimeter wave sources.

OPTICAL control of microwave and millimeter-wave devices has attracted recent attention because of potential applications that involve both the advantages of optical interconnections and microwave propagation. Various control functions including gain control of amplifiers, oscillation tuning, locking and frequency modulation, switching, optical mixing, and optically induced negative photoconductivity have already been demonstrated [1]–[6]. In this letter, we report the first generation and propagation of 60-GHz tunable, continuous wave millimeter-wave radiation using optical mixing in integrated GaAs FET printed circuit structures. The optically generated and transmitted millimeter-wave radiation was detected with a highly sensitive FET antenna circuit using heterodyne detection techniques.

Previously, we demonstrated coherent mixing of optical radiation in FET's, HEMT's, and related three terminal devices [3]. This technique was then extended to 64 GHz using a GaAs FET integrated with a printed circuit antenna, which was designed to couple to millimeter wave frequencies [5]. This configuration permitted direct injection of a fundamental local oscillator and the optical radiation simultaneously to the device active region and demonstrated the mixing capability of these devices at high frequencies. In the series of experiments reported here, the active region of a GaAs FET antenna circuit is illuminated simultaneously by optical radiation from a CW dye laser and a stabilized HeNe laser. The difference frequency between these optical signals radiates from the antenna and propagates in free space. It is then

detected in a similar planar FET structure. This is the first report of the generation and detection of millimeter wave radiation by optical mixing in these three terminal devices integrated with printed circuit antennas. The use of two FET antenna circuits further demonstrates the capabilities of these circuits in an optically controlled transmitter and receiver system. Based on recent studies of optically controlled phased array antennas, this technique is well suited for applications in such systems [7], [8].

A schematic representation of the experimental arrangement is illustrated in Fig. 1. Commercially available FET's (NEC/NE71000) having gate lengths of $0.3\ \mu\text{m}$ and drain to source distances of $2\ \mu\text{m}$ were integrated on printed circuit RT/Duroid microstrip antennas. Identical twin dipole antennas with integrated FET's were used not only to transmit, but also to receive the radiation. However, in the case of the transmitter, the drain and source of the FET were connected to the antenna, while in the case of the receiver, the gate and source were connected to the antenna. The full characterization of the integrated FET antenna circuit as a microwave gate mixer has been described previously, and results show the circuit has a conversion loss of approximately 6 dB when used as a heterodyne detector [9].

The transmitting FET was illuminated with light from a Kiton Red dye laser (600 nm to 640 nm, 400 mW) and a frequency stabilized HeNe laser (632.8 nm, 0.6 mW). The penetration depth of these lasers is about $0.3\ \mu\text{m}$, which is of the same order as the thickness of the active region of the FET, and therefore sufficient to excite the GaAs active layer. The wavelength of the dye laser was locked to an external temperature stabilized Fabry-Perot reference cavity. The wavelength of the laser was monitored with both an optical wavemeter that had 0.001 nm resolution ($< 1.0\ \text{GHz}$), and an optical spectrum analyzer that had a 30-GHz free spectral range. The linewidth and stability of both lasers was typically less than 2 MHz. The beams were combined using a variable beam splitter which permitted changing the ratio of dye laser power to the HeNe laser power. In these experiments, the transmitting FET active region was excited by 20 to 80 milliwatts ($25\text{--}100\ \text{W}/\text{cm}^2$) from the dye laser and 0.15 to 0.36 milliwatts ($200\text{--}450\ \text{W}/\text{cm}^2$) from the HeNe laser. Using a lens, the beams were focused to a spot size of $10\ \mu\text{m}$ in diameter. A reflex klystron, tunable from 55.5 to 62 GHz was used as a local oscillator for heterodyne detection of the radiation. The detected signal output from the receiving FET

Manuscript received February 11, 1991; revised March 21, 1991. This work was supported by the Air Force Office of Scientific Research and The National Center of Integrated Photonics Technology.

D. V. Plant, D. C. Scott, and H. R. Fetterman are with the Department of Electrical Engineering, University of California, Los Angeles, 56-125B Engineering IV, Los Angeles, CA 90024-1594.

D. C. Ni is with AT&T Bell Laboratories, 480 Red Hill Road, Room 2K-081, Middletown, NJ 07748.

IEEE Log Number 9100258.

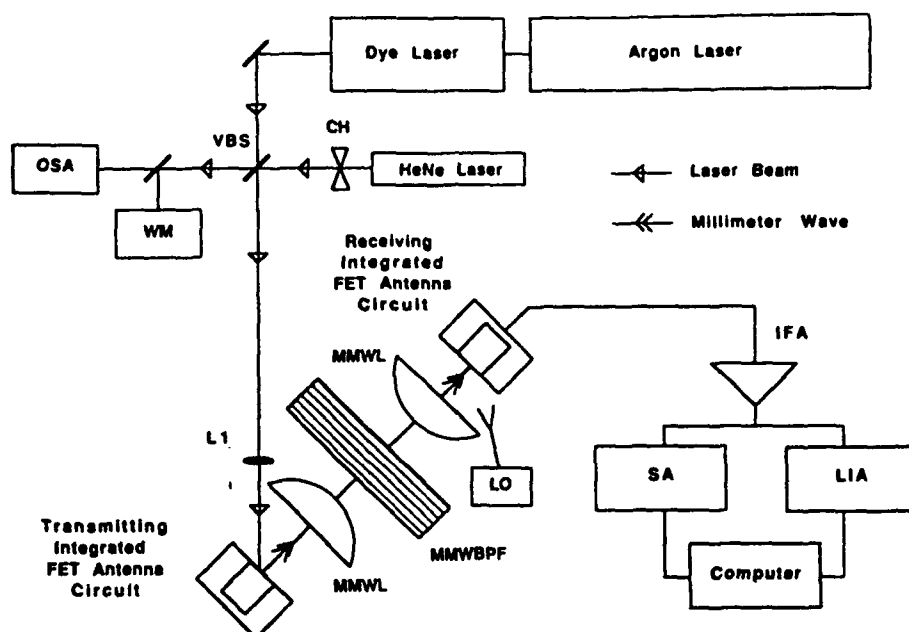


Fig. 1. Schematic of the experimental set-up. VBS, variable beam splitter; OSA, optical spectrum analyzer (30 GHz FSR); WM, wavemeter; L1, 25-mm focal length lens; MMWL, millimeter wave lens; MMWBPF, millimeter wave bandpass filter; IFA, 0.75–2.0 GHz 25-dB gain amplifier; LO, 55.5–62.0 GHz reflex klystron local oscillator; SA, spectrum analyzer; LIA, lock-in amplifier. Optical beam was injected into the device at an angle of 45 degrees with respect to the plane of the transmitting antenna. Teflon lenses were separated by 10 cm.

antenna circuit was sent through an IF amplifier (0.75–2.0 GHz with a gain of 25 db) and displayed on a spectrum analyzer. Two teflon lenses with 25.4 mm focal lengths were placed between the transmitter and the receiver to create a 10-cm long collimated beam into which millimeter wave filters were inserted. A Hewlett Packard 9836 computer was used for data acquisition and processing.

The optical excitation produces continuous wave, tunable, millimeter wave radiation that is optimized at 60 GHz due to the performance of the high gain antenna. A recording of a received signal at 60.25 GHz is shown in Fig. 2. Here, the transmitting FET was illuminated by 80 mW from the dye laser and 0.15 mW from the HeNe laser. The local oscillator is tuned to 61.54 GHz and is irradiating the receiving FET antenna circuit with approximately 25 mW of power. For this data, the devices are biased as follows: The transmitting FET was biased with $V_{ds} = 2.0$ V and $V_{gs} = -2.0$ V and the receiving FET was biased with $V_{ds} = 2.0$ V and $V_{gs} = -0.6$ V. In the case of the transmitter the device is biased below pinchoff (pinchoff voltage for this device at $V_{ds} = 2.0$ V is $V_{gs} = -1.1$ V), therefore photoexcited carriers via photoconduction mechanisms are responsible for generating the radiated laser difference frequency. For these FET's, previous studies show that the frequency response of the photoconduction mechanism is faster than that of the photovoltaic mechanism [10]–[12]. The typical achievable signal to noise ratio for experimental conditions similar to those of Fig. 2 was 30–35 db. Based on the receiver conversion losses and the millimeter-wave collecting optics, the power in the millimeter-wave beam was estimated to be 1 nW. The polariza-

tion of the radiation was measured and found to be linearly polarized as was expected from antenna design considerations.

In an effort to determine the lower limits at which the millimeter-wave radiation could be generated, the ratio of the laser powers was varied. Although a complete study of the performance of the transmitting FET antenna circuit under various conditions of bias and illumination is necessary, preliminary results indicate that the mixing and re-radiation mechanisms require only modest levels of optical power. A S/N of 13 dB was achievable with 20 mW of dye laser power and 0.38 mW of HeNe laser power. Conversely, saturation of the radiating signal strength was observed for dye laser powers in excess of 60 mW indicating a saturation of carriers in the active region of the transmitting device. Also, measurements of the radiating signal strength versus the orientation of the two laser's polarization showed that the optical mixing mechanism is optimized when the two beams are colinearly polarized. This result is critical with respect to the use of a fiber optic light delivery system, and experiments are currently under way using single-mode polarization-preserving fibers. This delivery system will be particularly useful in optically controlled phased array applications that are not limited by fiber-optic losses.

As a demonstration that we have tunable, narrow-band millimeter-wave radiation, we measured the response of a tunable Fabry-Perot interferometer. The filter consisted of two 50-lines/inch metal meshes mounted on optically flat retaining rings. The filter response was measured by tuning the dye laser and therefore, tuning the millimeter-wave radia-

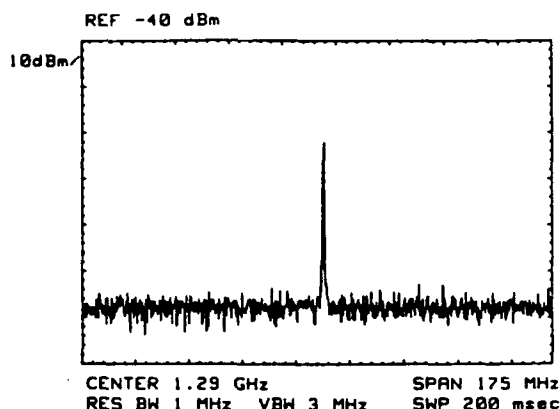


Fig. 2. Spectrum analyzer trace of the received millimeter-wave radiation at 60.25 GHz. Local oscillator is at 61.54 GHz. Transmitting FET was illuminated by 80 mW of dye laser power and 0.15 mW of HeNe laser power.

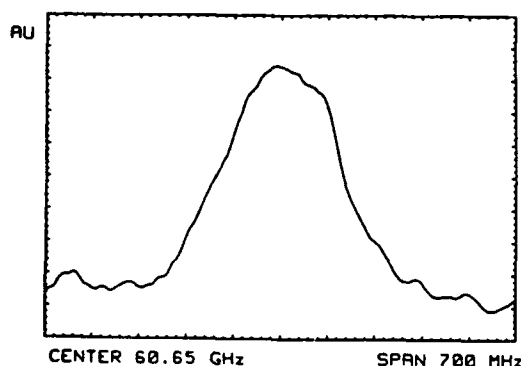


Fig. 3. Transmission response of a metal mesh Fabry-Perot interferometer tuned to resonance at 60.65 GHz. The response is measured by tuning the dye laser and therefore, tuning the millimeter-wave radiation frequency through the passband of the filter. Data were taken with a lock-in time constant of 1.0 second.

tion through the passband of the filter. The signal from the receiving FET was measured using a lock-in amplifier. The lock-in reference channel was locked to the chopped HeNe laser. Fig. 3 shows a recording of the response of the filter. The filter center frequency is at 60.65 GHz, and the full width at half maximum of the filter is 220 MHz. This is in good agreement with the calculated value.

Because the bandwidth of the radiation is limited primarily by the high gain antenna, future improvements to this technique will include the use of broadband, high frequency antennas integrated with high-speed three-terminal devices.

Cascading devices will provide optical mixing signal amplification prior to driving the antenna. Based on the preliminary study of the performance of the transmitting FET antenna circuit under varying conditions of illumination, our results indicate that low power, frequency stabilized, infrared semiconductor lasers could be used to replace the CW dye and HeNe lasers thus providing alternative compact light sources. Finally, this letter demonstrates the potential of converting millimeter-wave signals on light directly into propagating millimeter wave radiation using planar FET structures. It should now be possible to make arrays of distributed sources using this technology.

The authors would like to thank Prof. N. Luhmann and M. Espiau of the Center for High Frequency Electronics for providing microwave components and test equipment.

REFERENCES

- [1] A. J. Seeds and A. A. A. de Salles, "Optical control of microwave semiconductor devices," *IEEE Trans. Microwave Theory Tech.*, vol. MTT-38, no. 5, pp. 577-585, May 1990.
- [2] R. Simons, *Optical Control of Microwave Devices*. Boston: Artech House, 1990.
- [3] H. R. Fetterman, W. Y. Wu, and D. Ni, "Optical control of millimeter wave devices," *Proc. SPIE*, vol. 789, pp. 50-53, 1987.
- [4] C. S. Chang, H. R. Fetterman, D. Ni, E. Sovero, B. Mathur, and W. J. Ho, "Negative photoconductivity in high electron mobility transistors," *Appl. Phys. Lett.*, vol. 51, no. 26, pp. 2233-2235, 1987.
- [5] D. C. Ni, H. R. Fetterman, and W. Chew, "Millimeter-wave generation and characterization of a GaAs FET by optical mixing," *IEEE Trans. Microwave Theory Tech.*, vol. MTT-38, no. 5, pp. 608-614, May 1990.
- [6] P. R. Herzfeld, Guest Ed., "Special issue on applications of light-wave technology to microwave devices," *IEEE Trans. Microwave Theory Tech.*, MTT-38, no. 5, pp. 465-466, May 1990.
- [7] G. J. Simonis and K. G. Purchase, "Optical generation, distribution, and control of microwaves using laser heterodyne," *IEEE Trans. Microwave Theory Tech.*, vol. MTT-38, no. 5, pp. 667-669, May 1990.
- [8] W. Chew and H. R. Fetterman, "Printed circuit antennas with integrated FET detectors for millimeter-wave quasi-optics," *IEEE Trans. Microwave Theory Tech.*, vol. MTT-37, no. 3, pp. 593-597, Mar. 1989.
- [9] J. P. Noad, E. H. Hara, R. H. Hum, and R. I. MacDonald, "FET photodetectors: A combined study using optical and electron-beam stimulation," *IEEE Trans. Electron. Devices*, vol. ED-29, no. 11, pp. 1792-1797, Nov. 1982.
- [10] G. J. Papaionanou and J. R. Forrest, "On the photoresponse of GaAs MESFET's: Backgating and deep trap effects," *IEEE Trans. Electron. Devices*, vol. ED-33, no. 3, pp. 373-378, 1986.
- [11] R. B. Darling and J. P. Uyemura, "Optical gain and large-signal characteristics of illuminated GaAs MESFET's," *IEEE J. Quantum Electron.*, vol. QE-23, no. 7, pp. 1160-1171, July 1987.

Optically Generated 60 GHz Millimeter Waves Using AlGaAs/InGaAs HEMT's Integrated with Both Quasi-Optical Antenna Circuits and MMIC's

D. V. Plant, *Member, IEEE*, D. C. Scott, H. R. Fetterman, *Fellow, IEEE*, L. K. Shaw, W. Jones, and K. L. Tan

Abstract—Continuously tunable 49–67 GHz millimeter wave radiation has been generated using optical mixing in AlGaAs/InGaAs HEMT's integrated with both quasi-optical antenna circuits and multistage MMIC amplifiers. Using these systems, microwatt levels of millimeter wave power has been generated. A quantitative study of the signal strength versus bias, polarization, and light intensity was performed. In addition, the millimeter waves were modulated by applying a RF signal (< 1 GHz) to the FET gate. Using this technique, tunable electrical sidebands were added to the optically generated 60 GHz carrier, thus providing a method of transmitting information.

INTRODUCTION

OPTICAL-MILLIMETER wave interactions have attracted recent attention because of applications which involve the advantages of both lightwave and microwave techniques [1], [2]. It allows the use of optical-fiber technology for interconnection of microwave devices and circuits [3]. Concurrently, high electron mobility transistors (HEMT's) have gained widespread application in low-noise millimeter wave amplifiers due to their superior noise performance compared to MESFET's [4]. In this letter, we report the use of pseudomorphic AlGaAs/InGaAs HEMT's to generate tunable continuous-wave millimeter wave radiation by optical mixing. Three terminal devices offer unique advantages over two terminal devices for generating millimeter waves using optical mixing [5]. In particular, the gate provides a means of applying tunable RF sidebands to a tunable, optically generated carrier for use in communication systems. This technique eliminates the need to directly modulate one of the two heterodyned laser sources. Also, the illuminated HEMT can be optimized as a function of drain and gate bias thus increasing the optical mixing photocurrents.

Previously, we generated 60 GHz millimeter wave radia-

tion using low-frequency, commercially available GaAs MESFET's integrated with quasi-optical antennas [6]. In order to increase the optically generated millimeter wave power, 60 GHz pseudomorphic AlGaAs/InGaAs HEMT's were used in place of GaAs MESFET's [7]. The motivation was to use devices whose optical sensitivity and optical speeds are larger than GaAs MESFET's [8]–[10]. In particular, optically generated electrons are transferred to the high-mobility two-dimensional electron gas (2DEG) which increases the mixing photocurrent and increases the millimeter wave power.

Two different systems were investigated. First, HEMT's were integrated with printed circuit antennas in order to generate freely propagating millimeter wave radiation. Second, HEMT's were integrated into microstrip with 60 GHz multistage MMIC amplifiers to provide gain. Optical fibers were used to deliver light to pump both the optical mixer/antenna circuits and the optical mixer/amplifier circuits. The extension to optical fibers is important with respect to applications of these techniques in systems such as optically controlled phased arrays. [11].

EXPERIMENTAL SETUP

The devices used in both experiments were 60 GHz pseudomorphic $\text{Al}_{0.25}\text{Ga}_{0.75}\text{As}/\text{In}_{0.28}\text{Ga}_{0.72}\text{As}$ HEMT's [7]. The HEMT's were illuminated with light from an actively frequency stabilized Krypton red dye laser (600–640 nm) and an actively frequency stabilized He–Ne laser (632.8 nm). The wavelength of each linearly polarized laser was monitored with a wavemeter which had 0.001 nm resolution. The frequency stability of each laser was better than 2 MHz. The beams were combined using a beam splitter and then were coupled into single-mode polarization preserving and nonpolarization preserving optical fibers. The fiber core diameters were 2.75 μm , and the output tips were brought to less than 1 mm from the device active region. In order to prevent feedback into the actively stabilized lasers, the input and output tips of the fibers were polished with 10° wedge angles.

In the optical mixer/antenna circuit experiments, the optically generated millimeter wave radiation was radiated into free space and then coupled into waveguide detectors using

Manuscript received October 1, 1991. The work at UCLA was supported by the Air Force Office of Scientific Research and by the National Center for Integrated Photonics Technology.

D. V. Plant, D. C. Scott, and H. R. Fetterman are with the Department of Electrical Engineering, University of California, Los Angeles, CA 90024.

L. K. Shaw, W. Jones, and K. L. Tan are with TRW Electronics and Technology Division, Redondo Beach, CA 90278.

IEEE Log Number 9105315.

lenses and horns. In the optical mixer/amplifier circuit experiments, the millimeter waves were launched into waveguide via microstrip to coaxial to waveguide transitions. The signals were measured using a heterodyne receiver which employed a tunable (55.5–62 GHz) klystron for a local oscillator. In both experiments, the optically generated millimeter waves and the local oscillator were combined in a directional coupler and fed into a waveguide mixer. The mixer outputs were sent through IF amplifiers and displayed on a computer-controlled spectrum analyzer.

OPTICAL MIXER/ANTENNA CIRCUIT RESULTS

In the first set of experiments, the HEMT's were integrated on printed circuit RT/Duriod microstrip antennas in a common source mode. Twin dipole antennas designed for optimum gain at 60 GHz were used. In the transmitter configuration, the drain to source was connected across the antenna. The optical mixing produced photocurrents at the desired reradiation frequency. Fig. 1(a) is a recording of a received signal at 61.342 GHz. This figure shows a signal to noise ratio of > 45 dB which is 10 dB larger than our previous results using low frequency GaAs MESFET's [6]. The optimum signals were obtained at pinchoff: $V_{gs} = -0.75$ V at $V_{ds} = 2.5$ V. Based on the transmittivity of the GaAs cap layer (66%), and the differences in the aspect ratios of the fiber output beam and the device active region, we calculated that 3% of the light from each laser is absorbed in the device [12]. Therefore, the maximum absorbed optical power in the device was 2.0 mW and 3.4 μ W for the dye laser and the He-Ne laser, respectively. Also, the radiation was measured to be linearly polarized which agreed with the antenna design.

We attribute the larger signals to an increase in the mixing photocurrents. In a HEMT, photoexcited carriers will not suffer from ionized impurity scattering in the channel as is the case for a MESFET. Since the HEMT's were illuminated with visible light which had a photon energy (1.96 eV) greater than the bandgap energy of each of the HEMT materials, photoexcited carriers are generated in each of the layers comprising this structure. Previous studies have shown that the optically controlled characteristics are most efficient at pinchoff [8]–[10]. This is because photogenerated holes in the top GaAs cap layer and the AlGaAs layer flow into the depletion layer under the negatively biased gate resulting in a decrease in the depletion region size and an opening of the 2 DEG channel. Photogenerated electrons in the InGaAs and the underlying GaAs superlattice experience a vertical field associated with the band bending of the AlGaAs/InGaAs heterojunction, and a lateral field associated with the applied drain voltage. These electrons are collected in the high mobility 2 DEG, and they are the dominant contribution to the optical mixing photocurrent.

As mentioned, three terminal devices can be directly RF modulated. This is demonstrated in Fig. 1(b) where a recording of a received signal at 61.342 GHz with 100 MHz electrical sidebands is shown. With an applied RF signal of 5 dBm, the signal power in the sidebands was large, 15 dB down from the carrier, and the sidebands were tunable over

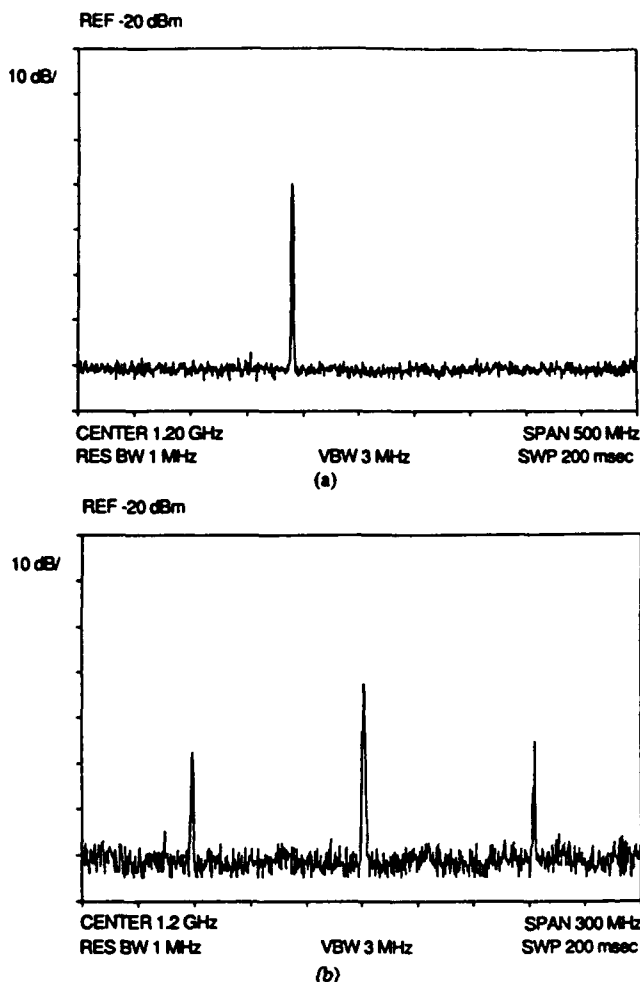


Fig. 1. (a) Recording of received 61.342 GHz radiation from transmitting HEMT/antenna circuit. (b) Recording of signal with 100 MHz RF modulation (5 dBm) applied to transmitter gate.

> 500 MHz of bandwidth. This result demonstrated one of the advantages of using three terminal devices; namely, the ability to apply an information signal without the need to modulate either of the two heterodyned laser sources.

OPTICAL MIXER/AMPLIFIER CIRCUIT RESULTS

In the second set of experiments, the HEMT's were integrated into 50 Ω microstrip with two-stage MMIC amplifiers designed for operation from 57.5 to 65 GHz with > 8 dB of gain [13]. The MMIC active device structures were the same pseudomorphic $\text{Al}_{0.25}\text{Ga}_{0.75}\text{As}/\text{In}_{0.28}\text{Ga}_{0.72}\text{As}$ devices. Fig. 2 is a schematic of the optical mixer/amplifier circuit. The test fixture was equipped with dc to 65 GHz coaxial connectors at both the input and the output. Light from the two lasers was injected into the HEMT using optical fibers. The optical mixing signal from the discrete HEMT device was amplified by the MMIC and launched into waveguide. Fig. 3 is a recording of a received signal at 60.395 GHz. A signal-to-noise ratio of > 55 dB is obtainable. Based on the microstrip to waveguide transition losses and the mixer conversion losses, the optically generated millimeter wave power was estimated to be > 0.3 μ W. This represented a 300-fold increase in power from our previous experiments using GaAs

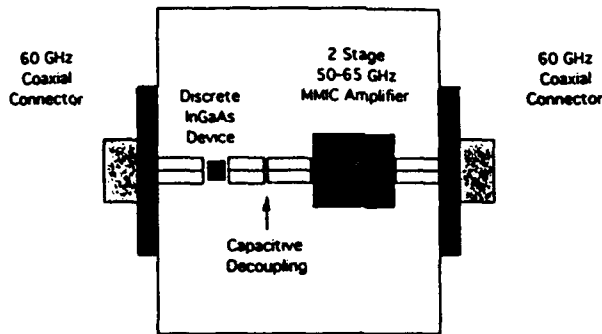


Fig. 2. Diagram of optical mixer/amplifier circuit. The devices were mounted with 50 Ω microstrip and dc to 65 GHz microstrip to coaxial connectors.

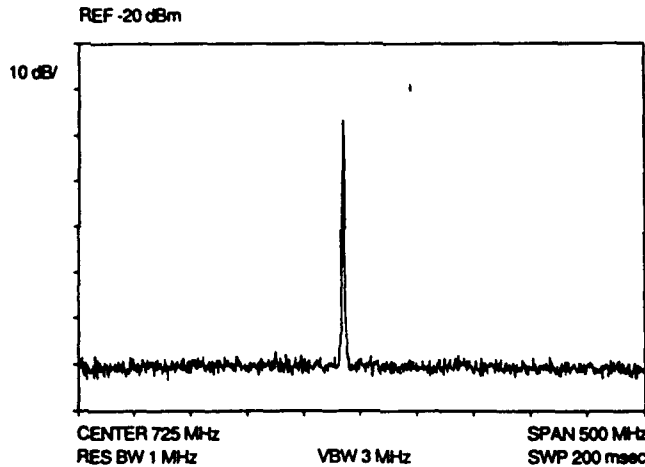


Fig. 3. Recording of measured signal at 60.395 GHz. The optically generated millimeter wave power was estimated to be $> 0.3 \mu\text{W}$ and the 3 dB linewidth of the signal was 3 MHz.

MESFET's. It is worth noting that in these experiments the optically generated millimeter waves could have been launched from a horn for use in free space propagation experiments. The electrical performance of the circuit was measured from 50 to 65 GHz. The circuit had gain from 56 to 61 GHz with a peak gain of 7.75 dB at 58.5 GHz. The bandwidth of the optically generated millimeter waves was also measured and we found that it extended from 49 to 67 GHz. The optimum signals, signal-to-noise ratios greater than 40 dB, were measured from 57.5 to 62 GHz which correlated well with the electrical measurements.

Using this circuit, quantitative measurements of the optical mixing efficiency versus polarization orientation were made. The data were taken using a lens to focus the light onto the device. As is expected from optical heterodyne theory [14], the signal strength was optimized when the beams were collinearly polarized. The decrease in signal strength for orthogonal beams was 25 dB. Based on these measurements, using polarization preserving fibers is preferred, although not essential to excite the optical mixer/amplifier. Using nonpolarization preserving fibers in which the polarization states were allowed to mix, we obtained a signal to noise ratio of 45 dB.

Next, the mixing efficiency versus intensity of the two lasers was examined. Fig. 4(a) and (b) are log/log plots of

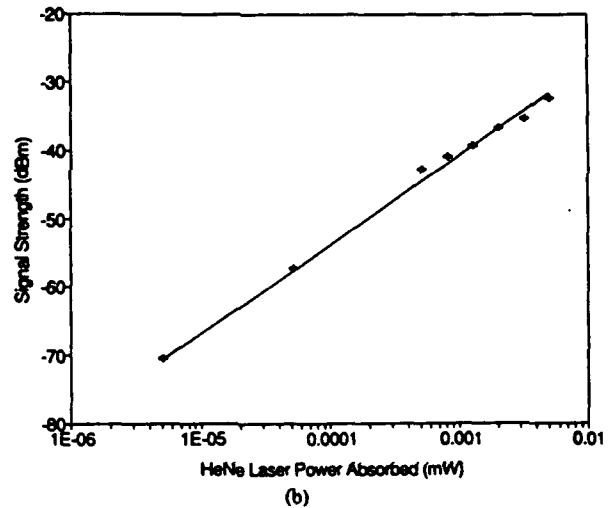
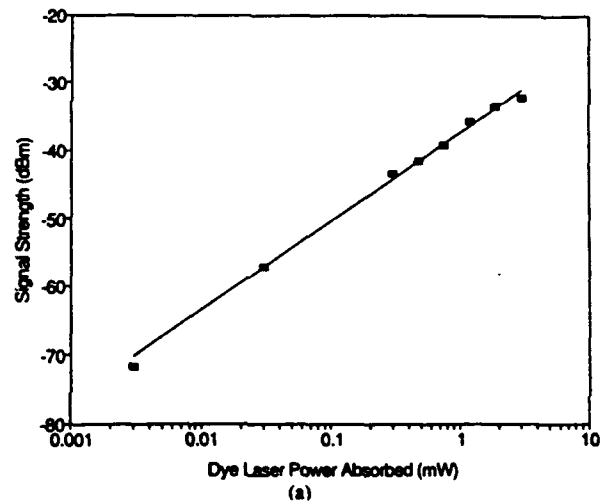


Fig. 4. (a) Signal strength versus dye laser power (He-Ne laser power fixed at $3.4 \mu\text{W}$ absorbed). (b) Signal strength versus He-Ne laser power (dye laser power fixed at 2.0 mW absorbed). The slopes of the lines fitted to the data were the same indicating that the optical illumination levels for both lasers was in the small signal regime.

the signal strength versus dye laser and He-Ne laser power, respectively, coupled into the device while the second laser power was held constant. The slopes of the lines which were fit to the data are the same. This is expected from optical heterodyne theory, which predicts that the optical mixing output power is linearly proportional to the input signal power. Because the data do not show any saturation behavior, we concluded that the optical illumination levels for both lasers was in the small signal regime. These results also indicated that improved optical coupling efficiency could provide larger millimeter wave powers.

CONCLUSIONS

In summary, we have generated useful amounts of millimeter wave power using HEMT's in conjunction with quasi-optical antennas and MMIC's. Direct modulation of the gate produced RF sidebands on the optically generated carrier. The characteristics of the optical mixing were studied and the results agree well with what is expected from optical heterodyne theory. Based on the optical mixing power versus

optical input power measurements, similar experiments can be done using low-power, frequency stabilized laser diodes which have temperature tunability over millimeter wave frequencies.

REFERENCES

- [1] P. R. Herczfeld, Guest Ed., "Special issue on applications of light-wave technology to microwave devices," *IEEE Trans. Microwave Theory Tech.*, vol. MTT-38, 1990.
- [2] R. Simons, *Optical Control of Microwave Devices*. Boston and London, Artech House, 1990.
- [3] A. J. Seeds and A. A. A. de Salles, "Optical control of microwave semiconductor devices," *IEEE Trans. Microwave Theory Tech.*, vol. MTT-38, pp. 577-585, 1990.
- [4] P. C. Chao, *et al.*, "DC and microwave characteristics of sub-0.1- μm gate-length planar doped pseudomorphic HEMT's," *IEEE Trans. Electron Devices*, vol. 36, pp. 461-471, 1989.
- [5] G. J. Simonis and K. G. Purchase, "Optical generation, distribution, and control of microwaves using laser heterodyne," *IEEE Trans. Microwave Theory Tech.*, vol. MTT-38, pp. 667-669, 1990.
- [6] D. V. Plant, D. C. Scott, D. C. Ni, and H. R. Fetterman, "Generation of millimeter-wave radiation by optical mixing in FET's integrated with printed circuit antennas," *IEEE Microwave Guided Wave Lett.*, vol. 1, pp. 132-134, 1991.
- [7] K. L. Tan, R. M. Dia, D. C. Streit, L. K. Shaw, A. C. Han, M. D. Sholley, P. H. Liu, T. Q. Trinh, T. Lin, and H. C. Yen, "60-GHz pseudomorphic AlGaAs/InGaAs low-noise HEMT's," *IEEE Electron Device Lett.*, vol. 12, pp. 23-25, 1991.
- [8] R. N. Simons and K. B. Bhasin, "Analysis of optically controlled microwave/millimeter wave device structures," *IEEE Trans. Microwave Theory Tech.*, vol. MTT-34, pp. 1349-1355, 1986; R. N. Simons, "Microwave performance of an optically controlled AlGaAs/GaAs high electron mobility transistor and GaAs MESFET," *IEEE Trans. Microwave Theory Tech.*, vol. MTT-35, pp. 1444-1445, 1987.
- [9] C. Y. Chen, A. Y. Cho, C. G. Bethea, P. A. Garbinski, and B. F. Levine, "Ultrahigh speed modulation-doped heterostructure field-effect photodetectors," *Appl. Phys. Lett.*, vol. 42, pp. 1040-1042, 1983; C. Y. Chen, Y. M. Pang, A. Y. Cho, and P. A. Garbinski, "New minority hole sinked photoconductive detector," *Appl. Phys. Lett.*, vol. 43, pp. 1115-1117, 1983.
- [10] T. Umeda, Y. Cho, and A. Shibatomi, "Picosecond HEMT photodetector," *Japan. J. Appl. Phys.*, vol. 25, pp. L801-L803, 1986.
- [11] P. R. Herczfeld and A. S. Daryoush, "Recent developments related to an optically controlled microwave phased array antenna," *Proc. SPIE*, vol. 996, pp. 108-115, 1988.
- [12] R. B. Darling and J. P. Uymura, "Optical gain and large-signal characteristics of illuminated GaAs MESFET's," *IEEE J. Quantum Electron.*, vol. QE-23, pp. 1160-1171, 1987.
- [13] L. K. Shaw, D. Brunone, T. Best, B. Nelson, W. Jones, D. Streit, and P. Liu, "A monolithic 60 GHz multistage InGaAs HEMT low noise amplifier," in *Tech. Dig. 15th Internat. Conf. Infrared Millimeter Waves*, 1991, pp. 523-525.
- [14] M. C. Teich, "Infrared heterodyne detection," *Proc. IEEE*, vol. 56, pp. 37-46, 1968.

60 GHz board-to-board optical interconnection using polymer optical buses in conjunction with micropism couplers

R. T. Chen, H. Lu, D. Robinson, Z. Sun, and T. Jansson
Physical Optics Corporation, 2545 West 237th Street, Suite B, Torrance, California 90505

D. V. Plant and H. R. Fetterman
Department of Electrical Engineering, University of California at Los Angeles, Los Angeles, California 90024

(Received 3 September 1991; accepted for publication 16 November 1991)

We have demonstrated for the first time 60 GHz wide-band board-to-board optical interconnection with a signal-to-noise ratio of 22 dB. The total interconnection distance is 55 cm from the input coupling prism to the detector. Board-to-board optical interconnection was realized using micropisms which had a measured coupling bandwidth of more than 250 nm. The graded index of the polymer waveguide allows us to implement such an interconnection scheme on an array of substrates. The elimination of backplane interconnection greatly enhances the interconnection speed. The implementation of a high-speed on-board transceiver in connection with a polymer waveguide lens will generate a fully on-board optical interconnect involving modulation/demodulation.

We are reporting for the first time a 60 GHz board-to-board optical interconnection using polymer optical buses in conjunction with micropism couplers. An intraboard interconnection distance as long as 30 cm was previously demonstrated.¹ The result demonstrated in this paper employs two optical bus boards containing a graded index (GRIN) polymer waveguide.^{2,3} Board-to-board interconnection was realized using micropism couplers made out of LaSF glass. The current performance of state-of-the-art electronic systems, especially large computers, is limited by electrical interconnects rather than the on-chip processing speed. As the number of components per chip and the processing speed increase drastically, electrical interconnection becomes inadequate on module-to-module and board-to-board levels.⁴ A multichip module (MCM) for a high-speed, highly parallel electronic system (e.g., IBM's System/390 mainframe uses a MCM that holds 121 chips, spaced about 3/8 in. apart) was implemented to minimize the speed limitation imposed on electrical interconnections (EI). However, the intrinsic characteristics of conventional electrical interconnections jeopardize transmitting a 1-GHz signal farther than 1 mm.⁵ The use of transmission lines involves ground-plane implementation, which becomes dispersive and results in significant losses from the skin effect as the speed increases.

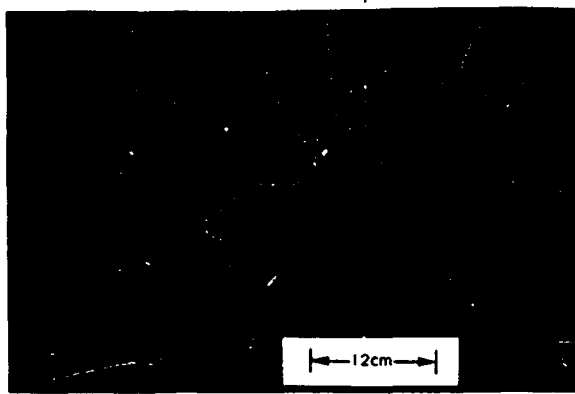
In this letter, the demonstration of 60 GHz board-to-board optical interconnections with distances as long as 55 cm is presented. The demonstration used single-mode GRIN polymer waveguides in conjunction with micropisms. The high-speed optical signal was generated by coherently mixing two lasers $\psi_1 = A \cos \omega_1 t$ and $\psi_2 = B \cos \omega_2 t$.

At the receiving end, the demodulation process involves a square-law detector which displays the intensity of the optical signal as a photocurrent⁶

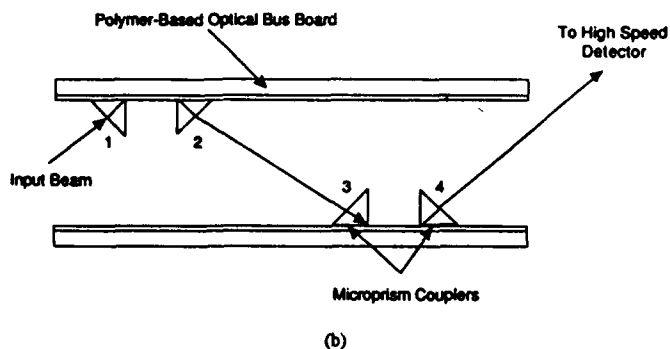
$$I = \frac{e\eta}{\hbar\omega} [A^2 + B^2 + 2C(\omega_{\text{beat}})\cos\varphi AB \cos(\omega_{\text{beat}}t)], \quad (1)$$

where $\omega_{\text{beat}} = \omega_1 - \omega_2$, e is the electron charge, η is the quantum efficiency, $\hbar\omega$ is the photon energy, $C(\omega_{\text{beat}})$ is the frequency response of the detector, and φ is the angle between the polarized directions of the two light waves. The frequency of the beat signal is controlled by the frequency separation of the two lasers. By coherently mixing ψ_1 and ψ_2 , the detected signal represented by Eq. (1) contains a combination of the dc part and a modulated part. The result represented by Eq. (1) is equivalent to that of an optical wave, modulated at a microwave frequency ω_{beat} . The two lasers we employed were a Kiton red dye laser (600–640 nm up to 400 mW) and a frequency-stabilized HeNe laser (632.8 nm, 0.6 mW). The wavelength of the dye laser was locked to an external-temperature-stabilized Fabry–Perot reference cavity. The linewidth and stability of both lasers was typically less than 2 MHz. Propagation of the mixed optical waves from input port to output port is illustrated in Fig. 1(a). A schematic representation of Fig. 1(a) is further depicted in Fig. 1(b). The coupling stages are not shown in Fig. 1(b). Due to the GRIN property of the polymer thin film,^{2,3} the optical bus boards can be made out of any substrate of interest, such as Al_2O_3 , Si, GaAs, glass, PC board, etc. Our demonstration was done using BK-7 glass substrates. The measured optical insertion loss from location 1 to location 4 (Fig. 1) was ~ 6 dB (excluding Fresnel reflection). The input TEM_{00} mode (location 1) and the m dots coupled out at locations 2 and 4 are shown in Figs. 2(a), 2(b), and 2(c), respectively. Formation of the well-defined m dots verified the quality of the polymer waveguide. The in-plane scattering of the optical bus board was very small. The polymer waveguide implemented has a wide optical transmission bandwidth from ~ 300 to ~ 2800 nm.² As a result, intraboard optical interconnections using ultraviolet, visible, and near-infrared wavelengths as the signal carrier can be realized.

The experimental setup for the high-speed board-to-board optical interconnection is shown in Fig. 3, where the



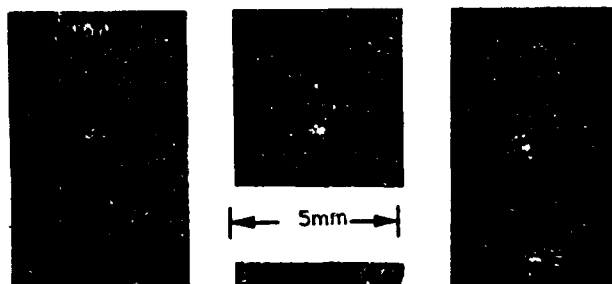
(a)



(b)

FIG. 1. (a) Photograph of board-to-board optical interconnection using polymer-based optical data boards in conjunction with microprisms. (b) Schematic of (a). The coupling stages are not shown.

coherently mixed optical signal is collinearly coupled into the first optical bus board through a prism coupler. The optical bus board is adjusted such that the tangential components of the electromagnetic fields are continuous at the prism/gap/waveguide interface to generate "optical tunneling." The optical beam containing the ω_{beat} [Eq. (1)] propagates across the first optical bus board and then couples out of the first board using another prism coupler. To efficiently couple the optical wave from the first optical board to the second one, control of the profile of the beam



(a)

(b)

(c)

FIG. 2. Near-field images of (a) TEM_{00} laser light at location 1 [Fig. 1(b)], (b) mode dot at location 2, and (c) mode dot at location 4.

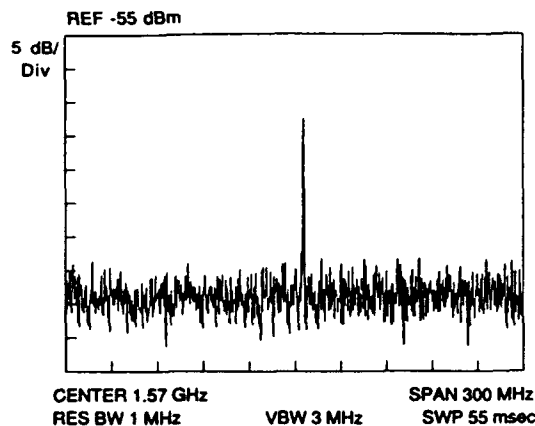


FIG. 3. Generation, transmission, and detection of 60 GHz signal for 55-cm board-to-board optical interconnection.

coupled out from the output prism coupler of the first optical data board is extremely important. A good quality optical waveguide and an appropriate prism-to-waveguide attachment provided us with an output beam with well-defined m dots [Fig. 2(b)] which facilitated the coupling into the second optical bus board. By employing a similar technique, a good-quality m dot was coupled out of the second optical data board [Fig. 2(c)]. The optical "signal" coupled out of the second optical bus board was focused onto the detector using an $10\times$ objective lens. The demodulation scheme is shown in Fig. 3. The detector is a three-stage amplifier circuit consisting of a discrete AlGaAs/InGaAs high-electron-mobility transistor (HEMT)⁷ in series with a two-stage 60 GHz millimeter-wave monolithic integrated circuit (MMIC) amplifier⁸ (a complete description of the optical mixer/amplifier will be presented elsewhere⁹). The optical mixing takes place in the active region of the discrete HEMT device. The 60 GHz output was amplified by the MMIC and fed into waveguide via a microstrip to coaxial to waveguide transition. The signal was then downconverted to intermediate frequencies (1–2 GHz) using a directional coupler fed local oscillator (klystron) and a waveguide mixer. In the initial phases of this experiment, continuous tuning of ω_{beat} from 1 to 25 GHz was demonstrated to establish the large bandwidth capability of this system. We then switched to the highest frequency of our new detection system and the result shown in Fig. 4 is the heterodyne detected signal at 60 GHz. As previously mentioned, the beat signal represented by Eq. (1) is equivalent to a modulated base band signal using a high-speed laser diode or an external modulator driven by a single-frequency microwave source. The availability of a high-speed transceiver will allow us to demonstrate board-to-board optical interconnections with fully on-board modulation and demodulation capabilities.^{10,11} A GRIN polymer waveguide lens¹² can also be used to provide a diffraction-limited spot and thus achieve high-speed signal detection.

The experimental results demonstrated in this letter conclude that the GRIN polymer waveguide can be used as a high-speed optical bus for board-to-board optical in-

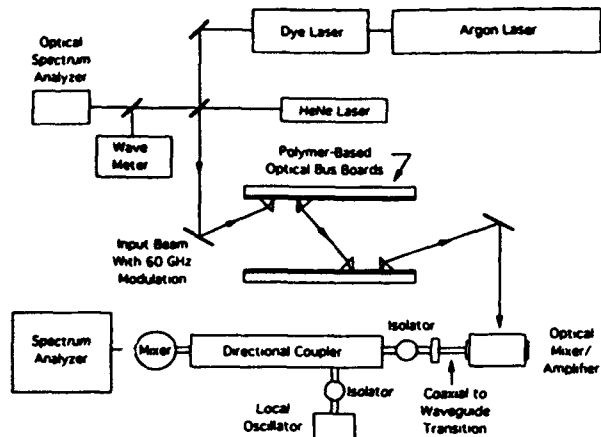


FIG. 4. 60-GHz signal detected at location 4 [Fig. 1(b)]. A 22-dB signal-to-noise ratio is clearly indicated.

interconnection with speeds as high as 60 GHz and bit error rates (BER) of 10^{-10} (22 dB signal-to-noise ratio). It should be noted that the limit on speed was imposed by the system power budget rather than the polymer-based optical bus board. A 1 GHz board-to-board optical interconnection through free space was previously demonstrated.¹³ Here a 60 GHz board-to-board optical interconnection involving a single-mode polymer waveguide is reported for the first time. For the three-dimensional (3D) optical interconnection demonstrated in this program, board-to-board interconnections were realized through free space rather than an optical backplane.¹⁴ Optical interconnections through a backplane introduce an extra degree of material dispersion and thus impose a more stringent speed limit for 3D optical interconnections. 3D optical interconnections using holographic optical elements (HOEs) turn out to be impractical⁴ due to the required phase-matching condition associated with them. Such coupling devices are intrinsically narrow band which strictly limits the availability of light sources. To cover the required interconnection distances using HOE while still maintaining a good power budget, the entire area of the detector has to be enlarged to compensate for the deviation of the optical beam propagation due to the shift of optical wavelength. On the other hand, the microprism we employed is a wide-band coupler. By fixing the input beam at the coupling angle which is phase matched to the effective index of the guided wave, a 3-dB coupling bandwidth of more than 250 nm was experimentally confirmed using a Ti-sapphire laser. Figure 5 shows the demonstrated experimental results. Note that such wide-band coupling is realizable only if the material dispersion of the GRIN polymer waveguide and the prism as a function of wavelength has a coherent pace within the full spectrum of optical wavelength tuning. The selection of a microprism with this dispersion characteristic is a paramount factor in the results presented here.

In summary, we are reporting for the first time a 60 GHz board-to-board optical interconnection using polymer optical buses in conjunction with wide-band microprism couplers. A signal-to-noise ratio of 22 dB was exper-

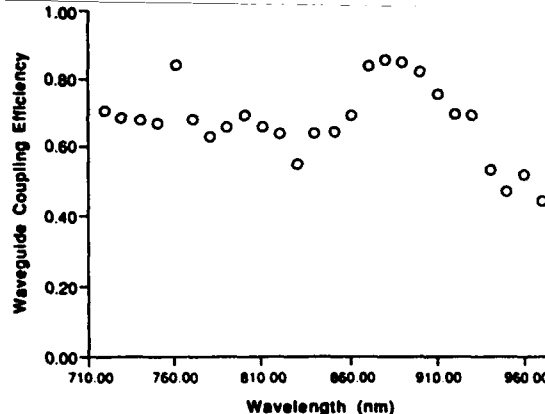


FIG. 5. Experimental result of free space to polymer-based optical bus board coupling using a microprism. A 3-dB bandwidth of more than 250 nm is shown.

imentally confirmed which is equivalent to BER of 10^{-10} . The beat signal, which was 60 GHz in our demonstration, is equivalent to an optical signal modulated by either an external modulator or a laser diode using a 60 GHz single-frequency microwave as the modulation source. Implementation of a polymer waveguide lens onto the optical data board will provide us with a diffraction-limited spot and thus ease the demodulation criterion. Finally, the combination of a GRIN polymer waveguide and a LaSF microprism provided us with a 250-nm free space to optical data board coupling bandwidth, which is two orders of magnitude higher than for an HOE.

Physical Optics Corporation's research is sponsored by SDIO, the Army Research Office, the Department of Energy and UCLA's research is sponsored by AFOSR and NCIPT.

¹ R. T. Chen, Proc. SPIE, 1374 (1990).

² R. T. Chen, M. R. Wang, G. J. Sonek, and T. Jansson, Opt. Eng. 30, 622 (1991).

³ R. T. Chen, W. Phillips, T. Jansson, and D. Pelka, Opt. Lett. 14, 892 (1989).

⁴ R. T. Chen, H. Lu, M. R. Wang, D. Robinson, and T. Jansson, IEEE/OSA J. Lightwave Technol. (to be published).

⁵ M. R. Feldman, S. C. Esener, C. C. Guest, and S. H. Lee, Appl. Opt. 27, 1742 (1988).

⁶ S. Kawanishi, A. Takada, and M. Saruwatari, IEEE/OSA J. Lightwave Technol. 7, 92 (1989).

⁷ K. L. Tan, R. M. Dia, D. C. Streit, L. K. Shaw, A. C. Han, M. D. Sholley, P. H. Liu, T. Q. Trinh, T. Lin, and H. C. Yen, IEEE Electron Device Lett. 12, 23 (1991).

⁸ L. K. Shaw, D. Brunone, T. Z. Best, B. Nelson, W. Jones, D. Streit, and P. Liu, in the Technical Digest of the 15th International Conference on Infrared and Millimeter Waves (1991), p. 523.

⁹ D. V. Plant, D. C. Scott, H. R. Fetterman, L. K. Shaw, W. Jones, and K. L. Tan, IEEE Photon. Technol. Lett. (in press).

¹⁰ S. Y. Wang and D. M. Bloom, Electron. Lett. 19, 554 (1983).

¹¹ S. R. Forrest, Proc. 75, 1488 (1987).

¹² R. T. Chen, Final Report to Army Harry Diamond Lab, Contract No. DAAL02-91-C-0034 (1991).

¹³ A. Yang, in Integrated Photonics Research, 1991, Technical Digest Series (OSA, Washington, DC, 1991), p. 590; D. Z. Tsang, Proc. SPIE 1563, 10 (1991).

¹⁴ J. W. Parker, in Topical Meeting on Optical Computing, 1990, Technical Digest Series (OSA, Washington, DC, 1990), p. 286.

High-Speed Optical Response of Pseudomorphic InGaAs High Electron Mobility Transistors

M. Z. Martin, *Member, IEEE*, F. K. Oshita, *Member, IEEE*,
M. Matloubian, *Member, IEEE*, H. R. Fetterman, *Fellow, IEEE*,
L. Shaw, *Member, IEEE*, and K. L. Tan, *Member, IEEE*

Abstract—Optical response of very high-frequency pseudomorphic InGaAs HEMT's with f_T of 140 GHz has been successfully performed. These measurements were done using the picosecond time domain optoelectronic technique at room and low temperatures. The optical photovoltaic responses of these HEMT's show FWHM of 8.4 and 7.5 ps at room temperature and 20 K, respectively. Photoconductive responsivity as high as 4 A/W with an external quantum efficiency of > 600% is reported here.

INTRODUCTION

THREE terminal devices, such as GaAs-MESFET's, HEMT's and HBT's, have been studied under optical illumination to evaluate their performance as high-speed optical detectors [1]–[4]. Very high values of responsivities much better than p-i-n photodiodes have been previously reported [5], [6]. In addition, their structure is easy to integrate for their use in optical circuits. In our experiments we report high sensitivity, large external quantum efficiency, and very broad bandwidths (~ 200 GHz) for the PM-InGaAs HEMT's for the first time. There are a number of mechanisms which contribute to the optical response of GaAs-MESFET's, including the source-drain channel resistivity modulation, source-gate and drain-gate photoconductivity changes, and depletion layer width variation with light intensity [5], [6], [8].

The gate and the drain response of very high-speed state-of-the-art pseudomorphic devices have been studied at different biasing conditions and at room and low temperatures. We have obtained the optical response of these devices using the technique of picosecond optoelectronic sampling of electrical waveforms produced by an optically

excited PM-HEMT. This is the technique of choice because we can measure impulse responses on the order of 5 ps.

MEASUREMENTS

The devices tested were PM-HEMT's with gate width and gate length of 40 and 0.15 μm , respectively. The detailed fabrication and structure of these devices have been reported elsewhere [7]. The fixture consists of a PM-HEMT mounted in the center of two photoconductive switches. This fixture was placed inside a closed cycle helium refrigerator. The temperature was lowered in steps and the optical response of the device was obtained. In the experimental setup, an actively mode-locked frequency doubled Nd: YAG laser was used to pump a dual jet dye laser. The dye laser is operated with a repetition rate of 7.6 MHz at a wavelength of 600 nm, an average power of 70 mW and a FWHM of 1.2 ps. The light beam emerging from the dye laser is divided by a beam splitter into two arms. One arm is the generating arm and the other is the sampling arm, which travels a path of variable length and samples the electrical pulse generated by the first arm. For optical response measurements, the generating beam was focused directly onto the device and the sampling beam was focused onto a photoconductive switch nearest to the device on the gate and the drain side to obtain the gate and the drain waveforms, respectively. The spot size on the device was 8–10 μm .

RESULTS AND DISCUSSION

The transconductance curve for the device at 300 and 20 K is shown in Fig. 1. An improvement is observed in the transconductance of the device at 20 K as compared to the transconductance at room temperature. This is attributed to the fact that Hall mobility measurements on these devices indicate a 2-DEG concentration of $2.7 \times 10^{12} \text{ cm}^{-2}$ with a mobility of 6730 $\text{cm}^2/\text{V}\cdot\text{s}$ at 300 K, and a 2-DEG concentration of $2.6 \times 10^{12} \text{ cm}^{-2}$ with a mobility of 14600 $\text{cm}^2/\text{V}\cdot\text{s}$ at 77 K [7].

Typical time domain waveforms of the optical response both from the gate and drain terminals of the device are shown in Fig. 2. The gate signal under bias is purely

Manuscript received March 13, 1992; revised June 8, 1992. This work was supported by the Air Force Office of Scientific Research under the direction of H. R. Schlossberg and by the National Center for Integrated Photonic Technology.

M. Z. Martin, F. K. Oshita, and H. R. Fetterman are with the Department of Electrical Engineering, University of California, Los Angeles, CA 90024.

M. Matloubian was with the Department of Electrical Engineering, University of California, Los Angeles, CA 90024. He is now with Hughes Research Laboratories, Malibu, CA 90265.

L. Shaw and K. L. Tan are with the Electronics and Technology Division, TRW, Redondo Beach, CA 90278.

IEEE Log Number 9202470.

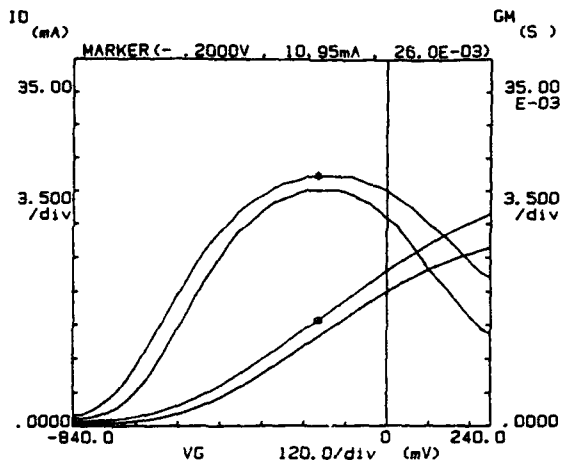


Fig. 1. Transconductance of the HEMT at 300 and 20 K.

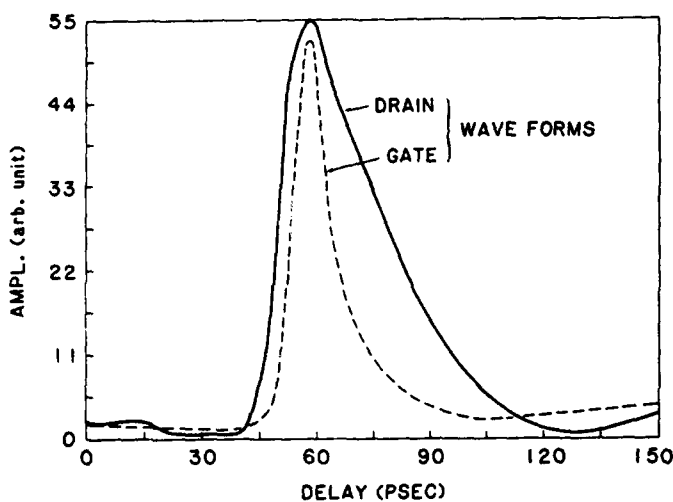


Fig. 2. Optical response of the HEMT from both the gate and the drain terminals of the device.

photovoltaic without any photoconductive gain because the gate contact forms a Schottky diode, while the drain response is a photoconductive effect. The longer decay times in the drain waveform is from the contribution of long lived carriers because of the existence of trapping states at the substrate-channel interface.

The gate response of the HEMT at constant drain voltage of 1.5 V both at 300 and 20 K is shown in Fig. 3. The FWHM of the optical response is observed to increase when the negative gate bias voltage was increased. This is opposite to the effect observed in a GaAs-MESFET [8] in which shorter sweepout times are observed when negative gate voltages are applied, i.e., the increase in the size of the depletion region under negative biases, results in faster collection of the photogenerated carriers under the gate. The difference between the GaAs-MESFET and the pseudomorphic-InGaAs HEMT's is attributed to the existence of a quantum well in the valence band when the InGaAs channel ($L \sim 200 \text{ \AA}$, $E_g \sim 0.9 \text{ eV}$) is sandwiched between AlGaAs ($E_g \sim 1.74 \text{ eV}$) and GaAs ($E_g \sim 1.42 \text{ eV}$). This quantum well acts as a trap for holes in the

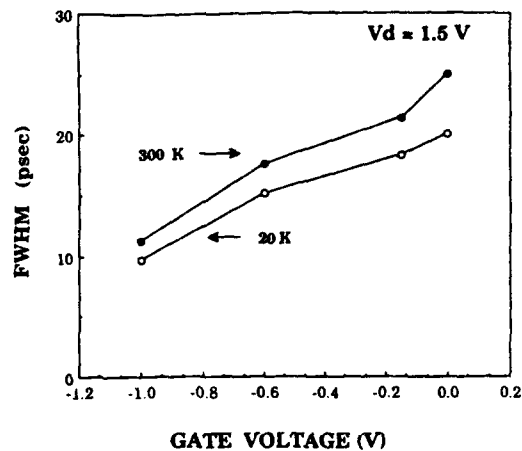


Fig. 3. The FWHM of the gate response as a function of gate bias at a constant drain voltage of 1.5 V at 300 and 20 K.

valence band [9], and when the negative bias is increased the quantum well gets deeper. The capture and re-emission of the holes from this quantum well will degrade the time response in these and similar quantum-well devices.

The drain response of the HEMT at constant drain bias of 1.5 V at 300 and 20 K is shown in Fig. 4. By the illumination of light pulses of $\lambda = 600 \text{ nm}$ used in this experiment, photocarriers are generated everywhere in each layer down to approximately the undoped buffer layer [5]. In this experiment the contribution from the top layers is negligible because these layers are thin and the electrons in these layers have lower velocities as compared to the electrons in the 2-DEG along the heterointerface between the AlGaAs and InGaAs layers. The resultant channel current constitutes most of the drain current and hence a high-speed photoresponse is expected. In this case the FWHM of the optical response decreases as the negative bias on the gate increases. Increasing the negative bias on the gate, increases the field experienced by the electron and accelerates it towards the 2-DEG; hence, we see an improvement in the device time response.

The drain response of the HEMT at a constant gate bias of -1.5 V and increasing drain bias both at 300 and 20 K is shown in Fig. 5. In this case the FWHM of the drain response waveform decreases as we increase the positive drain bias. This indicates that as the electric field between the gate and the drain is increased the carriers are swept quickly into the 2-DEG which explains the fast optical response of the device.

The optical performance of these devices have been evaluated by calculating the responsivity R , which is expressed as

$$R = I_p / P_{\text{opt}} \quad (1)$$

where I_p is the drain current when the incident optical power is P_{opt} . The measured responsivity of the HEMT is 4 A/W with a drain to source voltage of 1.5 V and a gate to source voltage of -0.75 V and P_{opt} is $\sim 1 \text{ mW}$ which when compared to a calibrated Si p-i-n photodiode has an

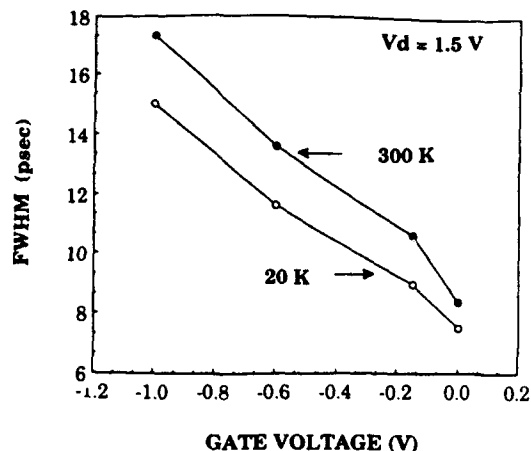


Fig. 4. The FWHM of the drain response as a function of gate bias at a constant drain voltage of 1.5 V at 300 and 20 K.

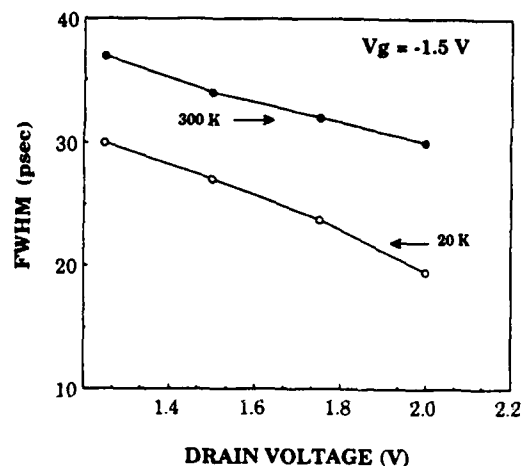


Fig. 5. The FWHM of the drain response as a function of drain bias at a constant gate voltage of -1.5 V.

external quantum efficiency $> 600\%$. Measurements were done using higher incident optical powers and a saturation of the signal was observed smearing out the fast response. Therefore, an incident optical power of ~ 1

mW has been used for all the optical response measurements.

CONCLUSIONS

We report for the first time a record optical response for PM-HEMT of 8.4 and 7.5 ps at 300 and 20 K, respectively. These devices can be used as high-speed photodetectors when biased with 1.5 V on the drain and 0 V on the gate. Such resolution in measurements is made possible by the technique of sampling the optical response using photoconductive switches. A very high value of responsivity of about 4 A/W has been determined and different responses of the gate and the drain configurations have been obtained. Measurements to validate our models are currently underway using infrared lasers.

REFERENCES

- [1] C. Baack, S. Elze, and G. Walf., *Electron. Lett.*, vol. 13, p. 193, 1977.
- [2] J. C. Gammel and J. M. Ballentyne, "GaAs MESFET high speed optical detector," presented at Electron Device Meet., Washington, DC, 1978, p. 120.
- [3] T. Umeda, Y. Cho, and A. Shibatomi, "Picosecond HEMT Photodetector," *Japan. J. App. Phys.*, vol. 25, no. 10, p. L801, 1986.
- [4] M. Matloubian, H. Fetterman, M. Kim, A. Oki, J. Camou, S. Moss, and D. Smith, "Picosecond optoelectronic measurement of s parameters and optical response of an AlGaAs/GaAs HBT," *IEEE Trans. Microwave Theory Tech.*, vol. 38, no. 5, p. 683, 1990.
- [5] R. N. Simons, "Microwave performance of an optically controlled AlGaAs/GaAs high electron mobility transistor and GaAs MESFET," *IEEE Trans. Microwave Theory Tech.*, vol. MTT-35, p. 1444, Dec. 1987.
- [6] C. Y. Chen, A. Y. Cho, C. G. Bethea, P. A. Garbinski, Y. M. Pang, B. F. Levine, and K. Ogawa, "Ultrahigh speed modulation-doped heterostructure field-effect photodetectors," *Appl. Phys. Lett.*, vol. 42, no. 12, p. 1040, 1983.
- [7] K. L. Tan, R. M. Dia, D. C. Streit, A. C. Han, T. Q. Trinh, J. R. Velebir, P. H. Liu, T. Lin, H. C. Yen, M. Sholley, and L. Shaw, "Ultralow-noise W-band Pseudomorphic InGaAs HEMT's," *IEEE Electron Dev. Lett.*, vol. 11, no. 7, p. 303, 1990.
- [8] D. E. Cooper and S. C. Moss, "Picosecond optoelectronic sampling of electrical waveforms produced by an optically excited field effect transistor," *Ultrafast Phenomena*, vol. V, p. 117, 1986.
- [9] P. A. Martin, K. Meehan, P. Gavrilovic, K. Hess, N. Holonyak, Jr., and J. J. Colman, "Transient capacitance spectroscopy on large quantum well heterostructures," *J. Appl. Phys.*, vol. 54, no. 8, p. 4689, 1983.

Cryogenic Performance of a Monolithic W-Band Amplifier Using Picosecond Optoelectronic Technique

F. Oshita, *Member, IEEE*, M. Martin, *Student Member, IEEE*, M. Matloubian, *Member, IEEE*, H. Fetterman, *Fellow, IEEE*, H. Wang, *Member, IEEE*, K. Tan, *Member, IEEE*, and D. Streit, *Member, IEEE*

Abstract—Cryogenic characterization of a monolithic W-band pseudomorphic InGaAs HEMT amplifier has been demonstrated for the first time using the picosecond optoelectronic technique. Low temperature, millimeter-wave measurements have been performed without the use of conventional millimeter-wave sources, components, and transitions. At 94 GHz, the single-stage amplifier exhibits gain of 4.5 dB at 300 K, which increases to 7 dB at 70 K.

I. INTRODUCTION

THE DEVELOPMENT of InGaAs HEMT technology has made possible the design of high performance monolithic integrated circuits at W-band frequencies [1]–[4]. To date, very little broad-band millimeter-wave measurements have been performed due to cumbersome conventional techniques based on HP8510 network analyzers with frequency extenders or six-port network analyzers. These methods rely on bandwidth limited waveguide components and complex de-embedding procedures to remove the effect of waveguide-to-microstrip transitions. In addition, millimeter-wave on wafer probes are only available up to V-band frequencies [5]. As a result, such limitations have made cryogenic measurements at millimeter-wave frequencies difficult to perform.

As technological advances extend devices and circuits to higher operating frequencies, increasing attention has been focussed on optical techniques based on generation and sampling of picosecond pulses with photoconductive switches to characterize these high speed devices and MMIC's [6]–[8]. In this letter, we report the first broad-band and low-temperature characterization of a W-band monolithic amplifier using the picosecond optoelectronic technique. This method has been successfully applied to obtain *S*-parameters of discrete devices and validated with conventional network analyzer measurements at W-band frequencies [8]. Calibration is simplified with this technique, since there are no transitions to de-embed; only the responsivity of each photoconductive switch is cali-

brated. In addition, low-temperature measurements are easier to perform, since all electrical information is extracted with low-frequency components. Such low-temperature measurements are important for applications of enhanced performance MMIC's in cryogenic systems.

II. MEASUREMENTS

Picosecond optoelectronic measurements were performed on a single-stage monolithic W-band amplifier based on pseudomorphic InGaAs HEMT technology. 0.1- μ m *T*-gate PM HEMT's MBE grown on GaAs substrates have been shown to exhibit excellent noise and gain characteristics at millimeter-wave frequencies [9], and thus, are ideal candidates for high-performance GaAs-based MMIC's. Further details on the device/circuit design and fabrication have been reported elsewhere [2].

The amplifier is mounted between a pair of photoconductive switches in an optoelectronic test fixture [7]. DC bias is provided through SMA connectors and 100 pF off chip capacitors bonded to on chip bias networks. The photoconductive switch material is heavily ion-implanted silicon-on-sapphire. When a picosecond pulse strikes a biased photoconductive gap, a short electrical pulse (FWHM 5 ps) is launched along the center transmission line. A time delayed sampling pulse is used to sample the reflected or transmitted signal. This time domain information is then converted into the frequency domain via Fourier transformation and normalized to yield the wide bandwidth (> 100 GHz) circuit response.

The experimental setup utilizes an actively mode-locked frequency-doubled Nd:YAG laser to pump synchronously a cavity dumped picosecond dye laser that puts out a train of picosecond pulses (600 nm, 70 mW average power, 1.2 ps FWHM). The laser output is divided into a generation and sampling path and focussed onto the appropriate pair of photoconductive switches. The sampling beam passes through a time delay stage that varies the arrival of the sampling pulse relative to the generation pulse. A closed cycle Helium refrigerator has been incorporated into the experimental setup to allow device/circuit characterization at cryogenic temperatures down to 15 K. In this configuration, the circuit under test is kept under ideal vacuum conditions, with the laser pulses coupled through an optical window and the electrical signals extracted through low-frequency SMA feedthroughs.

Manuscript received April 22, 1992. This work was supported by the Air Force Office of Scientific Research and the National Center for Integrated Photonic Technology.

F. Oshita, M. Martin, and H. Fetterman are with the Department of Electrical Engineering, University of California, Los Angeles, 64-147 Engineering IV, Los Angeles, CA 90024.

M. Matloubian is with Hughes Research Laboratories, Malibu, CA 90265.

H. Wang, K. Tan, and D. Streit are with the Electronics Technology Division, TRW, Redondo Beach, CA 90278.

IEEE Log Number 9202001.

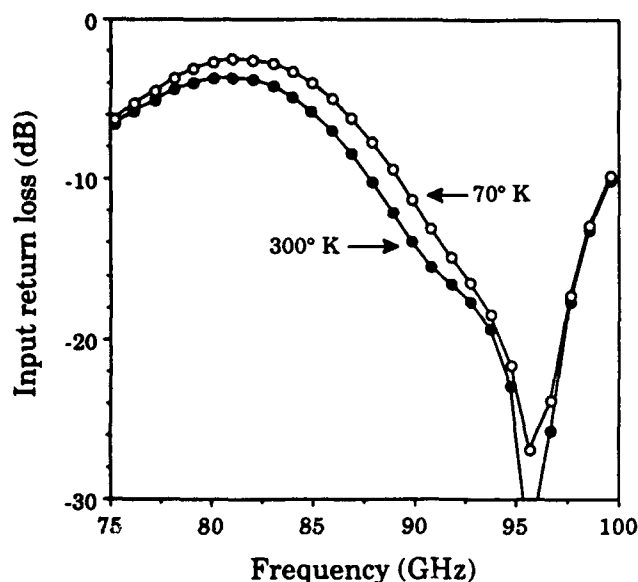


Fig. 1. Measured input return loss of monolithic W-band single-stage amplifier at 300 K and 70 K.

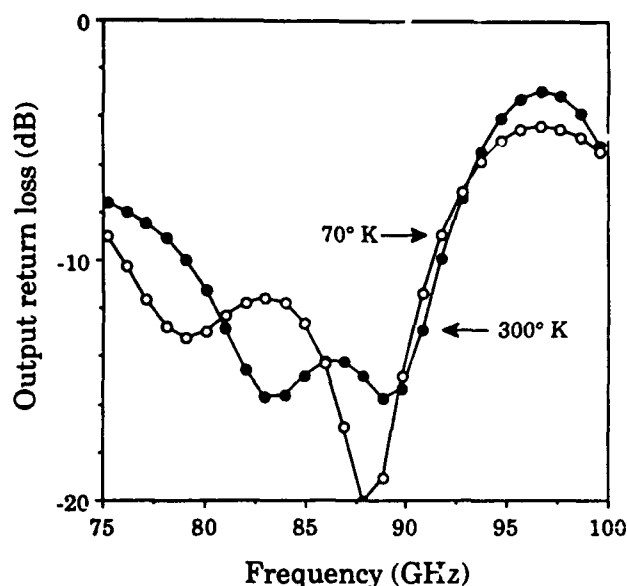


Fig. 2. Measured output return loss of monolithic W-band single-stage amplifier at 300 K and 70 K.

Before circuit measurements are performed, a calibration fixture is prepared with similar photoconductive switches wire bonded together with multiple (5 mil long, 0.7 mil diameter) bond wires. The measured back-to-back insertion loss of this fixture is less than 3 dB with greater than 15-dB return loss from 75 to 100 GHz. When the measurements were repeated at cryogenic temperatures, very little change is observed in the insertion loss; thus, any enhanced circuit performance is expected from the circuit itself rather than the switches or transmission lines. For optimum gain performance, the W-band amplifier is biased at $V_d = 3$ V and $V_g = 0$ V.

III. RESULTS

The input and output return loss measurements of the amplifier at 300 K and 70 K are shown in Figs. 1 and 2. In the optoelectronic reflection measurements, time windowing has been performed to remove to first order the effect of unwanted reflections such as wirebonds. Waveguide measurements at 94 GHz made on a similar amplifier that was bonded with ribbons between a pair of finline transitions yielded input and output return losses of -11 dB and -6 dB, respectively. These measurements were not de-embedded to remove the effect of transitions and wirebonds, and thus, accounts for the discrepancy with the optoelectronic measurements.

The calibration fixture measurements are used to obtain a first order correction for wirebond loss in the measured gain of the amplifier. This corrected gain at 300 K and 70 K is shown in Fig. 3. At 85 GHz, the single-stage amplifier shows an increase in gain from 9 dB at 300 K to 10.5 dB at 70 K. An overall improvement in gain of 1.5 dB to 2.5 dB over the bandwidth of 75 to 100 GHz is observed when the amplifier is cooled. These results are consistent with cryogenic measurements reported elsewhere on other amplifiers at lower frequencies [10], [11]. Based on the calibration fixture measurements, approximately 2.5 dB loss at 300 K is expected from the wirebonds at 94 GHz.

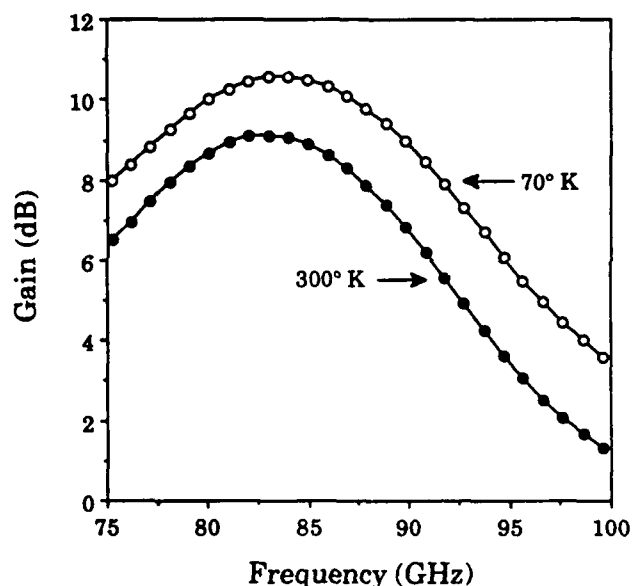


Fig. 3. Measured gain of monolithic W-band single-stage amplifier at 300 K and 70 K. Gain has been corrected for wirebond loss from calibration fixture measurements.

When this is used to compensate the uncorrected amplifier gain data, a room temperature corrected gain of 4.5 dB at 94 GHz is obtained. This is in reasonable agreement with the waveguide measurements, which yielded a corrected gain of 6 dB for a similar amplifier at 94 GHz. Since the repeatability of the optoelectronic measurements has been measured to be within 1 dB, this difference in amplifier gain is likely due to the method used to approximate wirebond loss in the optoelectronic measurements.

IV. CONCLUSION

Picosecond optoelectronic measurements have been successfully performed on a pseudomorphic InGaAs HEMT W-

band single-stage monolithic amplifier at cryogenic temperatures. The amplifier showed a gain improvement of 1.5–2.5 dB when cooled to 70 K. Work is currently in progress to eliminate the effect of wirebonds in these measurements by monolithically integrating photoconductive switches with MMIC's on the same chip. The experimental setup is also being used to characterize the millimeter-wave and optical responses of pseudomorphic InGaAs HEMT discrete devices at low temperatures.

ACKNOWLEDGMENT

The authors would like to thank Dr. J. Berenz and G. S. Dow for providing the monolithic W-band amplifier used in this study, and P. Liu for EBL support.

REFERENCES

- [1] K. W. Chang *et al.*, "A W-band monolithic downconverter," *IEEE Trans. Microwave Theory Tech.*, vol. 39, pp. 1972–1979, Dec. 1991.
- [2] H. Wang *et al.*, "A high performance W-band pseudomorphic InGaAs HEMT LNA," *IEEE MTT-S Int. Microwave Symp. Dig.*, May 1991, pp. 943–946.
- [3] H. B. Sequeira *et al.*, "Monolithic GaAs W-band pseudomorphic MOD-FET amplifiers," *IEEE GaAs IC Symp. Dig.*, Nov. 1990, pp. 161–164.
- [4] R. Majidi-Ahy *et al.*, "100 GHz high-gain InP MMIC cascode amplifier," *IEEE GaAs IC Symp. Dig.*, Nov. 1990, pp. 173–176.
- [5] E. Godshalk, "A V-band wafer probe using ridge-trough waveguide," *IEEE Trans. Microwave Theory Tech.*, vol. 39, pp. 2218–2228, Dec. 1991.
- [6] H. Hung *et al.*, "Millimeter-wave monolithic circuit characterization by a picosecond optoelectronic technique," *IEEE Trans. Microwave Theory Tech.*, vol. 37, pp. 1223–1231, Aug. 1989.
- [7] M. Matloubian *et al.*, "Picosecond optoelectronic measurement of *S*-parameters and optical response of an AlGaAs–GaAs HBT," *IEEE Trans. Microwave Theory Tech.*, vol. 38, pp. 683–686, May 1990.
- [8] M. Matloubian, S. Rosenbaum, H. Fetterman, and P. Greiling, "Wide-band millimeter-wave characterization of sub-0.2 micrometer gate-length AlInAs–GaInAs HEMT's," *IEEE Microwave Guided Wave Lett.*, vol. 1, pp. 32–34, Feb. 1991.
- [9] K. Tan *et al.*, "94-GHz 0.1- μ m *T*-gate low-noise pseudomorphic InGaAs HEMTs," *IEEE Electron Device Lett.*, vol. 11, pp. 585–587, Dec. 1990.
- [10] C. Moore, W. Trimble, M. Edwards, and T. Sanderson, "Cryogenic performance of a GaAs MMIC distributed amplifier," *IEEE Trans. Microwave Theory Tech.*, vol. 39, pp. 567–571, Mar. 1991.
- [11] K. Duh *et al.*, "32-GHz cryogenically cooled HEMT low-noise amplifiers," *IEEE Trans. Electron Devices*, vol. 36, pp. 1528–1535, Aug. 1989.

60 GHz sources using optically driven heterojunction bipolar transistors

D. C. Scott, D. V. Plant, and H. R. Fetterman
 Department of Electrical Engineering, University of California at Los Angeles,
 Los Angeles, California 90024

(Received 14 February 1992; accepted for publication 17 April 1992)

Millimeter wave sources at 60 GHz have been demonstrated using optically driven heterojunction bipolar transistors configured as photodetectors. Two techniques were used to optically generate the millimeter waves; the mixing of two cw lasers and the mode locking of a semiconductor laser. The millimeter wave power generated from these two configurations was radiated into free space using integrated planar twin-dipole antennas and heterodyne detected with signal-to-noise ratios > 40 dB. As part of these experiments, the dc optical gains and quantum efficiencies of the heterojunction bipolar transistor photodetectors were determined.

There has been a growing interest in the use of optical wavelengths both in the transmission and generation of millimeter wave signals. The development of large bandwidth millimeter wave systems requiring a low-loss, light-weight, and interference-free transmission medium has stimulated recent research in the area of optically controlled millimeter wave devices.^{1,2} In addition, there has been considerable interest in the development of heterojunction bipolar transistors (HBTs) as an alternative to *p-i-n* detectors because HBTs can provide large photocurrent gains without high bias voltages and excess avalanche noise characteristics.³ In the series of experiments presented here, high frequency heterojunction bipolar transistors are used as photodetectors integrated with planar twin-dipole antenna structures to generate 60 GHz radiation. Our initial efforts employed two cw lasers in a mixing configuration to demonstrate proof of principle. In subsequent experiments, a mode-locked semiconductor laser was substituted for the mixing system to produce a compact and highly stable radiation source.^{4,5} This combination of an optical transit time device (mode-locked laser) and a high speed phototransistor (HBT) defines a new type of optoelectronic millimeter wave source which can be distributed to form novel coherent arrays.

The devices used in these experiments were abrupt emitter-base junction $\text{Al}_{0.48}\text{In}_{0.52}\text{As}/\text{Ga}_{0.47}\text{In}_{0.53}\text{As}$ heterojunction bipolar transistors with dc common-emitter current gains of 15. These transistors can have cutoff frequencies (f_T) and maximum oscillation frequencies (f_{max}) of 90 and 70 GHz, respectively.⁶ However, in order to allow optical access to the device active region, an $8 \times 8 \mu\text{m}$ emitter window was included, which significantly reduced the frequency performance of the device. The device layer structure is shown in Fig. 1. The HBTs were mounted onto twin-dipole printed circuit antennas that were designed to have optimum gain at 60 GHz.⁷ The optically generated millimeter waves were then radiated into free space and collected into waveguide using a large aperture horn. Using a Gunn diode as a local oscillator, the millimeter wave signals were heterodyne detected via a waveguide mixer.

In the first set of experiments, the HBTs were illuminated with light from a frequency stabilized Kiton Red dye laser (600–640 nm, 0.6 mW) and a frequency stabilized HeNe laser (632.8 nm, 0.6 mW). The wavelength of each

linearly polarized laser was monitored with a wavemeter that had 0.001 nm resolution. Using a beam splitter, the two output beams of the lasers were made collinear and then were focused onto the HBT using a $5\times$ lens objective. The total electric field vector, E_t , impinging on the HBT can be written as

$$E_t = E_h \exp(j\omega_h t) + E_d \exp(j\omega_d t), \quad (1)$$

where E_h , E_d are the field amplitudes and ω_h , ω_d are the optical frequencies of the HeNe and dye laser, respectively. It can be shown that the optically induced output current of the HBT is proportional to the square of the electric field:⁸

$$i(t) \propto |E_t|^2 = E_h^2 + E_d^2 + 2E_h E_d \cos(\omega_h - \omega_d)t. \quad (2)$$

The first two terms in Eq. (2) correspond to the dc component of the optically generated output current of the HBT. Rewriting this component in terms of the incident optical power shows that the dc component of the optically generated output current is proportional to $P_h + P_d$. The dc photocurrent gain (M), which relates the number of electrons (or holes) in the collector current to the number of incident photons is given by^{3,9}

GaInAs	CONTACT	$n^* = 1 \times 10^{18}$	100 nm
AlInAs	EMITTER CONTACT	$n^* = 1 \times 10^{19}$	80 nm
AlInAs	EMITTER	$n = 8 \times 10^{17}$	180 nm
GaInAs	BASE	$p^* = 1 \times 10^{20}$	80 nm
GaInAs	COLLECTOR	$n = 4 \times 10^{18}$	270 nm
GaInAs	SUBCOLLECTOR	$n^* = 1 \times 10^{19}$	80 nm
GaInAs	BUFFER	UNDOPED	10 nm
InP SEMI-INSULATING SUBSTRATE			

FIG. 1. HBT device layer structure.

$$M = \frac{h\nu}{qP_i} (I_c - I_D), \quad (3)$$

where I_c is the collector current measured with a floating base, I_D is the dark current, ν is the frequency of the incident photon, h is Planck's constant, q is the electronic charge, and P_i is the incident optical power. Given that $P_h = P_d = 0.6$ mW, the total incident optical power as given by $P_h + P_d$ is $P_i = 1.2$ mW. At 633 nm, the reflectivity of the top $\text{Ga}_{0.47}\text{In}_{0.53}\text{As}$ layer is 30%,¹⁰ thus reducing the incident optical power to $P_i = 0.84$ mW. The measured collector current, I_c , is 1.5 mA and the measured dark current, I_D , is 130 nA. Substituting these values into Eq. (3) yields a dc photocurrent gain (M) of 3.5. The quantum efficiency can be determined using the relation¹¹

$$\eta = \frac{M}{\beta + 1}, \quad (4)$$

where M is the dc photocurrent gain and β is the dc common-emitter current gain which was measured to be 15. Substituting these values into Eq. (4) yields a dc quantum efficiency of 22%.

Looking back at Eq. (2), we see that the last term oscillates at the difference frequency $|\omega_h - \omega_d|$ with magnitude proportional to $2E_h E_d$. We tune the frequency of the dye laser such that the difference frequency, $|\omega_h - \omega_d|$, is at 60 GHz and this millimeter wave signal is efficiently radiated into free space by the twin-dipole antenna. Converting to optical powers, the magnitude of the input optical signal that is responsible for this millimeter wave signal can be shown to be $2\sqrt{P_h P_d}$, where P_h, P_d are the HeNe and dye laser powers, respectively. Since $P_h = P_d = 0.6$ mW, the magnitude of the input optical signal as given by $2\sqrt{P_h P_d}$ is 1.2 mW. Taking into account the reflectivity of the top layer of the device in the same manner as before reduces the incident millimeter wave optical power to 0.84 mW. Figure 2 is a radiated signal with a center frequency of 59.5 GHz, a signal-to-noise ratio of 45 dB, and a 3 dB linewidth of 2.5 MHz. Based on the receiver conversion losses, the power in the millimeter wave signal was estimated to be 10^{-5} mW. Part of the losses in the conversion from the incident optical power to the output millimeter wave power result from the parasitics associated with the 8×8 μm emitter window. Grading the base of the HBT and impedance matching the device to the antenna will significantly improve the performance of the system. We estimate that the output millimeter wave power can become comparable to the incident light power.

In order to illustrate how the above experiment could be useful for applications in phased array antenna systems, we electrically injected a -9 dBm, 118 MHz IF signal into the base of the antenna mounted HBT while simultaneously optically mixing at 59.4 GHz (see Fig. 3). This configuration produced sidebands spaced 118 MHz away from the 59.4 GHz carrier. This result demonstrates that one can encode an IF information signal onto an optically generated millimeter wave signal.

In a second set of experiments, a mode-locked GaAs/AlGaAs multiple-quantum-well semiconductor laser was

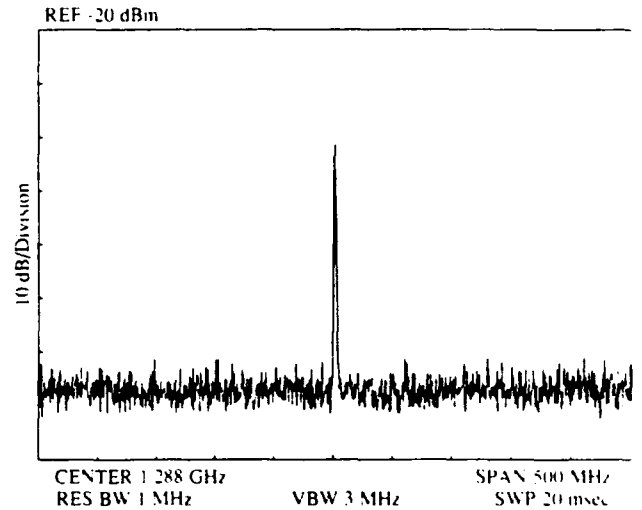


FIG. 2. Spectrum analyzer trace of the received millimeter wave radiation at 59.5 GHz. Transmitting HBT was illuminated by 0.6 mW of dye laser power and 0.6 mW of HeNe laser power.

used to drive the HBT/antenna circuit as is shown in Fig. 4.⁴ The diode lasers used were two section lasers which were mode locked using one section as a saturable absorber. In these devices, the saturable absorber region is biased to adjust the steady state absorption to the point where small round-trip oscillations become unstable and mode locking occurs. The laser produces pulses < 2.5 ps at 830 nm with an average power of 1.6 mW. The mode-locked output can be regarded as a highly efficient means of directly modulating an optical carrier at a millimeter wave frequency, and this output can be used to directly drive the HBT/antenna circuit. At 830 nm, the absorption coefficient of the $\text{Ga}_{0.47}\text{In}_{0.53}\text{As}$ is $\approx 1.5 \times 10^4 \text{ cm}^{-1}$ (Ref. 3) and the $\text{Al}_{0.48}\text{In}_{0.52}\text{As}$ layers are transparent.¹² Therefore, it is reasonable to assume that all of the light is absorbed in the base and collector regions and contributes to the photocurrent. Given that the reflectivity of the top

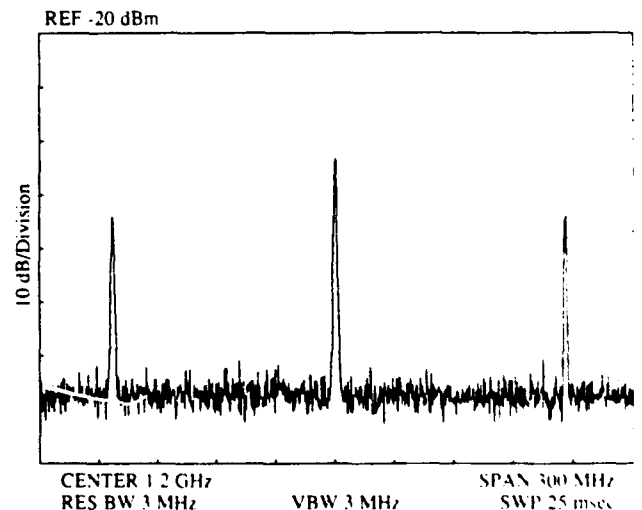


FIG. 3. Received millimeter wave signal with 118 MHz (-9 dBm) IF modulation electrically applied to the base of the HBT.

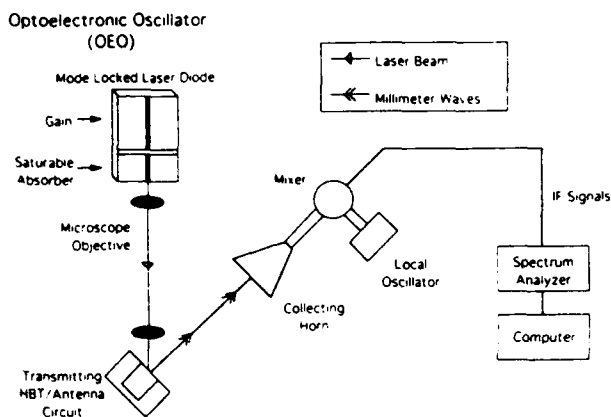


FIG. 4. Experimental setup of the millimeter wave Optoelectronic Oscillator (OEO).

$\text{Ga}_{0.47}\text{In}_{0.53}\text{As}$ contact layer is 30%, we calculate that the amount of light absorbed in the HBTs active region is $P_i = 1.12$ mW. The measured collector current is $I_c = 7.6$ mA and the dark current is the same as before. Substituting these values into Eq. (3) gives a dc optical gain of $M = 10$. From Eq. (4), this leads to a dc quantum efficiency of $\eta = 50\%$. The millimeter wave output had a signal-to-noise ratio of 40 dB and a 3 dB linewidth of < 500 KHz. The center frequency was 65.12 GHz, which corresponds to the laser mode locking frequency. The output millimeter wave power was measured to be 10^{-4} mW. As shown in Fig. 4, the combination of the laser diode and the HBT results in a fixed frequency, narrow linewidth source and defines a new type of semiconductor-based optoelectronic millimeter wave oscillator. This compact millimeter wave source lends itself well to monolithic integration and an array of on-wafer sources can be assembled for use in phase array radar.

The previous experiments showed that the experiments performed at 830 nm were more efficient than those at 633 nm. This can be explained by discussing the dynamics of the carriers generated by the absorption of light in the various regions of the HBT. The major component of the photocurrent is due to electron-hole pairs generated in the base, in the base-collector depletion region, and within a diffusion length of the depletion edge in the bulk collector. The electrons that are generated in these regions are collected by the field of the reverse biased base-collector junction leading to a current flow in the external circuit. The holes that are generated in these regions are swept into the base thereby increasing the base potential. This increases the forward bias at the base-emitter junction causing a large number of electrons to be injected from the emitter into the base, which results in a large electron current flow from the emitter to the collector. This is the mechanism for photocurrent gain. If light is absorbed in the emitter, than the emitter injection efficiency will be reduced and this will

reduce the photocurrent gain of the device. Based on the band gap of the AlInAs emitter, we find that at 830 nm the emitter is transparent and at 633 nm light is being absorbed.¹² This explains the reduced photocurrent current gain that was observed at 633 nm. From the above observations, it is clear that these heterojunction phototransistors are most efficient in the long wavelength range of 0.830–1.3 μm .

In summary, we have demonstrated the generation of usable amounts of coherent millimeter wave power using both optical mixing techniques and modulation techniques with mode-locked laser diodes. Future efforts to increase this millimeter wave power include incorporating faster HBTs with larger gains, optimizing the optical absorption interaction region using new materials and new structures, and coupling to specially designed matched broadband antenna systems. High frequency heterojunction phototransistors and optical waveguides can be used to form simple versatile systems with applications in communications and phased array radars. Because of the intrinsic gain of the high frequency HBTs and the ease in which amplifying MMIC circuits can be incorporated, substantial radiated powers can be obtained with this approach. Current efforts are underway to make integrated configurations with multiple planar optical waveguide feeds.

The authors would like to thank the Microwave Devices and Circuits Department at Hughes Research Laboratories in Malibu, California for providing the HBTs and Ortel Corporation in Alhambra, California for providing the mode-locked laser diodes used in these experiments. This work was supported by the Air Force Office of Scientific Research under the direction of H. R. Schlossberg and by the National Center for Integrated Photonics Technology.

- ¹ P. R. Herzfeld, IEEE Trans. Microwave Theory Tech. MTT-38, 465 (1990).
- ² R. Simons, *Optical Control of Microwave Devices* (Artech House, Boston, 1990).
- ³ L. Y. Leu, J. T. Gardner, and S. R. Forrest, J. Appl. Phys. 69, 1052 (1991).
- ⁴ S. Sanders, L. Eng, J. Paslaski, and A. Yariv, Appl. Phys. Lett. 56, 310 (1990).
- ⁵ K. Y. Lau, Appl. Phys. Lett. 52, 2214 (1988).
- ⁶ J. F. Jensen, W. E. Stanchina, R. A. Metzger, D. B. Rensch, R. F. Lohr, R. W. Quen, M. W. Pierce, Y. K. Allen, and P. F. Lou, IEEE J. Solid-State Circuits 26, 415 (1991).
- ⁷ W. Chew and H. R. Fetterman, IEEE Trans. Microwave Theory Tech. MTT-37, 593 (1989).
- ⁸ A. Yariv, *Optical Electronics* (Holt, Rinehart, and Winston, New York, 1985).
- ⁹ J. C. Campbell, in *Semiconductors and Semimetals* 22, edited by W. T. Tsang (Academic, New York, 1985), Chap. 5.
- ¹⁰ D. Olego, T. Y. Chang, E. Silberg, E. A. Caridi, and A. Pinczuk, Appl. Phys. Lett. 41, 476 (1982).
- ¹¹ N. Chand, P. A. Houston, and P. N. Robson, IEEE Trans. Electron Devices ED-32, 622 (1985).
- ¹² C. Y. Chen, Y. M. Pang, P. A. Garbinski, A. Y. Cho, and K. Alavi, Appl. Phys. Lett. 43, 308 (1983).

Suggested area: Quantum Electronics and Compound Semiconductor Devices
**Novel 100 GHz C.W. GaAs/AlGaAs Multiquantum Well
IMPATT Oscillators**

C. C. Meng and H. R. Fetterman
Department of Electrical Engineering
University of California, Los Angeles
Los Angeles, CA 90024

D. Streit, T. Block and Y. Saito
TRW
Electronic Systems Group
Redondo Beach, CA 90278

We have successfully fabricated and tested GaAs/Al_{0.3}Ga_{0.7}As MQW (Multiquantum Well) IMPATT oscillators at 100 GHz. For the first time to our knowledge, C.W. operation of MQW IMPATT devices at 100 GHz has been achieved. GaAs IMPATT devices show a fall-off in efficiency at high frequencies because of the saturation of ionization rates at high electric fields. MQW GaAs/AlGaAs IMPATT devices potentially can outperform conventional GaAs IMPATT devices because the quantum wells improve the nonlinearity of the avalanche process and reduce the ionization rate saturation limitations [1][2]. Preliminary results yielded, in a non-optimized circuit, 1.1 mW C.W. power at 103.8 GHz and 320 mA bias current. The C.W. operation of MQW IMPATT devices at frequencies above 100 GHz opens up a new field for the applications of modern epitaxy technologies to two terminal high frequency sources.

The epitaxial layer structure shown in figure 1 was grown by MBE on p⁺ GaAs. The structure is a p⁺n junction with five periods of multiquantum wells (100Å barrier length and 100Å well length) in the avalanche region. The active layer doping densities of $2 \times 10^{17}/\text{cm}^3$ for GaAs layers and $1.4 \times 10^{17}/\text{cm}^3$ for Al_{0.3}Ga_{0.7}As layers were designed for the simple growth condition of a constant Si flux rate in an MBE system. The room temperature I-V curve in figure 2 for the structure in figure 1 shows the desired hard breakdown at 10.2 V and low leakage current density (less than $10^{-2}\text{A}/\text{cm}^2$).

Figure 3a shows a picture of the fabricated diodes before mounting on a diamond heat sink. Diodes are 10 μm thick to minimize the ohmic loss and have AuGe(900Å), Ni(150Å) and Au(1 μm) on both sides. Figure 3b shows a diagram of the device which is packaged inside a 18 mil I.D. quartz ring. The device area is trimmed to 1 pf at zero bias and a Kurakawa type circuit is used for r.f. testing. Figure 4 shows the spectrum of the C.W. MQW IMPATT oscillator at 101.3 GHz. The relation between output power and bias current is shown in figure 5. Optimization for device-circuit impedance matching is under way and significantly higher powers are anticipated.

REFERENCES

- [1] D. Lippens, O. Vanbesien, and B. Lambert, "Multiquantum Well GaAs/AlGaAs Structures Applied to Avalanche Transit Time Devices", Journal De Physique, C5-487(1987).
- [2] C. C. Meng and H. R. Fetterman, "A Theoretical Analysis of Millimeter-wave GaAs/AlGaAs Multiquantum Well Transit Time Devices by the Lucky Drift Model", to be published at Solid-State Electronics

4000 Å	GaAs	$n^+ 2 \times 10^{18} / \text{cm}^3$
1500 Å	GaAs	$n 2 \times 10^{17} / \text{cm}^3$
100 Å	$\text{Al}_{0.3}\text{Ga}_{0.7}\text{As}$	$n 1.4 \times 10^{17} / \text{cm}^3$
100 Å	GaAs	$n 2 \times 10^{17} / \text{cm}^3$
100 Å	$\text{Al}_{0.3}\text{Ga}_{0.7}\text{As}$	$n 1.4 \times 10^{17} / \text{cm}^3$
100 Å	GaAs	$n 2 \times 10^{17} / \text{cm}^3$
100 Å	$\text{Al}_{0.3}\text{Ga}_{0.7}\text{As}$	$n 1.4 \times 10^{17} / \text{cm}^3$
100 Å	GaAs	$n 2 \times 10^{17} / \text{cm}^3$
100 Å	$\text{Al}_{0.3}\text{Ga}_{0.7}\text{As}$	$n 1.4 \times 10^{17} / \text{cm}^3$
100 Å	GaAs	$n 2 \times 10^{17} / \text{cm}^3$
100 Å	$\text{Al}_{0.3}\text{Ga}_{0.7}\text{As}$	$n 1.4 \times 10^{17} / \text{cm}^3$
100 Å	GaAs	$n 2 \times 10^{17} / \text{cm}^3$
5000 Å	buffer GaAs	$p^+ 2 \times 10^{19} / \text{cm}^3$
GaAs substrate		$p^+ 2 \times 10^{19} / \text{cm}^3$

Figure 1. MQW IMPATT device epitaxial layer structure.

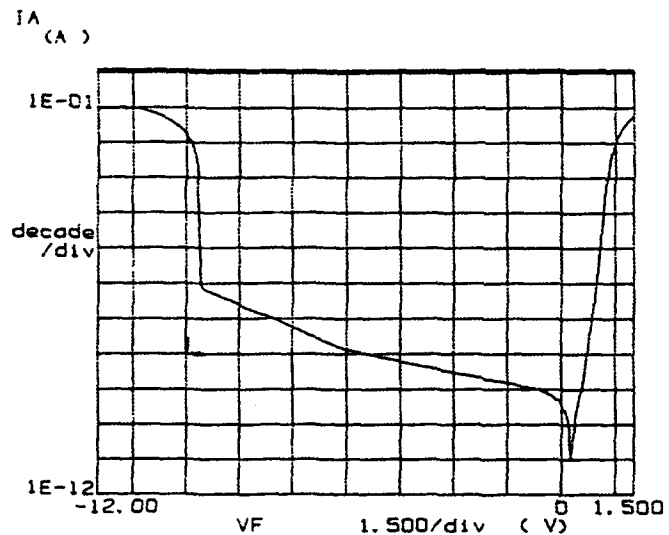


Figure 2. Room temperature I-V curve for the MQW IMPATT structure in figure 1.

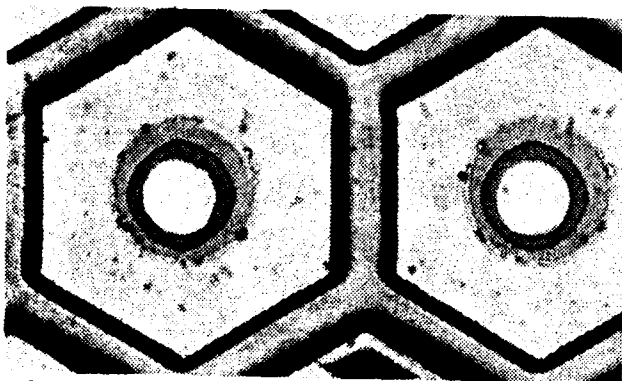


Figure 3a. Photograph of the fabricated diodes.

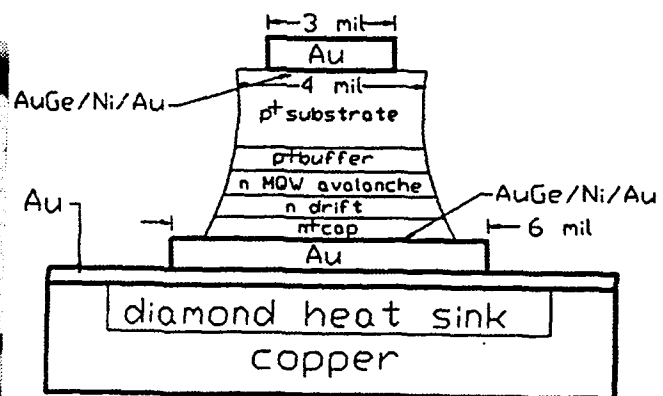


Figure 3b. Diagram of an MQW IMPATT diode on a diamond heat sink.

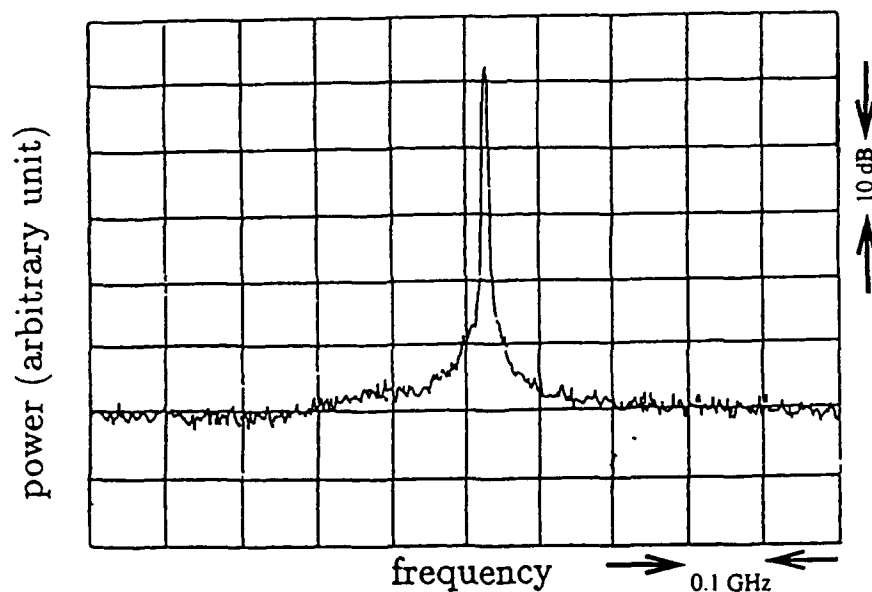


Figure 4. Spectrum of the C.W. MQW IMPATT diode at 101.3 GHz, the resolution bandwidth is 3MHz.

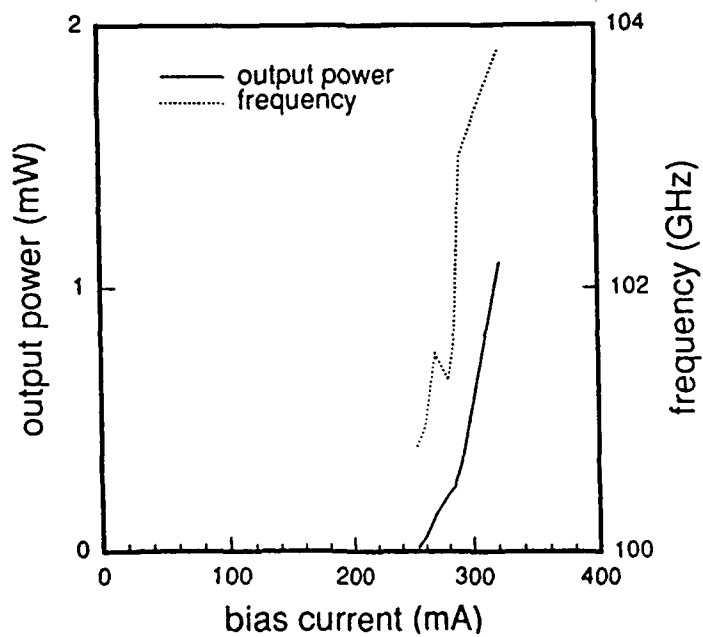


Figure 5. Output power and frequency as a function of bias current for an MQW IMPATT oscillator.

**A THEORETICAL ANALYSIS OF MILLIMETER-WAVE GaAs/AlGaAs
MULTIQUANTUM WELL TRANSIT TIME DEVICES BY THE
LUCKY DRIFT MODEL**

C. C. Meng and H. R. Fetterman
Department of Electrical Engineering
University of California, Los Angeles
Los Angeles, CA 90024-1594

ABSTRACT

Multiquantum well structures are potentially better than bulk materials in millimeter-wave avalanche transit time oscillator applications. They are potentially superior because multiquantum well structures can increase the nonlinearity of the avalanche process in high electric fields. In this paper, we incorporate the multiquantum well ionization rates described by a lucky drift model into a modified Read type large signal simulation. The simulations show that 13% efficiency at 100 GHz and 9% efficiency at 150 GHz can be achieved with properly designed GaAs/AlGaAs multiquantum well avalanche transit time devices. These results are comparable to the state of the art experimental results in Si IMPATT devices.

I INTRODUCTION

The recent development of fine epitaxial techniques such as MBE (Molecular Beam Epitaxy) and MOCVD (Metal Organic Chemical Vapor Deposition) have made possible the fabrication of ultrathin heterostructures. This capability in synthetic electronic materials allows the adjustment of many physical parameters that were previously thought to be solely determined by the bulk material. One example of the physical phenomena affected by modern epitaxial techniques is the avalanche process in multi-quantum well structures. This concept has been successfully applied to the avalanche photodiode to reduce avalanche noise[1, 2]. Little work has been developed along the direction for IMPATT (IMPact ionization Avalanche Transit Time) devices. Typically, the efficiency of a single-drift flat-profile GaAs IMPATT device shows a fall-off at frequencies above 50 GHz. This fall-off is mainly due to the saturation of ionization rates in high electric fields[3]. This drastic decrease in the nonlinearity of ionization rates results in a broadened injected current pulse in a less localized avalanche region. The saturation of ionization rates in high electric fields can be improved by substituting a multiquantum well structure for a bulk material in the avalanche region. The improvement in the nonlinearity of the avalanche process leads to a narrow injected pulse in the avalanche region, thus the efficiency of a multiquantum well device becomes higher. Lippen et al.[4, 5] performed a simplified particle simulation and projected an increase of the conversion efficiency on several GaAs/AlGaAs multiquantum well structures at 100 GHz. Christou et al.[6] made a GaAs/AlGaAs multiquantum well MITATT (MIXed Tunnel Avalanche Transit Time) device and achieved 2% efficiency at 94 GHz under pulsed operation. These earlier works have shed light on the applications of modern epitaxial techniques to two terminal high frequencies devices.

In a multiquantum well structure, a carrier starts from a non-zero energy (E_0)

to reach the ionization threshold energy[7]. Thus, the effect of a multiquantum well structure is to reduce the effective ionization threshold energy. The effective ionization threshold energy (E'_T) can be expressed as $E'_T = E_T - E_0$, where E_T is the ionization threshold energy for the narrow bandgap material in a multiquantum well structure. The non-zero energy (E_0) consists of the band offset energy and the energy obtained from the potential barrier. A carrier gains more energy from the potential barrier as the electric field becomes higher. In general, the energy obtained from the potential barrier is quite large in the high electric fields used for the IMPATT device applications at W-band frequencies (75-110 GHz) and becomes small in the low electric fields used for the avalanche photodiode applications. In other words, the amount of reduction in the effective ionization threshold energy becomes larger in a higher electric field. Thus, the saturation of ionization rates is improved in high field regions. This non-zero energy is also responsible for the large α/β ratio, where α and β are the electron and hole ionization rates, respectively. However, the enhancement of the ratio, α/β , is diminished in the high electric fields.

In the present paper an analytical method based on the lucky drift model is applied to describe the avalanche process of multiquantum well structures. A detailed description of the analytical method is given in the following section. In section 3, a modified Read type simulation is used to evaluate the device efficiency. The simulations clearly show that GaAs/AlGaAs multiquantum well IMPATT devices have an efficiency advantage over GaAs bulk IMPATT devices for the frequencies above 100 GHz. A discussion of the results and conclusion are given in the last section.

II LUCKY DRIFT MODEL FOR THE MULTIQUANTUM WELL STRUCTURE

Impact ionization is characterized by an ionization threshold energy. Electrons (holes) under the heating influence of an electric field try to reach this ionization threshold energy. Most electrons (holes) never actually achieve this threshold energy due to the energy relaxation by phonons. In wide bandgap semiconductors, the dominant scattering process for high energy electrons and holes comes from interactions with optical phonons. Phonons with small energy effectively randomize a carrier's momentum, but do not relax most of the carrier's energy. Therefore, the energy relaxation length is much longer than the momentum relaxation length. In the case of a simple parabolic band, we can write the relation between energy relaxation length λ_E and momentum relaxation length λ_m as follows.

$$\lambda_E = \frac{e\xi\lambda_m}{2 \langle E_p \rangle} \lambda_m, \quad (1)$$

where e is the electronic charge, and ξ is the electric field, $\langle E_p \rangle$ is the effective phonon energy at temperature T .

The lucky drift model has been developed by many people to describe impact ionization events for an ideal parabolic band[7, 8]. This model is based on the distinction between the energy and the momentum relaxation time. In this model, an electron (hole) starts ballistically at zero energy and tries to reach the threshold energy. After the first momentum relaxation collision, the electron (hole) is in a drift motion state. Most of the unsuccessful attempts end in energy relaxation so that a carrier starts from zero energy again. Occasionally, an electron (hole) that suffers few phonon collisions can luckily attain the ionization threshold energy. In a successful attempt, a carrier

travels only a distance l_0 ,

$$l_0 = \frac{E_T}{e\xi}, \quad (2)$$

to reach the ionization threshold energy. As pointed out by many authors[7], these electrons (holes) that are responsible for impact ionization are in a state called the lucky drift state. This model was further modified when a “soft” threshold energy was introduced[9-11]. A “soft” threshold means that an electron (hole) has a finite impact ionization probability, even if the energy exceeds the threshold energy. This situation is in contrast to a hard threshold energy model, which assumes that impact ionization occurs immediately after a carrier reaches the threshold energy. The degree of “softness” is reflected by a non-zero ionization mean free length (λ_{ion}) in the lucky drift model. These four physical parameters, the momentum relaxation length (λ_m), the energy relaxation length (λ_E), the minimum distance to reach the threshold energy (l_0) and the ionization mean free length (λ_{ion}), constitute the fundamentals for the lucky drift model. Furthermore, λ_m and λ_{ion} are constants and λ_E and l_0 are given in equation (1) and (2) for the case of a parabolic band.

From Woods’ derivation[11], the electron (hole) ionization rate α (β) can be expressed as follows:

$$\alpha, \beta = \frac{\lambda_E f(\lambda_E) - \lambda_m f(\lambda_m)}{\lambda_E^2 (1 - f(\lambda_E)) - \lambda_m^2 (1 - f(\lambda_m))}, \quad (3)$$

where

$$f(\lambda) = \exp\left(-\frac{l_0}{\lambda}\right) \left[1 - \frac{\lambda_{ion}}{\lambda} \exp\left(\left(\frac{\lambda_{ion}}{\sqrt{\pi}\lambda}\right)^2\right) \text{erfc}\left(\frac{\lambda_{ion}}{\sqrt{\pi}\lambda}\right) \right], \quad (4)$$

and erfc is the complementary error function.

From our multiquantum well structure design approach, the carrier starts from a non-zero energy instead of zero energy. A multiquantum well structure consists of

two alternative materials; one has a wide bandgap (potential barrier) and the other, a narrow bandgap (potential well). Consider the case of an undoped GaAs/AlGaAs multiquantum well structure under bias. When an electron (hole) enters the wide bandgap material, it gives up some energy to the band discontinuity and encounters a higher ionization threshold energy. Therefore, impact ionization is difficult in the barrier region. As long as the barrier thickness is comparable to the energy relaxation length, an electron (hole) can accelerate to a higher energy without energy relaxation. On the other hand, when a high energy electron (hole) exits the barrier and enters the well, the electron (hole) starts from a non-zero energy to reach the ionization threshold energy. The periodic property of a multiquantum well structure serves as a constant supply for the non-zero energy. The non-zero energy (E_0) can be expressed as follows: $E_0 = \Delta E + e\xi l_{eff}$. ΔE is the band discontinuity and $e\xi l_{eff}$ is the energy obtained from the potential barrier, where l_{eff} is the effective energy acceleration length and is equal to the smaller value of the two quantities, (1) energy relaxation length and (2) barrier length. For the case of a parabolic band, the energy relaxation length is proportional to the electrical field as shown in equation (1).

The physical meaning of the non-zero starting energy is to reduce l_0 (the minimum distance to reach the ionization threshold energy). Thus, the effect should appear in $f(\lambda)$. The derivation of a new formula for ionization rates using the assumption that a carrier starts from E_0 is provided in the appendix of this paper. Equation (4) for the ionization rate still holds except that one variable $\eta = E_0/e\xi$ is introduced to modify $f(\lambda)$. For $\eta < l_0$,

$$f(\lambda) = \exp\left(-\frac{l_0 - \eta}{\lambda}\right) \left[1 - \frac{\lambda_{ion}}{\lambda} \exp\left(\frac{\lambda_{ion}}{\sqrt{\pi}\lambda}\right)^2 \operatorname{erfc}\left(\frac{\lambda_{ion}}{\sqrt{\pi}\lambda}\right)\right]. \quad (5)$$

and for $\eta \geq l_0$,

$$f(\lambda) = 1 - \frac{\lambda_{ion}}{\lambda} \exp \left[\frac{\lambda_{ion}}{\sqrt{\pi}\lambda} + \frac{\sqrt{\pi}(\eta - l_0)}{2\lambda_{ion}} \right]^2 \operatorname{erfc} \left[\frac{\lambda_{ion}}{\sqrt{\pi}\lambda} + \frac{\sqrt{\pi}(\eta - l_0)}{2\lambda_{ion}} \right]. \quad (6)$$

Some trade-offs must be made in the design of a multiquantum well structure. The well length should be long enough so that carriers from the barrier can ionize easily and gain enough energy to get out of the well. On the other hand, if the well length is too long, bulk type impact ionization can occur. The length of the barrier layer should be long enough so that carriers can gain enough energy from the electric field to improve the saturation of the ionization rates. However, the barrier layer length should not be too long such that impact ionization can occur in the barrier region. From our estimate, the optimal length for both barrier and well length should be between 100Å to 200Å for IMPATT devices at W-band frequencies.

III LARGE SIGNAL SIMULATION

Many full scale simulation schemes for IMPATT devices are described in the literature [12, 13]. Accurate results can be obtained provided that the precise relation between ionization rates and electric fields is given. However, these techniques require a great amount of computing time. On the other hand, a Read type analysis, which has well-defined avalanche and drift regions, can provide more physical insights and is more economical. Because our goal is to show the efficiency advantage of a properly designed GaAs/AlGaAs multiquantum well structure over a GaAs bulk material at high frequencies, a Read type analysis is sufficient.

In the design of a multiquantum well IMPATT device, quantum wells are placed in the avalanche region only. Here, a 100Å well length is chosen for all the structures to accommodate many quantum wells in the avalanche region. In general, there does not exist a well-defined boundary for the avalanche region. The avalanche region is the

region where most of the avalanche multiplication takes place. For the case of a p^+n single-drift flat-profile IMPATT device, an avalanche region was defined as the region from the junction interface to the point where the electron current equals to 95% of the total current.

A knowledge of ionization rates as a function of the electric field is required to analyze the dynamics in the avalanche region. The junction temperature of an IMPATT oscillator is normally close to 500°K. The device operates over very high electric fields at millimeter-wave frequencies and the ionization rates in such high electric fields are difficult to obtain. Moreover, almost all the available experimental data were measured at room temperature. However, ionization rates over a wide range of electric fields at 500°K for various design parameters (barrier length and well length) are needed for simulations of the multiquantum well IMPATT structure. It is feasible to use the model developed in the previous section to obtain the ionization rates for a multiquantum well structure.

For the lucky drift model, another set of parameters, λ_m , $\langle E_p \rangle$, E_T , and λ_{ion} are used because they are independent of the electric field and have a simple dependence on temperature. At temperature T , we have

$$\lambda_m = \frac{\lambda_m(0)}{2n+1}, \quad \langle E_p \rangle = \frac{E_p}{2n+1}, \quad \text{and} \quad \lambda_{ion} = \frac{\lambda_{ion}(0)}{\sqrt{2n+1}},$$

where E_p is the phonon energy, n is the average number of phonons at temperature T , and $\lambda_m(0)$ and $\lambda_{ion}(0)$ are the momentum relaxation length and ionization mean free path at zero degrees Kelvin, respectively. The ionization threshold energy is proportional to the bandgap energy and has a weaker dependence on the temperature than other parameters. In this paper, we neglect the small dependence on temperature for the ionization threshold energy.

Bulman et al.[14] undertook a systematic and detailed study on the ionization rates

for GaAs material in electric fields up to $6.25 \times 10^5 \text{ V/cm}$ for GaAs material. A total of 44 pn junctions from a large number of wafers were measured and the results are claimed to be the most reliable data up to date. When $E_p=29\text{meV}$, $E_T=1.7\text{eV}$ for electrons and $E_T=1.424\text{eV}$ for holes were chosen to fit the experimental data measured by Bulman et al., Woods[11] obtained

$$\lambda_m(0) = 86.4\text{\AA}, \quad \lambda_{ion}(0) = 680\text{\AA} \quad \text{for electrons in GaAs,}$$

$$\lambda_m(0) = 73.6\text{\AA}, \quad \lambda_{ion}(0) = 681.4\text{\AA} \quad \text{for holes in GaAs.}$$

Here, we use a 75/25 rule for the band offsets[15]. For the $\text{Al}_{0.3}\text{Ga}_{0.7}\text{As}/\text{GaAs}$ multi-quantum well structure, ΔE_c is equal to 0.281eV and ΔE_v is equal to 0.094eV. We assume that both GaAs and AlGaAs materials have the same momentum relaxation length. The above physical parameters, together with the barrier length, allow us to model the ionization rates for the multi-quantum well structure at the operating temperature (500°K).

In large signal analysis, the multi-quantum well avalanche region is replaced by an equivalent "bulk" material. The "bulk" material has the same ionization rate as a function of the electric field as the corresponding multi-quantum well structure. The concept of an equivalent "bulk" material is straightforward for a low-high-low profile IMPATT device because there exists a constant electric field in the avalanche region. However, this is also the case for other doping profile designs, as long as the electric field in the avalanche region changes smoothly.

A modified Read type large signal analysis[3] is used to investigate the cases of p^+n single-drift flat-profile multi-quantum well IMPATT diodes. The large signal analysis used here provides for different ionization rates for electrons and holes. A single-drift flat-profile structure is relatively easy to design. The doping density of the flat-profile

structure is designed so that the punch through condition occurs at breakdown. Fixed depletion layer boundaries are assumed and the diffusion effect is not included in order to simplify the analysis. In this section, all the governing equations are put in their normalized forms to facilitate analysis at different frequencies.

Figure 1 shows the layer structure of a W-band GaAs/Al_{0.3}Ga_{0.7}As multiquantum well IMPATT device based on large signal simulation. The structure has quantum wells with 100Å barrier length and 100Å well length in the avalanche region. The governing equation for the normalized injected current in the avalanche region is

$$\frac{d \frac{J_{inj}(\omega t)}{J_{dc}}}{d\omega t} = -\frac{\frac{J_{inj}(\omega t)}{J_{dc}} \frac{W}{V_n}}{\kappa M_n \tau_n \frac{\omega W}{V_n}}, \quad (7)$$

where ω is the angular frequency, J_{inj} is the injection current density, J_{dc} is the bias current density, W is the depletion width, and V_n is the electron saturation velocity. In equation (7), we use the quasi-static model developed by Decker et al.[16] to calculate κ . In Read's original derivation, κ becomes unity. In equation (7), M_n and τ_n are defined as:

$$M_n = \frac{1}{1 - \int_0^{W_A} \alpha \exp(-\int_0^x (\alpha - \beta) dx) dx}, \quad (8)$$

$$\tau_n = \frac{1}{V_n + V_p} \int_0^{W_A} \exp\left(\int_0^x (\alpha - \beta) dx\right) dx, \quad (9)$$

where W_A is the width of the avalanche region, α is the electron ionization rate, β is the hole ionization rate, and V_p is the hole saturation velocity. The saturation velocities of electrons and holes are very close in GaAs material. We also assume that the electron saturation velocity is equal to the hole saturation velocity in multiquantum well structures. The space charge effect is neglected in this modified Read type analysis, thus $(\kappa M_n \omega \tau_n)^{-1}$ can be calculated as a function of the peak electric field at the junction interface for a given doping density.

Figure 2 illustrates the $(\kappa M_n \omega \tau_n)^{-1}$ as a function of the normalized electric field

$((\xi_0 - \xi_c)/\xi_c)$ for several structures, where ξ_0 is the electric field at the junction interface, ξ_c is the electric field at the junction under static breakdown, $-(\kappa M_n \omega \tau_n)^{-1}$ is the growth rate if the instantaneous electric field at the junction interface is larger than the peak electric field under static breakdown, otherwise $-(\kappa M_n \omega \tau_n)^{-1}$ is the decay rate. The saturation of the ionization rate leads to a slowly varying behavior of $-(\kappa M_n \omega \tau_n)^{-1}$ as a function of the normalized electric field. The improvement by multiquantum well structures is evident by the fact that the growth rate (or decay rate) changes more rapidly as a function of the normalized electric field when the barrier length increases. The slowly varying behavior causes a wide injected pulse; however, quickly varying behavior causes a sharp narrow injected pulse that will increase the efficiency correspondingly.

Using Poisson's equation, the normalized peak electric field at the junction interface ($x = 0$) in figure 1 can be shown to be related to the terminal voltage and the injected current as follows:

$$\frac{\xi_0(\omega t)}{\xi_c} = 1 + \frac{V(\omega t) - V_B}{W \xi_c} - \frac{J_{dc}}{\frac{\epsilon \xi_c V_n}{W}} \int_{W_A}^W \left(1 - \frac{x}{W}\right) \frac{J_{inj} \left(\omega t - \frac{\omega(x - W_A)}{V_n}\right) dx}{J_{dc}} \frac{dx}{W}, \quad (10)$$

where $V(\omega t)$ is the applied voltage across the diode, ϵ is the dielectric constant, and V_B is the static breakdown voltage. Here, we consider the case where $V(\omega t) = V_{dc} + V_r \sin(\omega t)$, and V_{dc} is the bias voltage when the device oscillates.

The injected current as a function of time can be calculated from equation (7) once the peak electric field is given. On the other hand, the peak electric field is also a function of the injected current as shown in equation (10). Thus, the two coupled equations can be solved by iteration methods. For the first iteration, the space charge effect in the drift region (the last term in equation (10)) is set at zero. In solving equation (7), the bias voltage (V_{dc}) is adjusted until the injected current is continuous and periodic. The terminal induced current can be obtained from the injected current

through the relationship below,

$$\frac{J_{ind}}{J_{dc}} = \frac{W_A}{W} \frac{J_{inj}(t)}{J_{dc}} + \int_{W_A}^W \frac{J_{inj} \left(\omega t - \frac{\omega(x-W_A)}{V_n} \right)}{J_{dc}} \frac{dx}{W}. \quad (11)$$

Using equation (11), admittance can be calculated as a function of the r.f. voltage amplitude by performing a Fourier transform of the induced current. The injected current from the previous iteration is used to calculate the peak electric field for the next iteration. The iteration process is repeated until a convergent self-consistent solution is reached. The criterion for the convergence is that the percentage change in admittance from one iteration to the next iteration is less than 1%.

A prior knowledge of the carrier's saturation velocity is not needed in the simulations when $\omega W/V_n$ is set to π . This value for $\omega W/V_n$ makes the transit angle, $\omega(W-W_A)/V_n$, close to 0.74π and optimizes the transit time effect. Thus, efficiency can be calculated as a function of the r.f. voltage amplitude for a given depletion width. A saturation velocity of $5 \times 10^6 \text{ cm/s}$ for electrons at 500°K was adopted to get the corresponding frequency for any depletion width. Figure 3 illustrates the efficiency dependence on the r.f. voltage amplitudes for three different multiquantum well structures as well as the bulk GaAs material at 100GHz (0.25 μm depletion width). For multiquantum well structures, one has a barrier length of 100Å, another has a barrier length of 150Å and the other has a barrier length of 200Å. The normalized D.C. current density, $J_{dc}/(\epsilon \xi_c V_n/W)$, is set to 0.1 for all the simulations. The multiquantum well IMPATT devices at 100 GHz has a higher efficiency than bulk GaAs devices for any normalized r.f. amplitude. The improvement on efficiency becomes higher for the multiquantum well structure with a larger barrier length because the enhancement in the nonlinearity of the avalanche process is stronger.

Figure 4 shows the efficiency as a function of frequency. The normalized r.f. amplitude (V_{rf}/V_B) is set to 0.5 and the normalized D.C. current density is set to 0.1 for all

the simulations. For comparison purposes, the simulation results for GaAs IMPATT devices at different frequencies are also shown in figure 4. The state of the art experimental results[17] [18] [19] [20] for single-drift GaAs IMPATT devices are also shown in figure 4. The simulation results for GaAs agree well with the available experimental results. The simulations show that multiquantum well IMPATT devices can achieve 13% efficiency at 100GHz (200Å barrier length) and 9% efficiency at 150GHz (150Å barrier length). The results in figure 4 clearly demonstrate that a multiquantum well IMPATT device has an efficiency advantage over a bulk IMPATT device for frequencies above 100 GHz.

The normalized admittances for a GaAs IMPATT device with 0.25μm depletion width and a 200Å barrier length multiquantum well IMPATT device of the same depletion width are plotted in figure 5. The transit angle varies from 0.7π to 1.5π in 0.2π intervals and the normalized r.f. amplitude varies from 0.1 to 0.5 in 0.1 intervals. The larger conductance for the multiquantum well structures comes from the increase in the nonlinearity of the avalanche process, while the susceptance mainly comes from the cold capacitor, $\epsilon A/W$, where A is the device area. The increase in conductance also makes multiquantum well IMPATT devices less susceptible to the series resistance associated with the remaining substrate and ohmic contacts to both p^+ and n^+ layers. Moreover, the decrease in quality factor for multiquantum well structures facilitates the impedance matching to the oscillator circuit.

IV DISCUSSION AND CONCLUSION

A multiquantum well structure can increase the nonlinearity in the avalanche process. This strong nonlinearity limits the particle generation to a confined region. Therefore, a Read type simulation becomes an appropriate way to analyze the performance of mul-

multiquantum well IMPATT devices. Although the extrapolation of the ionization rates in high electric fields and the exclusion of diffusion effects in our Read type analysis affect the accuracy of the simulation, the relative improvement achieved by a multiquantum well structure is preserved. Because the degree of saturation in ionization rates is less in multiquantum well structures, either a hi-low or low-hi-lo Read type design can be used for the purpose of efficiency optimization[21]. The avalanche region has an inductive effect and does not contribute to the power generation. A Read type structure reduces the voltage drop in the avalanche region, thus efficiency is enhanced due to the increase in amplitude modulation (V_{rf}/V_{dc}). The output power and efficiency can be further improved by using a double-drift type design.

A well width parameter does not appear in the design model. If the well width is not properly designed, the geometrical effect can take into place and degrade efficiency[22]. The geometrical effect could be more pronounced for the case of a soft threshold energy due to the fact that a carrier has the chance to see more quantum wells before impact ionization. The ionization mean free paths used here for electrons and holes are about 350\AA at 500°K . Thus, the ionization threshold energy is not very hard. However, the band structure for GaAs material deviates strongly from the parabolic shape for energy near the threshold energy. The "soft" threshold energy could come from the band structure effect because a parabolic band is used in the lucky drift model[23]. For the case of equal barrier and well length, a factor of 2 reduction in ionization rates is used to present the worst case of the geometrical effect. This reduction in ionization rate raises the operating point to a higher saturation region, thus degrading the efficiency of the device. The efficiency for a structure with 200\AA barrier length and 200\AA well length drops from 13% to 10% for the worst case of the geometrical effect. For the detailed influence on device efficiency, a more sophisticated design model incorporating

the effects of well width and "soft" threshold energy is required.

In conclusion, our simulation confirms the efficiency advantage of multiquantum well IMPATT devices for the frequencies above 100 GHz. The efficiency improvement in multiquantum well structures opens up a new field for the applications of modern epitaxy technologies to two terminal high frequencies sources.

ACKNOWLEDGEMENT

This work was supported in part by the Air Force Office of Scientific Research under the direction of H. R. Schlossberg.

APPENDIX

The ionization rate is the reciprocal of the average distance $\langle l \rangle$ travelled between ionization events. If on the average it takes $\langle N \rangle$ attempts before a successful attempt occurs, $\langle l \rangle$ can be expressed as follows

$$\langle l \rangle = (\langle N \rangle - 1) \langle z \rangle_E + \langle z \rangle_I, \quad (\text{A.1})$$

where $\langle z \rangle_E$ is the average distance travelled for an unlucky attempt that ends in energy relaxation, and $\langle z \rangle_I$ is the average distance travelled for a lucky attempt that ends at impact ionization. In a multiquantum well structure, a carrier starts from a non-zero energy E_0 to reach the threshold energy. Because both the energy relaxation length (λ_E) and the momentum relaxation (λ_m) are independent of the energy in a parabolic band, the probability ($P(z)$) that a carrier starts from $z=0$ to reach z without energy relaxation is not a function of the non-zero starting energy. The probability, $P(z)$, is composed of the ballistic component and the drift component ($P_E(z)$). The formula for $P(z)$ and $P_E(z)$ can be expressed as follows:

$$P_E(z) = \frac{\lambda_E}{\lambda_E - \lambda_m} \left[\exp\left(-\frac{z}{\lambda_E}\right) - \exp\left(-\frac{z}{\lambda_m}\right) \right] \quad (\text{A.2})$$

$$P(z) = \frac{\lambda_E \exp\left(-\frac{z}{\lambda_E}\right) - \lambda_m \exp\left(-\frac{z}{\lambda_m}\right)}{\lambda_E - \lambda_m} \quad (\text{A.3})$$

If the non-zero starting energy is less than the threshold energy, ionization can only occur when a carrier travels a distance of $l_0 - \eta$, where $\eta = E_0/e\xi$. Thus, the probability ($P_I(z)$) that a carrier reaches z without ionization is given by the equation:

$$P_I(z) = \begin{cases} 1 & \text{for } z < l_0 - \eta \\ \exp\left(\frac{-\pi(z - (l_0 - \eta))^2}{4\lambda_{ion}^2}\right) & \text{for } z \geq l_0 - \eta \end{cases} \quad (\text{A.4})$$

Here, we have the following formula:

$$\frac{1}{\langle N \rangle} = \int_{l_0 - \eta}^{\infty} P(z) P_I(z) \frac{dz}{\lambda_I(z)}, \quad (\text{A.5})$$

$$\frac{\langle z \rangle_I}{\langle N \rangle} = \int_{l_0 - \eta}^{\infty} z P(z) P_I(z) \frac{dz}{\lambda_I(z)}, \quad (\text{A.6})$$

$$\langle z \rangle_E \left(1 - \frac{1}{\langle N \rangle} \right) = \int_0^{\infty} z P_E(z) P_I(z) \frac{dz}{\lambda_E}. \quad (\text{A.7})$$

Where $dz/\lambda_I(z)$ is the probability of impact ionization at z and dz/λ_E is the probability of energy relaxation at z . Therefore, the equations for ionization rates are the same as equations (3) and (4), except l_0 is replaced by $l_0 - \eta$ in equation (4).

For the case where the non-zero starting energy is larger than the threshold energy, the probability of reaching z without ionization can be expressed as follows:

$$P_I(z) = \exp\left(-\frac{\pi z^2}{4\lambda_{ion}^2}\right) \exp\left(-\frac{\pi(\eta - l_0)}{2\lambda_{ion}^2} z\right). \quad (\text{A.8})$$

Here, we have

$$\frac{1}{\langle N \rangle} = \int_0^{\infty} P(z) P_I(z) \frac{dz}{\lambda_I(z)}. \quad (\text{A.9})$$

When the right hand side of (A.9) is integrated by parts using the relation $-dP(z) = P_E(z)dz/\lambda_E$, $\langle N \rangle^{-1}$ can be expressed as follows.

$$\begin{aligned} \frac{1}{\langle N \rangle} &= 1 - \int_0^{\infty} P_I(z) P_E(z) \frac{dz}{\lambda_E} \\ &= \frac{\lambda_E}{\lambda_E - \lambda} \left[1 - \frac{1}{\lambda_E} \int_0^{\infty} \exp\left(-\frac{\pi z^2}{4\lambda_{ion}^2}\right) \exp\left(-\frac{\pi(\eta - l_0)}{2\lambda_{ion}^2} z\right) \exp\left(-\frac{z}{\lambda_E}\right) dz \right] \\ &\quad - \frac{\lambda}{\lambda_E - \lambda} \left[1 - \frac{1}{\lambda} \int_0^{\infty} \exp\left(-\frac{\pi z^2}{4\lambda_{ion}^2}\right) \exp\left(-\frac{\pi(\eta - l_0)}{2\lambda_{ion}^2} z\right) \exp\left(-\frac{z}{\lambda}\right) dz \right] \end{aligned} \quad (\text{A.10})$$

Here, we have

$$\frac{\langle z \rangle_I}{\langle N \rangle} = \int_0^{\infty} z P(z) P_I(z) \frac{dz}{\lambda_I(z)} \quad (\text{A.11})$$

When the right hand side of (A.11) is integrated by parts using the relation $-dP(z) = P_E(z)dz/\lambda_E$, $\langle z \rangle_I \langle N \rangle^{-1}$ can be expressed as follows.

$$\frac{\langle z \rangle_I}{\langle N \rangle} = \int_0^{\infty} P_I(z) P(z) dz - \int_0^{\infty} z P_I(z) P_E(z) \frac{dz}{\lambda_E} \quad (\text{A.12})$$

Therefore,

$$\begin{aligned}
& \frac{\langle z \rangle_I}{\langle N \rangle} + \langle z_E \rangle \left(1 - \frac{1}{\langle N \rangle} \right) \\
&= \int_0^\infty P_I(z) P(z) dz \\
&= \frac{\lambda_E^2}{\lambda_E - \lambda} \left[\frac{1}{\lambda_E} \int_0^\infty \exp\left(-\frac{\pi z^2}{4\lambda_{ion}^2}\right) \exp\left(-\frac{\pi(\eta - l_0)}{2\lambda_{ion}^2} z\right) \exp\left(-\frac{z}{\lambda_E}\right) dz \right] \\
&- \frac{\lambda^2}{\lambda_E - \lambda} \left[\frac{1}{\lambda} \int_0^\infty \exp\left(-\frac{\pi z^2}{4\lambda_{ion}^2}\right) \exp\left(-\frac{\pi(\eta - l_0)}{2\lambda_{ion}^2} z\right) \exp\left(-\frac{z}{\lambda}\right) dz \right]. \quad (A.13)
\end{aligned}$$

In summary, by using the definite integral:

$$\int_0^\infty \exp(-(ax^2 + 2bx)) dx = \frac{1}{2} \sqrt{\frac{\pi}{a}} \exp \frac{b^2}{a} \operatorname{erfc} \frac{b}{\sqrt{a}}, \quad (A.14)$$

we can obtain the following formula for impact ionization rates of a multiquantum well structure:

$$\alpha, \beta = \frac{\lambda_E f(\lambda_E) - \lambda_m f(\lambda_m)}{\lambda_E^2 (1 - f(\lambda_E)) - \lambda_m^2 (1 - f(\lambda_m))}, \quad (A.15)$$

If $\eta < l_0$, then

$$f(\lambda) = \exp\left(-\frac{l_0 - \eta}{\lambda}\right) \left[1 - \frac{\lambda_{ion}}{\lambda} \exp\left(\frac{\lambda_{ion}}{\sqrt{\pi}\lambda}\right)^2 \operatorname{erfc}\left(\frac{\lambda_{ion}}{\sqrt{\pi}\lambda}\right) \right]. \quad (A.16)$$

If $\eta \geq l_0$, then

$$f(\lambda) = 1 - \frac{\lambda_{ion}}{\lambda} \exp\left[\frac{\lambda_{ion}}{\sqrt{\pi}\lambda} + \frac{\sqrt{\pi}(\eta - l_0)}{2\lambda_{ion}}\right]^2 \operatorname{erfc}\left[\frac{\lambda_{ion}}{\sqrt{\pi}\lambda} + \frac{\sqrt{\pi}(\eta - l_0)}{2\lambda_{ion}}\right]. \quad (A.17)$$

References

- [1] R. Chin, N. Holonyaki, Junior, G. E. Stillman, J. Y. Tang, and K. Hess, *Electron. Letts.* **16**, 467(1980).
- [2] F. Capasso, W. T. Tsang, A. L. Hutchinson, and G. F. Williams, *Appl. Phys. Lett.* **40**, 38(1982).
- [3] T. Misawa, *Solid-St. Electron.* **15**, 457(1972).
- [4] D. Lippens, O. Vanbesien, and B. Lambert, *Journal De Physique*, C5-487(1987).
- [5] D. Lippens, J. N. Ski, and E. Constant, *Physica 134B*, 72(1985).
- [6] A. Christou and K. Varmazis, *Appl. Phys. Lett.* **48**, 1446(1986).
- [7] B. K. Ridley, *J. Phys. C:Solid-St. Phys.* **16**,3373(1983).
- [8] S. Mckenzie and M. G. Burt, *J. Phys. C: Solid-St. Phys.* **19**,1959(1986).
- [9] B. K. Ridley, *Semicond. Sci. Technol.* **2**, 116(1987).
- [10] J. S. Marsland, *Solid-St. Electron.* **30**, 125(1987).
- [11] R. C. Woods, *IEEE Trans. Electron Dev.* **ED-34**, 1116(1987).
- [12] P. Bauhahn and G. I. Haddad, *IEEE Trans. Electron Dev.* **ED-24**, 634(1977).
- [13] R. K. Mains and G. I. Haddad, *Infrared and Millimeter waves Vol 10*, p. 111. Academic Press, Inc., London(1983).
- [14] G. E. Bulman, V. M. Robbins, and G. E. Stillman, *IEEE Trans. Electron Dev.* **ED-32**, 2454(1985).
- [15] K. Brennan, T. Wang, and K. Hess, *IEEE Electron Dev. Lett.* **EDL-6**, 199(1985).

- [16] D. R. Decker, *IEEE Trans. Electron Dev.* ED-21, 469(1974).
- [17] X. Zhang and J. Freyer, *Electron. Letts.* 20, 359(1984).
- [18] X. Zhang and J. Freyer, *Electron. Letts.* 20, 752(1984).
- [19] H. Eisele and H. Grothe, *Proc. MIOP '89, session 3A.6(1989).*
- [20] K. Chang, J. K. Kung, P. G. Asher, G. M. Hayaahibara, and R. S. Ying, *Electron. Letts.* 17, 471(1981).
- [21] S. M. Sze, *Physics of Semiconductor Devices*, 2nd Edn, p. 592. Wiley-Interscience, New York (1981).
- [22] B. K. Ridley, *IEE Proc. J* 132, 177(1985).
- [23] N. Sano, T. Aoki, and A. Yoshii, *Appl. Phys. Lett.* 55, 14(1989).

FIGURE CAPTION

Fig. 1 The layer structure of a 100 GHz GaAs/Al_{0.3}Ga_{0.7}As multiquantum well IMPATT device. The quantum wells with 100Å barrier length and 100Å well length are placed in the avalanche region.

Fig. 2 Normalized growth (decay) factor, $\left(\frac{1}{\kappa M_n \omega \tau_n}\right) / \left(\frac{\pi}{\omega W / V_n}\right)$, as a function of the normalized electric field $\left(\frac{\xi_0 - \xi_c}{\xi_c}\right)$ for bulk GaAs material and GaAs/Al_{0.3}Ga_{0.7}As multiquantum well structures. The depletion width is 0.25μm for each structure.

Fig. 3 Efficiency as a function of V_{rf}/V_B for GaAs and GaAs/Al_{0.3}Ga_{0.7}As single-drift flat-profile multiquantum well IMPATT devices at 100 GHz.

Fig. 4 Calculated efficiency as a function of frequency for GaAs and GaAs/Al_{0.3}Ga_{0.7}As single-drift flat-profile multiquantum well IMPATT devices. Calculated results for multiquantum well IMPATT devices with 100Å barrier length(Δ), 150Å barrier length(▽), 200Å barrier length◇ and bulk GaAs IMPATT devices(o). •, ♦ and × are the state of the art experimental data for single-drift flat-profile GaAs IMPATT devices. + is the experimental result of a single-drift Read type GaAs IMPATT device at 130 GHz.

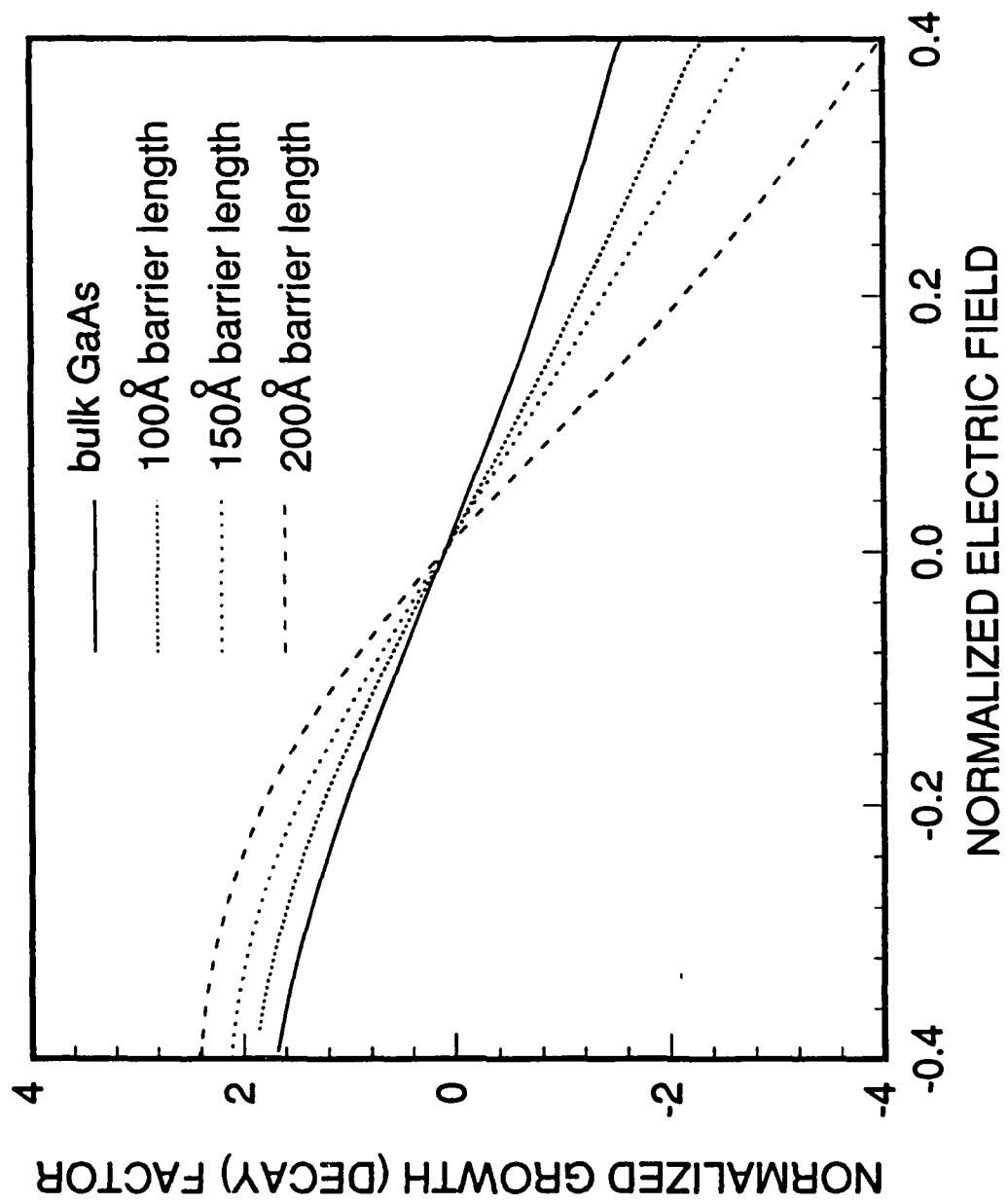
Fig. 5 Normalized conductance and susceptance plot for GaAs and 200Å barrier length multiquantum well IMPATT devices. The unit for conductance and susceptance in the plot is $\frac{eV_n A}{W^2}$. Solid arrows point to the normalized frequencies and dash arrows point to the normalized r.f. voltage amplitudes, where frequency is normalized to 100 GHz and r.f. voltage amplitude is normalized to V_B .

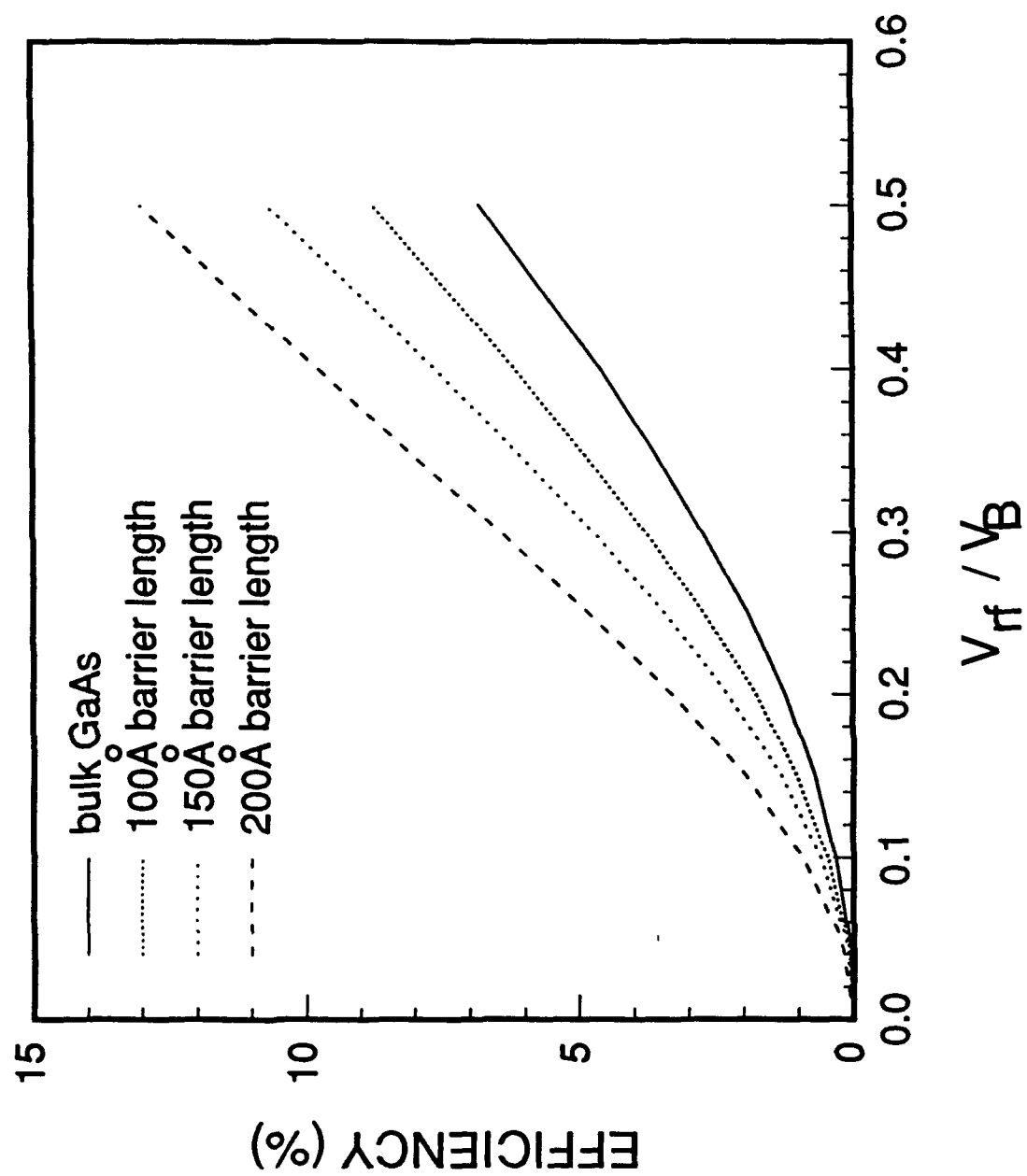
• $x=0$

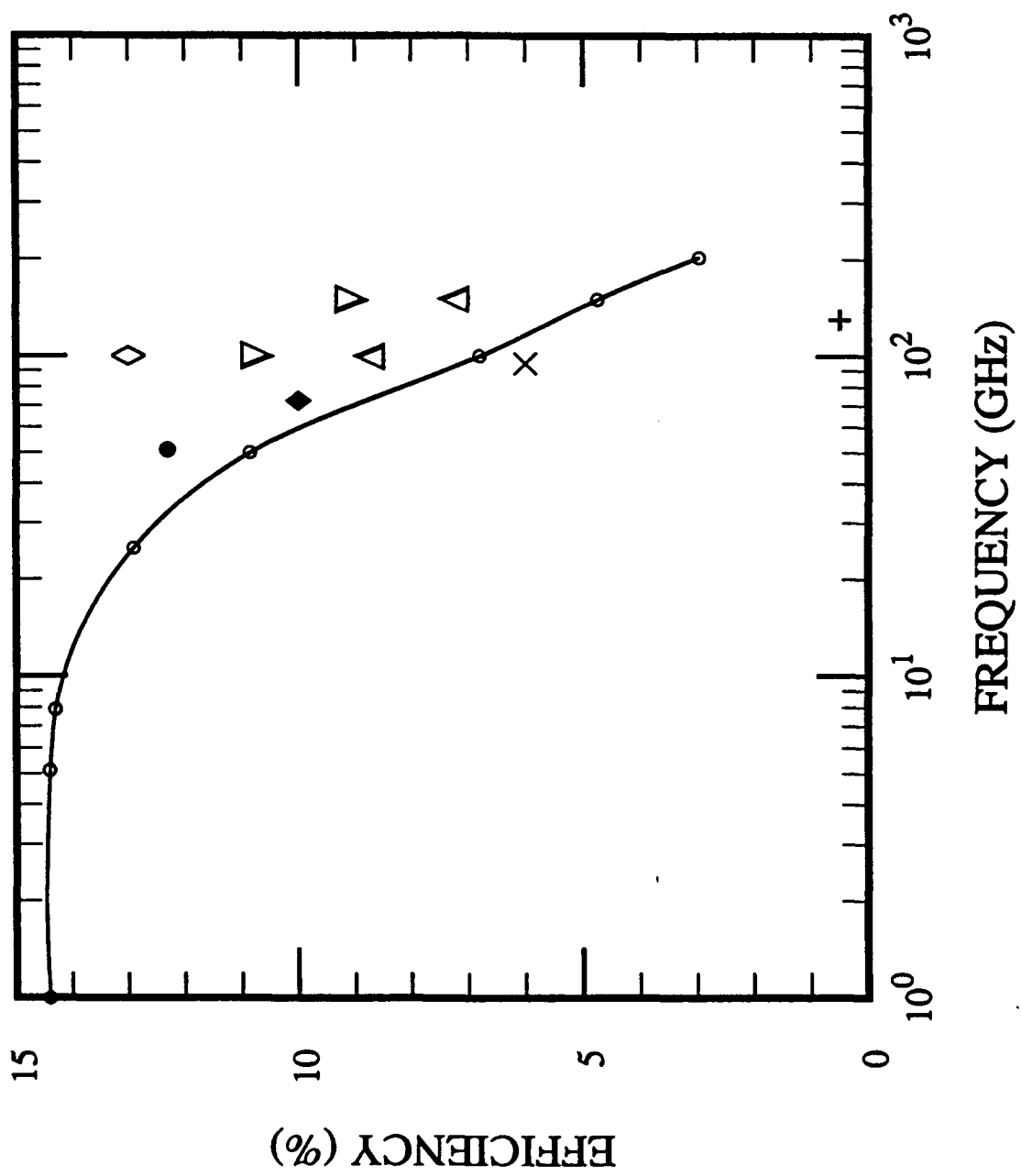
• $x=W_A$

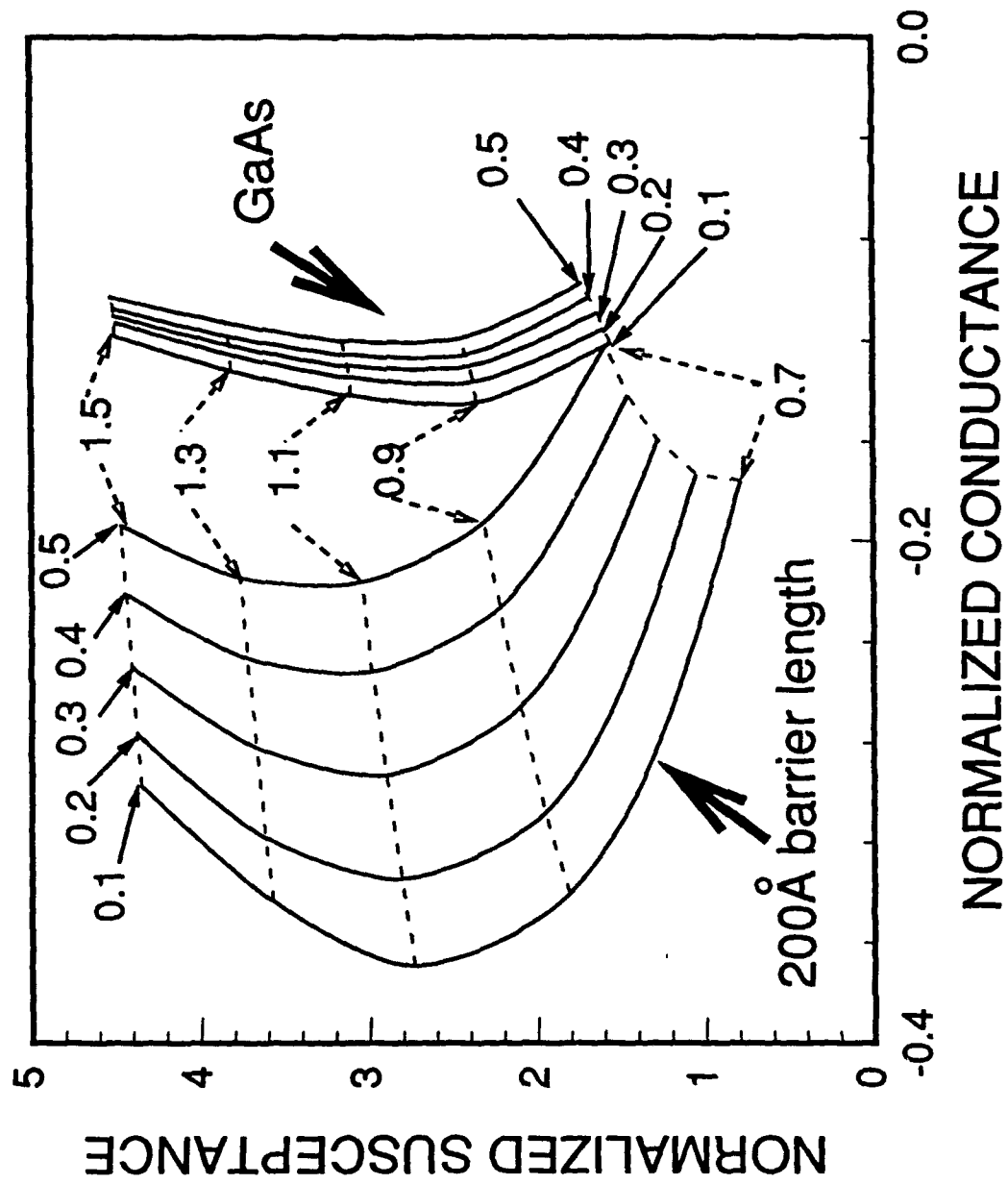
• $x=W$
↓

p^+ GaAs		
n	AlGaAs	100\AA
n	GaAs	100\AA
n	AlGaAs	100\AA
n	GaAs	100\AA
n	AlGaAs	100\AA
n	GaAs	100\AA
n	AlGaAs	100\AA
n	GaAs	100\AA
n	AlGaAs	100\AA
n	GaAs	100\AA
n	AlGaAs	100\AA
n	GaAs	1400\AA
n^+ GaAs		









Optical transmission of millimeter wave signals through polyimide channel waveguides fabricated using direct laser writing

by

D.P. Prakash, D.V. Plant, D. Zhang, and H.R. Fetterman

Department of Electrical Engineering
University of California at Los Angeles
Los Angeles, CA 90024

ABSTRACT

High speed wafer-scale optical interconnections have been achieved using hybrid opto-electronic integrated circuits (OEIC's). Polyimide channel waveguides fabricated using direct laser writing (DLW) served as the interconnect media between the high frequency signal sources and the high speed detectors. The 50 GHz optical interconnection reported here could potentially be used in the implementation of sophisticated wafer scale systems such as phased array radars.

1. INTRODUCTION

The aim of this work was to realize high speed interconnects at the wafer level. Recently, Hewak et al. have reported studies on polyimide channel waveguides fabricated using DLW.¹⁻³ Using this simple yet powerful technique, we have fabricated waveguide structures that could form the basic units of OEIC's. Experiments were performed to demonstrate millimeter wave optical interconnections using these waveguides in a hybrid OEIC configuration. This work can be extended to form optically integrated millimeter wave circuits.

2. WAVEGUIDE FABRICATION AND CHARACTERIZATION

In these experiments, a commercially available polyimide from Ciba Geigy, probimide 293, was used as the waveguide material. The substrates used were Silicon and Gallium Arsenide. The index of refraction of the polyimide in the 400nm-800nm range was ~ 1.65 while the substrates had a high index of ~ 3.5 . Therefore SiO_2 buffer layers with an index of ~ 1.45 and a thickness of 1-2 μm were used to reduce the substrate leakage losses.⁴ Thermal oxidation on Si and

repeated spin coating of a Silica Gel solution on GaAs, respectively provided the required buffer layers. Silicon substrates were given preference during the later parts of the study primarily due to the ease of fabrication although the concepts apply for GaAs as well.

Fig. 1 shows the three-step process sequence used to fabricate channel waveguides on the buffered substrates. During the pre-writing stage, the polyimide was spin-coated on the substrates at 1500 rpm for 30 sec. This was followed by a soft-bake at 50°C for 30 minutes which provided a semi-hardened film. In the laser writing step, the substrates were mounted on a computer controlled X-Y translation stage and moved at a speed of 100 $\mu\text{m/s}$ while being exposed to a stationary laser beam. The polyimide is virtually transparent to the laser radiation at 457.9 nm and therefore heating caused by absorption in the substrate led to localized solvent evaporation (curing) and selective hardening of the polyimide film. During the post-writing step the soft polyimide is etched away by dipping the substrates in polyimide thinner for 15 min (using an ultrasonic bath decreases this time). The uncured polyimide was soft and therefore etched much faster compared to the laser-hardened regions. Finally, nitrogen blow-dry and hardbaking at 125°C for 1 hour completed the waveguide fabrication. Light guiding multimode structures with typical dimensions of 45 μm x 12 μm and smooth sidewalls were obtained using this technique. It should be noted that the parameters involved must be carefully monitored for successful yields. In particular, a low softbake temperature resulted in films which were too soft thus making it difficult to induce differential etching rates by laser writing. Too high a softbake temperature induced excessive stress in the film causing cracks to develop during the etching step.

2. LOSS MEASUREMENTS

Channel propagation loss measurements were carried out using a cornerbend structure shown in Fig. 2a. The assumption made is that light scattered out of the waveguide is directly proportional to the light guided within the waveguide. Under these conditions simply by detecting the scattered light it is possible to estimate the scattering losses.⁴ We used a 100 μm core multimode optic fiber coupled to a photodetector to detect the scattered light in the straight section of the waveguide. The cornerbend structure minimises stray light pick-up and thereby increases the accuracy of loss measurement. Also, a lock-in amplifier was used to increase the sensitivity of the detection set-up. Fig. 2b shows a typical plot used to obtain propagation losses. A relatively high loss of $\alpha=4$ dB/cm was observed.

To understand the loss mechanisms involved we studied the light prism-coupled out of a planar polyimide waveguide on buffered Silicon substrates. The

image at the output showed streaks around a central bright spot indicating the existence of severe in-plane scattering. The polyimide material used was not optimised for its optical properties and only a 3 μm filtration process was used for its production. This could be one of the main reasons for the in-plane scattering and therefore the resulting losses observed in this material at 0.633 μm . Filtering down to 0.2 μm , fine tuning of the fabrication process, and operating at longer wavelengths (1.3 μm) will result in much lower losses.³

3. PASSIVE WAVEGUIDE STRUCTURES

3.1 POWER SPLITTERS/COMBINERS

The power splitter/combiner structure used in these studies is shown in Fig. 3a. A typical photograph of a power splitter junction is shown in Fig. 3b. By varying the radius of curvature we obtained different power splitting ratios as shown in the following table:

Radius (mm)	% Power splitting
1	10
3	25
7	50

note- % Power splitting with respect to the output end = $100 \times P_2 / (P_1 + P_2)$

These results could serve as guidelines to be used while routing optical power around a wafer. Knowing that the propagation loss for any waveguide structure is due to linear scattering and/or absorption losses (α dB/cm) and bending losses (β dB/rad), we can write total losses $L = \alpha l + \beta \theta$, where α is the linear propagation loss (a constant for the material), l is the length of the waveguide, β is the bending loss (a function of radius) and θ is the bending angle. Our current efforts include studying the dependence of β on r .

3.2 REPETITION-RATE MULTIPLIER

A delay element and a power combiner in series with a power splitter can result in another useful structure, the repetition-rate multiplier, which can serve to increase the frequency of an incoming picosecond pulse train.⁵ Fig. 4a illustrates the concept. When the repetition rate is very high (in the 10's of GHz range), the length of the delay element falls in the wafer scale regime and can be fabricated using the direct writing technique. Fig 4b shows a multiplier designed

and fabricated for a 30 GHz input rep-rate with a delay of 16.7 ps (i.e $T/2$). The output from this structure is expected to have a rep-rate of 60 GHz. This structure is currently under test.

4. MILLIMETER-WAVE OPTICAL INTERCONNECTS

The three basic units needed to realise high speed optical interconnects at millimeter wave frequencies are a) optical sources modulated at millimeter-wave frequencies, b) an interconnect medium capable of transmitting the high frequency signals, c) a high speed photo- detector. It is difficult to modulate lasers directly beyond 10 GHz and therefore the millimeter-wave signals used in these experiments were generated using either optical mixing techniques⁶ or mode-locked laser diodes.⁷ The polyimide waveguide with its wide optical bandwidth served as the interconnect media. The high frequency signals were detected using a HEMT photodetector mounted on a test fixture with a bandwidth of 65 GHz.

4.1 10 GHz INTERCONNECT BY OPTICAL MIXING

Fig. 5a shows the experimental set-up used to achieve 10 GHz interconnects. The beam from a tunable frequency dye laser (600-640 nm) that was pumped by an Argon laser was co-propagated and thereby mixed with a fixed frequency HeNe laser. Both the dye and the HeNe laser were frequency stabilised. Tuning the dye laser provided the desired millimeter wave signals. The channel waveguide end-faces were prepared for butt-coupling by simply cleaving the substrate along with the waveguide. The collinear beams were focussed and butt-coupled into the channel waveguide. At the output end, the 3 cm long straight section of waveguide was butt-coupled directly to the HEMT device. Continuous tuning of the optical mixing signal from 1 GHz to 10 GHz was performed. Fig 5b shows a S/N of 25-30 dB obtained at 10 GHz. This method can be extended to demonstrate the interconnection capability of the channel at higher frequencies.⁸

4.2 50 GHz INTERCONNECT USING MODE-LOCKED LASERS

In an effort to move towards wafer scale integration of optical systems, the large optical system used in the above experiment to generate the millimeter-wave signals was replaced by a compact solid-state laser diode. The mode-locked AlGaAs/InGaAs laser diode produced a train of 2 picosecond long optical pulses at 850 nm with a frequency of 50 GHz. Fig. 6a shows the schematic of the experimental set-up. A 1.5 cm long straight section of polyimide channel waveguide was used as the high speed interconnect. The light source, waveguide,

and HEMT effectively formed a hybrid OEIC. The light from the laser diode was butt-coupled into the waveguide using a 40X microscope objective. The light conducted through the waveguide was coupled out using another 40X objective. The collimated beam was focussed onto the HEMT using a 10X lens. The spectrum analyser cannot respond directly to the high speed electrical signals from the HEMT device, therefore a heterodyne arrangement was used to down-convert the 50 GHz signal to an IF of 10 GHz by mixing with a tunable local oscillator.

Fig. 6b shows the preliminary experimental results. The larger amplitude signal corresponds to the output of the detector without the waveguide in the circuit and the smaller amplitude signal corresponds to the attenuated output due to the insertion of the waveguide. The losses are primarily due to intrinsic waveguide losses, coupling losses, and the mismatch in dimensions between the waveguide and the detector. Although this result has not yet been optimised, it does show a 50 GHz channel waveguide optical interconnect at the wafer scale.

5. CONCLUSIONS

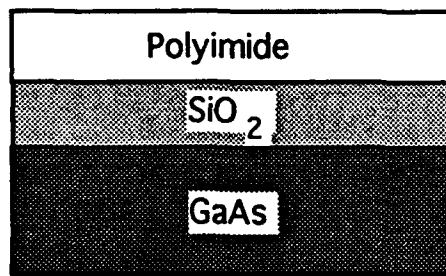
Passive waveguide structures made of polyimide were fabricated using a large area patterning technique, namely direct laser writing. These waveguides were used in a hybrid OEIC configuration to achieve high speed interconnections upto 50 GHz. This result has many applications. The 50 GHz source along with appropriate power splitters could provide high speed on-wafer optical clock distribution. Further, if the 50 GHz source is coupled to a rep-rate multiplier with a delay element designed for 10 ps (i.e $T/2$), it is possible to obtain a 100 GHz optical source without any active elements. This work can be extended to integrate complex and sophisticated millimeter wave optical systems at the wafer scale. Fig. 7 shows one such potential application - the wafer scale integration of phased array radars using diode lasers feeding HEMT's via branching structures to form distributed millimeter wave sources⁹ - which could lead to the formation of a radar on a chip.

6. ACKNOWLEDGEMENTS

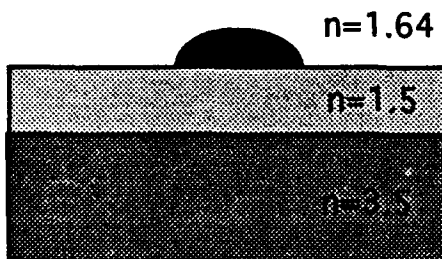
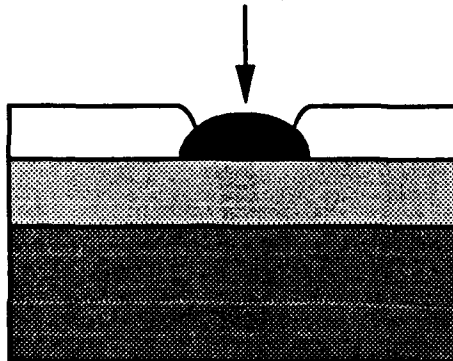
It is a pleasure to thank D.W. Hewak of the National Optics Institute, Canada, for his helpful discussions regarding the laser writing technique, J. Paslaski of Ortel Corp. for providing semiconductor diode lasers, and Toni Bray of Ciba Geigy for providing the polyimides. This work was supported by the Air Force Office of Scientific Research and by the National Center for Integrated Photonics Technology.

7. REFERENCES

- 1) D.W. Hewak, F. Picard, and H. Jin, "Channel optical waveguides in polyimide for optical interconnection by direct laser writing and contact printing," SPIE, vol 1213, pp. 86-99, 1990.
- 2) D.W. Hewak, "Optical waveguides in polyimide by direct laser writing," presented at ANTEC, Montreal, Canada, 1991.
- 3) D.W. Hewak, private communication.
- 4) H. Nishihara, M. Haruna, and T. Suhara, Optical Integrated Circuits, McGraw-Hill, New York, 1985.
- 5) A. Mooradian, "Use of spatial time-division repetition rate multiplication of mode-locked laser pulses to generate microwave radiation from opto-electronic switches," Appl. Phys. Lett., 45 (5), pp. 494-496, 1984.
- 6) D.V. Plant, D.C. Scott, H. R. Fetterman, L.K. Shaw, W. Jones, and K.L. Tan, "Optically generated 60 GHz millimeter waves using AlGaAs/InGaAs HEMT's integrated with both quasi-optical antenna circuits and MMIC's," IEEE Photon. Technol. Lett., vol. 4, no. 1, pp. 102-105, 1992.
- 7) D.C. Scott, D.V. Plant, and H.R. Fetterman, "60 GHz sources using optically driven heterojunction bipolar transistors," Appl. Phys. Lett., 61 (1), pp. 1-3, 1992.
- 8) R.T. Chen, H. Lu, D. Robinson, Z. Sun, T. Jansson, D.V. Plant, and H.R. Fetterman, "60 GHz board-to-board optical interconnection using polymer optical buses in conjunction with microprism couplers," Appl. Phys. Lett., 60 (5), pp. 536-538, 1992.
- 9) P.R. Herczfeld and A. Daryoush, "Fiber-optic feed network for large aperture phased array antennas: Systems considerations," Microwave Journal, vol. 30, no. 8, p. 160, August, 1987.



Focussed
Laser beam



Pre Writing:

- Spin Coat at 1500 RPM for 30 sec
- Bake at 50° C, 30 min

Laser Writing:

- 300 mW
- 457.9 nm

Post Writing:

- Etch in Polyimide thinner for 15 min
- Post bake 125° C, 1 hr

Note: n = Refractive index at 633 nm.

Fig. 1. The 3 step process sequence used for fabricating polyimide channel waveguides on buffered Silicon substrates

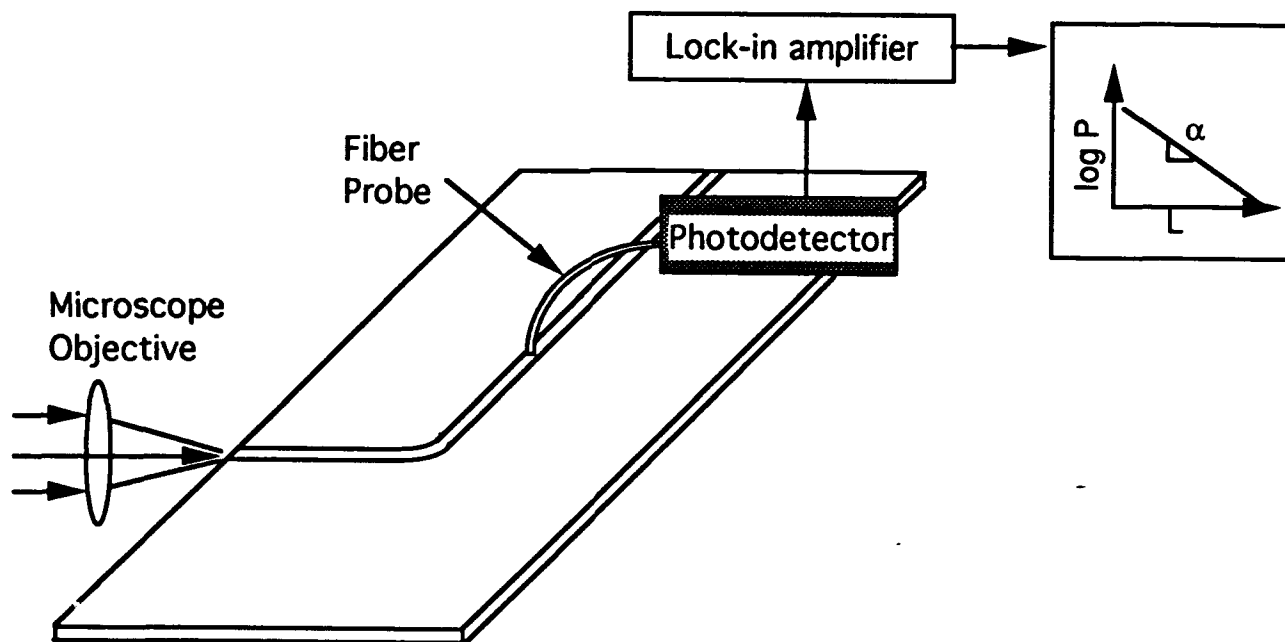
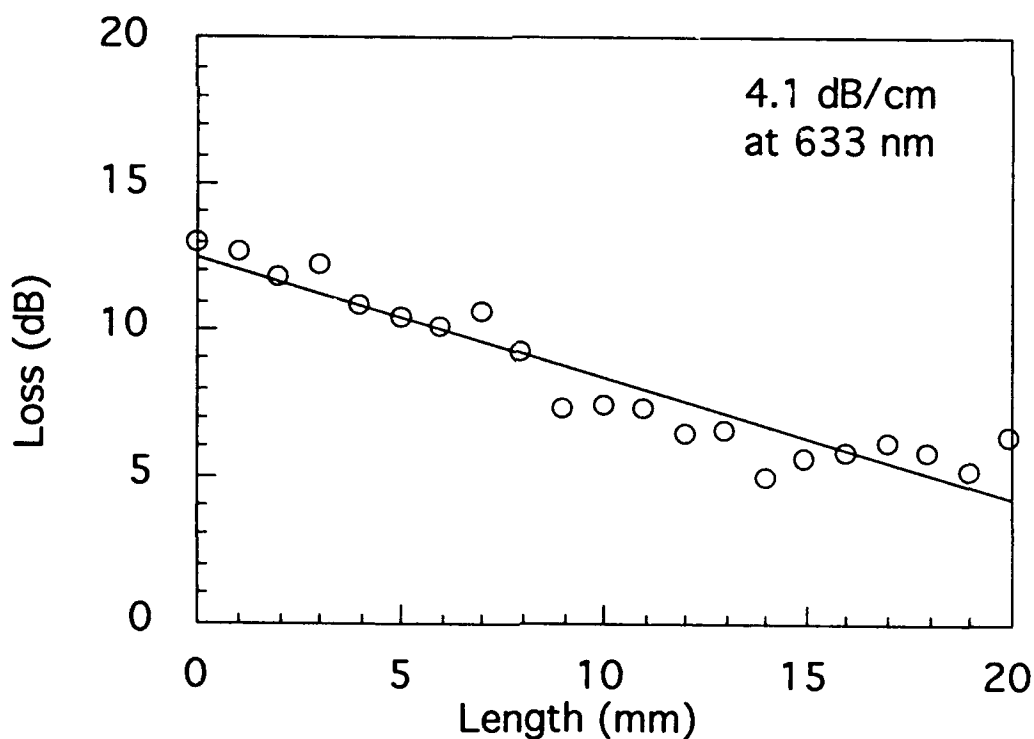


Fig. 2a. Channel loss measurements using the scattering-detection method



Note: $\text{Loss} = 10 \log_{10}(V)$, where v = normalized measured voltage

Fig. 2b. Plot of $\log P$ vs L showing typical losses

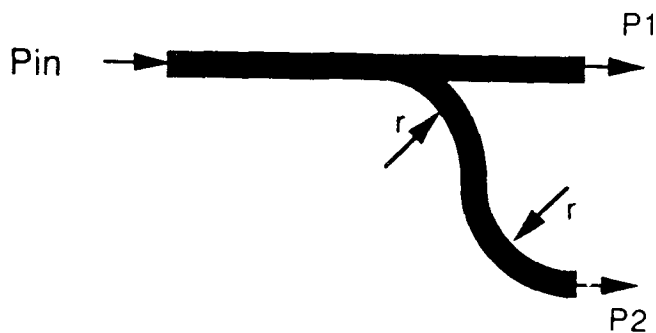


Fig. 3a. Power divider/combiner structure

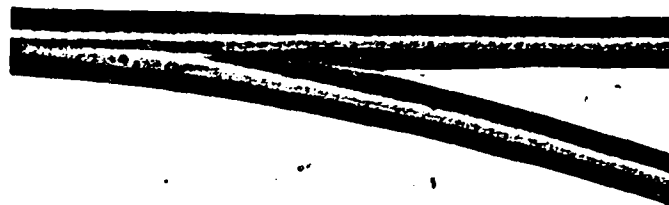


Fig. 3b. Photograph of a typical power divider/combiner junction

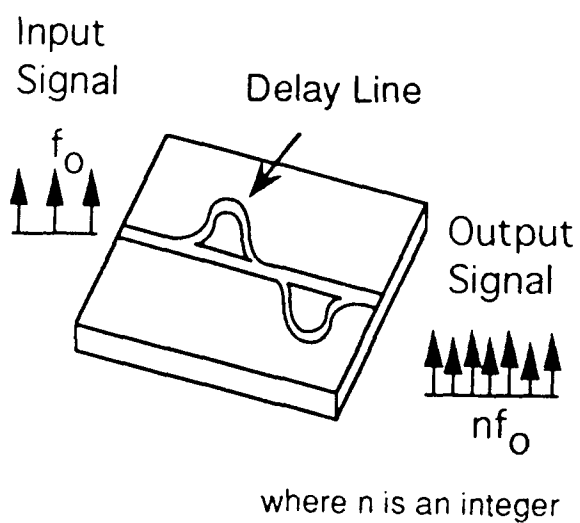


Fig. 4a. On-wafer Repetition-Rate Multiplier Structure

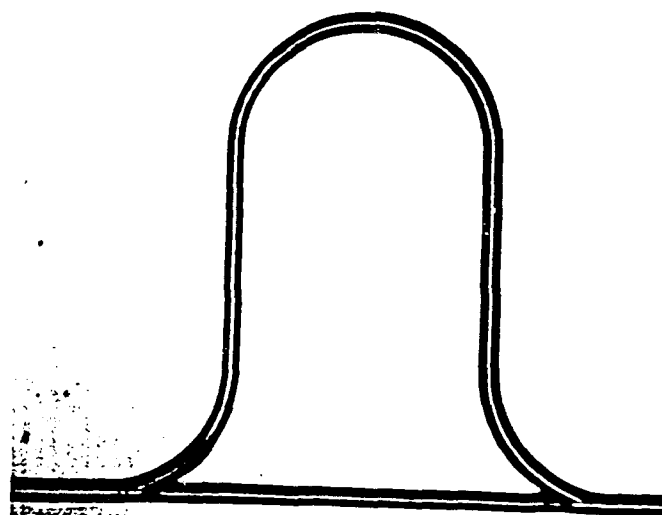


Fig. 4b. Photograph of a typical multiplier

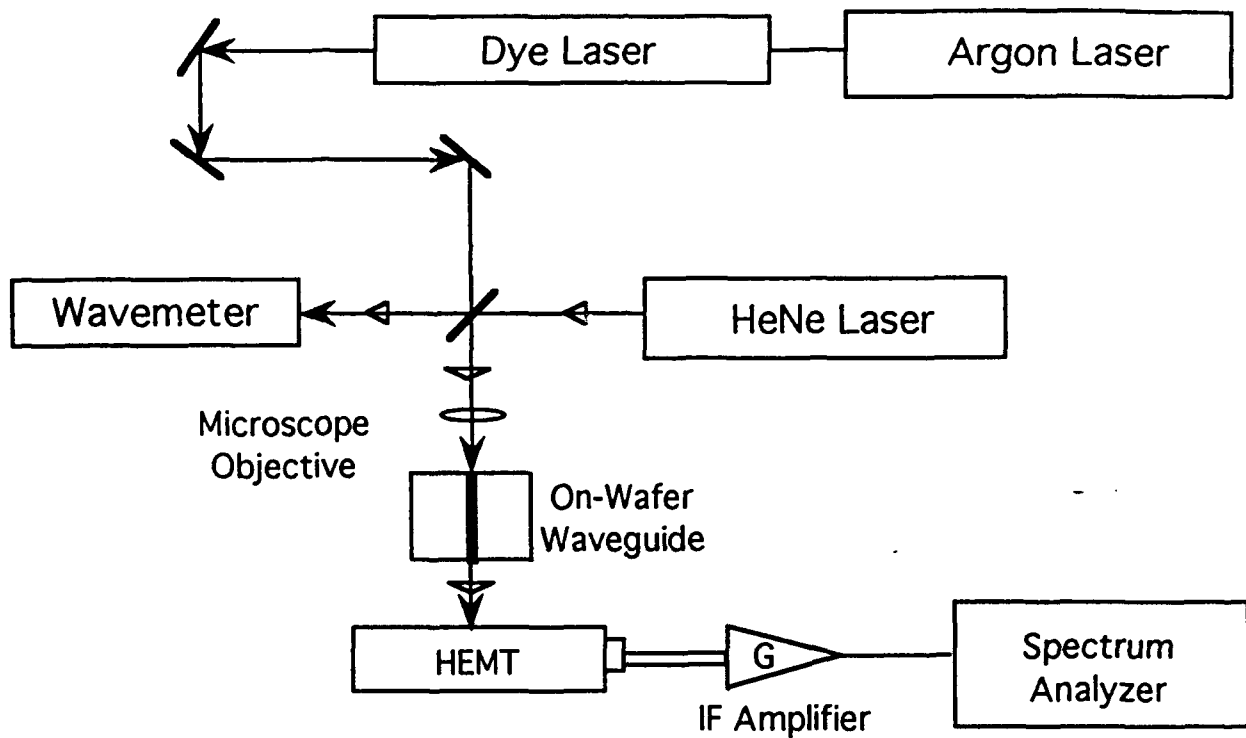


Fig. 5a. Schematic of the experimental set-up used for a 10 GHz interconnection via optical mixing

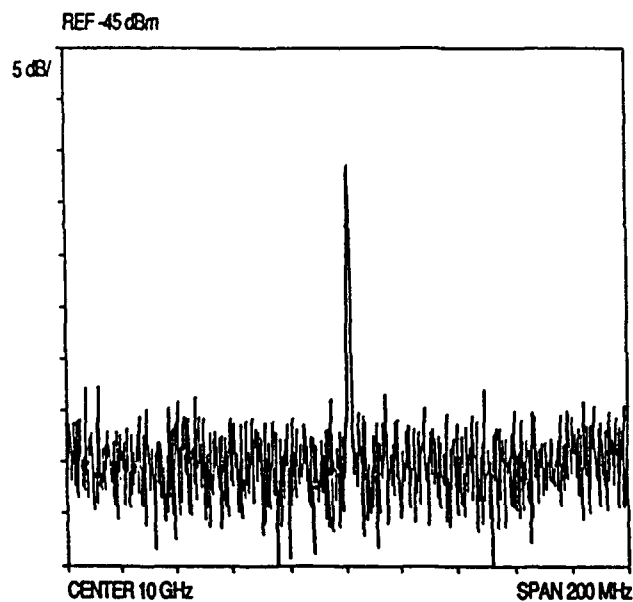


Fig. 5b. Experimental result showing the 10 GHz Interconnection with a $S/N = 25$ dB

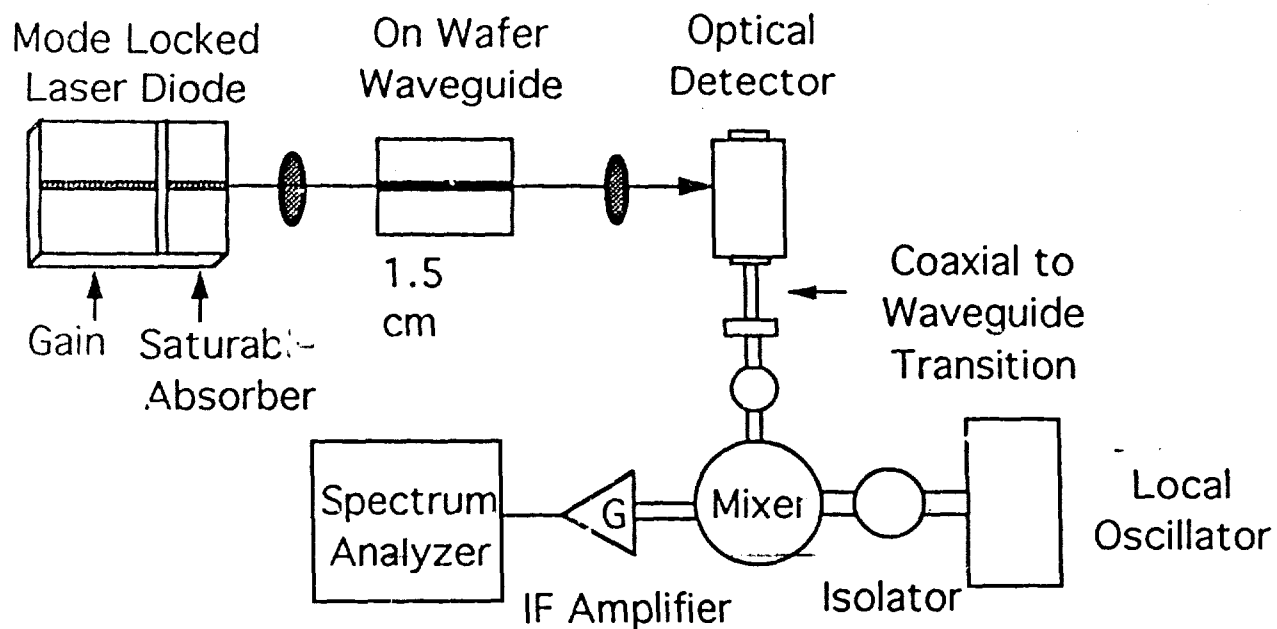


Fig. 6a. Schematic of the hybrid OEIC used to demonstrate a 50 GHz Optical Interconnection

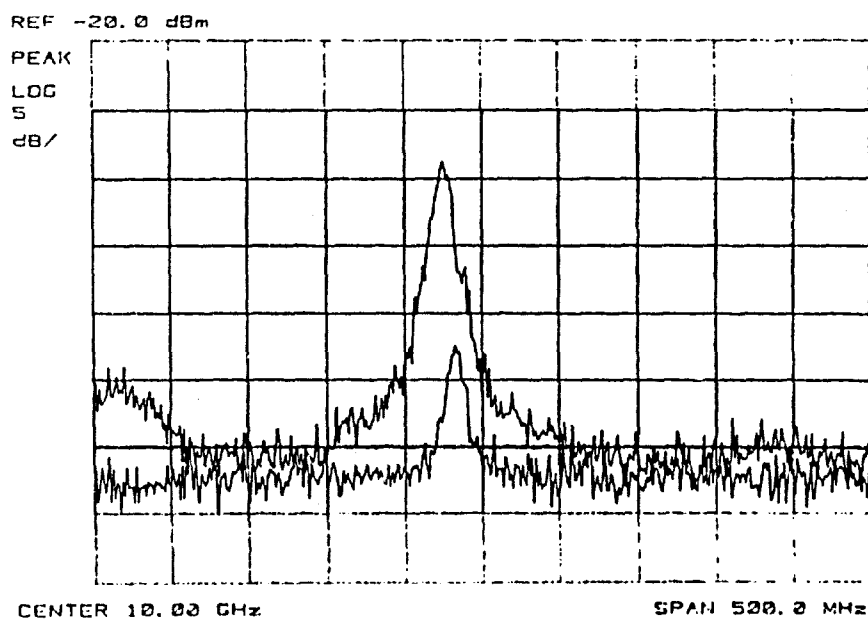


Fig. 6b. Preliminary experimental result showing the 50 GHz interconnection

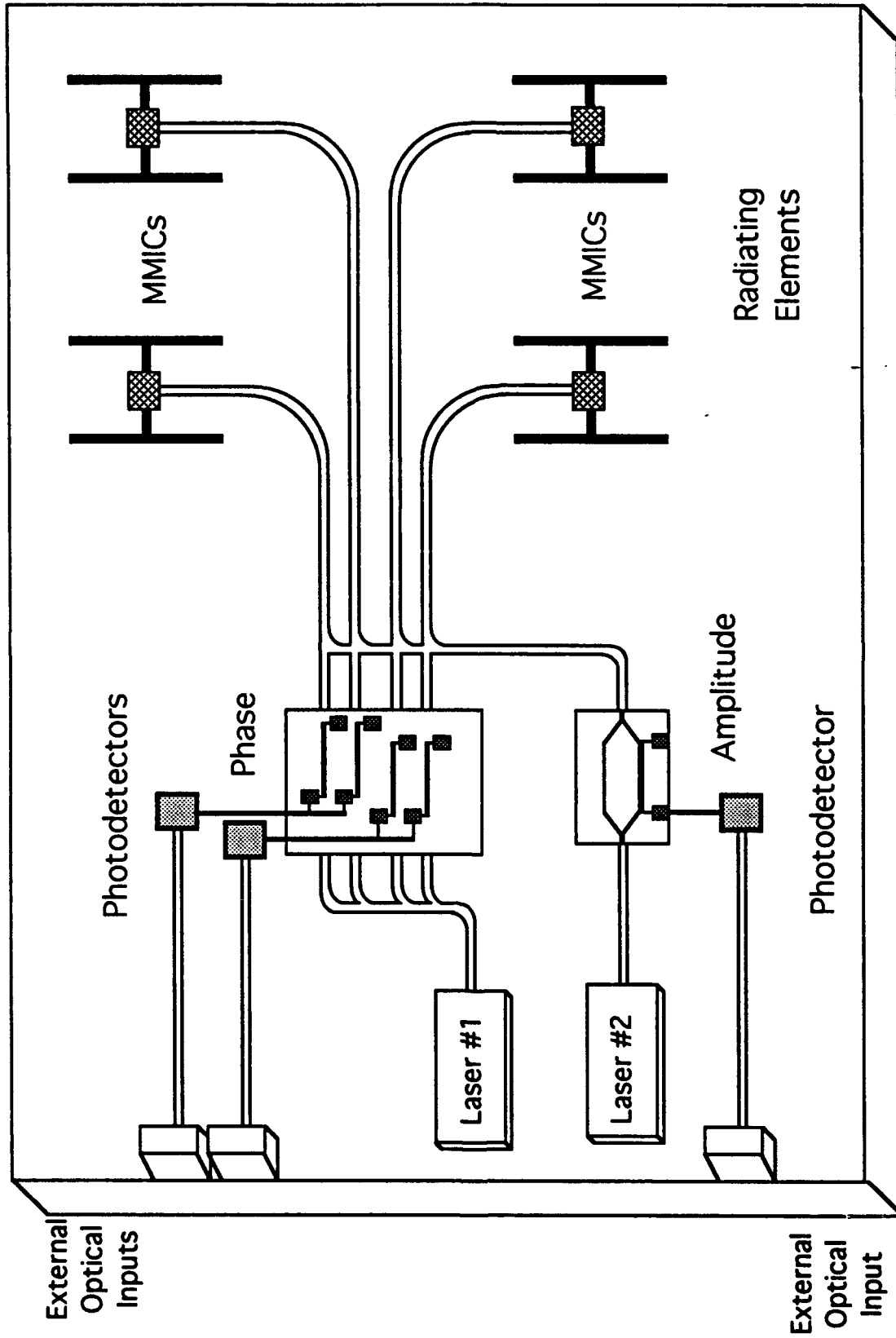


Fig. 7. Millimeter Wave Wafer Scale Integration for Phased Array Radars

Terahertz Bandwidth Graded Index Polymer

Madhavi Z. Martin, Floyd K. Oshita,

David Plant, and H.R. Fetterman

Department of Electrical Engineering, UCLA

Los Angeles, CA 90024

Ray. T. Chen and Daniel Robinson

Physical Optics Corporation

Torrance, CA

INTRODUCTION

Microwave signal communications are implemented in either analog or digital formats, which require interconnects with time and space multiplexibilities. This means that high speed performances, high fan-out, and reasonably large distances are desirable. The communication distance of a mm to a cm is provided by electrical interconnections, for a clock speed of 1 Gbit/sec [1]. Optical interconnects provide high speed interconnections from chip to chip, module to module, board to board, and machine to machine, beyond the capability of electrical interconnects. The minimum allowed pin spacing needed to avoid signal cross-coupling in typical chips is a major concern at the board level. This problem is solved by using an optical interconnect in which the minimum space between the interconnects is the size of a single-mode waveguide. The density of these single-mode waveguides can be increased without affecting the signal bandwidths. Furthermore, the optical channels can cross in space without any interaction between the channels.

Polymer gelatin thin film waveguides with step index profiles have previously been

prepared [2]. Also, the ability to change the index from a step to a graded-index profile with higher surface index has been demonstrated and discussed in detail elsewhere [2]. The lower index portion of the graded-index polymer film functions as a waveguide cladding layer and reduces the evanescent field overlap with the underlying substrate, thereby, providing tighter mode confinement closer to the polymer film surface.

The graded index polymer waveguide is an extremely low loss material (< 1 dB/cm) as compared to the step-index polymer waveguides (> 40 dB/cm) and have previously been fabricated on a variety of substrate materials such as ceramics, insulators, conductors, and also semiconductors with a transmission bandwidth of 2000 nm. These polymer waveguides have large index modulations (~ 0.2) and are insensitive to temperature changes exceeding 280°C . The above mentioned benefits of the graded-index polymer waveguide makes it an attractive candidate and a key element for use in high-density optoelectronic and optically interconnected systems. In this paper we would like to show the dispersion of a 1.2 ps optical pulse in a step-index and graded-index polymer waveguide. A 1000 GHz bandwidth for a graded-index polymer waveguide has been demonstrated for the very first time.

EXPERIMENTAL SETUP

The experimental setup used in our measurements is shown in Figure 1. This setup consists of an actively mode-locked frequency doubled Nd: YAG laser, used to pump a dual jet dye laser. The dye laser is equipped with a cavity dumper to change the repetition rate of the pulses. The dye laser is operated with a repetition rate of 7.6 MHz at a wavelength of 600 nm with average powers of 70 mW and a pulse FWHM of 1.2 ps which is measured by an autocorrelator. The laser beam is coupled into a polymer channel waveguide using a prism

coupler. The light travels a distance of 5 and 10 cm and is then coupled out using another prism. The output beam is then collected by a lens and focussed into a camera lens of focal length 5 cm. The camera lens aperture is used to collimate the beam up to a distance of 1 m. Three mirrors are used to divert the beam into two pinhole apertures which align the beam into an autocorrelator. This autocorrelator allows the real time monitoring of the picosecond pulse before and after it is coupled out of the waveguide. The autocorrelator electrical output is input into an oscilloscope. The computer controlled data acquisition system is used to collect data in the time domain and Fourier transformed to obtain its bandwidth in the frequency domain. The optical autocorrelation signal is recorded once by going through the waveguide and next by sending the picosecond beam directly into the autocorrelator. Hence, a comparison between the optical autocorrelation signals with and without the waveguide can be obtained. Measurements were done with two sets of polymer waveguides (step and graded-index) and at two different distances (5 and 10 cm). It is important to note that all the optical components such as lens, camera lens, and the number of mirrors were maintained to be same throughout the different sets of measurements. Also the direction of the beam entering the autocorrelator is kept constant to get a consistent comparison between all the measurements performed. The time domain autocorrelation curves for the two types of waveguides for equal distance is shown in Figure 2. More dispersion in the time domain transforms to lower bandwidths in the frequency domain which is shown in Figure 3.

It has been demonstrated that there is much less dispersion due to graded-index waveguide. A reduction in the overlap between guided-mode evanescent field and the underlying substrate, demonstrates a lower dispersion of the high frequency components in the graded-index polymer. The importance of this paper is as follows:

- (a) Much less dispersion due to graded-index polymer.
- (b) Compression molded polymer-based optical Bus can be fabricated and this is not limited by the lithographic tools.
- (c) We have demonstrated a bandwidth up to 1000 GHz.
- (d) Less dispersion is extremely important for optical control of microwave signals using integrated optical circuits.

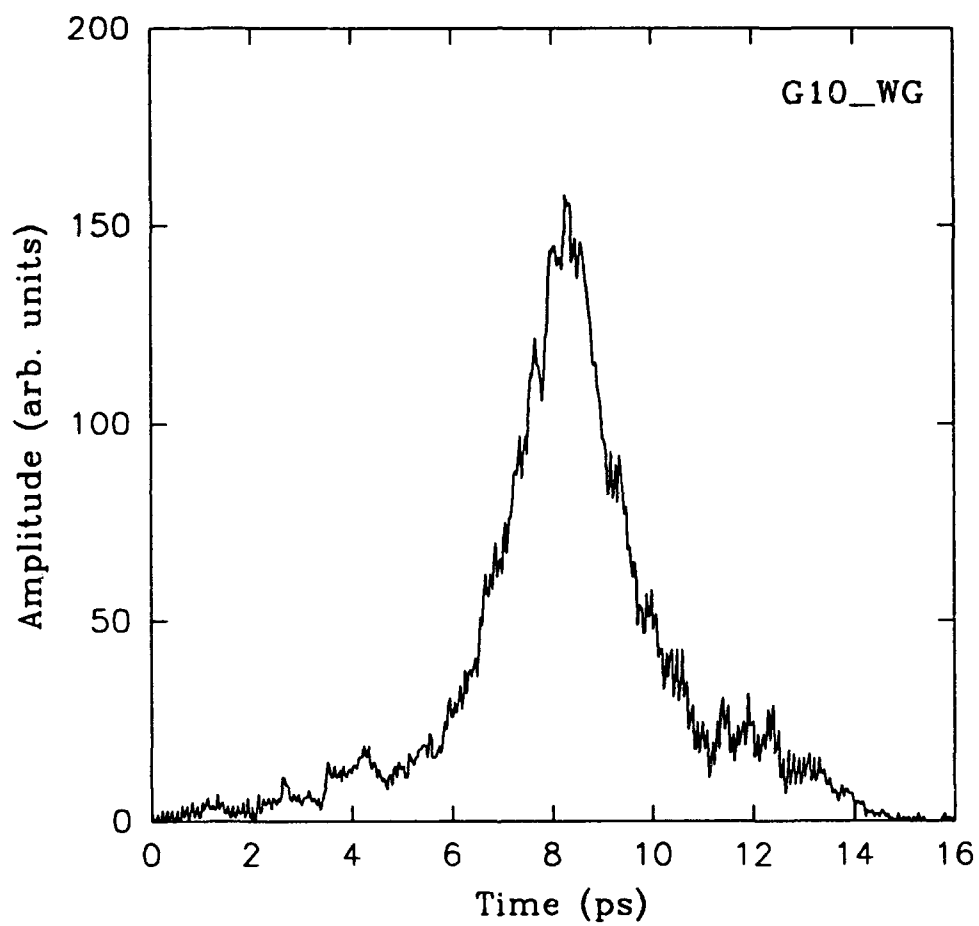
Further applications of these graded index polymers are:

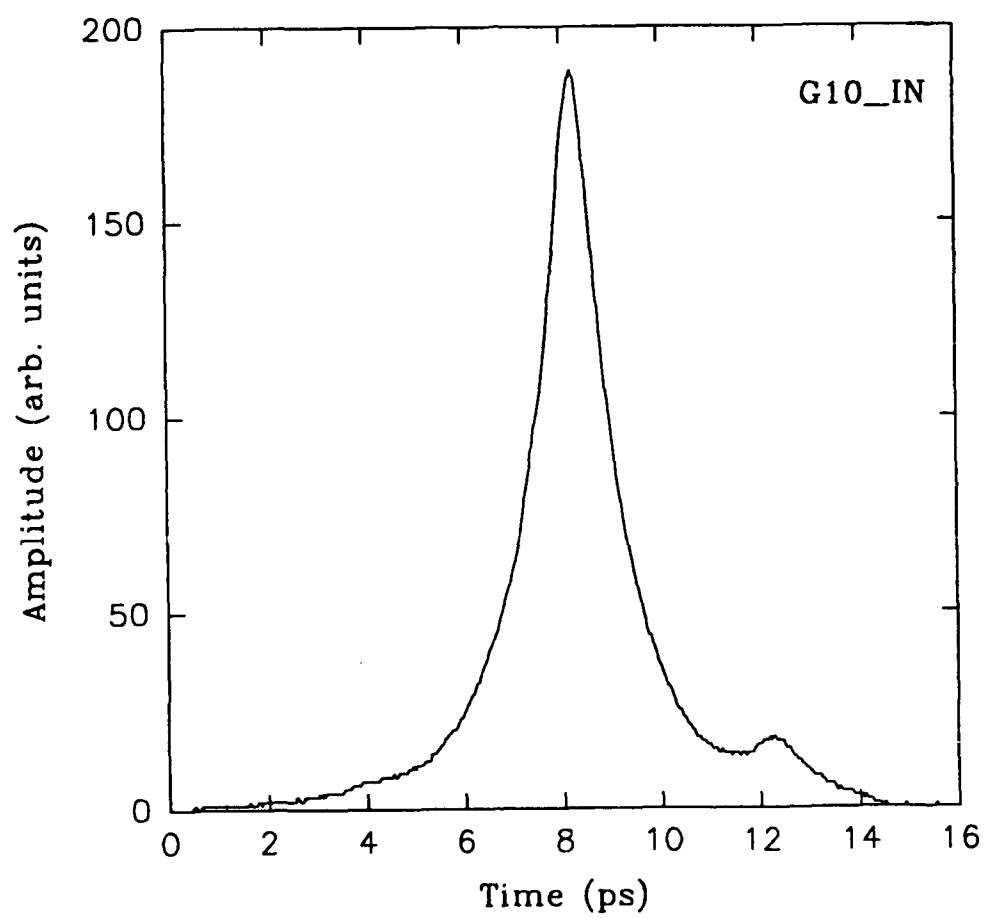
Low loss and very low dispersion of the optical signal fed to an electrical component is important to integrated graded index polymer waveguides with other optical components, such as coherent sources and photodetectors, to produce polymer-based optoelectronic systems that can simultaneously transmit, route, and receive optical signals such as phased array antennas.

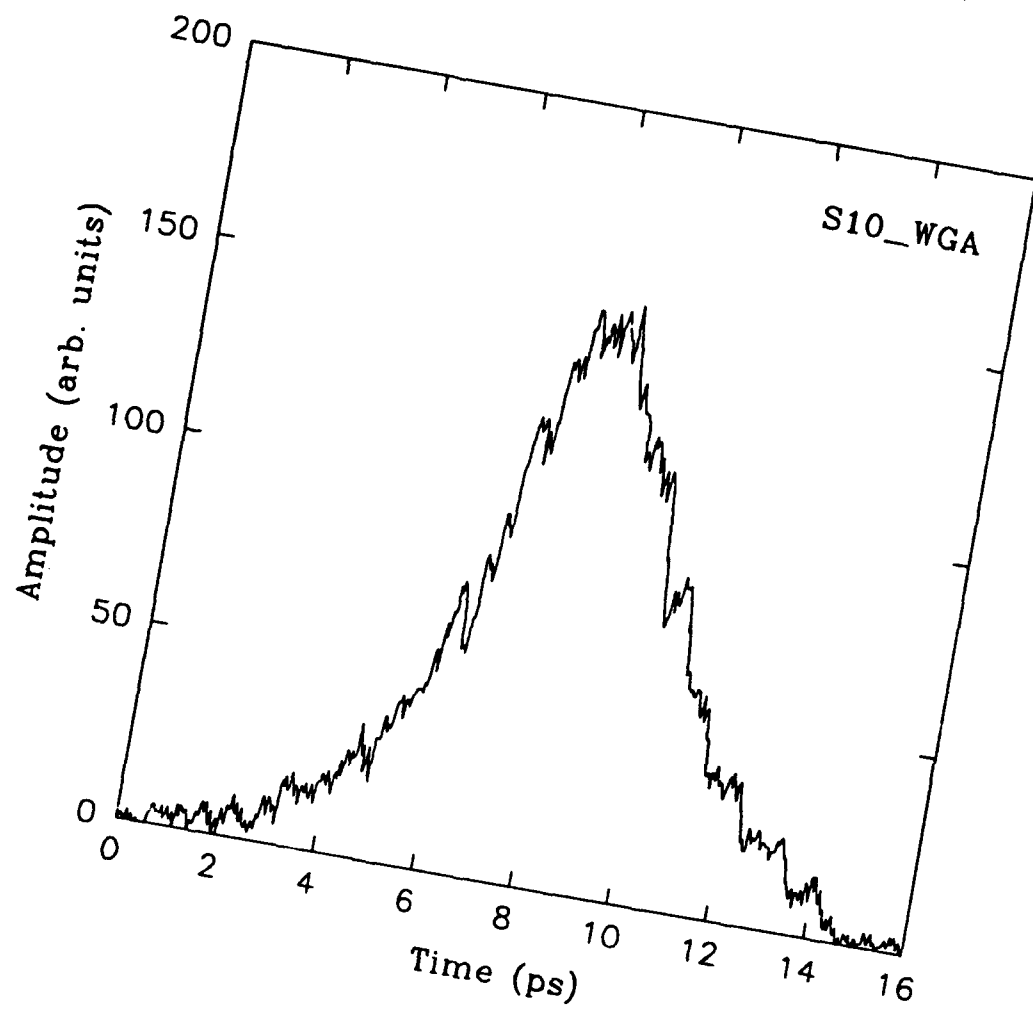
As was discussed earlier, the graded index polymer waveguide has an ability to be deposited on virtually any kind of substrate, hence backplane substrate that serves as the main interconnection hub between multiple IC boards which increases parallelism and enhancement in interconnect capabilities and would add several back planes to the same board.

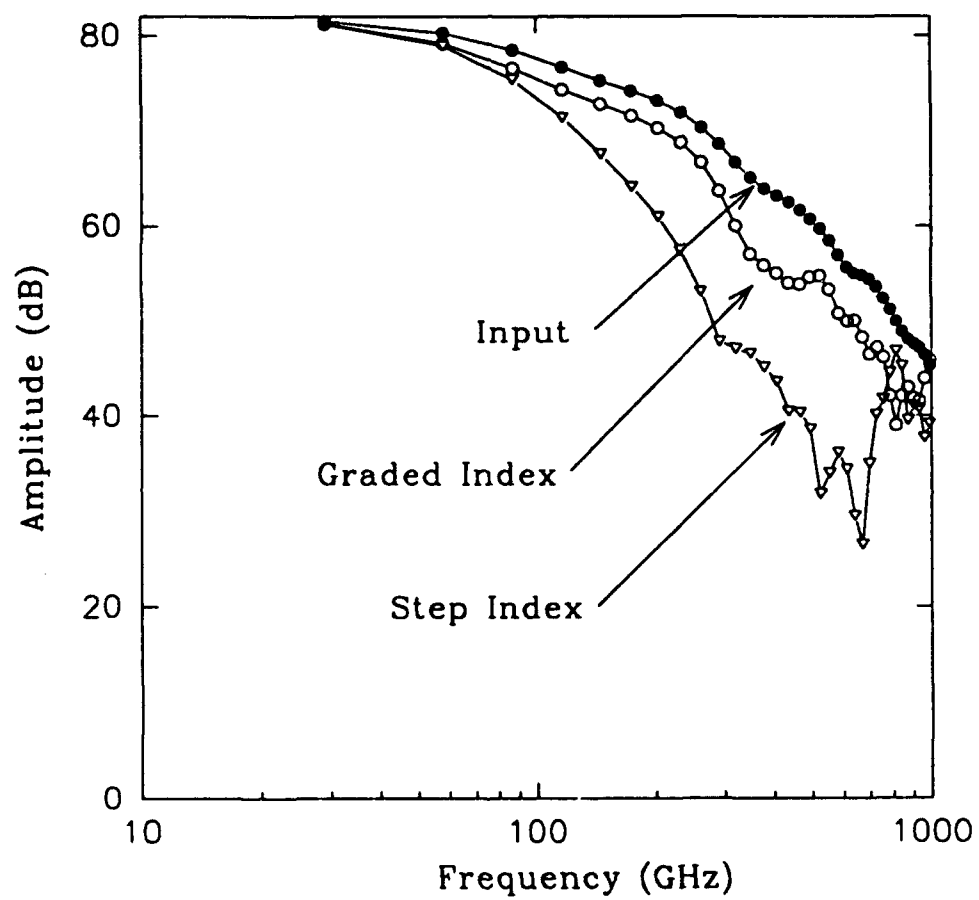
CONCLUSIONS

The graded index polymer is a suitable candidate for producing polymer-based optoelectronic systems which can transmit and receive optical signals e.g. phased array antennas. The fabrication of compression molded polymer-based optical Bus is not limited by lithographic tools. This polymer has demonstrated a bandwidth up to 1000 GHz. The low dispersion is extremely important for optical control of microwave signals using integrated optical circuits.









Growth and Characterization of MBE Grown Thin InSb on Si

H.C. Lu and H. R. Fetterman

Department of Electrical Engineering
University of California, Los Angeles, CA 90024

C.J. Chen

Department of Materials Science and Engineering
University of California, Los Angeles, CA 90024

C. Hsu and T. M. Chen

Taly High Vacuum Tech Inc.
Hsin-Chu, 30014, Taiwan, R.O.C.

Abstract

Thin($<1000 \text{ \AA}$) InSb single crystal film with $<111>$ orientation has been successfully grown by molecular beam epitaxy(MBE) on Si wafer with sandwich-type buffer, $\text{BaF}_2/\text{InSb}/\text{BaF}_2$, for use in semiconductor-on-insulator(SOI) high-speed devices. Both the inter-diffusion between adjacent layers and the atomic composition in each layer were examined by Auger electron spectroscopy. The InSb film on the sandwich-type buffer was characterized by X-ray and Hall mobility measurements. The X-ray diffraction patterns indicated the crystallinity and the strain of different structures. The mobility-temperature dependences were related not only to impurity and lattice scattering but also to dislocation scattering.

I. Introduction

In the recent progress of microelectronics, enormous effort has been devoted to the preparation of high-density and high-speed integrated circuits using a multi-layer structure. In this structure, an upper circuit layer can be prepared on an insulating layer which covers the underlaying circuits. Therefore, information pertaining to the hetero-epitaxial crystal growth of high-mobility SOI film is very important in microelectronics especially in 3-dimension(3-D) very large scale integrated(VLSI) circuits and infrared(IR) detector arrays. In order to provide high-speed capability for VLSI circuits, InSb was chosen as the active layer due to its highest electron mobility among existing semiconductor materials. Si wafer has been used as the substrate because of well established Si VLSI technology. As the dimension scales down to sub-half-micron, the interest on ultra-thin, fully-depleted SOI devices has been growing at a rapid rate recently because of their many unique features such as eliminating kink effect¹, reducing short channel effect², etc³.

In this paper we demonstrated a new approach to grow thin(1000 Å) InSb film by MBE on Si wafer with sandwich-type buffer, BaF₂/InSb/BaF₂. The interface properties were examined by Auger electron spectroscopy. The InSb film was characterized by X-ray and Hall mobility measurements. It turns out that thin InSb film with high electron mobility can be obtained by using the sandwich-type buffer .

II. Growth and Characterization of InSb/BaF₂ On Si

N-type(3-5 Ω -cm) 2" Si wafers with $\langle 111 \rangle$ were used in the experiment. Same results were obtained by using $\langle 100 \rangle$ Si wafers because of BaF₂ strong $\langle 111 \rangle$ preferential growth. The MBE growth process which produced epitaxial InSb/BaF₂ on Si was designed in a home-made MBE system. First of all, Si flux cleaning⁴ at 750 °C for 30 minutes was applied to remove native SiO₂. BaF₂ was deposited on Si at the growth rate of 0.3 Å/s and the substrate temperature of 600 °C after Si flux cleaning. InSb was grown on the BaF₂ when the substrate temperature was cooled down to 350 °C. The flux ratio of Sb/In was 2 and the growth rate was 1.75 Å/s. Finally, BaF₂ and InSb were grown respectively at the same growth conditions as above.

In MBE InSb growth, there are three outcomes of the co-evaporation of In flux and Sb flux: (In+ δ)Sb, InSb and In(Sb+ δ). The critical growth parameter is the flux ratio of Sb/In. Theoretically, the flux ratio of Sb/In is equal to 1. Unfortunately, Sb will re-evaporate out of the heated sample. The re-evaporation rate depends on the temperature of the sample holder, vacuum pressure and the source flux of Sb. Normally, the flux ratio of Sb/In is in the range of 1.5-2.0. In MBE InSb growth on Si with single-layer BaF₂ buffer, four domains will frequently be found: Si-strained BaF₂, InSb-strained BaF₂, BaF₂-strained InSb and relaxed InSb. In order to obtain a good-quality InSb film with single-layer BaF₂ buffer, the InSb film is required to be thick($\sim \mu\text{m}$) enough to dissolve defects

itself. However, in order to fabricate the fully depleted devices, the thickness of the active layer requires to be less than 1000 Å. An effective dislocation-blocking method should be introduced to obtain a suitable thin InSb film on Si. One of the most efficient ways is to use the interfacial misfit strain to eliminate or cancel it in the interfaces of epitaxial thin films. The mechanism can be explained thermodynamically by total system energy difference between a strained and a non-strained layer⁵. In a large lattice-mismatch(>15%) system, the energy difference for a non-strained layer and a strained layer in the strain energy, ΔE_{ϵ} , is a result of the strain-energy relaxation due to the creation of a misfit segment L, which is given by

$$\Delta E_{\epsilon} \sim -L\epsilon \quad (1)$$

where L is the length of misfit dislocation and ϵ is the misfit elastic strain. The negative sign indicates a reduction in the system energy. The total difference in the energy ΔE that accompanies the movement of a dislocation line L along the strained interface is the sum of the change in the strain energy ΔE_{ϵ} , the dislocation self-energy ΔE_D and the dislocation interaction energy ΔE_I . In a large lattice-mismatch system, the strain energy difference is dominated:

$$\Delta E = \Delta E_{\epsilon} + \Delta E_D + \Delta E_I \approx \Delta E_{\epsilon} \quad (2)$$

In the lattice-match system the misfit strain ϵ is almost zero and so is the $L\epsilon$ product. Unlike the strain in a lattice match-system, ϵ in the interface of InSb and BaF₂ is large(>15%) but L is small. The optimum of $L\epsilon$ product gives the largest reduction of dislocations, which may occur in the case of equal-thickness alternative layers. If each of the alternative layers has the same thickness, the probability for a dislocation to obtain expansive and compressive strain will be equal. Furthermore from rotational angle point of view, BaF₂ (<111> orientation) has type-B structure with respect to InSb (<111> orientation) in the multiple layer growth, which means InSb lattice orientation is 180° with respect to BaF₂. When a dislocation propagates from substrate through the equal-thickness alternative layers to the top layer, the overall probability for a dislocation to be twisted clockwise(CW) or counter-clockwise(CCW) is equal. Therefore, from either strain or orientation point of view, dislocations will see equal probability to propagate through the whole equal-thickness alternative layers. The dislocations in the alternative layers have 50% to be cancelled each other because of equal chances to be compressed/expanded and twisted CW/CCW. In other words, a dislocation will repeatedly obtain the same amount of expansive/compressive and CW/CCW shear strain as it propagates toward the top surface. Physically speaking, as a dislocation enters into a compressive lattice from a expansive lattice, the direction of the force applied on dislocations will be immediately changed from being pulled to being pushed at the interface. Likewise, for CW/CCW

shear strain will give the maximum breaking force to a dislocation at the interface. These maximum breaking forces at the interfaces will give high probability to eliminate the dislocation as it passes through the interfaces. A sandwich-type buffer structure, $\text{BaF}_2/\text{InSb}/\text{BaF}_2$, was designed for fully depleted InSb devices on Si as shown in Fig.1. The more interfaces the buffer has, the more will be the reduction of dislocations. However there is a tradeoff between adhesion and dislocation. Adhesion quality depends on the atomic bonding and the thermal expansion coefficient between two materials. Growth conditions have also to be changed for different numbers of layers. Growth rate range of 0.75-1.75 Å/S at substrate temperature of 300-350 °C was of good crystallinity and adhesion for ultra-thin InSb film MBE growth with sandwich-type buffer.

To examine the inter-diffusion at the boundaries of adjacent layers and the atomic composition in each layer, Auger depth profile was suggested to measure as shown in Fig.2. The top surface of the multiple layers was passivated by an extra BaF_2 layer at the end of MBE growth to prevent contamination from the ambient atmosphere. In InSb layers, the ratio of In/Sb was about 1, indicating good In/Sb flux control. BaF_2 occupied 10% in the InSb layer, which resulted in the decrease of the mobility of InSb film. The BaF_2 between InSb and Si substrate provided a good electrical insulation(>5 V breakdown) for SOI structure. The substrate temperature during BaF_2 growth on Si was 600 °C, preventing In and Sb from incorporating into BaF_2 layer. The percentage of BaF_2 between InSb layers was low (about 35%) because the substrate temperature during BaF_2 growth must be

low(350 °C) to avoid the existing bottom InSb film from evaporating out. In the passivation BaF₂ growth, the heating power and shutters of both In and Sb effusion cells were shut off, which enhanced BaF₂ incorporation rate. The loss of F atoms near the passivation top surface may be due to the reaction with the ambient species such as oxygen, moisture, etc.

Several ways were employed to characterize InSb/BaF₂ film on Si. First of all, X-ray diffraction is the simplest way to determine crystallinity. The X-ray diffraction pattern of poly crystal BaF₂ on Si was illustrated in Fig.3 where the strain between Si and BaF₂ can be seen on the right edge of the BaF₂ peak. In Fig.4, the X-ray diffraction pattern of 500 Å InSb was shown with the growth condition of flux ratio Sb/In=1.5 at 300 °C substrate temperature. The thickness of single-layer BaF₂ was the same as InSb. Four domains of poly crystal InSb and BaF₂ were found in Fig.4: Si-strained BaF₂, InSb-strained BaF₂, BaF₂-strained InSb and relaxed InSb. To obtain a good quality InSb film with single-layer BaF₂ buffer, a thicker BaF₂ and InSb film were required to dissolve defects itself. Fig.5 illustrates the X-ray diffraction pattern of a single crystal InSb/BaF₂ film on Si. The thickness of InSb was about 3 μm and that of BaF₂ buffer layer was 2000 Å. However, the thick InSb on a single-layer BaF₂ cannot be used in the thin SOI devices. Finally, a sandwich-type buffer structure, BaF₂/ InSb/ BaF₂, was found to be a good buffer for fully depleted InSb devices on Si. A 500Å InSb layer has been grown on Si with the sandwich-type buffer(500Å for each layer). The X-ray diffraction pattern was

shown in Fig.6. The bottom BaF₂ and InSb films might be still polycrystal. The top InSb was single crystal, which was further justified by Hall measurement and Fourier Transform Infrared(FTIR) spectroscopy. The electrical properties and optical response of top InSb film were close to bulk wafer quality, which may be ready for devices fabrication.

In addition to crystallinity and adhesion, mobility is one of the most important parameters for high-speed devices. In order to compare mobility-temperature dependences, four samples were prepared as follows:

#1-InSb(500Å)/BaF₂(500Å)/InSb(500Å)/BaF₂(500Å) on Si.

#2-InSb(3 μm)/BaF₂(500Å)/InSb(500Å)/BaF₂(500Å) on Si.

#3-InSb(3 μm)/BaF₂(2000Å) on Si.

#4-Bulk InSb(600 μm)

Hall mobilities were measured between room temperature(300 °K) and liquid nitrogen temperature(77 °K). The average results were illustrated in Fig.7. To be quantitative, the reciprocal mobility was given by⁶

$$1/\mu = \alpha_i T^{1.5} + \alpha_j T^{-1.5} + \alpha_d T^{-1} \quad (3)$$

where the α 's are temperature independent parameters and the subscripts l, i, d denote the contributions to the scattering from the lattices, the impurities and the dislocations. By fitting our data to Eq.3, the α 's parameters from sample#1 to sample#4 were obtained as follows:

	α_l	α_i	α_d
Sample#			
1	1.16×10^{-8}	1.15×10^{-2}	2.67×10^{-3}
2	6.52×10^{-9}	6.44×10^{-3}	3.11×10^{-3}
3	6.99×10^{-9}	6.90×10^{-3}	3.70×10^{-3}
4	2.33×10^{-9}	2.30×10^{-3}	-

Table I. Scattering coefficients α 's for four samples.

Except for the bulk(sample#4), the dislocation scattering in the sample#1 was the smallest but the impurity and lattice scattering were the largest. The small dislocation scattering justified our idea that sandwich-type buffer reduced a lot of dislocations. The large

impurity and lattice scattering of the thin InSb film might be resulted from the limited thickness effect. Furthermore, inter-diffusion from BaF₂ into InSb(~10%) as shown in Fig.2 may cause extra impurity scattering too. In sample #1, the mobility dependence of temperature, increasing as temperature decreasing, was close to the behavior of bulk material. In samples #2 and #3, the mobilities decreased as temperature decreased due to the scattering from dislocations, thermal strains and phase changes in the grown film.

CONCLUSIONS

In conclusion, MBE grown single crystalline thin InSb/BaF₂ film on Si was demonstrated. InSb was chosen as the active layer due to its highest electron mobility among current semiconductor materials. Si wafer has been used as the substrate because of its being extensively used in the existing VLSI industry. In our new structure, high-speed fully depleted InSb devices may be stacked on top of the VLSI Si circuits to increase packing density. Sandwich-type structure, BaF₂/InSb/BaF₂, was found to be a good buffer between InSb and Si. The inter-diffusion between layers and the atomic composition in each layer were examined by using Auger electron spectroscopy. The top InSb film was characterized by X-ray and Hall mobility measurements. The mobility-temperature dependences were related not only to impurity and lattice scattering but also to dislocation scattering.

ACKNOWLEDGEMENT

This work was supported in part of Air Force Office of Scientific Research under the direction of H.R. Schlossberg.

REFERENCES

- 1 J. P. Colinge, *IEEE Electron Device Lett.*, **9**, 97, (1988).
- 2 K. K. Young, *IEEE Trans. Electron Devices*, **36**, 399, (1989).
- 3 J. P. Colinge, *SOI Technology: Materials to VLSI*, Kluwer Academic, (1991).
- 4 T.L. Lin, *A New Silicon MBE SOI Technology*, Ph.D Dissertation, UCLA, Los Angeles (1988).
- 5 N.A. El-Masry, J.C.L. Tarn and S. Hussien, *Appl.Phys.Lett.*, **55**, 2096 (1989).
- 6 D. L. Dexter and F. Seitz, *Phys. Rev.*, vol.**86**, 964 (1952).

FIGURE CAPTIONS

Fig.1. The elimination of dislocations by multi-layer hetero-interfaces.

Fig.2 Auger depth profile of BaF_2 /InSb/ BaF_2 /InSb/ BaF_2 on Si. The sputter rate was about 200 Å/min.

Fig.3. X-ray diffraction pattern for MBE grown BaF_2 on Si.

Fig.4. X-ray diffraction pattern for MBE grown InSb/ BaF_2 on Si. Four domains can be seen as

(i) Si strained BaF_2 : $\text{BaF}_2(\text{Si})$

(ii) InSb strained BaF_2 : $\text{BaF}_2(\text{InSb})$

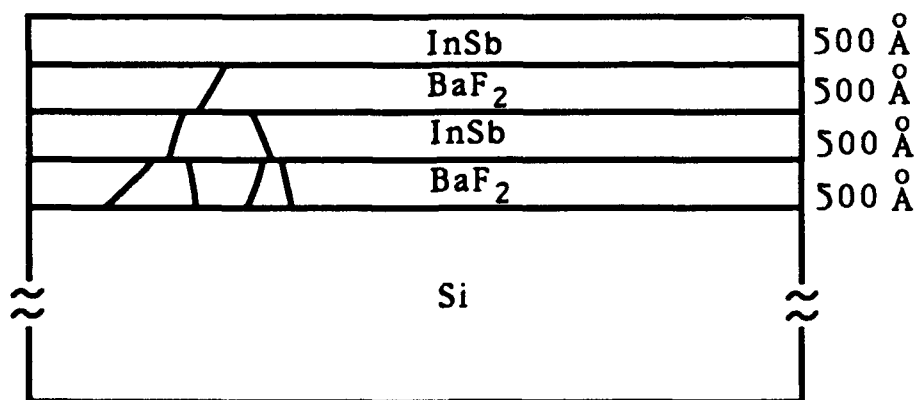
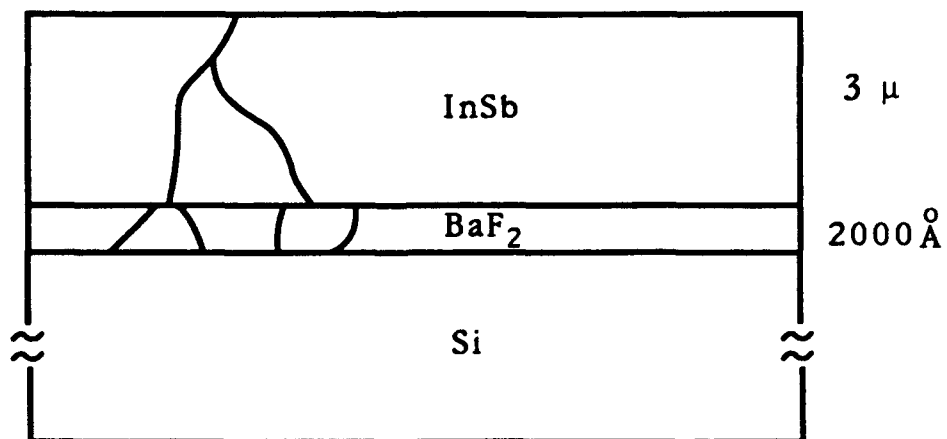
(iii) BaF_2 strained InSb: $\text{InSb}(\text{BaF}_2)$

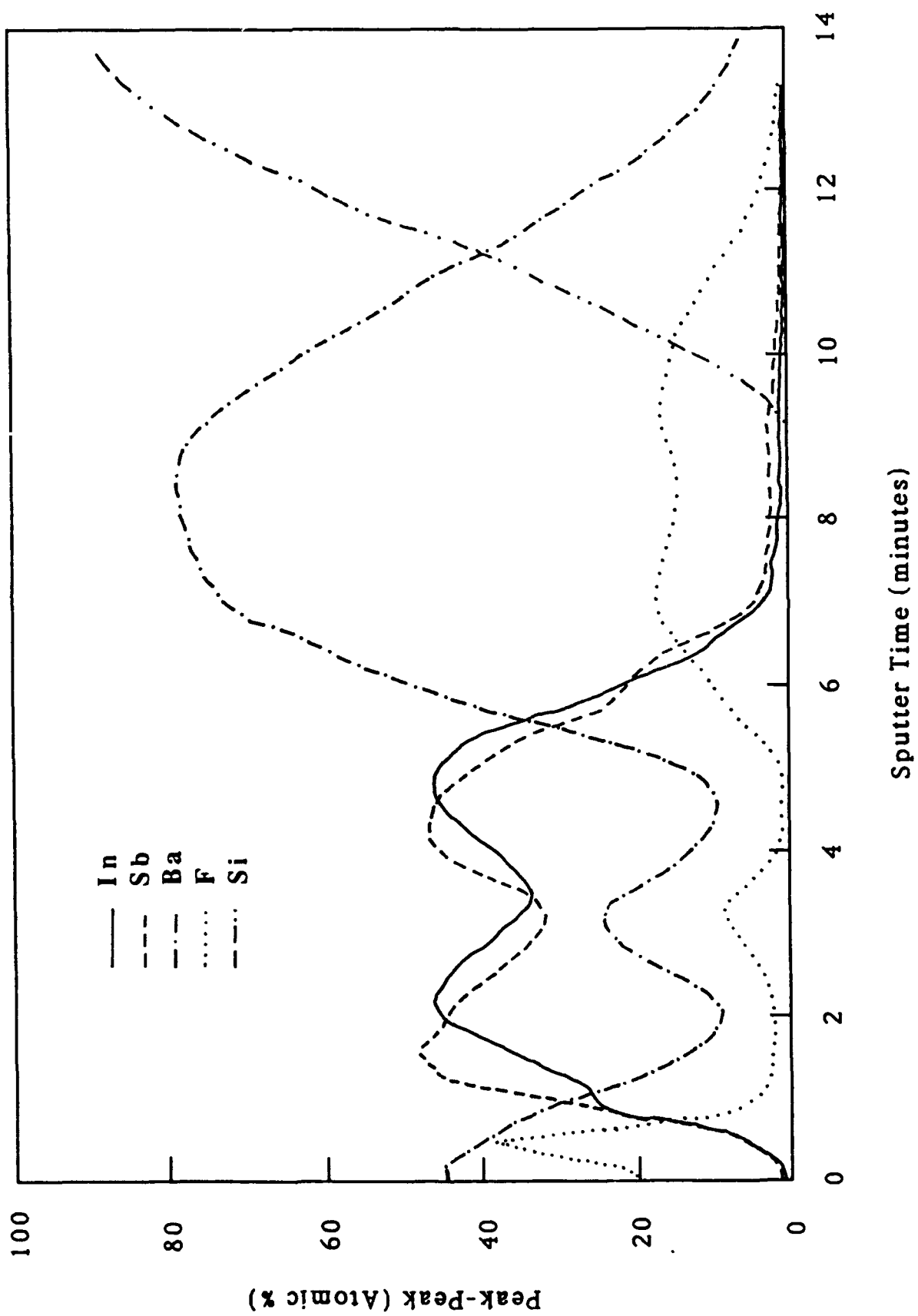
(iv) relaxed InSb.

Fig.5. X-ray diffraction pattern for single crystalline InSb/ BaF_2 on Si.

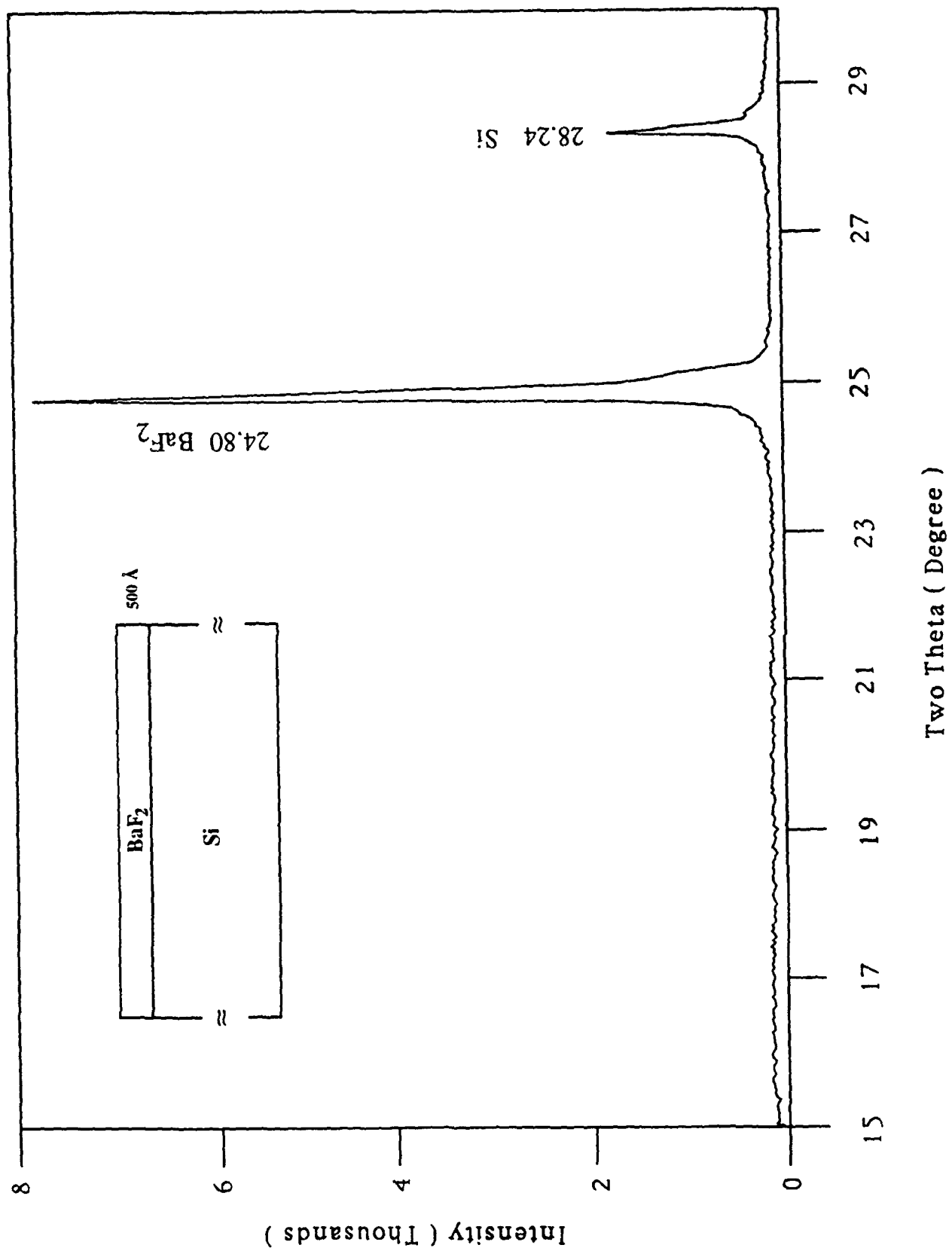
Fig.6. X-ray diffraction pattern for thin InSb/ BaF_2 /InSb/ BaF_2 on Si.

Fig.7. Mobility vs. operation temperature for different samples.

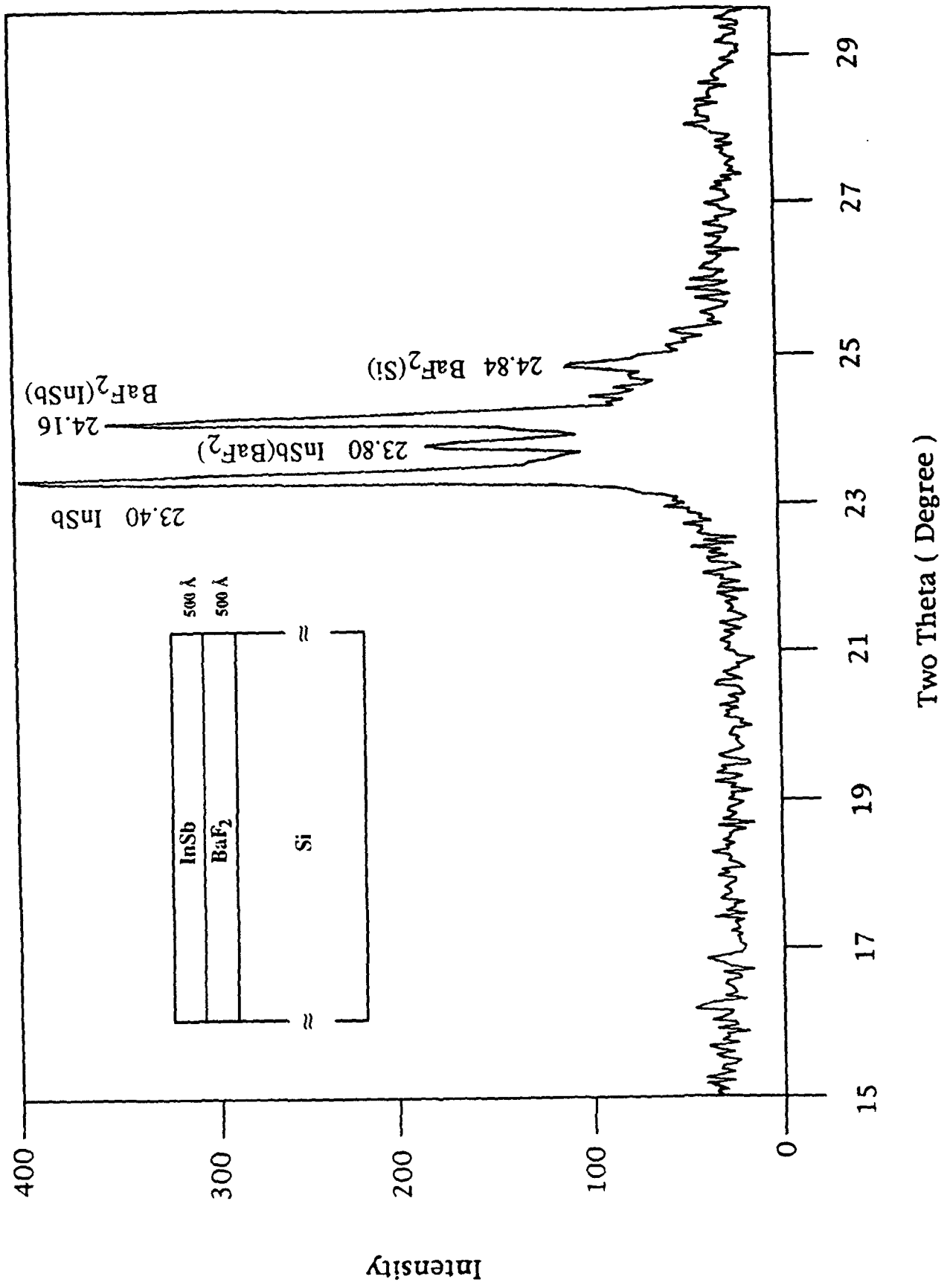


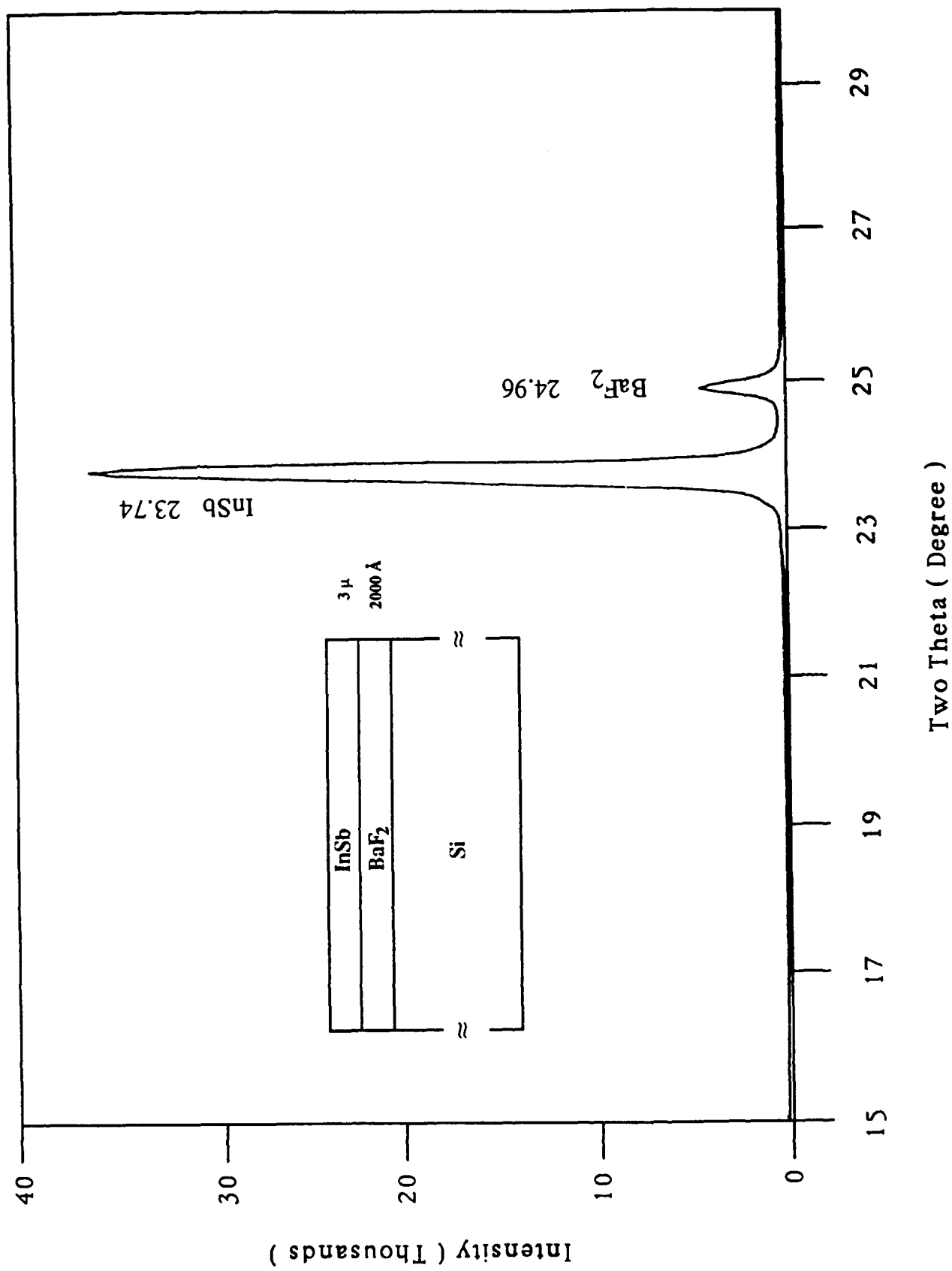


2.2

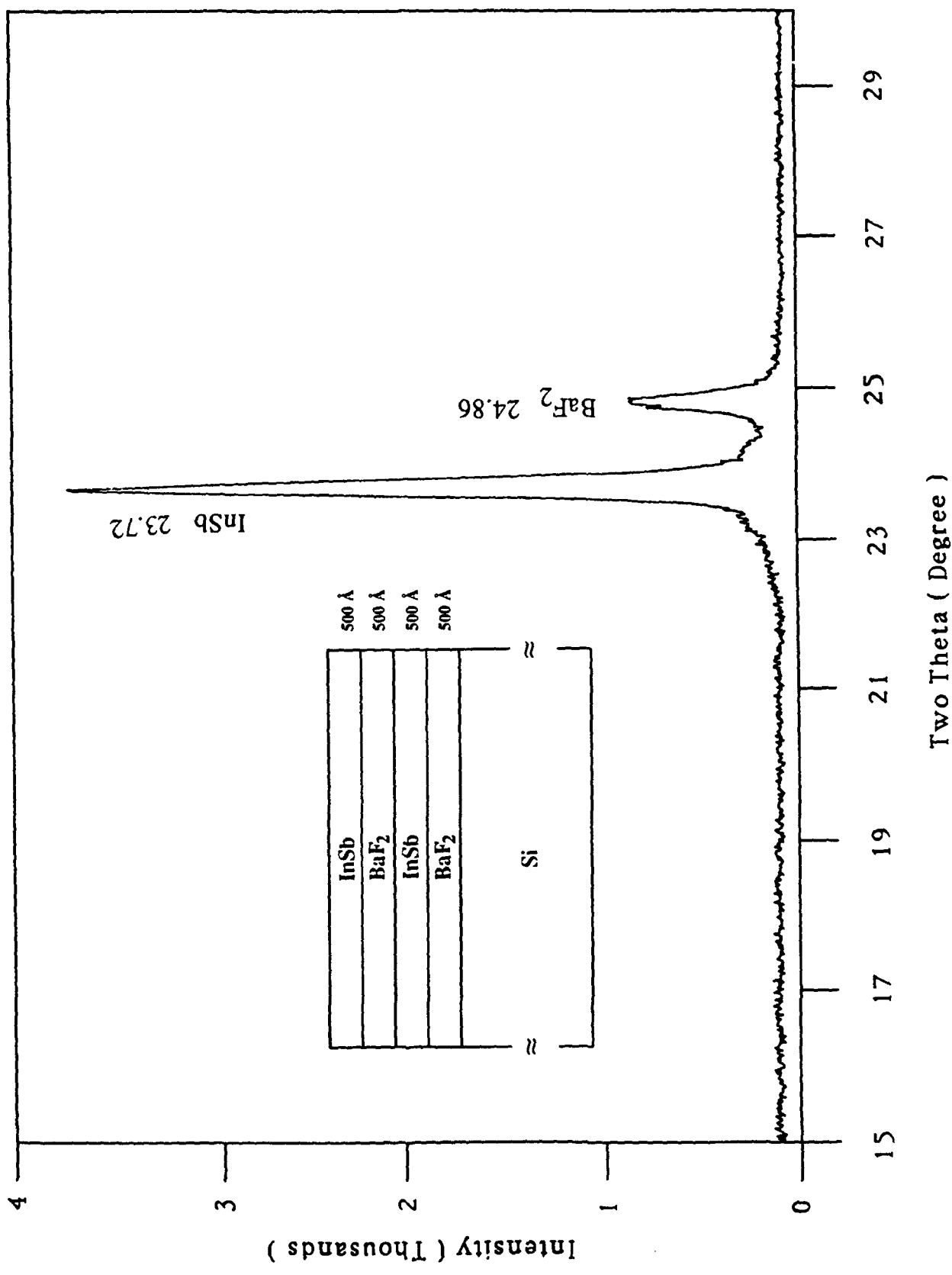


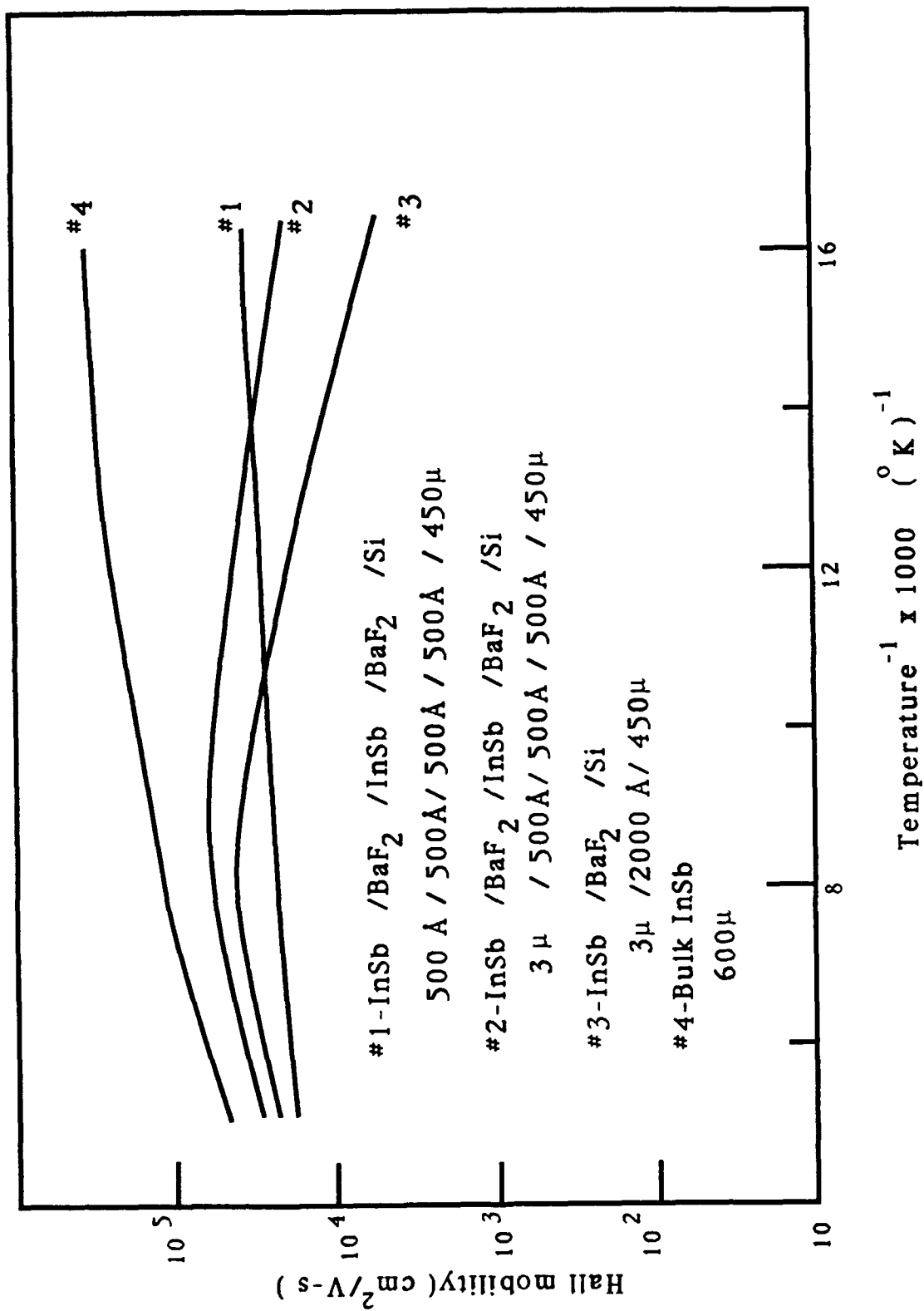
F 4





6





Nonlinear Microwave Optics in Liquid Suspensions of Shaped Microparticles

D. Rogovin, R. McGraw, W. Ho, R. Shih, H. R. Fetterman, and Bradley Bobbs

Abstract—The unique properties of shaped microparticle suspensions make them suitable as candidate media for such active optical process as phase conjugate via degenerate four-wave mixing at microwave and millimeter wavelengths. We have generated up to 250 mW of phase conjugate radiation, a medium composed of rod shaped carbon fibers suspended in a passive fluid dielectric that is maintained in a waveguide. The theory for the nonlinear optical properties of shaped particle suspensions is presented and shown to be in excellent agreement with the available experimental data.

I. INTRODUCTION

UNTIL recently, attempts to achieve active phase control using nonlinear optical schemes have been limited to the visible and the infrared regions of the spectrum, employing laser beams as the driving fields [1]. Typical optical processes that are utilized include nonlinear phase shifting [2], optical phase conjugation [3], two beam coupling [4] and optical birefringence [5]. Efforts to extend these processes down to millimeter or microwave frequencies have, until recently [6]–[9], failed due to a lack of suitable nonlinear optical materials.

This lack of success in achieving nonlinear optical effects at microwave and millimeter wavelengths can be appreciated by considering the challenges one must overcome to achieve optical phase conjugation at these comparatively long wavelengths. In particular, contrast the four-wave mixing coefficient $\kappa = 16\pi^2\chi^{(3)}I_p/c\lambda$ at visible and microwave frequencies. Here I_p is the pump power, λ is the free space wavelength and $\chi^{(3)}$ is the third-order nonlinear susceptibility. At visible and infrared wavelengths, pump sources can readily achieve power levels of tens to hundreds of MW/cm². At cm wavelengths, standard laboratory power supplies are usually limited to under one kW/cm² as the beam cannot be focused down to spot sizes smaller than an optical wavelength due to diffraction effects. This five orders of magnitude reduction in pump power is further compounded by an additional four orders of magnitude decrease in κ , caused by the increase in λ that one encounters in going from the visible to the microwave region of the electro-

magnetic spectrum. Thus, κ scales as λ^{-3} . These considerations are summarized in Table I which reveals that active media with nonlinear susceptibilities on the order of 10^{-3} to 10^{-4} esu are required if one is to achieve optical phase conjugation at 18 GHz.

Artificial dielectrics, such as liquid suspensions of microparticles, are known to have exceptionally large nonlinear optical susceptibilities and might be suitable candidates as active media for microwave applications. Ashkin and Smith achieved self-focusing [10], optical bistability [11] and optical phase conjugation [12] with an aqueous suspension of 1000 Å polystyrene microspheres as the nonlinear medium and cw Argon-ion laser beams as the optical source. Third-order optical susceptibilities were found to be as large as 10^{-8} esu, five orders of magnitude greater than CS₂. Since the third-order susceptibility scales as the sixth power of the microparticle radius, it seems reasonable to consider scaling the particle size up to microns to realize nonlinear susceptibilities on the order of 10^{-2} esu, for microwave applications.

Unfortunately, this scheme is not viable since the mechanism responsible for the nonlinear optical properties for this class of media is too slow for the observation of any nonlinear effects at these wavelengths. More precisely, forces due to an electrostrictive interaction between the microparticle polarizability and the incident probe and pump beams give rise to microparticle density gratings which coherently scatter pump radiation to form a phase conjugate wave. The formation of these index gratings, essential for optical phase conjugation, requires that the microparticles translate a grating spacing, typically several optical wavelengths. At visible wavelengths, grating formation requires that the particles diffuse several microns through a viscous medium. If the host fluid is water, this requires several hundred milliseconds. Since the particle motion is essentially Brownian in nature, the response time scales inversely with the square of the grating spacing and directly with fluid viscosity. Scaling to millimeter or centimeter wavelengths increases the medium response time by six to eight orders of magnitude. This implies grating formation times that are on the order of days, not seconds which are not feasible as thermal currents will suppress the formation of these optical index gratings. Another complication arises from the fact that water is a strong absorber of microwave and millimeter wave radiation, so that a nonabsorbing host must be found. This requires a nonpolar fluid and care must be exercised to avoid coagulation of the microparticles.

Manuscript received July 22, 1991; revised February 25, 1992.

D. Rogovin, R. McGraw and W. Ho are with Rockwell Science Center, Thousand Oaks, CA 91360.

R. Shih and H. R. Fetterman are with the Department of Electrical Engineering, University of California, Los Angeles, Los Angeles, CA 90024.

B. Bobbs is with Rockwell International, Rocketdyne Division, Canoga Park, CA 91303.

IEEE Log Number 9201717.

TABLE I
DIFFICULTIES AT LONG WAVELENGTHS

Physical Parameter	Visible Wavelengths	Microwave/Millimeter Wavelengths
Wavelength	0.5 μ	1 cm-0.1 cm
Pump Intensity	10^8 W/cm ²	10^3 W/cm ²
Typical values of $\chi^{(1)}$	10^{-10} esu	10^{-10} esu
Optical Pathlength	2 mm	30 cm
κL	1.2	10^{-9}
Efficiency	gain	negligible

Another class of artificial dielectrics that can be potential active media at microwave and millimeter wavelengths are shaped microparticle suspensions [13]. This class of nonlinear materials have third-order optical susceptibilities that also scale as the square of the microparticle volume. Therefore they should have a sufficiently large nonlinear susceptibility to overcome the scaling characteristics of κ with radiation wavelength. In addition to the usual translational gratings (that are useless for our purposes), shaped particle suspensions also form orientational index gratings. These index gratings consist of periodic spatial arrangements in which the particles within a given region tend to be randomly oriented and regions in which some fraction of them are oriented in a direction specified by the polarization vector of the incident radiation. A major advantage of this class of index grating is that their formation requires only that the microparticles rotate into desired orientations; they do not have to trans-

$3 \mu\text{m} \times 3 \mu\text{m} \times 8 \mu\text{m}$, act as perfect conductors at 18 GHz. The host fluid is highly transparent to microwave radiation and at 18 GHz the suspension's absorption constant is 140 cm^{-1} . The small size of the particles relative to the radiation wavelength ensures that scattering loss's are negligible. The suspension is maintained in a metal waveguide, with dimensions of $1.46 \text{ cm} \times 1.46 \text{ cm} \times 72 \text{ cm}$. The waveguide acts to enhance the microwave intensity and also reduces thermal eddy currents thus allowing the formation of microparticle orientational index gratings.

This paper is divided into four parts of which this, the Introduction, is the first. Section II outlines the theoretical model used to describe the interaction of shaped microparticles with coherent radiation. In Section III, we present our findings regarding microwave phase conjugation in liquid suspensions of shaped microparticles. Finally, in Section IV we summarize our studies and present our conclusions regarding nonlinear optics at these long wavelengths.

II. PHYSICS OF SHAPED MICROPARTICLE SUSPENSIONS

We assume a monodisperse suspension of shaped microparticles whose polarizability tensor $\alpha(\theta, \phi)$ is

$$\alpha(\theta, \phi) = \alpha_s I + \frac{1}{3} \beta K(\theta, \phi). \quad (2.1)$$

Here (θ, ϕ) specifies the orientation of the microparticle polarizability relative to a lab fixed reference frame, α_s is the isotropic component of the polarizability, β is the anisotropic component, I is the unit tensor and $K(\theta, \phi)$ is the orientation tensor whose components are

$$K(\theta, \phi) = \begin{pmatrix} 3 \sin^2 \theta \cos^2 \phi - 1 & 3 \sin^2 \theta \sin \phi \cos \phi & 3 \sin \theta \cos \theta \sin \phi \\ 3 \sin^2 \theta \sin \phi \cos \phi & 3 \sin^2 \theta \sin^2 \phi - 1 & 3 \sin \theta \cos \theta \cos \phi \\ 3 \sin \theta \cos \theta \sin \phi & 3 \sin \theta \cos \theta \cos \phi & 3 \cos^2 \theta - 1 \end{pmatrix} \quad (2.2)$$

late. Thus, the response time is independent of grating spacing and therefore of wavelength. The grating formation time is on the order of the angle through which the particles rotate ($\Delta \theta$), divided by the angular velocity, (Ω) . Thus, the time scale involves the particle size ρ instead of the grating spacing Λ and the ratio of the orientational to the translational response times (τ_0/τ_T) is $(\rho/\Lambda)^2$. For 10μ size particles, the orientational response time is seconds for typical nonpolar fluids. Although this is too long for some applications, it is sufficiently short that laboratory experiments can be conducted on a convenient time-scale and the effects can be readily observed.

We have successfully carried out microwave phase conjugation [8] in shaped microparticle suspensions consisting of 0.01%-0.1% volume fractions of carbon fibers suspended in a 60% mineral oil-40% heptane host fluid mixture. Power levels of up to 250 mW, with only 14.65 W of pump power were generated at 18 GHz. The measured host fluid viscosity is 5 cp and the microparticle response time is on the order of ten seconds. The carbon fibers, which are ellipsoidal in shape with dimensions of

If the microparticles are illuminated by an electromagnetic field [denoted by $E(r, t)$], they each acquires an induced dipole moment $p(\theta, \phi; r, t) = [\alpha_s I + (1/3)\beta K(\theta, \phi)] \cdot E(r, t)$. This induced dipole moment couples back to the electromagnetic field giving rise to an interaction potential $U(\theta, \phi; r, t)$, equal to

$$U(\theta, \phi; r, t) = -\frac{1}{2} \overline{p(\theta, \phi; r, t) \cdot E(r, t)}. \quad (2.3)$$

The overbars imply a time average that is long compared to the optical period, but short compared to the medium response time. The interaction potential gives rise to an electrostrictive force $F(r, t) = -\nabla U(\theta, \phi; r, t)$ that tends to move the particles towards regions where $U(\theta, \phi; r, t)$ is a minimum. This force favors particular particle orientations and weakly couples the center-of-mass and orientational coordinates. $U(\theta, \phi; r, t)$ also generates a torque $\Gamma(\theta, \phi; r, t) = -L U(\theta, \phi; r, t)$ where L is the particle angular momentum operator. This field-induced torque tends to rotate the particles in a direction specified by the vector polarization of the radiation field. When the suspension is irradiated by a plane polarized beam, the particles tend to point in a given direction and the propaga-

tion features of incident radiation will depend upon beam polarization, giving rise to optical birefringence [6], [7]. If the suspension is irradiated by more than one field, then coherent interference between the electromagnetic waves will give rise to a modulation of the preferred particle orientation. This modulation of the dielectric constant is an optical index grating that can be utilized for phase conjugation.

If the interaction potential is time dependent, as occurs with a single beam or degenerate beams, then in steady-state the particle orientational distribution $n(\theta, \phi; r) = n_0 \exp[-U(\theta, \phi; r)/kT]/Z$ with n_0 the particle density in the absence of external fields and Z the partition function.

We first consider the case of a single microwave or millimeter wave pump beam irradiating a shaped microparticle suspension that is kept in a waveguide. The incident pump beam is written as $E(r, t) = eA(r) \cos[K \cdot r - \omega t]$ where e is the unit polarization vector, $A(r)$ is the field amplitude, K the propagation wavevector and ω is the frequency. The interaction potential is

$$U(\theta, \phi; r, t) = -\frac{1}{2}A(r)^2[\alpha_s + \frac{1}{3}\beta e \cdot K(\theta, \phi) \cdot e^*]. \quad (2.4)$$

If the pump beam intensity is unaffected by the medium, the microparticle orientational distribution for a suspension irradiated plane electromagnetic wave is

$$n(\theta, \phi; r) = n_0 \exp\left[\frac{1}{3}g_1 e \cdot K(\theta, \phi) \cdot e^*\right] \int d\phi \int d\theta \sin \theta \exp[g_1 e \cdot K(\theta, \phi) \cdot e^*] \quad (2.5)$$

where $g_1 = \beta A^2/4 kT$ is a dimensionless field strength. The isotropic part of the microparticle polarizability is coupled to the particle's translational degrees of freedom and does not enter into the problem. For the shaped microparticle distribution used in our microwave experiments, $\beta = 10^{-11}$ esu, and for a pump intensity of 20 W/cm², $g_1 = 5$. In the weak field limit, where $g_1 \ll 1$, only a small fraction, $\delta n(\theta, \phi)$ of the microparticles are oriented by the pump beam

$$\delta n(\theta, \phi) = n_0 g_1 e \cdot K(\theta, \phi) \cdot e^*. \quad (2.6)$$

In the strong field regime, where $g \gg 1$, most of the microparticles are aligned by the pump beam. If the pump wave is linearly polarized, then the microparticle orientational distribution is

$$n_z(\theta, \phi) = (g_1/\pi)^{1/2} n_0 \exp[g_1 \cos^2 \theta] / \text{erf}[g_1^{-1/2}]. \quad (2.7)$$

The macroscopic dipole moment $P(r, t) = \langle p(\theta, \phi; r, t) n(\theta, \phi; r, t) \rangle$ where the brackets imply an angular average over (θ, ϕ) . If U is independent of position, the particle density will be spatially uniform and

$$P(r, t) = \alpha_s n_0 E(r, t) + \frac{1}{3}\beta \langle n(\theta, \phi; t) K(\theta, \phi) \rangle \cdot E(r, t). \quad (2.8)$$

The first term on the rhs of (2.8) is negligible. The next term depends critically on the anisotropic properties of the suspension; it vanishes if $n(\theta, \phi; t) = n_0$. In the limit that $U/kT \ll 1$, this term can be written as

$$\delta P(r, t) = n_0 g_1 \langle e \cdot K(\theta, \phi) \cdot e^* K(\theta, \phi) \rangle \cdot E(r, t). \quad (2.9)$$

If we define $Q_{ij,kl} = \langle K_{ij}(\theta, \phi) K_{kl}(\theta, \phi) \rangle$, then it is obvious that only those components of $\delta P(r, t)$ are nonzero for which all of the indices are the same or ones in which pairs are equal. Thus, if all of the beams are linearly polarized in the same direction (taken to define the z -direction), then only the z -component of $\delta P(r, t)$ is nonzero.

The microparticle suspensions dynamics are described by the Planck-Nernst (PN) equation [13] for the particle density, $n(\theta, \phi; r, t)$. This equation specifies how $n(\theta, \phi; r, t)$ changes in time under the action of field-induced forces, torques and diffusion due to Brownian motion. At microwave and millimeter wavelengths, only the orientational coordinates vary on the time scales of interest and we can ignore changes in the microparticle density at a given point r .

The PN equation is basically a conservation equation in the sense that the change in density of particles pointing in a given direction (θ, ϕ) obeys $\partial n(\theta, \phi)/\partial t = -L \cdot J(\theta, \phi)$, with $J(\theta, \phi)$ the particle flux. There are two contributions to J : a diffusive current $J_D(\theta, \phi) = -\Theta_0 L n(\theta, \phi)$ and a drift current $J_F(\theta, \phi) = \Theta_0 [\Gamma(\theta, \phi)/kT] n(\theta, \phi)$. The PN equation is then

$$\begin{aligned} \partial n(\theta, \phi)/\partial t + \Theta_0 L^2 n(\theta, \phi) \\ = -\Theta_0/kTL \cdot [\Gamma(\theta, \phi) n(\theta, \phi)]. \end{aligned} \quad (2.10)$$

In steady-state, $\partial n(\theta, \phi)/\partial t = 0$ and the solution of (2.10) is the Maxwell-Boltzman distribution. In the weak field regime, where $U/kT \ll 1$, only a small fraction of the microparticles $\delta n \ll n_0$ are influenced by the applied fields and the PN equation can be solved perturbatively. Setting $n(\theta, \phi) = n_0 + \delta n(\theta, \phi)$ where $\delta n(\theta, \phi)$ is of order U/kT , we have

$$\begin{aligned} \partial \delta n(t; \theta, \phi)/\partial t + \Theta_0 L^2 \delta n(t; \theta, \phi) \\ = (\Theta_0/kT) n_0 L^2 [U(t; \theta, \phi)]. \end{aligned} \quad (2.11)$$

The angular dependence of $U(\theta, \phi)$ is given by the matrix elements of $K(\theta, \phi)$. Since these elements can all be expressed as a linear combination of the $Y_2^m(\theta, \phi)$ it follows that $L^2[U(\theta, \phi)] = 6U(\theta, \phi)$. The orientational diffusion time is defined by, $\tau_R = 1/6\Theta_0$, and noting that $\delta n(t; \theta, \phi) = 0$ at $t = 0$,

$$\delta n(t, \theta, \phi) = n_0 \int_0^t dt' \exp\left[-\frac{(t-t')}{\tau_R}\right] \frac{U(t', \theta, \phi)}{kT}. \quad (2.12)$$

In the strong field regime, where $U/kT \geq 1$, most of the microparticles are oriented by the applied fields. In

that case (2.15d) must be solved exactly. This can be done by expanding the density in the spherical harmonics

$$n(r; \theta, \phi) = \sum_{l=0}^{\infty} c_{2l}(t) Y_{2l}^0(\theta, \phi) \quad (2.13)$$

where we have used the fact that symmetry requires that only the even-order terms contribute to the sum. The resultant equations are of the form $dn(t)/dt = An(t)$ where A is a non-Hermitean matrix and can be solved numerically.

III. MICROWAVE PHASE CONJUGATION

The theory for microwave phase conjugation using a shaped particle suspension is discussed in III-A. In III-B and III-C the detailed properties of the suspension and our experimental procedure are reviewed. In III-D the experimental observations are presented and correlated them with theory.

A. Theoretical Formulation

In our phase conjugation experiments, the suspension was irradiated by two, degenerate microwave beams that wrote a volume index grating. The vector sum of these two write beams, each oscillating at the frequency ω , is denoted by $E_D(r, t) = E_1(r, t) + E_2(r, t)$, where

$$E_j(r, t) = \frac{1}{2} E_{0j} [A_j(z, t) e_x + B_j(z, t) e_y] \cdot \exp[i(K_j \cdot r - \omega t)] + cc \quad (3.1)$$

with E_{0j} and K_j the initial amplitude and wave vector of the j th beam. The functions $A_j(z, t)$, $B_j(z, t)$ specify the two polarization components of the j th beam as it propagates through the shaped microparticle suspension, and e_x (e_y) is a unit vector in the x (y) direction. The interaction potential, $U_D(r, \Omega)$ between the particles and the write beams is

$$U_D(r) = g[A_1 A_2^* K_{xx} + B_1 B_2^* K_{xx} + (A_1 B_2^* + B_1 A_2^*) K_{xy}] \cdot \exp[iQ \cdot r] + cc \quad (3.2)$$

with $Q \equiv K_1 - K_2$, $g \equiv \beta E_{01} E_{02} / 4 kT$ and $K_{jk} \equiv e_j \cdot K \cdot e_k$. For static index gratings, the portion of the microparticle distribution function of interest is $\delta n(r; \theta, \phi) = -n_0 U_D(r, \theta, \phi) / kT$. The $\mu\nu$ component of the optical index tensor grating, $\delta\epsilon_{\mu\nu}(r, \theta, \phi)$ arising from these microparticle gratings, is given by

$$\delta\epsilon_{\mu\nu}(r) = -\frac{1}{3} n_0 g \langle [A_1 A_2^* K_{xx} + B_1 B_2^* K_{xx} + (A_1 B_2^* + B_1 A_2^*) K_{xy}] \alpha_{\mu\nu} \rangle \cdot \exp[iQ \cdot r] + cc \quad (3.3)$$

The microparticle distribution is, to first-order in the write beams,

$$n(r) = n_0 - \frac{1}{3} n_0 g [A_1 A_2^* K_{xx} + B_1 B_2^* K_{xx} + (A_1 B_2^* + B_1 A_2^*) K_{xy}] \exp[iQ \cdot r] + cc \quad (3.4)$$

The terms that are proportional to g give rise to the orientational grating and tend to point in a direction specified by the write beams.

In standard optical phase conjugation all of the beams are focussed into the medium at the same time; and energy can be exchanged between the probe and conjugate waves. Furthermore there are two gratings that are formed by the pump and probe beams. These gratings have spatial periodicities of $K \pm Q$. Each grating will diffract the counterpropagating pump and form a conjugate beam.

For the case of collinear pump and probe beams, as was used in the waveguide experiments, there are significant difficulties associated with beam discrimination. To this end, we modulated one of the pump beams so as to ensure identification of conjugate beam photons. When this beam coherently diffracted off of the grating formed by the unmodulated pump and probe waves, the conjugate beam so formed maintained the original amplitude modulation. On the other hand, the grating formed by the modulated pump and probe wave will also be static because the medium cannot respond to a signal that changes at 300 Hz. However, since the beam is amplitude and not phase modulated, the time averaged response of the medium will not be zero, but rather one-half that for an unmodulated beam. The counterpropagating pump beam will scatter off of this static grating to form an unmodulated phase conjugate wave. This beam is unmodulated and cannot be distinguished from back reflections of the probe beam. Although we can model the experiment outlined in Section III-C by including only the orientational grating set up by the unmodulated pump and probe beams, it is of interest to examine the effects of both gratings.

The nonlinear polarization vector is

$$P(r, t) = n_0 \frac{\beta^2}{18 kT} \langle [\overline{E \cdot K \cdot E}] K \cdot E(r, t) \rangle \equiv \Delta\epsilon \cdot E \quad (3.5)$$

where we have used the fact that an average of $\langle K(\theta, \phi) \rangle = 0$ for an isotropic distribution. For phase conjugation,

$$E(r, t) = \sum_{j=1,2,p,c} E_{0j}(r, t) e_j \exp[i(\omega_j t - k_j \cdot r)] + cc \quad (3.6)$$

where $j = 1(2)$ is the modulated (unmodulated) pump beam, $j = p$ the probe wave, and $j = c$ the phase conjugate beam. Here $E_{0j}(r, t)$ is the complex field amplitude, e_j the normalized polarization vector and $\omega_j(k_j)$ the frequency (wave vector) of the j th beam. Only the amplitude modulated pump beam and the phase conjugate wave are time-dependent. In the fully degenerate case: $\omega_j = \omega$, $k_1 = -k_2 = K$ and $k_p = -k_c = Q$. Since the probe and conjugate waves vary as $\exp[i(\omega t \pm Q \cdot r)]$, it follows that only those terms with the same phasors will contribute to the form the conjugate wave. The component the third-order polarization of interest, $P_{NL}(r, t) = P_{NL}^{a+} + P_{NL}^{a-}$, with P_{NL}^{a+} (P_{NL}^{a-}) is the nonlinear polarizability associated with the conjugate wave (amplification of the probe

beam):

$$\begin{aligned} P_{NL}^{a,+}(r, t) = & n_0 \beta g E_p^* \left[\frac{1}{2} \langle (e_p^* \cdot K \cdot e_1) K \cdot e_2 \rangle \right. \\ & + \langle (e_p^* \cdot K \cdot e_2) K \cdot e_1 \rangle f(t) \left. \right] \\ & \cdot \exp [i(\omega t + Q \cdot r)] + cc. \end{aligned} \quad (3.7)$$

A similar expression holds for $P_{NL}^{a,-}$. The factor of 1, 2 arises from the averaging of the grating created by the amplitude modulated pump beam and the probe wave. The quantity $f(t)$ is the amplitude modulation function.

Next, we construct the wave equations for the propagation of the phase conjugate beam and the probe wave for steady-state situations. Inserting the nonlinear polarization into the wave equation, separating the modulated and unmodulated terms probe and conjugate waves

$$\begin{aligned} (2Q \cdot \nabla + Q/2L_S) E_C^{\text{mod}} e_C \\ = i n_0 \beta Q^2 (g/9) \langle (e_p \cdot K \cdot e_2) e_1 \cdot K \rangle E_p^* \end{aligned} \quad (3.8a)$$

$$\begin{aligned} (2Q \cdot \nabla + Q/2L_S) E_C^{\text{mod}} e_C \\ = + \frac{1}{2} i n_0 \beta Q^2 (g/9) \langle (e_p \cdot K \cdot e_1) e_2 \cdot K \rangle E_p^{un*} \end{aligned} \quad (3.8b)$$

$$\begin{aligned} (2Q \cdot \nabla - Q/2L_S) E_p^{\text{mod}} e_p \\ = -i n_0 \beta Q^2 (g/9) \langle (e_C^* \cdot K \cdot e_2) e_1 \cdot K \rangle E_C^* \end{aligned} \quad (3.8c)$$

$$\begin{aligned} (2iQ \cdot \nabla - Q/2L_S) E_p^{un} e_p \\ = \frac{1}{2} i n_0 \beta Q^2 (g/9) \langle (e_C^* \cdot K \cdot e_1) e_2 \cdot K \rangle E_C^{\text{mod}*}. \end{aligned} \quad (3.8d)$$

The angular brackets imply an orientational average over an isotropic distribution. Note that the total conjugate and probe beams enter into the nonlinear polarization for the modulated components. This feature arises because for amplitude modulated functions, $f(t) = f(t)^2$. Also only the unmodulated components enter into the nonlinear polarizations for E_C^{unmod} and E_p^{unmod} . In the small signal regime energy transfer between the probe and conjugate beams is negligible and we can replace E_p^* in (3.8a) and (3.8b) by the initial probe beam and integrate these equations directly. This gives

$$\begin{aligned} E_C^{\text{mod}} = i n_0 Q L g \beta / 9 \langle (e_p \cdot K \cdot e_2) e_1 \cdot K \cdot e_C \rangle E_p^*(0) \\ \equiv i \kappa L E_p^*(0) \end{aligned} \quad (3.9a)$$

$$\begin{aligned} E_C^{un} = i n_0 Q L g \beta / 18 \langle (e_p \cdot K \cdot e_2) e_1 \cdot K \cdot e_C \rangle E_p^*(0) \\ \equiv \frac{1}{2} i \kappa L E_p^*(0). \end{aligned} \quad (3.9b)$$

The depth of the grating formed by the modulated pump and probe beams is one-half that of the grating formed by the modulated pump and probe beams. In the small signal regime, the intensity of the modulated conjugate wave is $(\kappa L)^2 I_p$ while that of the unmodulated beam is

$(1/4)(\kappa L)^2 I_p$, provided the pump beams are parallel polarized as was done in the experiment.

For the case in which the probe beam is polarized orthogonal to the two pump waves $\kappa L = (8\pi/15) n_0 \beta g L / \lambda$. For typical suspensions, $n_0 \approx 10^8 \text{ cm}^{-3}$, $\beta \approx 10^{-11} \text{ cm}^3$, $L/\lambda \approx 100$ and $g \approx 1$. Thus, κL is on the order of 0.2; implying efficiencies on the order of a few percent at cm wavelengths.

B. Nonlinear Medium

Various types of shaped microparticle suspensions were investigated, including aluminum platelets (used in metallic paints), chromium dioxide microrods (used in magnetic recording media), ground up alumina fibers, silicon carbide fibers, boron fibers, zinc sulfide, guanine platelets (used in rheoscopic fluids (Kalliroscope Corp., Groton, MA)), liquid crystals, ferrofluids, iron fillings, and even magnetic bacteria! Severe problems exist with those materials such as microwave and millimeter wave attenuation, particle agglomeration, unstable particle suspension, irregular eddy currents created by nonuniform thermal effect, and insufficient orientational susceptibility difference. The medium finally found to exhibit a significant and controllable Kerr effect was a suspension of short graphite fibers 7 to 8 microns in diameter. These fibers are available commercially ("Fortifil 5" from Great Lakes Carbon) in 3 mm lengths, and ground up to yield lengths primarily in the range from 30 to 40 microns. Their low density helps to keep them in suspensions. The conductivity of graphite is sufficiently high on the order of 10^5 mho/m . The high conductivity of graphite is crucial in dispersing the particles in suspension. Dielectric particles tend to clump together due to the surface charges accumulated by the particles. Since one requirement of the suspending fluid is to be nonpolar due to the fact that polar solutions absorb microwave and millimeter wave radiation, the surface charges cannot dissipate. Therefore, the advantage of highly conductive microparticles is that they do not have local charge imbalance that would cause them to clump.

The suspending fluid used in the present study consists of a binary mixture of 60% mineral oil and 40% heptane. A maximum suspension stability of around 30 minutes was obtained which is adequate to perform the experiment. The resulting suspension with graphite particles with 0.1 volume percent is highly transparent, having loss lengths (1/e attenuation) of 140 cm at 18 GHz and 54 cm at 94 GHz. It is not known what fraction of the loss is due to scattering, although a small fraction is expected since the particles are much smaller than the wavelength.

C. Experimental Formulation

The experiments were conducted in a single-mode hollow metal waveguide to minimize thermal convection currents which might disrupt reorientation of the particles, to maximize signal intensity, and to allow interaction lengths limited only by absorption. These advantages are offset

by the difficulties encountered in discriminating between the various collinear waves emanating from the medium. The anisotropic characteristics of elongated microparticle suspensions give rise to a polarization dependence in $\chi^{(3)}$ which allows the use of the geometry utilized for isolating the conjugate wave depicted in Fig. 1. The polarizations of the probe and conjugate waves are linear and parallel to each other, but orthogonal to both the pump waves. Pump wave #1 is amplitude modulated at 300 Hz, while pump wave #2 and the probe are unmodulated. Two anisotropic volume gratings are created by the probe wave interacting with each of the pumps. Although one of the pump waves is amplitude modulated, neither grating is modulated because the medium response time (≈ 10 s) is much slower than the modulation period. Consequently, only the grating which scatters pumps wave #1 will generate phase conjugate radiation which is amplitude modulated at 300 Hz. This radiation is easily distinguished from the unmodulated probe reflection off the interfaces at the ends of the sample chamber. Scattering of pump #2 will produce an unmodulated phase conjugate wave which, however, cannot be readily distinguished from the reflected probe. The polarization of each pump wave is rotated by 90° as it scatters to form a conjugate wave. As shown schematically in Fig. 1, an rf oscillator at a frequency tunable around 18 GHz drives a traveling wave tube (TWT) amplifier which produces a maximum continuous power of 20 W. A 3-dB directional coupler splits the power equally to form the counterpropagating pump wave #2 and the probe wave. The probe wave goes through a variable attenuator and feeds into the H-plane port of the orthogonal-mode transducer (OMT) #1. An OMT is a waveguide analog of an optical polarizing beamsplitter which enables us to separate and combine beam polarizations. The probe wave passes through the 72-cm sample chamber inside a square waveguide of 1.36-c, 2 cross sectional area and terminates at the H-plane port of OMT #2. The liquid sample is contained by two TFE windows. Pump wave #1 is created by taking a fraction of the rf power via a 6-dB coaxial coupler. It is then square-wave modulated by a p-i-n diode at 300 Hz and amplified by a lower power amplifier with a maximum output of 100 mW. This modulated pump wave is fed into the E plane port of OMT #1. The modulated conjugate beam exits the H plane port of OMT #1 and is detected by a lock-in amplifier via the 10 dB directional coupler. The leakage from the E-plane to the H-plane port of OMT #2 is about -40 dB, so the power reaching the detector from pump wave #2 is below the detection limit.

D. Experimental Results and Comparison with Theory

Fig. 2 depicts the phase-conjugate power as a function of the probe power for the case in which the power of the modulated pump #1 is 12 mW and the cw pump #2 is 7.5 W. The phase-conjugate power varies linearly with probe power as expected and is 1 mW at a probe power of 10 W, corresponding to a nonlinear reflectivity of approxi-

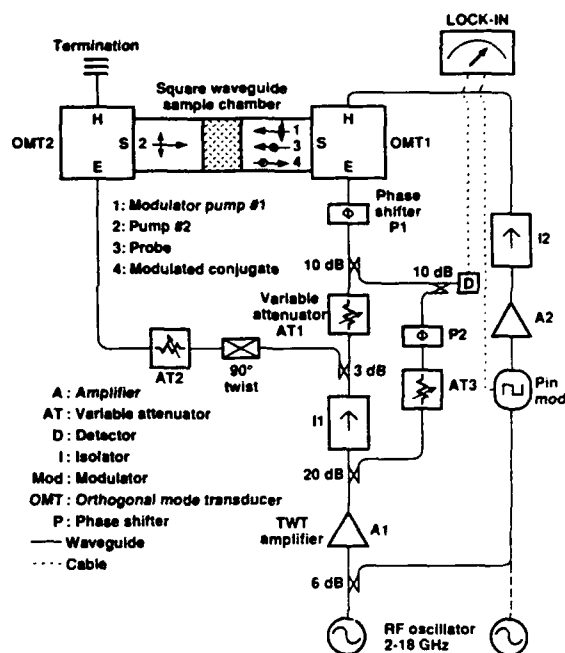


Fig. 1. Experimental configuration for demonstrating phase conjugation in a waveguide at 94 GHz.

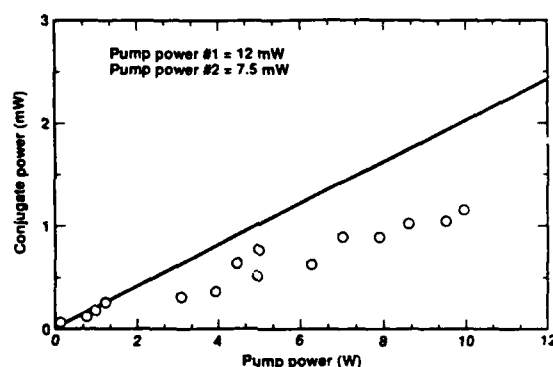


Fig. 2. Depicts the phase-conjugate power as a function of the probe power for the case in which the power of the modulated pump #1 is 12 mW and the cw pump #2 is 7.5 W.

mately 0.01%. If we employ the values of β and n_0 obtained from the optical-birefringence measurements, we obtain a theoretical average value of 0.02%. The discrepancy can be attributed partially to slight differences between the two suspensions and is discussed below. The low reflectivity can be attributed partially to the unconventional power ratios used in the present experiment in which the modulated pump has much less power than the probe wave.

The efficiency of the phase conjugate wave can be increased significantly if the power of the first pump is as great as that of the second pump, and the probe power reduced accordingly. It is implemented by replacing the low power amplifier A2 by a 10 W cw TWT amplifier in Fig. 1. The probe power can be decreased by the setting of the attenuator #1. Fig. 3 depicts the phase-conjugate power as a function of the probe power for the case in which the power of the modulated pump #1 is 8 W and cw pump #2 is 7.5 W. The phase conjugate power varies

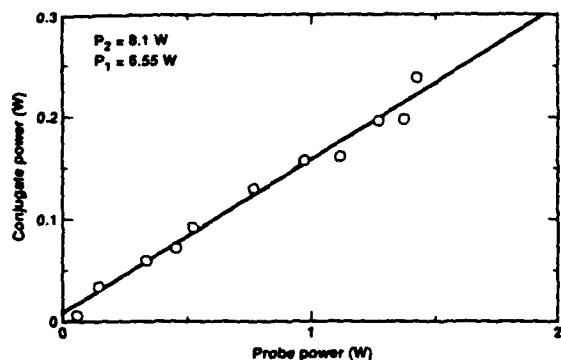


Fig. 3. Depicts the phase-conjugate power as a function of the probe power for the case in which the power of the modulated pump #1 is 8 W and cw pump #2 is 7.5 W.

linearly with the probe power as expected and corresponding to a nonlinear high efficiency of approximately 15%.

Measurements were also performed by keeping the probe power constant and varying the power of pump #1. Pump #2 was kept constant at 8 W. The measurements were done with three constant probe powers of 0.141 W, 0.8 W, and 1.41 W. In all case, the conjugate power varies linearly with pump power #1 which indicate that the measurements are still within the small signal regime. These measurements are presented in Fig. 4.

The transient evolution of the conjugate power is depicted in Fig. 5. It is obtained by first having the steady probe and modulated pump #1 initially on and then switching on pump #2, at $t = 0$. As soon as the second pump wave is switched on, a grating begins to form that diffracts pump #1 to produce a modulated conjugate wave which is observed on the lock in amplifier. Thus the transient behavior of the modulated conjugate wave reflects the formation and approach to steady state of the orientational grating formed by the nonlinear interaction of the probe and pump #2 waves. Pump wave #2 is subsequently turned off at time $t = 22$ seconds to allow the index grating to deteriorate due to thermal diffusion, leading to the observed decay of the modulated phase conjugate signal. The medium has grating formation and decay times of approximately 10 seconds, which is a factor of three faster than the earlier Mach-Zehnder interferometer experiment as well as the theoretical prediction of 33 seconds. This discrepancy implies that the particle size is somewhat smaller for this suspension than the one employed in the birefringence experiments and is consistent with the smaller than expected reflectivity measurement.

Confinement inside a single mode waveguide prevents the propagation of wavefront perturbations in this experiment. Phase conjugation therefore reduces to one dimension, capable only of correcting for longitudinal phase error. A phase shifter can be used to induce this phase error by inserting it in the probe's path before the H-plane port of OMT #1, as shown in Fig. 1. The phase information of the conjugate signal can be obtained by comparing it with a reference which is taken from the TWT amplifier via a 20-dB directional coupler. Variable attenuator #3

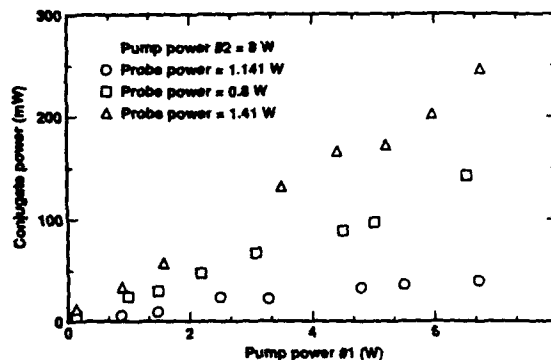


Fig. 4. Depicts the phase-conjugate power as a function of the power of the unmodulated pump beam for the cases in which the probe power is 0.141 W, 0.8 W and 1.41 W.

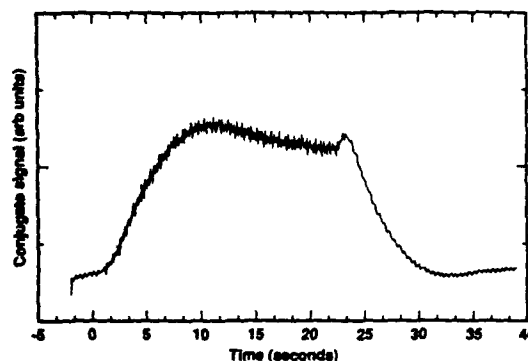


Fig. 5. The transient evolution of the conjugate power.

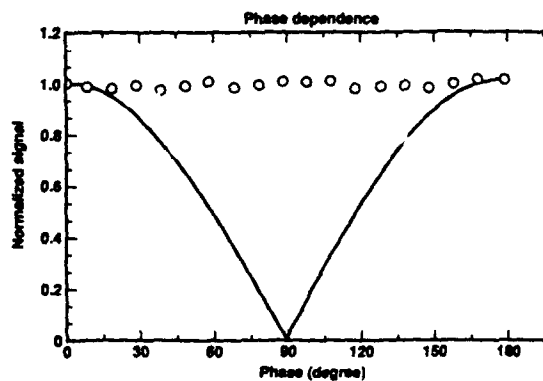


Fig. 6. Shows the equilibrium conjugated signal power (circles) as a function of the settings of phase shifter #1. For comparison, the solid curve represents the signal which is not conjugated.

and phase shifter #2 are inserted for proper adjustment of the reference which is combined with the conjugate beam via a 10 dB directional coupler. Phase shifter #2 is adjusted so that a maximum signal is shown on the lock-in amplifier. As phase shifter #1 is varied, the signal at the lock-in amplifier should not vary if the phase is truly corrected by the phase-conjugation process. In these measurements, the actual dynamics of the phase correction process is observed due to the slow response of the medium (time constant ≈ 10 s). The signal first decreases and then returns to its initial value as phase shifter #1 is varied. Fig. 6 shows the equilibrium conjugated signal power (circles) as a function of the settings of phase shif-

ter #1. For comparison, the solid curve represents the signal which is not conjugated. The same experiment was conducted on the secondary peak at 50 MHz, and phase conjugation was again observed.

IV. DISCUSSION AND CONCLUSIONS

Until now nonlinear optics has focused on visible and infrared wavelengths. This is due to the lack of suitable materials that can be used as the active medium in the microwave/millimeter wave region of the spectrum. In particular, since $\kappa \propto \lambda^{-3}$, there is a nine orders of magnitude decrease in κ , due to the increase in λ that one encounters in going from the visible to the microwave region of the spectrum. These considerations suggest that phase conjugation cannot be achieved at long wavelengths, unless novel materials can be found to overcome these difficulties.

Our studies indicate that shaped particle suspensions are well suited for achieving certain classes of nonlinear optical phenomena at microwave and millimeter wavelengths. Specifically, since they are highly polarizable their third-order susceptibilities are very large, approximately nine orders of magnitude greater than CS_2 . Thus, low microwave power sources will generate large changes in the dielectric constant of the suspension. This feature of suspension electrodynamics can be readily exploited for such static third-order processes as optical birefringence and phase conjugation via degenerate four-wave mixing. Furthermore, the mechanism by which these changes in the suspension's dielectric constant are achieved involves rotation of the microparticles in a direction specified by the applied fields. Thus in the diffusive regime, the response time depends only the particle size and shape, the fluid viscosity and temperature of the host.

Crucial to long wavelength applications is the fact that the response time for orientational gratings in shaped microparticle suspensions is independent of radiation wavelength or grating spacing. This feature can be appreciated by noting that for translational or density gratings, the grating formation time scales as the square of the grating spacing. Thus, density gratings are completely unsuitable for microwave applications, as typical formation times are on the order of days. However, the time it takes for a $10\ \mu$ particle to rotate through π radians is on the order of seconds, so that nonlinear optics using static orientational gratings in shaped microparticle suspensions are quite feasible at long wavelengths. Note, that the slow medium response times preclude the possibility of carrying out any frequency-mixing processes such as harmonic, frequency-difference or frequency-sum generation.

As a natural follow on of this research we are presently exploring a new class of artificial dielectrics, namely optomechanical media [14], [15]. These active media consist of a three-dimensional array of electrically small, anisotropic particles. These particles are supported by some mechanical means, and are free to either roll or reorient via the action of electrostrictive forces and torques gen-

erated by polarized radiation. These electrostrictive torques are similar to those discussed in this paper as they rotate the particles into a preferred direction set by the net polarization vector of the incident radiation. Rotation of the particles gives rise to orientation index gratings that can be used for active optical processes.

In conclusion, we note that in the past ten years optical phase conjugation, at visible and infrared wavelengths, has stirred intense interest in the scientific and engineering communities. This attention arises from the fundamental scientific significance as well as the vast number of important applications for this process. Until these studies were initiated very little had been achieved with regards to generating phase conjugate radiation at microwave and millimeter wavelengths. This statement is underscored by the enormous investment in communication and other equipment that modern nations have in this region of the spectrum. Obvious applications to radar, navigation and microwave communications as well as the salient scientific value of materials research and fundamental nonlinear optics justifies detailed research into achieving microwave phase conjugation. We hope that this work demonstrates the feasibility of working in this area and will stimulate research towards phase conjugation at these long wavelengths in other nonlinear media.

ACKNOWLEDGMENT

UCLA acknowledges partial support by the Air Force Office of Scientific Research.

REFERENCES

- [1] Y. R. Shen, *The Principles of Nonlinear Optics*. New York: Wiley, 1984.
- [2] E. G. Hanson, Y. R. Shen, and G. Wong, *Phys. Rev.*, vol. 14, p. 1281, 1986.
- [3] R. W. Hellwarth, *Prog. Quantum Electron.*, vol. 5, no. 1, 1977.
- [4] R. Pizzoferrato, D. Rogovin, and J. Scholl, *Opt. Lett.*, vol. 16, p. 297, 1991.
- [5] R. Pizzoferrato, M. Marinelli, U. Zammit, F. Scudieri, S. Martellucci, and R. Romagnoli, *Opt. Lett.*, vol. 68, p. 231, 1988.
- [6] B. Bobbs, R. Shih, H. R. Fetterman, and W. W. Ho, *App. Phys. Lett.*, vol. 52, no. 4, 1988.
- [7] R. McGraw, D. Rogovin, W. Ho, B. Bobbs, R. Shih and H. Fetterman, *Phys. Rev. Lett.*, vol. 61, p. 943, 1988.
- [8] R. Shih, H. Fetterman, W. Ho, R. McGraw, D. Rogovin, and B. Bobbs, *Phys. Rev. Lett.*, vol. 65, p. 579, 1990.
- [9] —, *SPIE*, vol. 1220, p. 46, *Nonlinear Optics*, 1990.
- [10] A. Ashkin, J. M. Dziedzic, and P. W. Smith, *Optics Lett.*, vol. 7, p. 276, 1982.
- [11] P. W. Smith, A. Ashkin, J. E. Bjorkholm, and D. J. Eilenberger, *Optics Lett.*, vol. 10, p. 276, 1984.
- [12] P. W. Smith, A. Ashkin, and W. J. Tomlinson, *Optics Lett.*, vol. 6, p. 276, 1981.
- [13] D. Rogovin, *Phys. Rev.*, A32, p. 2837, 1985.
- [14] D. Rogovin and T. P. Shen, "Active opto-mechanical media for nonlinear microwave processes," *IEEE Microwave Guided Wave Lett.*, vol. 1, p. 388, 1991.
- [15] D. Rogovin and T. P. Shen, "Orientational optomechanical media for microwave applications," *J. Applied Physics*, vol. 71, p. 5281, 1991, as a Communication.

D. Rogovin received the Ph.D. from the University of Pennsylvania in 1970 in theoretical physics, specializing in superconductivity and Josephson tunneling.

He went from there to Massachusetts Institute of Technology and following that to the Optical Science Center at the University of Arizona where he did fundamental studies in quantum and nonlinear optics, laser physics and superconductivity. He then joined Science Applications, Inc, where he continued this work. Following this, he joined Rockwell Science Center as a Member of the Technical Staff and for the last five years, as manager of the Mathematical Physics Group. Dr. Rogovin has published over 100 papers in physics and engineering literature.

R. L. McGraw received the B.S. degree in 1972 from Drexel University, and the M.S. and Ph.D. degrees from the University of Chicago in 1974 and 1979, respectively.

He is presently a member of Technical Staff, Rockwell International Science Center. At the Science Center since 1985, Dr. McGraw is currently engaged in studies of nucleation and nonlinear optics and is Program Manager for several programs in these areas. From 1980 to 1985 he held a scientific staff position in the Environmental Chemistry Division, Brookhaven National Laboratory. From 1977 to 1980 he was a postdoctoral research associate in the Chemistry Department at UCLA.

W. W. Ho is a member of the technical staff in the Applied Spectroscopy Department at Rockwell International Science Center. He joined the Science Center upon obtaining his Ph.D. from the Physics Department of Columbia University in 1967. Dr. Ho's current research interests include electromagnetic properties of matter and novel optical and microwave device concept development which utilizes various nonlinear properties of advanced materials.

R. Shih, photograph and biography not available at the time of publication.

H. R. Fetterman, photograph and biography not available at the time of publication.

B. Bobbs, photograph and biography not available at the time of publication.
